The Dissertation Committee for Amritesh Rai certifies that this is the approved version of the following dissertation:

Functionality Enhancement of Two-Dimensional Transition Metal Dichalcogenide-Based Transistors

Committee:

Sanjay K. Banerjee, Supervisor

Deji Akinwande

Leonard F. Register

S. V. Sreenivasan

Yaguo Wang

Functionality Enhancement of Two-Dimensional Transition Metal Dichalcogenide-Based Transistors

by

Amritesh Rai

Dissertation

Presented to the Faculty of the Graduate School of

The University of Texas at Austin

in Partial Fulfillment

of the Requirements

for the Degree of

Doctor of Philosophy

The University of Texas at Austin

August 2019

Dedicated to my grandparents and sister

Acknowledgements

I have had an absolutely incredible and transformational journey at The University of Texas at Austin over the past seven years thanks to the great pool of professors, research staff, peers, seniors and juniors that I crossed paths with, as well as the amazing opportunities that came my way. First and foremost, none of it would not have been possible without the opportunity I was given by my superstar advisor, Professor Sanjay K. Banerjee, to work as a graduate research assistant in his group. I still remember the day I received Professor Banerjee's offer *via* an email while I was an undergraduate student at The Ohio State University, and I was thrilled with joy. I could not have asked for a better Ph.D. advisor and it has been an honor working in the 'Banerjee Lab'. Thank you Professor Banerjee for the tremendous support and guidance all throughout these years, for supporting me financially, for providing me with all the necessary resources to conduct my research, for giving me the absolute freedom to explore, design and work on novel experiments, for allowing me to collaborate with various research groups both within and outside UT, for allowing me to do two internships, and for always having my back. Other than research and technical skills, there were several other useful non-technical skills and nuances that I picked up just by observing Professor Banerjee and the manner in which he led his troops and handled different situations. Thank you once again Professor Banerjee for being a great advisor, mentor and leader. I hope to be a superstar like you one day.

A special thank you to all the professors on my Ph.D. Dissertation Committee – Professor Deji Akinwande, Professor Leonard F. Register, Professor S. V. Sreenivasan and Professor Yaguo Wang. I am very grateful to Professor Akinwande for giving me a lot of great advice and support over the years, for inviting me to give several guest lectures in his graduate level course on 'Carbon and 2D Materials', and for agreeing to serve as the co-faculty advisor, along with Professor Jean Anne Incorvia, of the IEEE Graduate Student Chapter that I founded in the IEEE Central Texas Section. Under your dynamic leadership, I am sure that the IEEE Graduate Student Chapter will flourish in the years to come and will provide a great platform for our ECE graduate students to volunteer, take up leadership roles and grow in their careers. I am grateful to Professor Leonard F. Register for teaching

me the basics of Semiconductor Physics *via* his skillfully designed course and for his guidance in overseeing a lot of the theoretical work that has supported my research. I am very lucky to have had the opportunity to work with, and learn from, Professor S. V. Sreenivasan as part of UT's NSF NASCENT Engineering Research Center (ERC). Serving on the Student Leadership Council of the NASCENT ERC was one of my best experiences at UT. The invaluable lessons in management and leadership that I learned by being part of this council will certainly stand me in good stead in the years to come. I am grateful to Professor Yaguo Wang for letting me collaborate with her research group and learn about her novel research techniques. Thank you for having faith in me and letting me present on your behalf at the 2018 APS March Meeting in Los Angeles. I am certain that this collaboration between the two groups will continue to grow and result in plenty more published papers in the years to come.

Other than my committee members, I would like to thank all the wonderful professors at UT and other universities who have positively shaped my life and experience. I am extremely grateful to Professor Paul R. Berger of Ohio State for giving me the opportunity to work as an undergraduate researcher in his group. The research experience I gained as an undergrad at Ohio State certainly established a solid foundation for the years that were to follow. I am lucky to have collaborated with Professor Andrew C. Kummel of UC San Diego. Professor Kummel has been one of the most friendly and approachable professors I have met and there was never a dull moment whenever he was around. Thank you Professor Kummel for all the fun conversations and for your valuable discussions and insights over the past few years. Together with Jun Hong Park, I am glad we were able to cross-collaborate across three different time zones and two continents to finally publish a paper in a top journal. I am grateful to Professor Emanuel Tutuc at UT for always agreeing to have insightful discussions with me on various research and academic topics, and for playing an important part in some of the research papers that I have published. I am grateful to Professor Roger T. Bonnecaze, past Co-Chair of the NASCENT ERC, for all the valuable advice I received during my tenure with NASCENT's Student Leadership Council. I would like to extend my gratitude to all the other professors whose courses I

took at UT – Professor Jack C. Lee, Professor Willy Fischler, Professor Paul S. Ho, Professor Michael Orshansky, Professor Nicole Benedek, Professor Allen H. MacDonald, Professor Seth R. Bank, and Professor Edward Yu. The technical content I learned from the courses taught by them were certainly indispensable for the understanding of all the research work I undertook at UT. I would also like to thank Professor Jaydeep Kulkarni for having insightful discussions with me and sharing his advice.

My research stint at UT's Microelectronics Research Center (MRC) as well as the NASCENT ERC would not have been successful without the support of all the fabulous MRC, NASCENT and Texas Materials Institute (TMI) administrative and support staff. They form the backbone and support system which allows our research centers to run smoothly and successfully. At MRC, I would like to thank Jean Toll for being incredibly nice and supportive all throughout these years. Thank you for your encouragement on many an occasion, and for discussing various topics with me. I am extremely grateful to Ricardo Garcia, Jesse James and Johnny Johnson for always lending their helping hands whenever I needed them, for the useful and informative conversations, and for teaching me the various tools and techniques inside the cleanroom. I would like to thank all other MRC staff for their continuous assistance and support over the years – James Hitzfelder, Darren Robbins, Joyce Kokes, Gerlinde Sehne, Marylene Palard, William Ostler, Rick Gomez, Christine Wood, Kenneth Ziegler, Robert Stephens, Jackie Srnensky, Brenda Francis and Htay Htay Shwe. At NASCENT, a special shout-out to Risa Hartman, Janet Monaco, Larry Dunn, Tricia Berry, Matt Weldon, Darlene Yanez, and Diane McNair. Thank you for supporting me, and helping me grow, both as a person and a professional during my time at NASCENT and as a member of NASCENT's Student Leadership Council. Your support was invaluable and there were a lot of useful lessons I learned based on my interactions with all of you. At TMI, I would like to thank Hugo Celio, Raluca Gearba, Andrei Dolocan, Karalee Jarvis, Shouliang Zhang, Josh Bolinger and Damon Smith for their assistance and support on various research projects and experiments. Lastly, I would also like to thank Ana M. Dison from the Women in Engineering Program at UT for her mentorship and providing me with a conference travel grant.

I am extremely grateful to have had excellent seniors and mentors during my undergraduate and graduate school journey who have held my hands and showed me the way. I would like to thank Anisha Ramesh for mentoring me during my undergraduate research at Ohio State – there were several lessons I learned from her early on which helped me during graduate school. At UT, I am thankful to Michael Ramon and Kristen Parrish for mentoring me in the initial phase of my graduate school and for teaching me the RF measurement technique. I am thankful for my interactions with Sayan Saha who, together with Michael Ramon, made for an excellent Table Tennis partner. Special thank you to our group's post-docs, past and present, – Anupam Roy, Sushant Sonde and Samaresh Guchhait – for teaching me various aspects of research and important lessons on how to build a successful research career. A special shout-out to Anupam Roy, our beloved 'Dada', for his support and friendship throughout the years. I will always cherish the conversations we had. I am thankful to Praveenkumar Pasupathy and Rudresh Ghosh for always imparting their wisdom and insightful views on various topics. I am thankful to Sangwoo Kang for helping me with various aspects of research and for his calm and reassuring presence that always exuded positive vibes. I am grateful to have had Hema C. P. Movva as a great mentor and friend. He was always there to answer my questions and help me out whenever I found myself stuck in situations. There's plenty that I learned from him. I am thankful to Tanuj Trivedi for his companionship and useful advice on various research and non-research related issues. There were several others who mentored, helped me in my research, supported and inspired me in various ways, and my heartfelt gratitude goes out to all of them – Kyoungwhan Kim, Chris Corbet, Emmanuel Onyegam, Sk. Fahad Chowdhury, Babak Fallahazad, Urmimala Roy, Dharmendar Reddy, Yujia Zhai, Jason Mantey, Donghyi Koh, Sarmita Majumdar, Jun Hong Park, Ke Chen, Sriram Krishnamoorthy, Sambuddha Chakrabarti, Seung Heon Shin, Jaehyun Ahn, Dax Crum, Milo Holt, Dan Fine, Xuehao Mau, Donghwan Kim, Mir Mohammad Sadeghi, Maryam Mortazavi, Li Tao, Nihal Arju, Karun Vijayraghavan, Nasibeh Rahimi, Priyamvada Jadaun, Yao-Feng Chang, Martha Serna, Hamed Dalir, Dan Fine, Vaidyanathan Krishnamurthy, Burt Fowler and Brad Bringhurst.

I have been really fortunate to have been surrounded by an amazing group of peers and juniors who have helped shaped my graduate school journey. The fruitful interactions I have had with them have taught me various useful lessons, helped me grow as an individual and have established long-lasting friendships which I will cherish forever. I am thankful to Amithraj Valsaraj and Alok Valsaraj for being great colleagues and friends – our trips to Belize and the U.S. Open were a lot of fun and much-needed respites from the graduate school grind. I am thankful to Maruthi Yogeesh for being a great friend and colleague, and for always being ready to have a conversation on any topic. In particular, I will cherish our trip to the Qualcomm Innovation Fellowship Finals in San Diego. I would like to thank Atresh Sanne for his friendship and for always being ready to accompany me to an NBA game. I would like to wholeheartedly thank several others for their great companionship, support and for making my graduate school journey memorable – Deepyanti Taneja, Michael Rodder, Sayema Chowdhury, Md. Hasibul Alam, Tanmoy Pramanik, Nitin Prasad, Rik Dey, Xian Wu, Saungeun Park, Joonseok Kim, Avinash Nayak, Myungsoo Kim, Ruijing Ge, Xiaohan Wu, Wei Li, Di Wu, Weinan Zhu, Emily Walker, Ying-Chen Chen, Connor McClellan, William Hsu, Andreas Hsieh, Omar Mohammed, Harry Chou, Nima Asoudegi, Feng Wen, Will Burg, Stefano Larentis, Subrahmanya Teja, Rachel Selina Rajarathnam, Jacob Rohan, Vignesh Radhakrishnan, Shruti Jain, Akhila Mallavarapu, Janaki Vamaraju, Piyoosh Jaysaval, Sukrith Dev, Anand Chamarthy, Xin Xu, Chris Brennan, Nathaniel Sheehan, Nish Nookala, Aqyan Bhatti, Mariana Castaneda, David Cayll, Andrew Cochrane, Brennan Coffey, Liam Connolly, Preyom Dey, Juan Faria Briceno, Ziam Ghaznavi, Yuqian Gu, Kelly Liang, Robert Malakhov, Raul Lema Galindo, Himamshu Nallan, Paras Ajay, Margaret Payne, Steven Stanley, Brandon Smith, Martin Ward, Yongjian Zhou, Calla McCulley, Otitoaleke Akinola, Pranav Kumar, David Villareal, Rony Saha, Shairi Anjum, Aref Asghari, Ali Rostamian, Elham Heidari, Dmitry Kireev, Chris Luth, Ryan Schalip, Matthew Disiena, Alexander Klatt, Hannah Maxwell and Jessica Depoy.

During my graduate studies, I had the wonderful opportunity to do a couple of internships – one at the Argonne National Laboratory in Lemont, IL, and the other one at

Micron Technology, Inc. in Boise, ID. These internships provided me the exposure to what research and work was like at a National Laboratory and an industrial setting, and really helped broaden my horizons. The knowledge and experiences I gained while working at Argonne and Micron were indeed invaluable and helped me grow both as a researcher and as a professional. I am extremely grateful to Saptarshi Das who served as a great mentor and friend at the Argonne National Laboratory, and continues to be one. There were several important lessons I learned while working under him at Argonne and all the advice I received from him has been truly indispensable. I am thankful to have met Dr. Andreas Roelofs and Dr. Anirudha Sumant at Argonne who gave me advice and shared their experiences on various topics. I am also grateful to Mathew Cherukara, Badri Narayanan, Kiran Sasikumar and Kiran Kumar Kovi for being great mentors, friends and for making Argonne a truly memorable experience. I am deeply indebted to Kunal Parekh for giving me the opportunity to intern in his group at Micron last summer and for all the mentorship and advice I continue to receive from him till date. Interning at Micron was a memorable and life changing experience and gave me a good understanding of how the semiconductor industry works. I am grateful to each and every one of the individuals who I met at Micron last summer for their advice and support. I couldn't have been more delighted, and proud, to be joining an industry leader like Micron as a full-time engineer after my Ph.D.

Finally, I would like to express my deepest gratitude to my kith and kin back in India who, despite asking me the forbidden question time and again – "When will you get done with your Ph.D.?", were always there to support me whenever I needed it. I am extremely thankful to my parents for giving me all the mental, emotional and financial support, for making occasional trips to the U.S. to take me on vacations, and for being there for me at all times. I am extremely grateful to my 'Mausi', 'Mausa' and my little cousins, Akshat and Avnish, for providing me with endless love and support. I am extremely thankful to my sister and brother-in-law for their well-wishes, love, support, and for making me an Uncle to my twin nephew and niece, Vikram and Anushka, who were born while I was at UT. 'Facetiming' with them every now and then, and watching them grow over the last few years, has been an extremely enjoyable experience. I would also like to

acknowledge all the well-wishes and continuous support that I have received from all my relatives and extended family throughout the years. Last but not the least, I am extremely grateful to my girlfriend, Akanksha, for being such an amazing human being, for her endless love and support, and for always being there for me.

The graduate school journey is not just about advanced courses, research, publishing papers or attending conferences. It is also a journey about self-discovery – one that is filled with successes and failures, elation and anguish, and one that will leave you completely metamorphosized. In addition to sharpening one's technical or 'Hard' skills, it also provides ample opportunities to learn about the all-important 'Soft' skills – such as communication, interpersonal, teamwork, time management and leadership skills – that are much needed for a successful career. Graduate school whets your curiosity, and instills in you the qualities of patience and tenacity. Graduate school is truly a unique experience and I am extremely fortunate and overwhelmingly grateful for my time spent here at The University of Texas at Austin – 'What Starts Here Changes The World.'

Abstract

Functionality Enhancement of Two-Dimensional Transition Metal Dichalcogenide-Based Transistors

Amritesh Rai, Ph.D.

The University of Texas at Austin, 2019

Supervisor: Sanjay K. Banerjee

Atomically thin molybdenum disulfide (MoS_2) and tungsten diselenide (WSe_2), members of the transition metal dichalcogenide family, have emerged as prototypical two-dimensional semiconductors with a multitude of interesting properties and promising device applications spanning all realms of electronics and optoelectronics. While possessing inherent advantages over conventional bulk semiconducting materials (such as Si, Ge and III-Vs) in terms of enabling ultra-short channel and, thus, energy efficient field-effect transistors, the mechanically flexible and transparent nature of 2D MoS_2 and WSe_2 make them even more attractive for use in ubiquitous flexible and transparent electronic systems. However, before the fascinating properties of these materials can be effectively harnessed and put to good use in practical and commercial applications, several important technological roadblocks pertaining to their contact, doping and mobility engineering must be overcome. This dissertation reviews the important technologically relevant properties of semiconducting 2D TMDs followed by a discussion of the performance projections of, and the major engineering challenges that confront, 2D MoS_2 and WSe_2-based devices. Finally, this dissertation provides a comprehensive insight into two novel and promising engineering solutions that can be employed to address the all-important issues of contact resistance, controllable and area-selective doping, and charge carrier mobility

enhancement (electrons in MoS_2 and holes in WSe_2) in these devices. Specifically, this work sheds light upon the interfacial-oxygen-vacancy mediated n-doping of MoS_2 by high-κ dielectrics, such as HfO_2, Al_2O_3 and TiO_2, using detailed experimental characterizations and theoretical calculations. This n-doping effect on MoS_2 by high-κ dielectrics is proposed as a mechanism responsible for the performance enhancement observed in MoS_2 devices upon encapsulation in high-κ dielectric environments. This work also sheds light upon the band structure engineering and p-doping of layered WSe_2 using a simple and facile one-step chemical functionalization technique utilizing ammonium sulfide solution. Detailed experimental and theoretical studies once again reveal the underlying mechanism responsible for the p-doping in WSe_2 after chemical treatment. Results show that the doping techniques presented in this dissertation can easily be adapted to obtain high-performance FETs based on 2D MoS_2 and WSe_2. Finally, some future research directions, based on the work presented in this dissertation, are highlighted.

Table of Contents

List of Figures

Chapter 1: An Overview of Semiconducting Two-Dimensional Transition Metal Dichalcogenides: Prospects and Challenges

1.1 Graphene and the Rise of 2D Materials

The isolation and characterization of graphene, an atomically thin layer of carbon atoms arranged in a hexagonal lattice, in 2004 by Geim and Novoselov ushered in the era of two-dimensional (2D) atomically thin layered materials[1]. This all-important discovery came at the backdrop of a continuous ongoing quest by the semiconductor industry to search for new semiconducting materials, engineering techniques and efficient transistor topologies to extend "Moore's Law"—an observation made in the 1960s by Gordon Moore which stated that the number of transistors on a complementary metal-oxide-semiconductor (CMOS) microprocessor chip and, hence, the chip's performance, would double every two years or so[2-4]. In effect, this law led to the shrinking down of conventional CMOS transistors (down into the nm regime) to enhance their density and performance on the chip[5-10]. However, in the past decade or so, the performance gains derived due to dimensional scaling have been severely offset by the detrimental short-channel effects (SCE) that cause high OFF-state leakage currents (due to loss of effective gate control over the charge carriers in the semiconducting channel and inability of the gate to turn the channel fully OFF) leading to higher static power consumption and heat dissipation (*i.e.*, wasted power), which have dire implications for Moore's Law[11-16]. With continued scaling (sub-10 nm regime), the SCE effect will get far worse and even state-of-the-art CMOS transistor architectures designed to enhance gate controllability (such as MuGFETs, UTB-FETs, FinFETs, etc.) will face serious challenges in minimizing the overall power consumption. Hence, the need of the hour is an appropriate transistor channel material that allows for a high degree of gate controllability at these ultra-short dimensions[17-20]. In this light, graphene has been thoroughly researched for its remarkable properties, such as 2D

Much of the discussions presented in this Chapter have been reproduced with permission from the following invited feature review article referenced as: Rai, A., Movva, H., Roy, A., Taneja, D., Chowdhury, S., & Banerjee, S. (2018). Progress in Contact, Doping and Mobility Engineering of MoS_2: An Atomically Thin 2D Semiconductor. *Crystals*, *8*(8), 316. The dissertator, A. Rai, planned and wrote the entire review article with contributions from all authors.

atomically thin nature, extremely high carrier mobilities, superior mechanical strength, flexibility, optical transparency, and high thermal conductivity, that can be useful for a wide range of device applications[21-23]. While graphene can allow for excellent gate controllability due to its innate atomic thickness, a major drawback of graphene is its "semi-metallic" nature and, hence, the absence of an electronic "band gap" (E_g)—a necessary attribute any material must possess to be considered for electronic/optoelectronic device applications. Hence, a graphene transistor cannot be turned "OFF"[24,25].

1.2 BEYOND GRAPHENE: 2D TRANSITION METAL DICHALCOGENIDES

Graphene's shortcomings led to the search for alternative materials with similar yet complementary properties. This led to the emergence of a laundry list of 2D layered materials ranging from insulators to semiconductors and metals[26,27]. Among these 2D materials, the family of transition metal dichalcogenides (TMDs) has garnered the most attention[28]. These TMDs are characterized by the general formula MX_2 where M represents a transition metal (M = Mo, W, Re, etc.) and X is a chalcogen (X = S, Se, Te)[29,30]. Analogous to graphene, these layered 2D TMDs can be isolated down to a single atomic layer from their bulk form. A TMD monolayer can be visualized as a layer of transition metal atoms sandwiched in-between two layers of chalcogen atoms (of the form X-M-X) with strong intra-layer covalent bonding, whereas the inter-layer bonding between two adjacent TMD layers is of the van der Waals (vdW) type. Moreover, depending on the specific crystal structure and atomic layer stacking sequence (1T, 2H or 3R), these TMDs can have metallic, semiconducting or superconducting phases[29,30]. Figure 1.1(a) schematically illustrates the 3D crystal structure of the 2H phase of molybdenum disulfide (MoS_2) the prototypical TMD. The 2H phase of tungsten diselenide (WSe_2) has a similar MX_2 crystal structure.

Of particular interest is the subset of semiconducting 2D TMDs as they offer several promising advantages over conventional 3D semiconductors (Si, Ge and III-Vs) such as: (i) inherent ultra-thin bodies enabling enhanced electrostatic gate control and carrier confinement versus 3D bulk semiconductors (this can help mitigate SCE in ultra-scaled

FETs based on 2D TMDs as their ultra-thin bodies can allow significant reduction of the so-called characteristic "channel length (L_{CH}) scaling" factor "λ", given by $\lambda = \sqrt{(t_{OX}t_{BODY}\varepsilon_{BODY})/\varepsilon_{OX}}$, where t_{OX} and t_{BODY} are the thicknesses of the gate oxide and channel, respectively, and ε_{OX} and ε_{BODY} are their respective dielectric constants; a simple relationship for the scaling limit of FETs, *i.e.*, minimum length required to prevent SCE, is given by $L_{CH} > 3\lambda$. Figure 1.1(c) shows the schematic cross sections of the gate-channel regions of FETs employing bulk 3D and 2D semiconducting channels and compares their electrostatic carrier confinements[31]; (ii) availability of a wide range of sizeable band gaps and diverse band alignments[32]; and (iii) lack of surface "dangling bonds" unlike conventional 3D semiconductors allowing for the formation of pristine defect-free interfaces (especially 2D/2D vdW interfaces)[33]. Figure 1.1(b) schematically compares the surface of bulk 3D and 2D materials. These attributes make the semiconducting 2D TMDs extremely promising for future "ultra-scaled" and "ultra-low-power" devices[30,31,33-39].

Among the semiconducting 2D TMDs, MoS_2 has been the most popular and widely pursued material by the research community owing to its natural availability and environmental/ambient stability. Like most semiconducting TMDs, MoS_2 is characterized by a thickness-dependent band gap as has been verified both theoretically and experimentally: in its bulk form, it has an indirect band gap of ~ 1.2 eV, whereas in its monolayer form, the band gap increases to ~ 1.8 eV due to quantum confinement effects and is direct[40-44]. Figure 1.1(d) illustrates the band structure evolution of MoS_2 with decreasing layer thickness. WSe_2, on the other hand, has properties analogous to that of MoS_2 and has emerged as another extremely promising semiconducting 2D TMD. WSe_2 is highly environmentally stable like MoS_2 and can afford ambipolar carrier transport relatively easily unlike MoS_2, thereby, making it very attractive for enabling 2D CMOS circuits[45,46]. This band gap variability, together with high carrier mobilities, mechanical flexibility, and optical transparency, make 2D MoS_2 and WSe_2 extremely attractive for practical nano- and optoelectronic device applications on both rigid and flexible platforms[47-53].

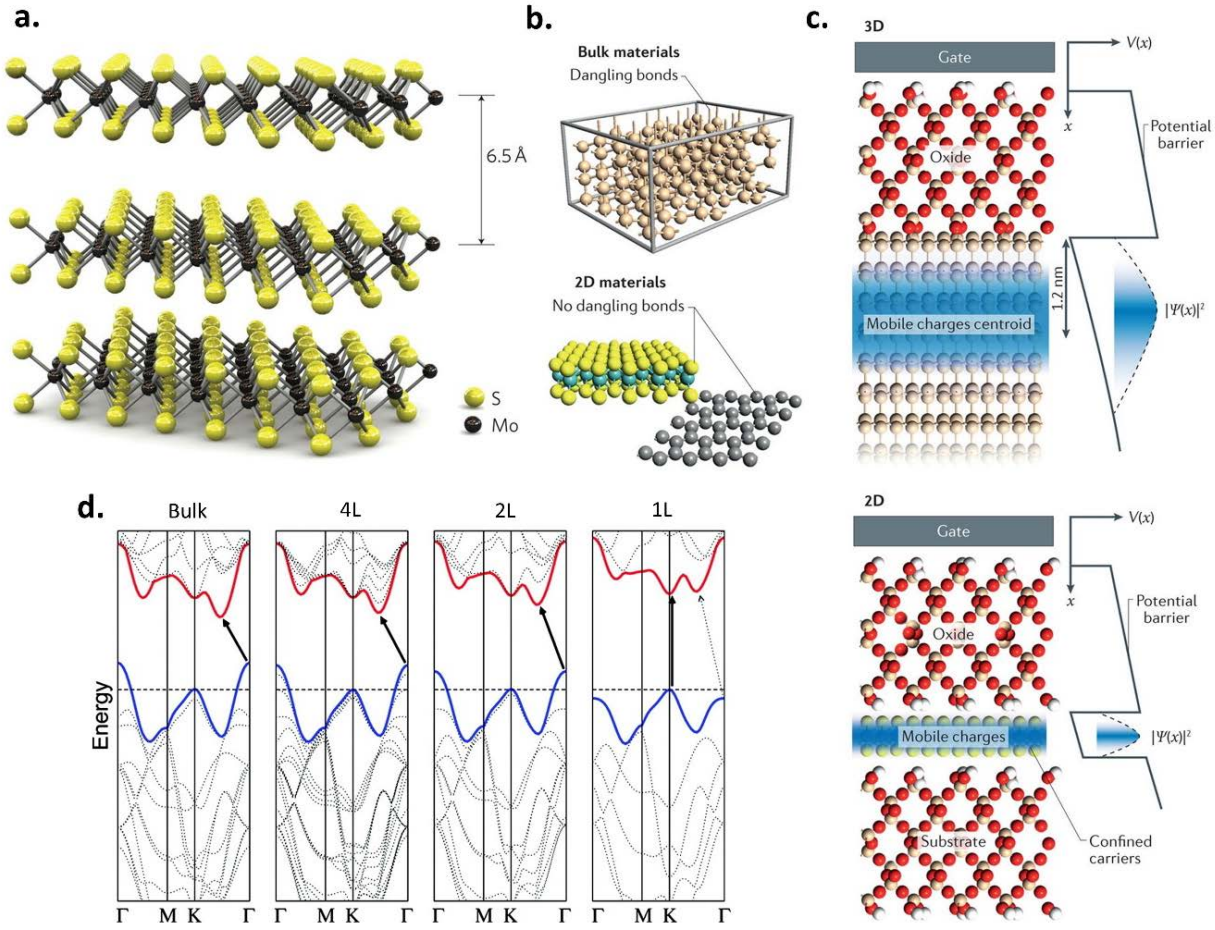

Figure 1.1: (a) 3D schematic of the crystal structure of semiconducting 2H MoS_2, the prototypical TMD, showing stacked atomic layers. Atoms in each layer are covalently bonded, whereas a vdW gap exists between adjacent layers with an interlayer separation of ~ 0.65 nm. Adapted with permission from [40]. Copyright Springer Nature 2011. (b) Schematic illustration of bulk 3D (top) versus 2D materials (bottom) showing the absence of surface dangling bonds in the latter. (c) Schematic illustration of the carrier confinement and electrostatic gate coupling in bulk 3D (top schematic) versus 2D semiconducting materials (bottom schematic) when used as the channel material in a conventional FET architecture. 2D semiconductors offer much better gate control and enhanced carrier confinement, as opposed to 3D semiconductors, owing to their innate atomic thickness. (b,c) Adapted with permission from [35]. Copyright Springer Nature 2016. (d) Band structure evolution of MoS_2 from bulk to monolayer (1L) showing the transition from an indirect to a direct band gap (as indicated by the solid black arrow). Adapted with permission from [41]. Copyright 2010 American Chemical Society.

MoS_2 and WSe_2 can also be combined with conventional 3D semiconductors (such as Si and III-Vs), other 2D materials (*e.g.*, TMDs or graphene), and 1D and 0D materials to form various 2D/3D, 2D/2D, 2D/1D and 2D/0D vdW heterostructure devices, respectively, enabling a wide gamut of functionalities[54-61]. Indeed, several device applications such as ultra-scaled FETs[62-65], digital logic[66-71], memory[72-77], analog/RF[78-81], conventional diodes[82-86], photodetectors[87-90], light emitting diodes (LEDs)[91-95], lasers[96-99], photovoltaics[100-103], sensors[104-108], ultra-low-power tunneling-devices such as tunnel-FETs (TFETs)[109-114], and piezotronics[115-118], among several others, have been demonstrated using 2D MoS_2 and WSe_2 (either on exfoliated flakes or synthesized films), highlighting their promise and versatility. Concurrently, massive research effort has been devoted to solving various key technical challenges, such as large-area wafer-scale synthesis using techniques like chemical vapor deposition (CVD) and its variants (such as metal–organic CVD or MOCVD), van der Waals (vdW) epitaxy,[119-124], reduction of parasitic contact resistance (R_C), and enhancement of charge carrier mobility (μ), that can improve the operational efficiency of these devices and allow MoS_2- and WSe_2-based circuits and systems to become technologically and commercially relevant.

1.3 PROJECTED PERFORMANCE OF SEMICONDUCTING 2D MoS_2 AND WSe_2

To realize low-power and high-performance electronic/optoelectronic devices based on 2D semiconducting TMD materials, several key parameters, such as contact resistance (R_C), channel/contact doping (n- or p-type) and charge carrier mobility (for both electrons and holes), need to be effectively engineered to harness the maximum intrinsic efficiency from the device[31,35,36,38,39]. In the case of MoS_2 and WSe_2, excluding the effect of any external factors, their calculated/predicted intrinsic performance are indeed extremely promising. Firstly, the quantum limit to contact resistance (R_{Cmin}) for crystalline semiconducting materials in the 2D limit is determined by the number of conducting modes in the semiconducting channel which, in turn, is connected to the 2D sheet carrier density (n_{2D}, in units of 10^{13} cm^{-2}) as $R_{Cmin} = 26/\sqrt{n_{2D}}$ Ω·μm[125-128]. Figure 1.2(a) depicts this quantum limit in a plot of R_C versus n_{2D}. For $n_{2D} = 10^{13}$ cm^{-2}, this yields an R_{Cmin} of 26

Ω·μm, which is well below the projected maximum allowable parasitic source/drain (S/D) resistances for high-performance Si CMOS technology (for example, 80 Ω·μm for multiple-gate FET technology) as per the ITRS requirements for the year 2026[129]. Thus, 2D MoS_2 and WSe_2-based devices have the potential of meeting the R_C requirements if a sheet carrier density of ~ 10^{13} cm^{-2} or higher is realized in their source/drain contact regions by doping or other means.

Secondly, the predicted room temperature (RT, *i.e.*, 300 K) phonon-limited, or "intrinsic", electron mobility for monolayer MoS_2 falls in the range of 130–480 cm^2/V-s[130-133]. On the other hand, the predicted phonon-limited hole mobility for monolayer MoS_2 is supposed to be as high as 200–270 cm^2/V-s[132,134]. For monolayer WSe_2, the predicted intrinsic electron and hole mobility values are as high as 250 and 270 cm^2/V-s, respectively. Moreover, the calculated saturation velocities (v_{sat}) of electrons and holes in monolayer MoS_2 are 3.4–4.8 × 10^6 and 3.8 × 10^6 cm/s, respectively, whereas the predicted v_{sat} of electrons and holes in monolayer WSe_2 are as high as 4.0 × 10^6 and 3.5 × 10^6 cm/s, respectively[132]. Note that the predicted carrier mobilities and saturation velocities in WSe_2 are comparable to that of MoS_2. This makes 2D MoS_2 and WSe_2 extremely promising for various semiconductor device applications and gives them a distinct advantage for use in thin-film transistor (TFT) technologies as their predicted carrier mobilities are higher than conventional TFT materials such as organic and amorphous semiconductors as well as metal oxides[135-137]. In fact, these TMDs offer channel mobilities that are comparable to single-crystalline Si[138]. Figure 1.2(b) compares the mobility of TMDs against various other semiconducting materials.

Moreover, MoS_2 and WSe_2 can potentially outperform conventional 3D semiconductor devices at aggressively scaled channel lengths (L_{CH} < 5 nm) thanks to their excellent electrostatic integrity[139-141], finite band gap, and preserved carrier mobilities even at sub-nm thickness (monolayer MoS_2/WSe_2 thickness ~ 0.65 nm), unlike 3D semiconductors that can experience severe mobility degradation (due to scattering from dangling bonds, interface states, atomic level fluctuations, surface roughness, etc.) and a large band gap increase (due to quantum confinement effects) with dimensional/body

thickness scaling below ~ 5–10 nm[35,36,142-144]. Thus, the high predicted mobilities and saturation velocities, coupled with their atomically thin nature, high optical transparency and mechanical flexibility, make 2D MoS_2 and WSe_2 very attractive for applications in ultra-scaled CMOS technologies as well as in flexible nanoelectronics and flexible "smart" systems[80,135,136,145-147].

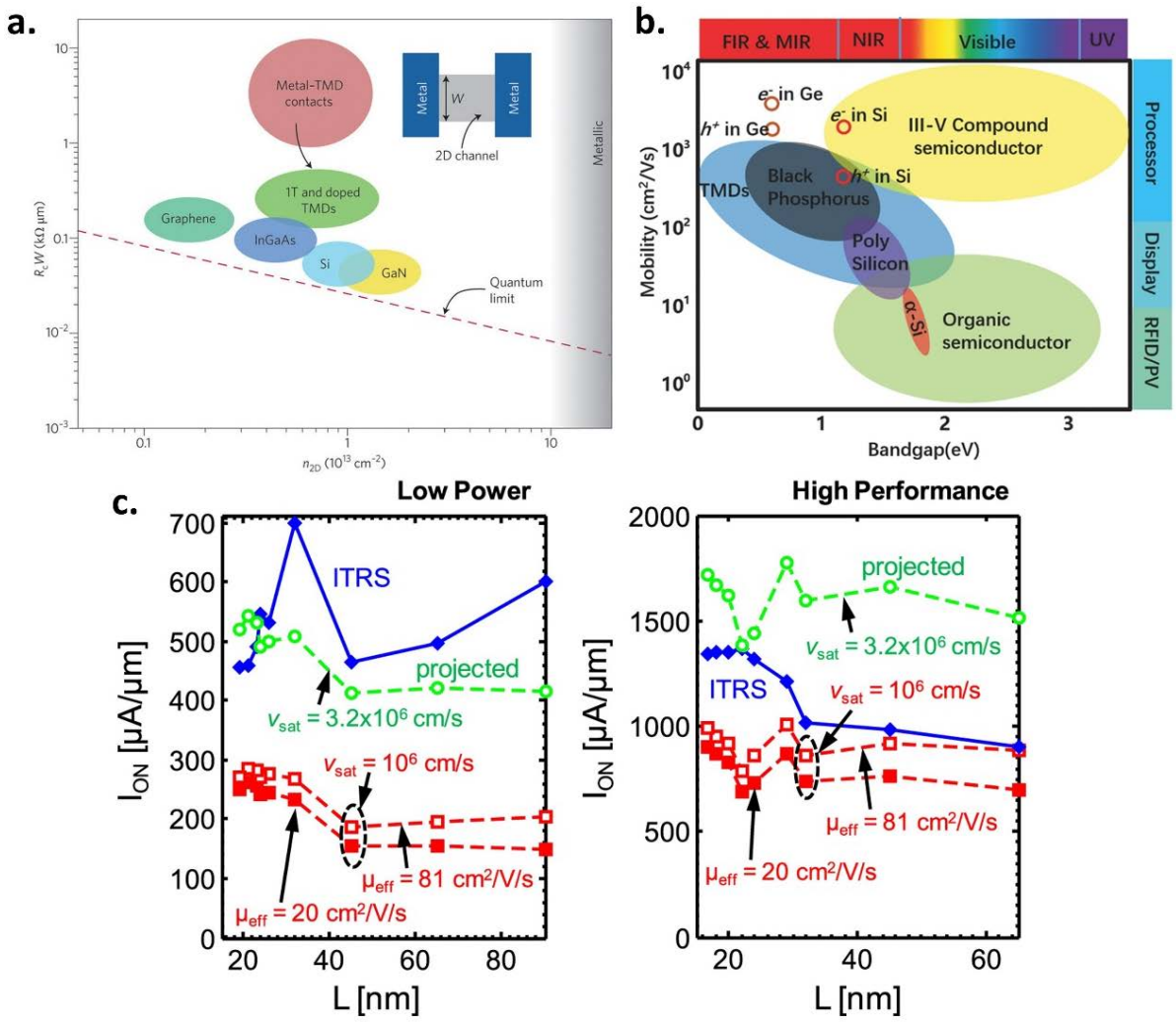

Figure 1.2: (a) Contact resistance (R_C) plotted as a function of the 2D sheet carrier density (n_{2D}) showing the respective contact resistances of various semiconducting materials (Si, III-Vs, graphene, and TMDs). The red dashed line represents the quantum limit to R_C. Top right inset shows the schematic top view of a basic transistor configuration. Adapted with permission from [128]. Copyright Springer Nature 2014. (b) Plot of carrier mobility versus

band gap for various semiconducting materials used in technological applications such as processors, displays, RFIDs and photovoltaics. TMDs have a distinct advantage over poly/amorphous Si and organic semiconductors, and their mobilities are comparable to that of single-crystalline Si. Adapted with permission from [148]. Copyright 2017 John Wiley and Sons. (c) Projected ON-current performance versus gate length L of monolayer MoS_2 FETs compared against low-power (LP) (left plot) and high-performance (HP) (right plot) ITRS requirements. ITRS requirements are shown in blue with fixed I_{OFF} = 10 pA/μm for LP and 100 nA/μm for HP. Simulations in red use $v_{sat} = 10^6$ cm s^{-1}, with solid symbols for CVD-grown MoS_2 (μ_{FE} = 20 cm^2/V-s) and open symbols for exfoliated MoS_2 (μ_{FE} = 81 cm^2/V-s). The green curve shows projections for MoS_2 FETs using both the higher mobility value (*i.e.*, 81 cm^2/V-s) and higher $v_{sat} = 3.2 \times 10^6$ cm s^{-1}, that meet ITRS requirements for both LP and HP applications for gate lengths L < 20 nm. Adapted with permission from [149]. Copyright 2016 IOP Publishing.

The projected performance potential of MoS_2 transistors has also been investigated by several research groups and compared to conventional CMOS devices for applicability in future technology nodes. For example, the performance of double-gated monolayer MoS_2 FETs was theoretically examined (in the presence of intrinsic phonon scattering) and compared to ultra-thin body (UTB) Si FETs by Liu *et al.*, with results showing that MoS_2 FETs can have a 52% smaller drain-induced barrier lowering (DIBL) and a 13% smaller subthreshold swing (SS) than 3-nm-thick-body Si FETs at an L_{CH} of 10 nm with the same gating[140]. This favorable performance and better scaling potential of monolayer MoS_2 FETs compared to UTB Si counterparts was attributed to its atomically thin body (~ 0.65 nm thick) and larger effective mass that can suppress direct source-to-drain tunneling at ultra-scaled dimensions. Moreover, the performance of MoS_2 FETs was found to fulfill the requirements for high-performance logic devices at the ultimate scaling limit as per the ITRS targets for the year 2023[140]. Through rigorous dissipative quantum transport simulations, Cao *et al.* found that bilayer MoS_2 FETs can indeed meet the high-performance (HP) requirement (*i.e.*, the ON-state current drive capability) up to the 6.6 nm node as per the ITRS. Moreover, they showed that with proper choice of materials and device structure engineering, MoS_2 FETs can meet both the HP and low-standby-power (LP, *i.e.*, good subthreshold electrostatics in the OFF-state) requirements for the sub-5 nm

node as per the ITRS projections for the year 2026[150]. Another recent simulation study by Smithe *et al.* revealed that, if the predicted saturation velocity of monolayer MoS_2 can be experimentally realized (*i.e.*, $v_{sat} > 3 \times 10^6$ cm/s), then MoS_2 FETs can potentially meet the required ON-currents (while meeting the OFF-current requirements) for both HP and LP applications at scaled ITRS technology nodes below 20 nm. Figure 1.2(c) compares the projected ON-currents of monolayer MoS_2 FETs against ITRS requirements for different MoS_2 v_{sat} and field-effect mobility (μ_{FE} or μ_{eff}) values, as a function of gate length "L"[149]. Like these, several other insightful simulation studies exist which discuss the projected DC and high-frequency RF device performance of 2D MoS_2 and WSe_2 at ultra-scaled gate lengths[151-154].

While these performance projections are extremely encouraging, it must be kept in mind that these calculations of contact resistance, mobilities, and FET performances assume an ideal or a near-ideal scenario wherein the 2D MoS_2 under consideration is pristine with a defect-free crystal structure, and its material/device properties are evaluated in the absence of extrinsic carrier scattering sources and while considering ideal contact electrodes (*i.e.*, Ohmic contacts). In practice, several non-idealities and inherent challenges exist that can have a detrimental effect on the key performance metrics, thereby, adversely affecting the overall MoS_2 device performance. The same holds true for WSe_2 devices.

1.4 Major Challenges in Contact, Doping and Mobility Engineering of 2D MoS_2 and WSe_2

1.4.1 The Schottky Barrier and the van der Waals (vdW) Gap

One of the biggest issues confronting 2D MoS_2- and WSe_2-based devices is the presence of a Schottky barrier (SB) at the interface between the TMD and the contact metal electrode. This results in a "non-Ohmic" or a Schottky electrical contact characterized by an energy barrier, called the Schottky barrier height (SBH or Φ_{SB}), that hinders the injection of charge carriers into the device channel[155]. Consequently, this notable SBH leads to a large R_C and a performance degradation (*e.g.*, low field-effect mobilities) in two-terminal TMD devices since a large portion of the applied drain bias gets dropped across this

R_C[156,157]. The presence of the SBH in MoS_2 and WSe_2 devices has been experimentally verified by several research groups[157-162], and these barriers are thought to be formed due to strong Fermi level pinning (FLP) effects at the contact metal/TMD interface[127,155,163]. Detailed microscopic and spectroscopic studies on natural MoS_2 flakes revealed high concentrations of defects and impurities, such as sulfur vacancies (SVs) and subsurface metal-like impurities, which are thought to be responsible for the strong FLP[164-167]. These SV defects/impurities lead to a large background n-doping in the MoS_2 and introduce unwanted energy levels or "mid-gap states" closer to the conduction band edge (CBE) that ultimately governs the location of the charge neutrality level where the metal Fermi level gets pinned resulting in fixed barrier heights at the contact/MoS_2 interface[168-170].

Further insight on the possible origin of this FLP effect was shed by theoretical calculations based on density functional theory (DFT). Kang *et al.* reported that interactions between certain metals and MoS_2 can lead to the formation of a "metal/MoS_2 alloy" at the contact interface with a much lower work function than unalloyed MoS_2. This leads to an abnormal FLP as if the MoS_2 is contacted to a low work function metal[171]. Gong *et al.*, on the other hand, claimed that the FLP mechanism at metal/MoS_2 interfaces is unique and distinctively different from traditional metal-semiconductor junctions. According to their calculations, the FLP at the metal/MoS_2 interface is a result of two simultaneous effects: first, a modification of the metal work function by interface dipole formation due to the charge redistribution at the interface and, second, by the formation of mid-gap states originating from Mo d-orbitals, that result from the weakening of the intralayer S-Mo bonds due to the interfacial interaction, and the degree thereof, between the metal and the S atom orbitals[172]. A qualitatively similar result was obtained by Farmanbar *et al.* where they studied the interaction between a wide range of metals and MoS_2 using DFT and found that this MoS_2/metal interaction leads to the formation of interface states due to perturbation of the MoS_2 electronic band structure, with energies in the MoS_2 band gap that pin the metal Fermi level below its CBE. The extent of this interfacial interaction depends on whether the metal is physisorbed (*i.e.*, weakly adsorbed) or chemisorbed (*i.e.*, strongly adsorbed) on the MoS_2 surface, resulting in a small

or large density of interface states, respectively. Moreover, the authors showed that by artificially enlarging the physical distance between MoS_2 and the metal, these interface states vanished[173]. Guo *et al.* suggested that the strongly pinned SBHs at the metal/2D MoS_2 interface arises due to strong bonding between the contact metal atoms and the TMD chalcogen atoms[174], in accordance with the age-old theory of metal-induced gap states (MIGS) established for metal contacts to conventional bulk 3D semiconductors[175-177]. The SBH prevalent at WSe_2/metal interfaces can be thought to have similar origins.

Regardless of the exact underlying physical mechanism involved, FLP is an undesired effect as it leads to fixed SBHs at metal/TMD interfaces. It is for this very pinning effect that most metal-contacted MoS_2 FETs typically show unipolar n-type behavior as the metal Fermi level gets strongly pinned near the CBE of MoS_2 irrespective of the contact metal work function[158,159,178,179]. In addition to degrading the device performance due to large R_C, the reduced tunability of the SBH due to FLP is detrimental towards realizing both n-type and p-type Ohmic contacts to MoS_2 desirable for CMOS applications[127]. In the case of WSe_2 devices, while both n-type and p-type transport (*i.e.* ambipolarity) can be achieved relatively easily, unlike MoS_2, by proper choice of the WSe_2 layer thickness, contact metal work function, contact gating etc.[161,180,181] , the FLP effect is still present and can lead to significant Schottky barrier heights and contact resistances for both electron and hole injection.

Besides SBH, another relevant parameter associated with these Schottky barriers is the width of its depletion region in the semiconductor channel or, simply, the Schottky barrier width (SBW). The SBW is largely dependent on the extent of semiconductor "band-bending" in the 2D TMD/MoS_2 channel under the electrode contacted region[182]. Both the SBH and the SBW together determine the charge injection in the 2D MoS_2 or WSe_2 channel. While SBH governs the extent of thermionic emission of carriers "over" the barrier, SBW determines the extent of thermionic field emission (*i.e.*, thermally-assisted tunneling) and/or field emission (*i.e.*, direct tunneling) "through" the width of this barrier due to the quantum mechanical tunneling of charge carriers[127,155,183,184]. Figure 1.3 shows the band alignment at the metal/2D TMD interface under different gating conditions and

illustrates the different charge carrier injection mechanisms. Note that although the figure illustrates the charge carrier injection mechanisms assuming an n-type contact, the same underlying concepts are also applicable to p-type contacts. Hence, both the SBH and SBW must be minimized to achieve efficient injection of charge carriers (electrons or holes) from the contact into the semiconducting TMD channel. Additionally, the FLP-induced SBH has been found to depend strongly on the MoS_2 layer thickness (especially in the limit of 1–5 layers) since the electronic band structure of MoS_2 undergoes a drastic change as its thickness is reduced (recall that band gap increases with decreasing MoS_2 thickness), leading to a modification of its electron affinity and relative shifts in its band edge positions (*i.e.*, CBE and valence band edge or VBE) in the energy-momentum (or E-k) space[44,185]. Owing to these factors, thinner MoS_2 with a larger band gap typically yields a larger SBH with metal contacts. Same concepts hold true for Schottky barriers in WSe_2 devices.

Finally, in addition to the SB, there are several other important issues that require careful consideration. In an ideal scenario, the surface of TMDs has an absence or at least a dearth of dangling bonds and, thus, MoS_2 does not tend to form interfacial covalent bonds with the as-deposited contact electrodes. Hence, the metal/MoS_2 interface is characterized by the presence of a van der Waals (vdW) gap, especially in the top contact geometry (which is most common). This vdW gap acts like an additional "tunnel barrier" for the charge carriers in series with the inherent metal/MoS_2 SB (as shown in Figure 1.3) and can increase the overall R_C [127,157,171]. Moreover, this vdW gap-induced tunnel barrier also manifests itself in multilayer MoS_2 devices as additional "interlayer" resistors (since adjacent MoS_2 atomic layers are also separated by a vdW gap) and can have implications on the overall device performance. Therefore, for purely electronic applications, the thickness of MoS_2 must be carefully chosen for optimum device performance. Some elegant ways to overcome this vdW gap issue are to realize "hybridized" top contacts and/or "edge contacts" (that have a greater degree of orbital interaction with the MoS_2 atoms/bonds resulting in a more intimate contact having lower R_C) instead of the regular top contacts[127,186].

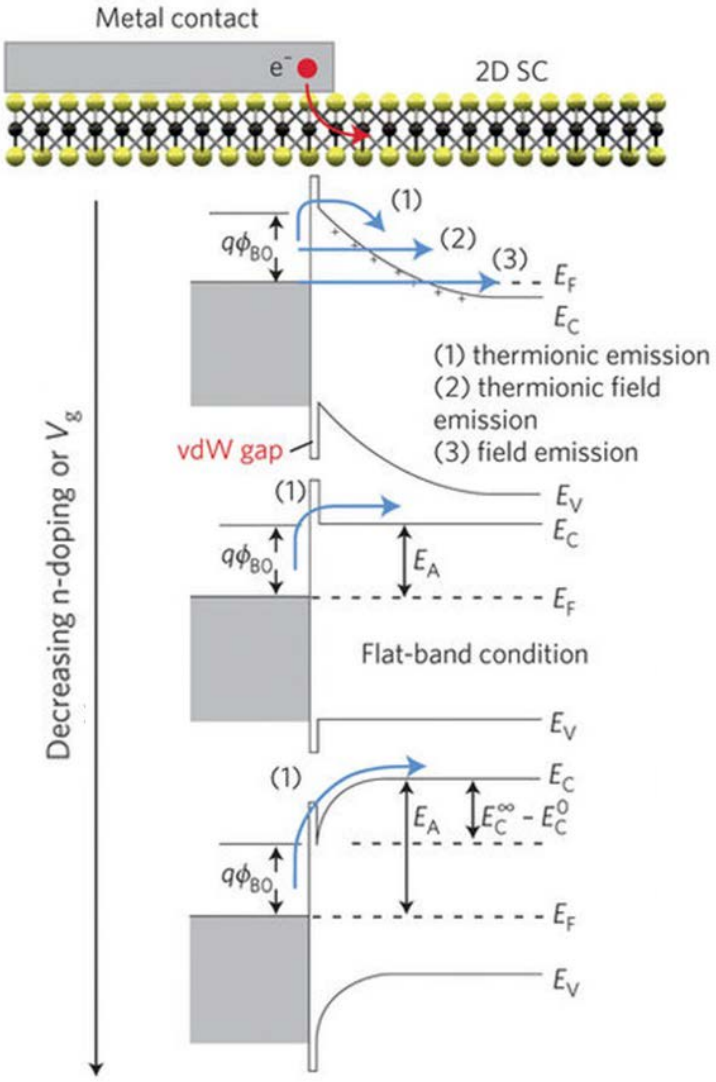

Figure 1.3: Energy band diagram of the n-type contact/MoS_2 interface under different gating (electrostatic n-doping) conditions depicting the different charge injection mechanisms/paths from the metal into the MoS_2 channel across the SB. $q\Phi_{B0}$ represents the SBH. Thermionic emission is represented by Path (1), thermionic field emission by Path (2) and field emission by Path (3) as shown in the top band diagram for the case of maximum n-doping or maximum gate voltage V_g (that causes maximum downward band-bending). The additional tunnel barrier due to the vdW gap is also shown (marked by the red text). The lateral distance through which the carriers "tunnel" through in Paths (2) and (3) represents the SBW. As V_g decreases (*i.e.*, n-doping decreases), the band-bending decreases and charge injection is governed by thermionic emission only, as shown by Path (1) in the middle and bottom energy band diagrams. Adapted with permission from [127].

1.4.2 CONTACT LENGTH SCALING, DOPING AND EXTRINSIC CARRIER SCATTERING

A major problem arises when we consider "contact length scaling" for MoS_2 and WSe_2. Contact length (L_C) scaling is required when we consider designing aggressively scaled ultra-short-channel devices based on any semiconductor, because L_C must be shrunk by a similar factor as the channel length (L_{CH}) as it will determine the final device footprint/density and can lead to chips with smaller area and faster speeds[187,188]. However, while scaling L_{CH} decreases the channel resistance (R_{CH}), scaling L_C increases R_C in 2D TMDs. These two effects are contradictory to each other and device performance will ultimately be limited by R_C for aggressively scaled devices[189]. L_C scaling issue mainly arises from the fact that in 2D TMDs like MoS_2, the transfer length (L_T)—*i.e.*, the average length over which the charge carriers move in the semiconductor before being transferred to the contact electrode (also referred to as the "current crowding" effect at metal/semiconductor contacts)[190-192]—is often large. Figure 1.4(a) shows the schematic illustration of this "current crowding" effect at the metal/2D TMD junction using a resistor network model. For example, L_T = 600 nm for monolayer MoS_2 [182] and 200 nm for six-layer MoS_2 with Ti contacts[192]. If the L_C is scaled below L_T (*i.e.*, $L_C << L_T$), then R_C increases as per the relation $R_C = \rho_C/L_C$ where ρ_C is the specific contact resistivity [note that R_C is independent of L_C when $L_C >> L_T$ and is then given by the relation $R_C = \sqrt{(\rho_C \rho_{SH})}$ where ρ_{SH} is the sheet resistance of the semiconducting channel underneath the contact][127,193]. Therefore, for ultra-short-channel FETs (targeting the sub-10 nm node) based on 2D TMDs, it is extremely important to minimize ρ_C or, in other words, minimize L_T [since $L_T = \sqrt{(\rho_C/\rho_{SH})}$] to achieve low R_C. This is important because the R_C of any FET must only be a small fraction (~ 20%) of the total FET resistance (*i.e.*, $R_{CH} + 2R_C$) for the transistor to operate properly while ensuring that its current-voltage (I-V) behavior is primarily determined by the intrinsic channel resistance R_{CH} [127,129]. Hence, it is imperative that R_C must scale (*i.e.*, reduce) together with both L_{CH} and L_C before TMD-based FETs can come anywhere close to rivaling the performance of state-of-the-art Si and III-V device analogs (for reference, the R_C values reported for most TMD FETs to date are about an order of magnitude higher than in today's Si Fin-FET technologies where R_C is well below

100 Ω·μm)[127,128,155]. Now, the ρ_C is strongly dependent on the SBH among other factors, hence minimizing or eliminating the SBH is a guaranteed way to alleviate the R_C issue in TMD FETs.

Next, the ultra-thin nature of the 2D MoS_2 and WSe_2 makes it incredibly challenging to employ conventional CMOS-compatible doping techniques (ion implantation or high-temperature diffusion) to perform controlled and area-selective doping to control the carrier type (n or p) and carrier concentration (ranging from degenerate in the source/drain contact regions to non-degenerate in the channel region) in MoS_2- and WSe_2-based FETs, especially at the monolayer limit[194]. This is primarily because the atomically thin TMD lattice is highly susceptible to structural damage and etching which, for example, is typically unavoidable in the ion implantation process[195]. Lastly, MoS_2 and WSe_2 devices typically show much lower intrinsic carrier mobilities in experiments than the predicted phonon-limited values, implying the existence of extrinsic carrier scattering sources. Thus, it is important to eliminate or minimize the effect of these extrinsic charge carrier scattering mechanisms, such as substrate remote phonons, surface roughness, charged impurities, intrinsic structural defects (*e.g.*, SVs), interface charge traps (D_{it}) and grain boundary (GB) defects that can severely degrade the mobility in 2D MoS_2- and WSe_2-based devices[148,185,196-203]. Figure 1.4(b) schematically illustrates some prominent extrinsic charge carrier scattering mechanisms prevalent in a 2D TMD device channel.

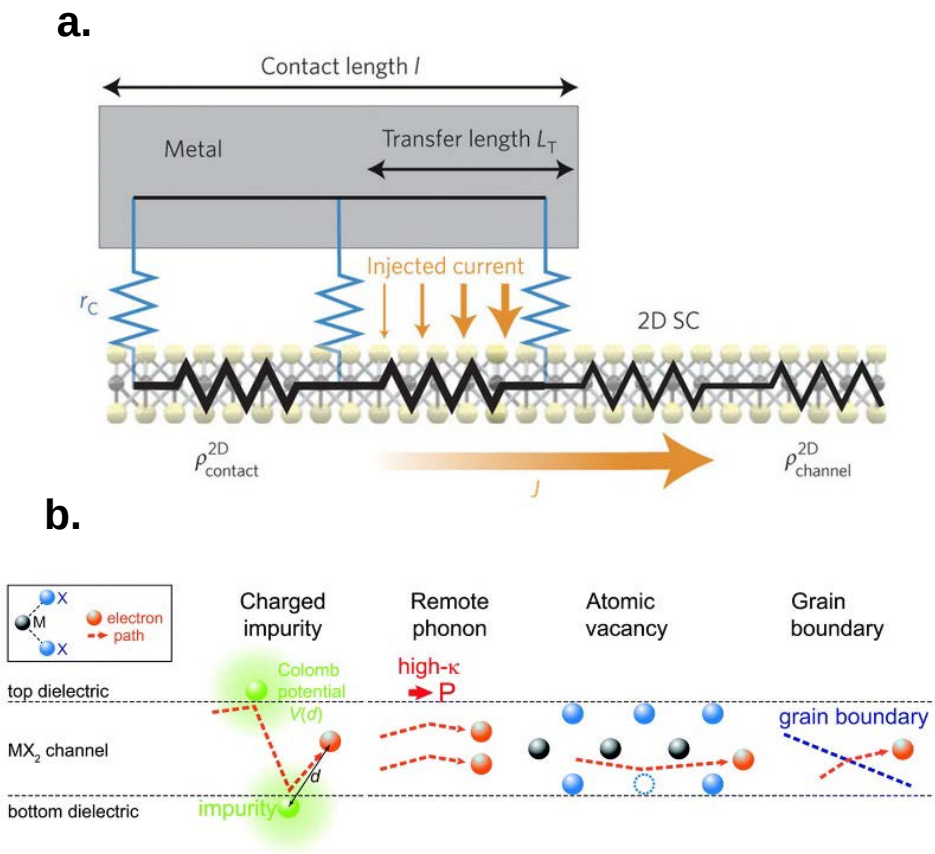

Figure 1.4: (a) Schematic illustration of the contact length (L_C), transfer length (L_T) and current injection (or the "current crowding" effect) near the metal contact/2D TMD interface edge. The different resistive components at play are marked in the resistor network model (note: in the figure, ρ_C is depicted as r_C, L_C is depicted as l, and TMD is depicted as SC). Adapted with permission from [127]. Copyright Springer Nature 2015. (b) Schematic illustration of the various extrinsic charge carrier scattering mechanisms in a 2D TMD/MX_2 device channel. The black and blue balls denote the M and X atoms, respectively. The orange balls and corresponding orange dashed arrows denote the electrons and their paths in the channel, respectively. Change in the direction of the carrier path denotes a scattering event. The green balls and the smeared green areas denote the charged impurities and their scattering potentials, respectively. The red arrow denotes the polar phonon in the top dielectric. Hollow blue circle represents atomic vacancies which tend to form in both natural and synthetic chalcogenides. Blue dashed line represents grain boundaries (GBs) which are typically present in synthetic chalcogenides. Adapted from [185] with permission of The Royal Society of Chemistry.

1.4.3 TACKLING THE MAJOR CHALLENGES

To achieve low-power, high-performance and ultra-scaled devices based on 2D MoS_2 and WSe_2, it is highly necessary to come up with effective solutions to alleviate the various issues, as highlighted above, that have an adverse effect on key device performance metrics. It is worth noting that solutions to several of these problems are intertwined and solving one can alleviate the other. As an obvious case, reduction of the SB (either by minimization of the SBH or thinning of the SBW) lowers the R_C and effectively improves the charge injection efficiency and the field-effect mobility (μ_{FE}) in TMD FETs. Reduction of the SBH can lead to a reduced specific contact resistivity ρ_C. With area-selective and controlled doping, one can potentially realize degenerately doped S/D contact regions in MoS_2 and WSe_2 devices, just like in the conventional Si-CMOS case, to achieve Ohmic contacts. Realization of edge contacts to mono-, few- or multilayer MoS_2 and WSe_2, such that each individual layer of the TMD stack is independently contacted from the side, can not only help in eliminating the vdW gap-induced tunnel barriers and interlayer resistances, but it can also be useful in terms of contact scaling and overall device area/footprint reduction. Unsurprisingly, therefore, there has been an extensive research effort in the past few years to explore effective solutions for mitigating the various challenges associated with the contact, doping and mobility engineering of 2D MoS_2 and WSe_2 devices.

This dissertation describes in detail some novel and promising engineering approaches to tune the charge carrier doping densities in devices based on 2D MoS_2 and WSe_2 (specifically, electrons in MoS_2 and holes in WSe_2). The doping consequently leads to the alleviation of the adverse effects of both the Schottky barrier-induced contact resistance and external charge carrier scattering, thereby, resulting in an improvement in the charge carrier field-effect mobilities in these devices. Thorough experimental characterizations, backed by theoretical DFT calculations, reveal the underlying mechanisms responsible for each of these doping effects.

Chapter 2: Interfacial-Oxygen-Vacancy Mediated N-Doping of MoS_2 by Solution-Processed Amorphous TiO_x

2.1 INTRODUCTION

In order to alleviate the large R_C in MoS_2 FETs, insightful work has been done by several groups over the past few years. Das *et al.* demonstrated the use of low work function scandium as an efficient electron injector into the conduction band of MoS_2[158]. N-type charge transfer dopants such as potassium ions (K)[204] and polyethylenimine (PEI)[205] have been utilized, although these doping reagents are unstable in ambient conditions. The use of graphene–metal heterocontacts[206] and air stable doping *via* benzyl viologen (BV)[207] were shown to be effective strategies, but the R_C values were still greater than 1 kΩ·μm and only moderate channel mobilities were achieved. More recently, the use of phase engineered contacts[208] and chloride doping[209,210] were demonstrated on MoS_2 with promising results. However, the stability of the phase engineered contacts under high-performance device operation is still unknown[208]. Furthermore, the chloride doping mechanism is unclear and it is speculated that the doping occurs due to filling of the naturally occurring sulfur vacancies in MoS_2 by chlorine atoms[210]. Besides doping and the corresponding R_C reduction, considerable effort has also been put into dielectric engineering utilizing high dielectric constant (high-κ) materials to reduce the scattering of carriers in MoS_2 devices. Although several high-κ dielectrics have been investigated, atomic layer deposition (ALD) of alumina and hafnia have been the most common choices[40,66,136,211-213].

In this Chapter, we demonstrate an air stable, self-encapsulating, n-type charge transfer doping technique on monolayer (ML) MoS_2 utilizing amorphous titanium suboxide (ATO) thin films. The ATO can be solution processed in the form of a sol–gel

---

The results, discussions and figures presented in this Chapter have been adapted with permission from the following reference: Rai, A., Valsaraj, A., Movva, H. C. P., Roy, A., *et al.* (2015). Air Stable Doping and Intrinsic Mobility Enhancement in Monolayer Molybdenum Disulfide by Amorphous Titanium Suboxide Encapsulation. *Nano letters*, *15*(7), 4329-4336. The dissertator, A. Rai, conceived and designed the experiment, fabricated the devices, performed the electrical, Raman and photoluminescence measurements, analyzed the data and largely wrote the manuscript with contributions from all the authors.

precursor and its application involves a simple spin-coating process, thereby making this approach extremely facile and easily scalable in contrast to the phase engineering or chloride doping schemes that require several hours of treatment with their respective chemical reagents[208,214]. Utilizing this technique, we achieved a very low R_C of ~ 180 Ω·μm on ML MoS_2, which compares favorably to the R_C values obtained on 2–3 layer MoS_2 with phase engineered contacts[208] and is ~ 2.5 times lower than the R_C reported on chloride-doped multilayer MoS_2 FETs[210]. An ON-current as high as 240 μA/μm was achieved for a 450 nm channel length (L) back-gated FET with an oxide thickness (t_{OX}) of 93 nm at a drain-to-source voltage (V_{DS}) of 2 V and back-gate overdrive voltage ($V_{BG} - V_T$) of 70 V. Field-effect mobilities (μ_{FE}) as high as 83 cm^2/V-s and intrinsic mobilities (μ_{int}) as high as 102 cm^2/V-s were achieved on ML MoS_2 devices at room temperature (RT) upon ATO encapsulation. Temperature-dependent measurements revealed enhanced intrinsic mobilities approaching 501 cm^2/V-s in ATO encapsulated ML MoS_2 at 77 K. Density functional theory (DFT) analysis was performed to gain further insight into the doping mechanism of ATO films on ML MoS_2.

2.2 DEVICE FABRICATION AND MATERIAL CHARACTERIZATION DETAILS

2.2.1 Materials and Device Fabrication Methods

MoS_2 flakes were mechanically exfoliated, using the conventional 'scotch-tape' method, from a bulk MoS_2 crystal (SPI Supplies) onto degenerately doped ($\rho < 0.005$ Ω-cm) n-type Si substrates covered with 93 nm thermally grown SiO_2. The oxide thickness was verified *via* ellipsometry measurements. Upon exfoliation, the samples were annealed in high vacuum (2 x 10^{-6} Torr) at 350°C for 8 h. This high vacuum annealing step helps minimize tape residues from the top surface of the flakes as well as trapped adsorbates, such as moisture, from in between the flake and the underlying SiO_2 substrate. A combination of optical contrast, atomic force microscope (AFM), Raman and photoluminescence (PL) measurements were used to identify atomically flat monolayer MoS_2 flakes of interest. Contacts on the flakes were patterned using standard electron beam lithography utilizing PMMA as the e-beam resist, followed by development in 1:3

MIBK:IPA to open up the pads. Electron beam evaporation (at a base pressure of 5 x 10^{-6} Torr) and acetone lift-off steps were used to deposit a 20/30 nm stack of silver/gold (Ag/Au) which served as the contact electrodes. Ag was chosen as the contact metal due to the superior interface quality that it forms with MoS_2[215] besides having good adhesion with the SiO_2 substrate. No annealing was done after contact deposition. The contact width was fixed at 1 μm. ATO thin films were deposited on top of the MoS_2 devices by spin-coating an ATO sol-gel precursor solution (85 mg/ml) followed by a short baking step, all of which was done in ambient conditions. The typical spin speed was 3000 rpm for a duration of 45 s, following which the samples were baked at 90°C on a hot plate for 15 min in order to dry the residual solvent and enable the conversion of the ATO precursor molecules into ATO through hydrolysis. The thickness of ATO films deposited in this manner was ~ 140 nm with an average surface roughness below 0.5 nm as determined from AFM. The κ value of the ATO film was extracted to be ~ 10 from high frequency capacitance-voltage (HFCV) measurements.

2.2.2 Characterization Tools and Techniques

Optical investigation was done using an Olympus BX51M Microscope using their proprietary Stream Essentials analysis software. Ellipsometry measurements were taken using a JA Woollam M-2000 ellipsometer. Raman spectroscopy measurements were taken with a Renishaw inVia micro-Raman system with an excitation wavelength of 532 nm and a grating of 3000 l/mm. Photoluminescence measurements were taken with a Renishaw inVia micro-Raman system configured for photoluminescence with specialized optics at an excitation wavelength of 532 nm and a grating of 1200 lines/mm to obtain high energy peaks. Atomic force microscopy images were taken with a Veeco Nanoscope 5 in tapping mode. X-ray Photoelectron Spectroscopy was performed in a MULTIPROBE system from Omicron NanoTechnology GmbH utilizing a monochromatic Al-Kα source. Electrical characterization of the devices was done in dark using the Agilent 4156C and B1500A Semiconductor Parameter Analyzers. Ambient measurements were carried out in a Cascade Summit 11000 AP probe station. Low temperature and vacuum measurements (<

5 x 10^{-5} Torr) were carried out in a Lakeshore Cryotronics cryogenic probe station. All electrical measurements prior to ATO encapsulation were performed in vacuum in order to exclude the degrading effects of atmospheric adsorbates on the MoS_2 channel. All measurements post encapsulation were performed in ambient conditions except the low temperature measurements which were done in vacuum. Note that the gate voltage sweep direction was from positive to negative voltages for the FET data presented in this Chapter.

2.2.3 Preparation of the Sol-Gel Precursor Solution

The ATO precursor solution was prepared utilizing the recipes as outlined in previous literature reports[216,217]. The sol-gel preparation procedure is as follows: 25 ml of 2-methoxyethanol ($CH_3OCH_2CH_2OH$, Aldrich, 99.9+%) and 2.5 ml of ethanolamine ($H_2NCH_2CH_2OH$, Aldrich, 99.0+ %) were first mixed in a cylindrical glass vessel equipped with a thermometer. The mixture was left for 10 min under magnetic stirring following which 5 ml of titanium (IV) isopropoxide (Ti [OCH $(CH_3)_2]_4$, Aldrich, 99.999%) was added to the mixture. The cylindrical vessel containing the final mixture was then placed in a silicone-oil bath and was heated to 80°C for a period of 2 h. under magnetic stirring. The temperature was then raised to 120°C for 1 h. This two-step heating cycle (80°C – 2 h + 120°C – 1 h) was then repeated a second time at the end of which the color of the solution turned yellowish orange, indicating the formation of the ATO precursor solution. The concentration of the as-prepared solution was determined to be ~ 85 mg/ml. This was done by completely evaporating the solvent from 5 mL of the as-prepared solution and measuring the weight of the residual crystallites. In the case of graphene, diluted solutions of the ATO precursor (10 mg/ml or 20 mg/ml) were used[217]. However, for doping the ML MoS_2, the as-prepared precursor solution with the high initial concentration was chosen because, unlike graphene, monolayer MoS_2 has a large band gap and would need substantial doping to achieve high carrier densities unlike graphene.

2.2.4 X-Ray Photoelectron Spectroscopy (XPS) Analysis of ATO Films

Figure 2.1 below shows the XPS spectra as measured from the surface of our as-formed ATO films showing the corresponding binding energies of the Ti 2p 3/2, Ti 2p 1/2 and O 1s states. The elemental composition of our ATO film was determined by integrating the peak areas of the Ti 2p and O 1s spectra by properly fitting the components to each peak. It is to be noted that the O 1s peak shows the presence of two components. The peak at ~ 532 eV represents the un-bonded component of O probably resulting from OH species and, hence, it was not considered in our ratio determination. Only the shifted O 1s component at ~ 531 eV was considered as it represents bonding between the O and Ti atoms. We found the Ti:O ratio in our ATO films to be ~ 1:1.5.

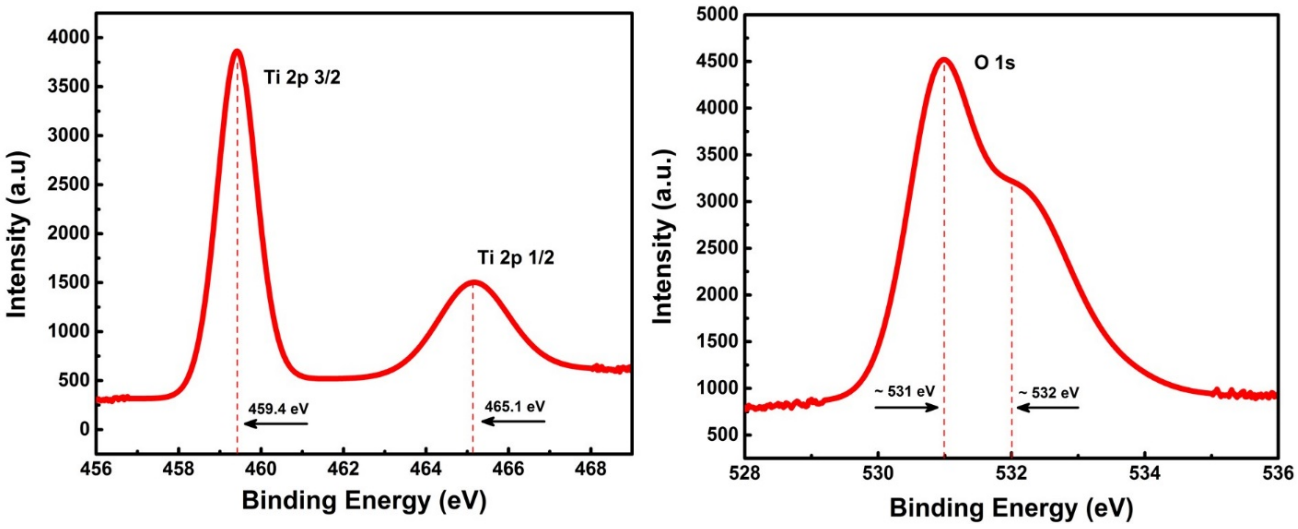

Figure 2.1: XPS spectra obtained from as-formed ATO films showing the Ti 2p (top plot) and O 1s (bottom plot) bonding states.

2.3 ATO Doping Scheme and Spectroscopic Characterization of ATO-Encapsulated Monolayer MoS_2

The mechanism of charge transfer doping is particularly attractive for ultrathin layered materials because it does not involve any substantial distortion of the 2D crystal lattice[207]. Several charge transfer doping techniques that were previously demonstrated on carbon-based nanomaterials were also successfully demonstrated on MoS_2[204,205,207].

Similarly, we investigate the effects of high-κ ATO thin films on MoS_2 that serve as an n-type charge transfer dopant. For the purpose of this experiment, only ML MoS_2 flakes were considered. ATO thin films were deposited on MoS_2 FETs by spin-coating at 3000 rpm and subsequent baking of an ATO sol–gel precursor solution at 90°C on a hot plate for 15 min to dry the residual solvent and convert the precursor solution into ATO through hydrolysis. ATO thin films obtained using this process were reported to have band gaps of ~ 3.7[216] and ~ 3.9 eV[217] corresponding to a Ti:O ratio of 1:1.34 and 1:1.59, respectively. The amorphous nature of these films and their large band gaps have been confirmed in literature by X-ray diffraction (XRD) and optical absorption measurements, respectively[216,217] . The Ti/O ratio in our films was estimated to be ~ 1:1.5 from the XPS data confirming the oxygen deficiency. Also, from the reported band gaps for ATO films with different Ti/O ratios[216,217], the band gap of our films can be estimated to be between 3.7 and 3.9 eV. Therefore, ATO can effectively be regarded as a wide band gap amorphous oxide semiconductor. As TiO_2 can serve as channel for n-type thin film transistors[218-220], it is important to first rule any parallel conduction paths that can be added to the MoS_2 channel by the encapsulating ATO layer. To test for possible conduction through the ATO film, a set of control devices without the MoS_2 channel were fabricated in exactly the same manner as the actual devices. No conduction was observed through the as-formed ATO layer even under higher biasing conditions (both back-gate and drain) than what was used in actual devices. Hence, the ATO films in our case were found to be completely insulating.

Figure 2.2(a) shows an image of the as-prepared ATO sol–gel precursor solution with a concentration of ~ 85 mg/mL. Figure 2.2(b) shows a schematic of the chemistry responsible for the formation of ATO from titanium isopropoxide, its precursor molecules. A schematic of a back-gated FET encapsulated by ATO is illustrated in Figure 2.2(c).

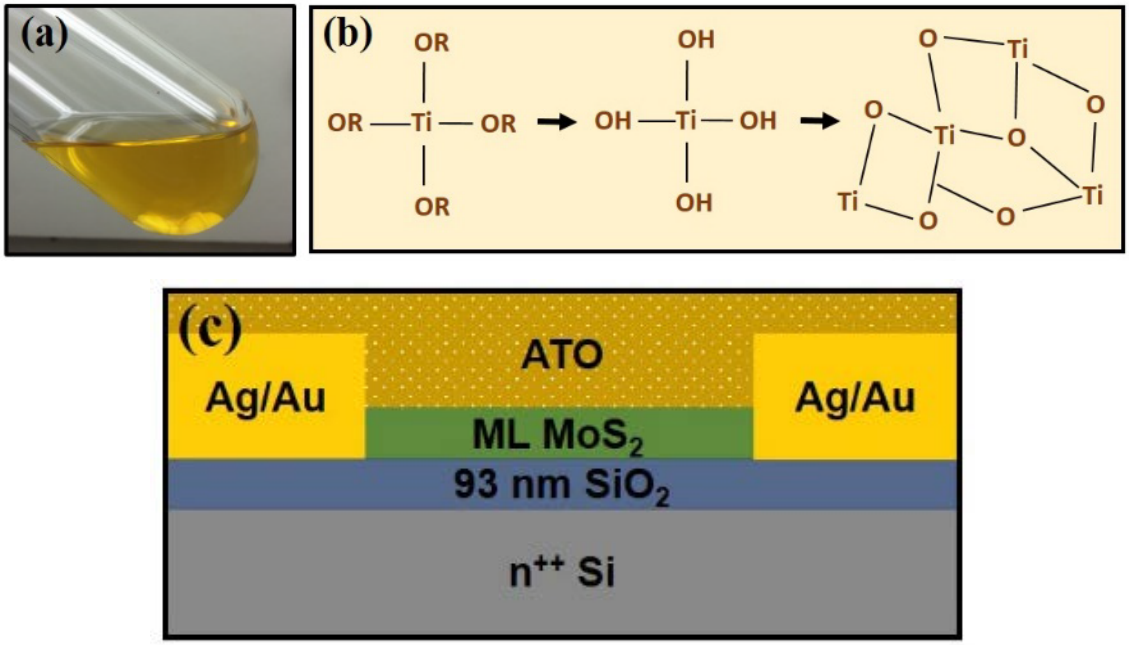

Figure 2.2: (a) Optical image of the as-prepared ATO precursor solution showing its characteristic yellowish-orange color. (b) Schematic of chemical steps involved in the formation of ATO from its precursor molecules, namely titanium isopropoxide (R = CH $(CH_3)_2$). (c) Schematic of a representative back-gated ML MoS_2 FET with Ag/Au source/drain contact electrodes and ATO encapsulation.

The doping of MoS_2 leads to changes in its Raman and photoluminescence (PL) spectra. Figure 2.3 compares the normalized Raman spectra of an as-exfoliated ML MoS_2 flake (blue) to that of the same flake after encapsulation by ATO (red). The peak positions of the out-of-plane A_{1g} and in-plane E^1_{2g} peaks for the bare ML MoS_2 are at 402.0 and 383.0 cm^{-1}, respectively, corresponding to a peak separation of 19 cm^{-1}. This peak separation is characteristic of ML MoS_2[221]. Upon encapsulation with ATO, the E^1_{2g} peak position and peak full-width half-maximum (FWHM) remain relatively unchanged. On the other hand, the A_{1g} peak shows a distinct broadening with its FWHM increasing from 6.6 to 8.1 cm^{-1}, as well as a redshift from 402.0 to 399.6 cm^{-1}. This redshift and peak broadening of the A_{1g} Raman mode are characteristic of doped MoS_2 and have been observed in previous doping studies[207]. Figure 2.4 compares the PL spectra of a ML MoS_2 flake before (blue) and after (red) encapsulation with ATO. Before encapsulation,

the peak position of the A exciton is at 1.86 eV, consistent with reported values for ML MoS_2[41]. Upon ATO encapsulation, the A exciton peak shows a decrease in intensity and a redshift of 16 meV, which can be attributed to the formation of negatively charged trions from excitons as a result of the increased electron concentration[222,223]. The pronounced changes in the Raman and PL spectra of ML MoS_2 upon ATO encapsulation clearly indicate the n-type doping effects of ATO on MoS_2.

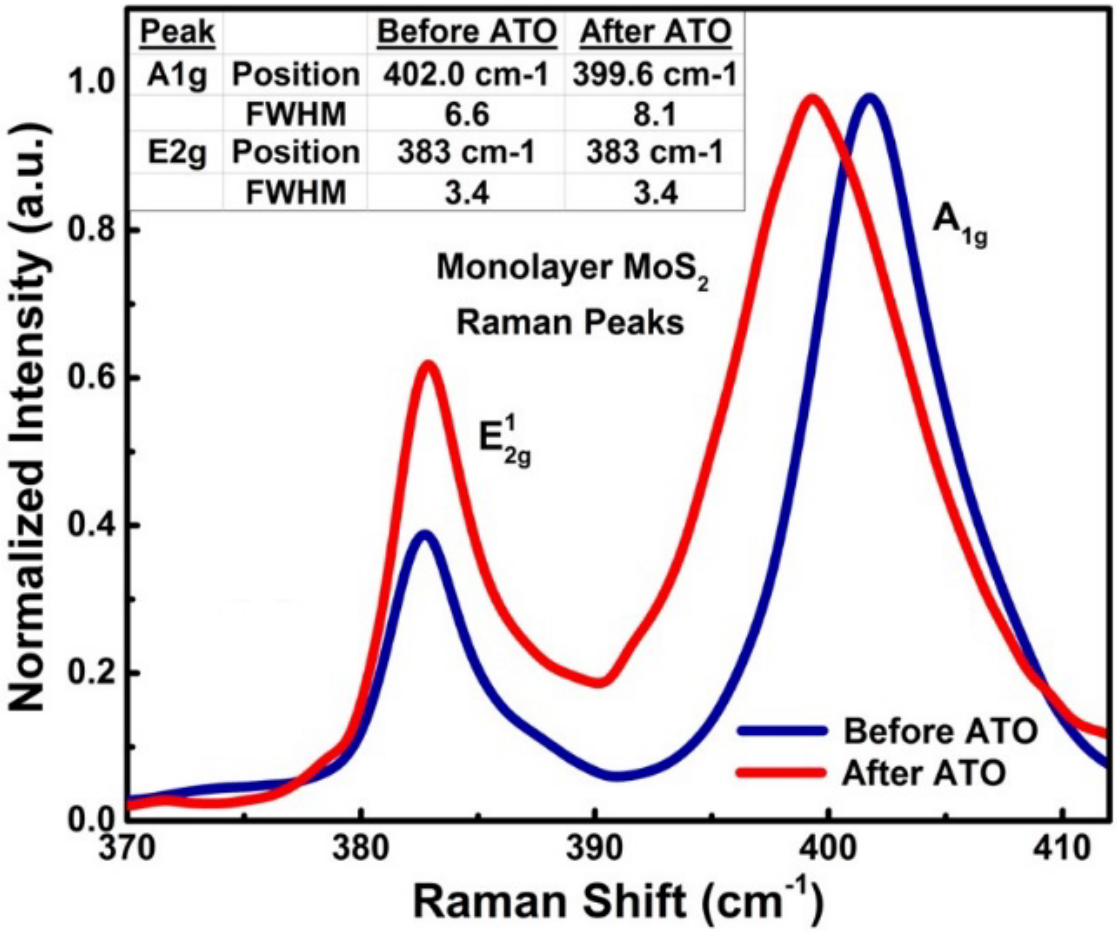

Figure 2.3: Raman spectra of ML MoS_2 showing its characteristic A_{1g} and E^1_{2g} peaks before (blue) and after (red) ATO encapsulation illustrating the electron doping-induced changes in the peak positions and peak widths.

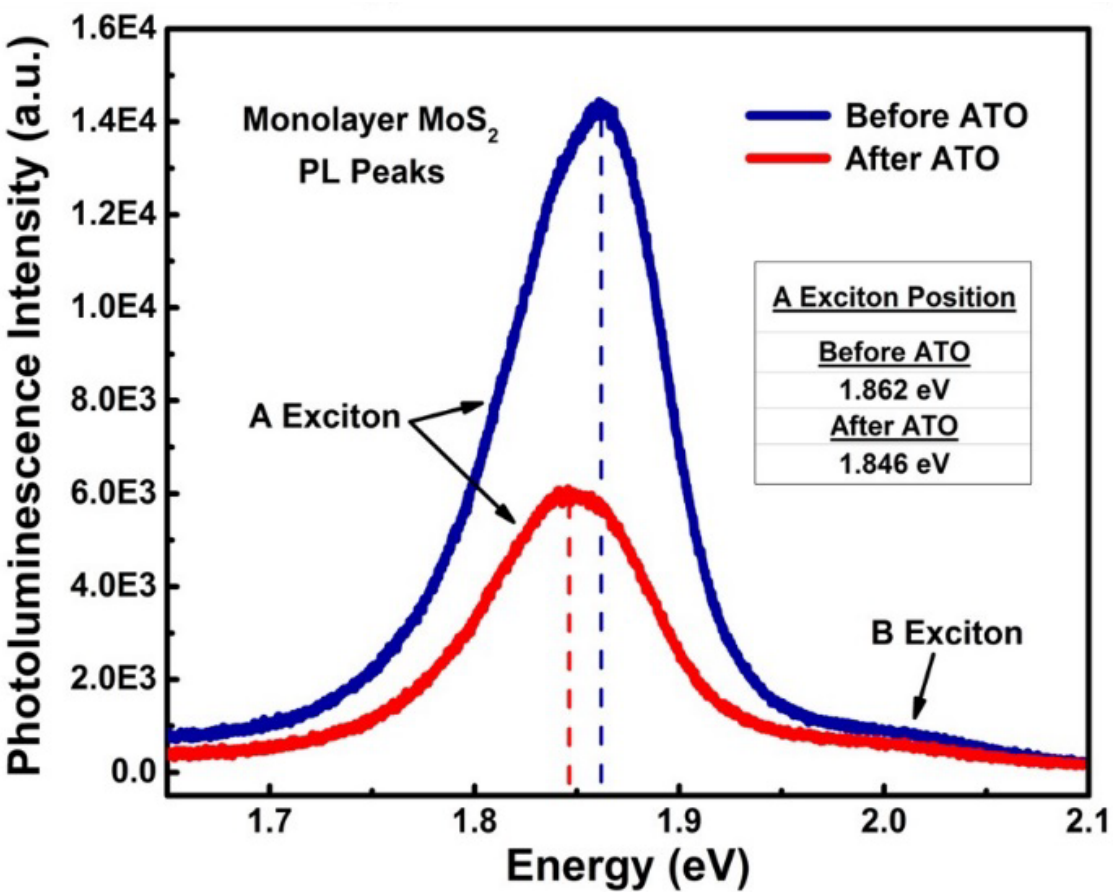

Figure 2.4: Photoluminescence spectra of ML MoS_2 before (blue) and after (red) ATO encapsulation showing a redshift in the peak position of the A exciton.

2.4 Electrical Characterization and Contact Resistance Evaluation of ATO-Doped Back-Gated MoS_2 Transistors

2.4.1 Transfer and Output Characteristics of ATO-Encapsulated Back-Gated MoS_2 Transistors

The transfer characteristics of a representative back-gated MoS_2 FET at V_{DS} = 1 V, before and after ATO encapsulation, as well as after one month of exposure to ambient conditions are shown in Figure 2.5 below. All FETs were fabricated on 93 nm SiO_2/n^{+2} Si substrates. The transfer curve before doping (blue) indicates a strong electrostatic gate control over the channel with a threshold voltage (V_T) of 7 V, extracted from the linear region of the transfer characteristics, and an I_{ON}/I_{OFF} ratio up to 10^8. Upon encapsulation

with ATO, the gate modulation is significantly reduced (red curve), and the V_T shifts to −25 V. This large negative V_T shift is indicative of the n-doping effect of ATO. The 2D sheet electron concentration (n_{2D}) after ATO doping can be estimated as $n_{2D} = (C_{OX} |\Delta V_T|)/q$, where q is the electron charge, $C_{OX} = 3.71 \times 10^{-8}$ F/cm^2 is the gate oxide capacitance, and $\Delta V_T = -32$ V is the shift in threshold voltage right after doping. The extracted value of n_{2D} for this device upon doping was 7.4×10^{12} cm^{-2}. Previous doping studies on MoS_2 utilizing K ions[204] and benzyl viologen[207] reported n_{2D} values of 1×10^{13} cm^{-2} and 1.2×10^{13} cm^{-2}, respectively. The n_{2D} value as a result of ATO doping is slightly lower in our case, however, it should be noted that our experiments used ML flakes unlike previous studies that utilized multilayer flakes. The long-term air stability of encapsulated ATO doping is evident from the electrical data as even after 30 days of exposure to ambient conditions, the device shows similar ON-currents, a weak gate modulation, and has an $n_{2D} = 3.7 \times 10^{12}$ cm^{-2} (green curve). Moreover, by virtue of being self-encapsulating, ATO films protect the underlying MoS_2 channel from the degrading effects of atmospheric adsorbates. However, there is slight performance degradation after extended ambient exposure in ATO encapsulated devices.

The inset of Figure 2.5 shows the transfer characteristics of the same device at larger gate and drain biases following the ATO encapsulation. The 450 nm channel length device could be switched off to a moderate extent ($I_{ON}/I_{OFF} = 4 \times 10^3$, subthreshold swing = 1.6 V/decade) at large negative gate biases even though V_{DS} was as high as 2 V. Further optimization and control over the starting concentrations of the ATO precursor solution or realization of top gated devices with ATO encapsulated S-D access regions would help yield an ideal balance between I_{ON}/I_{OFF} ratio and high saturation ON-currents. Figure 2.6 shows the output characteristics of the same device as in Figure 2.5. After ATO encapsulation, the ON current of the ML device at $V_{DS} = 1$ V and $V_{BG} = 25$ V is 144 μA/μm, which is 2.5 times greater than the corresponding value for the undoped device. The inset of Figure 2.6 shows the output characteristics of the same device subject to larger biasing conditions. At a V_{DS} of 2 V and V_{BG} of 45 V, the ON current is as high as 240 μA/μm showing the onset of current saturation at large positive gate and drain biases. Our ATO-

doped ML MoS_2 FET with an ON current of 240 μA/μm compares well with the highest drain current to date on chloride-doped multilayer MoS_2 FETs[210,214], taking into account the fact that the channel length in our case was 4.5 times larger and the device was made on a ML flake.

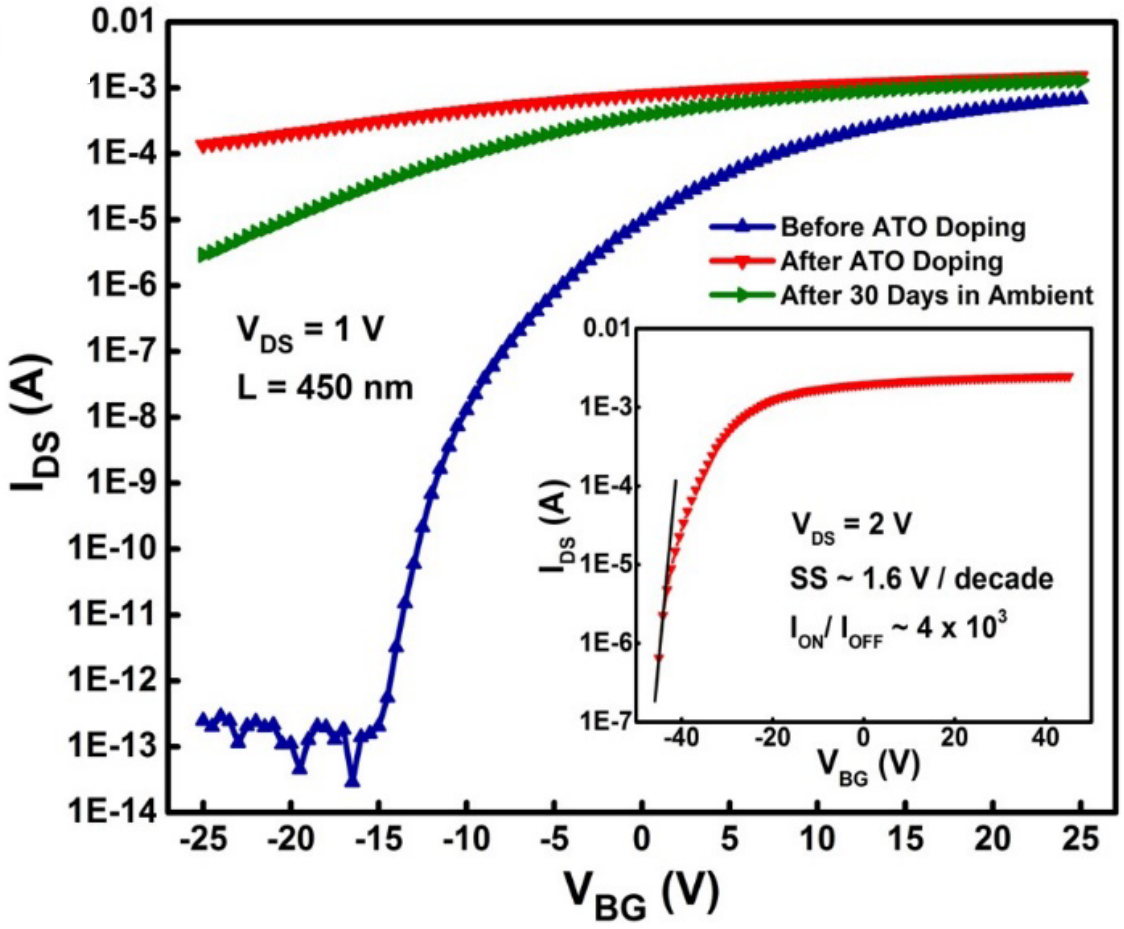

Figure 2.5: Transfer characteristics, shown on a semilog scale, of a representative ML MoS_2 FET at V_{DS} = 1 V before (blue) and after (red) ATO doping, and after 30 days of ambient exposure (green). Inset shows the transfer characteristics of the doped FET measured under larger gate (−45 to 45 V) and drain biasing (2 V) conditions. The channel length and width are 450 nm and 10.4 μm, respectively.

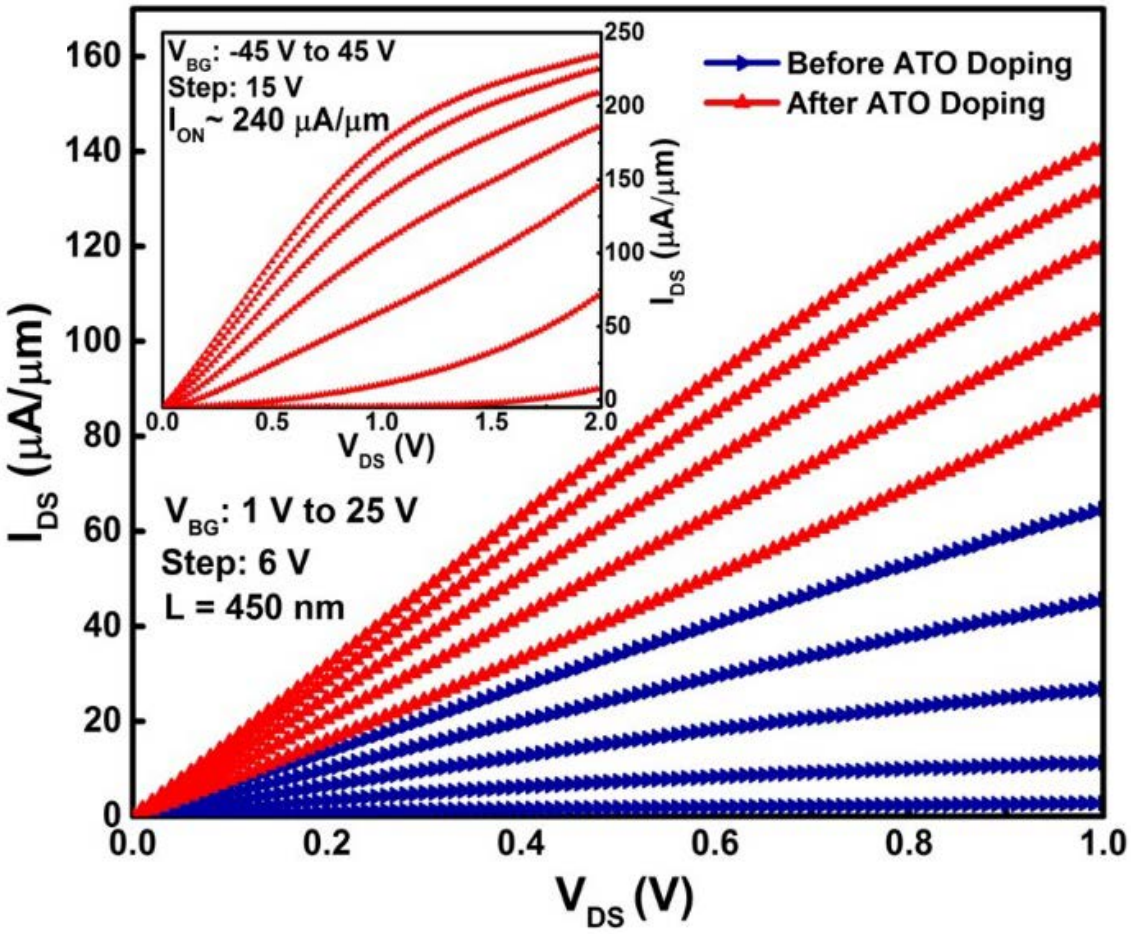

Figure 2.6: Output characteristics of the FET in Figure 2.5 before (blue) and after (red) ATO doping. Inset shows the output characteristics under larger biasing conditions with the ON-current reaching up to 240 μA/μm at a V_{BG} of 45 V and V_{DS} of 2 V.

2.4.2 Performance Degradation in ATO-Encapsulated Devices

As discussed above, the doping effect observed in ATO encapsulated devices is absent when it is replaced by stoichiometric TiO_2. Therefore, it is reasonable to assume that the slight degradation observed in the performance of ATO-encapsulated MoS_2 devices over long term air exposure (30 days) could be due to the ATO becoming more O-rich at the ATO–MoS_2 interface owing to its interaction with the pre-adsorbed oxygen and water molecules on the strongly hydrophilic SiO_2 substrate. The resulting oxide or hydroxide formation can adversely impact the electron donating capability of Ti atoms to

MoS_2 at the ATO–MoS_2 interface. Moreover, the pre-adsorbed oxygen or water molecules on the underlying SiO_2 substrate can react over time and degrade the quality of the ML MoS_2 itself. A possible way to eliminate any degradation effects could be to encapsulate the devices in ATO from both the top and bottom, especially since it has been shown that ATO is much more hydrophobic than SiO_2[216]. Other ways could be to use alternate substrates instead of SiO_2 such as h-BN. Moreover, further optimization of the preparation and deposition methods of the as-prepared ATO precursor solution is needed in order to minimize any impurities or trapped moisture in the overlaying dielectric.

2.4.3 Contact Resistance Evaluation of ATO-Doped Back-Gated MoS_2 Transistors

In order to quantify the effect of ATO doping on the electrical contact between the metal (Ag) and the ML MoS_2, a transfer length method (TLM) analysis was carried out. A suitable large area ML flake was identified, upon which a set of contacts were fabricated with different channel lengths as shown in the inset of Figure 2.8. The basic equation underlying the TLM analysis can be written as $R_{TOTAL} = (R_{SH}L)/W + 2R_C$, where R_{TOTAL} is the total measured resistance of a channel between two contacts, R_{SH} is the sheet resistance of the channel, L and W are the channel's length and width, respectively, and R_C is the contact resistance. By fitting a plot of ($R_{TOTAL} \cdot W$) as a function of L, key parameters such as R_{SH}, R_C, and transfer length (L_T) can be extracted. Figure 2.7 shows the total resistance, measured at a V_{BG} of 25 V and V_{DS} of 0.1 V, as a function of L before (blue) and after (red) ATO encapsulation. From a linear fit to the measured resistances before doping, an R_{SH} of 20.1 kΩ/□, R_C of 2.9 kΩ·μm and a transfer length (L_T) of 145 nm were extracted. Fitting the measured resistances after ATO encapsulation, we extracted an R_{SH} of 12.4 kΩ/□, R_C of ~ 180 Ω·μm (inset of Figure 2.7), and an L_T of 15 nm. This significant reduction in R_{SH}, R_C, and L_T upon ATO encapsulation reflects the efficacy of this doping technique. This is one of the lowest reported R_C value among all previous n-type doping studies on MoS_2[204,205,207], and compares well with the recently reported record low R_C value (~ 80 Ω·μm at a V_{BG} of 30 V) on MoS_2 with phase engineered contacts[208].

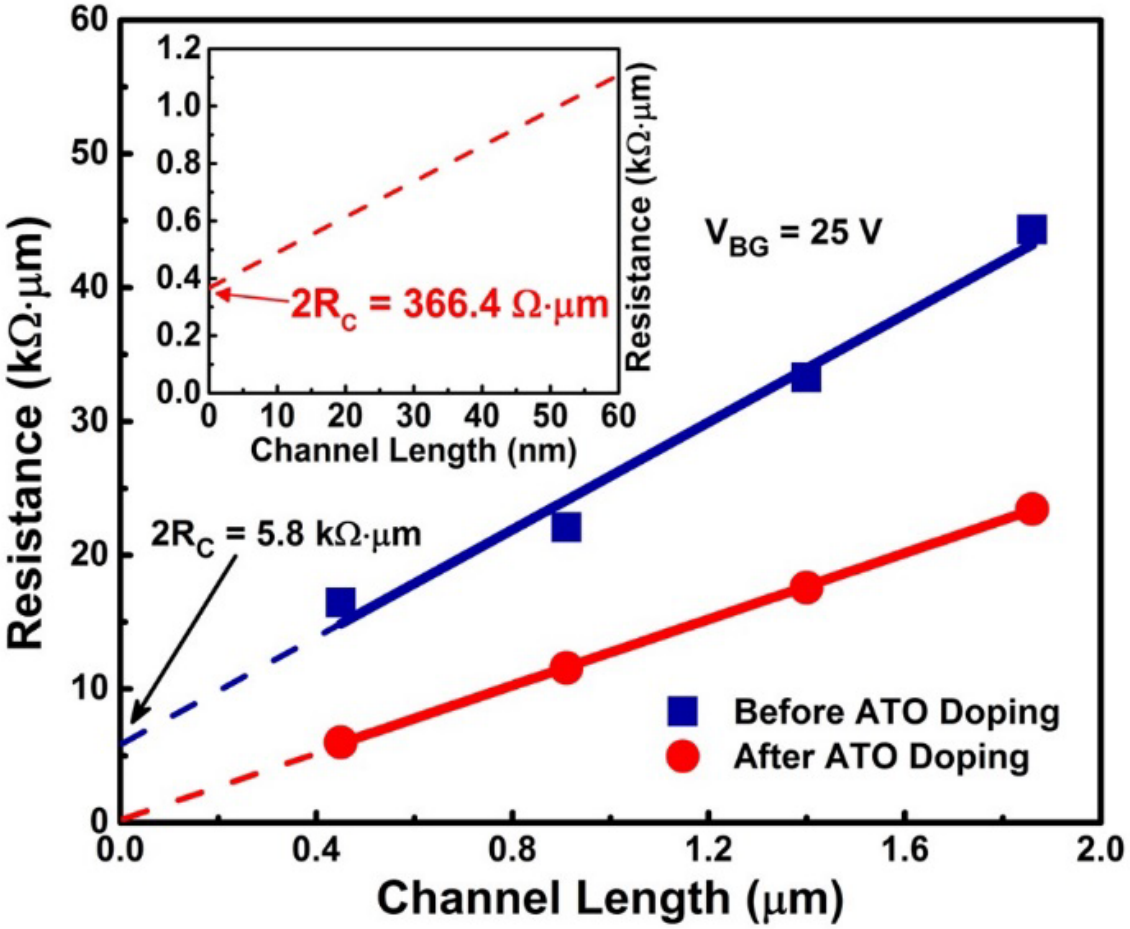

Figure 2.7: Plot of total resistance as a function of channel length as determined from the TLM structure before (blue) and after (red) ATO doping at a V_{BG} of 25 V. The solid blue and red lines are linear fits to the data. The R_C and L_T extracted before doping are 2.9 kΩ·μm and 145 nm, respectively. After ATO doping, the extracted R_C is ~ 180 Ω·μm and L_T is 15 nm. Inset: zoomed in view of the extrapolated dashed red line.

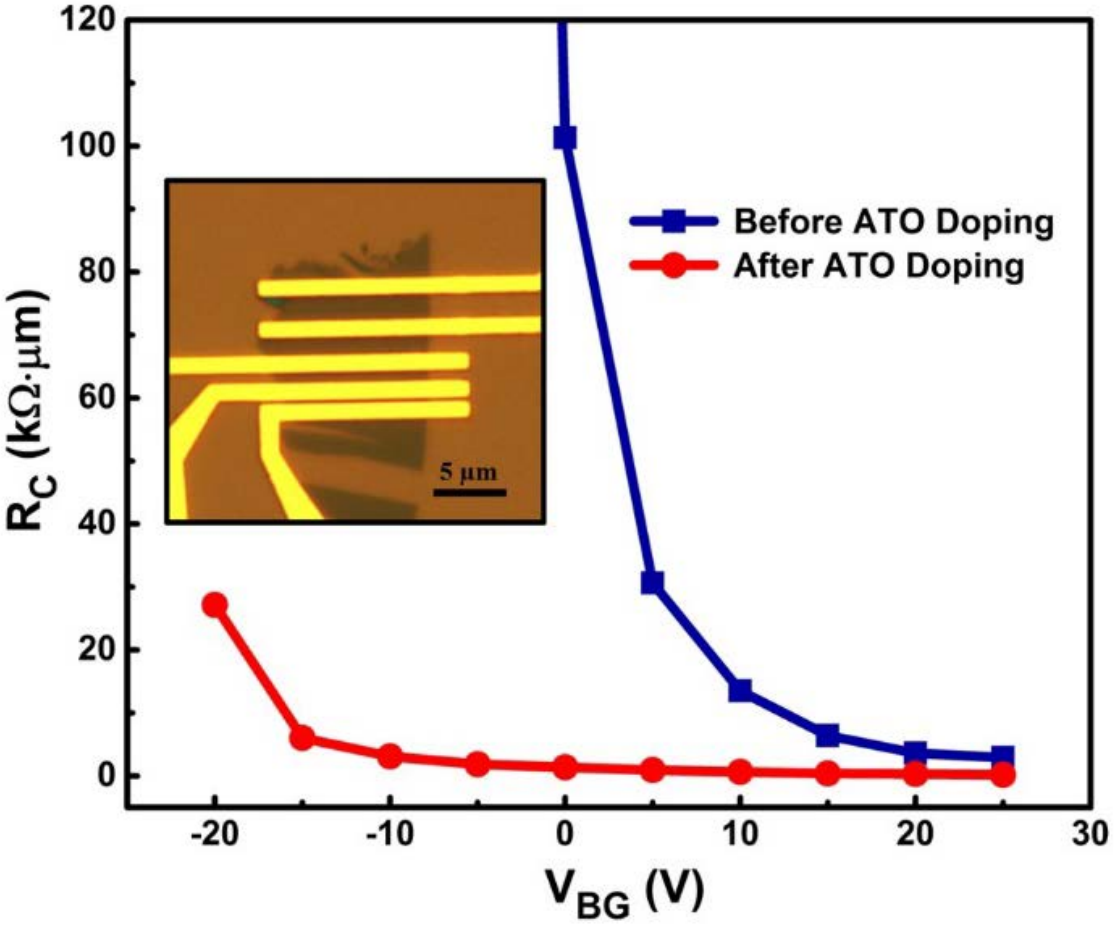

Figure 2.8: Extracted R_C as a function of V_{BG} before (blue) and after (red) ATO doping. The R_C shows a strong gate dependence before doping and a weak gate dependence after doping. Inset: optical micrograph image of the as-fabricated TLM structure.

Figure 2.8 above shows the extracted R_C values plotted as a function of V_{BG} before and after ATO encapsulation. For the undoped case (blue curve), the R_C shows a strong dependence on gate bias and increases exponentially at negative gate biases due to the large Schottky barriers present at the contacts. On the other hand, for the ATO doped case (red curve), the R_C is fairly independent of the applied gate bias for $V_{BG} > -10$ V. This results from the substantial thinning of the Schottky barrier width as a consequence of heavy doping at the contact regions. This Schottky barrier thinning effect is also apparent in the transfer characteristics temperature dependence, and in the output characteristics measured

at 77 K of a back-gated ML MoS_2 FET after ATO doping as discussed in Section 2.4.4 below. Thus, in the ATO-doped ML MoS_2 devices the effective Schottky barriers are significantly reduced even though the doping occurs along the contact edges as opposed to directly underneath the contacts. We note that this ATO doping effect on ML MoS_2 is absent when stoichiometric TiO_2 is used, as demonstrated previously in the case of graphene[217,224]. This was verified by depositing TiO_2 on back-gated ML MoS_2 FETs utilizing a recently demonstrated technique[225] as shown in Section 2.4.5 below.

2.4.4 Transfer Characteristics Temperature Dependence & Output Characteristics at 77 K of a Back-Gated ML MoS_2 FET Before/After ATO

Figure 2.9 below shows the temperature dependent transfer characteristics of a back-gated ML MoS_2 FET (L = 4 µm, W = 2 µm) at a V_{DS} of 100 mV. The x-axis is back-gate overdrive voltage ($V_{BG} - V_T$) and the V_T of each individual curve was taken into account in generating the above plots. Before ATO doping (plot on the left), the current at a fixed gate overdrive voltage decreases as the temperature is lowered indicating Schottky-barrier limited transport which is dominated by thermionic emission over the barriers. After ATO doping (plot on the right), the trend reverses and the current at a fixed gate overdrive voltage increases as the temperature is lowered which is characteristic of phonon-limited transport. The dominant transport mechanism is no longer thermionic emission, but tunneling through the barriers as a consequence of doping-induced Schottky barrier width thinning.

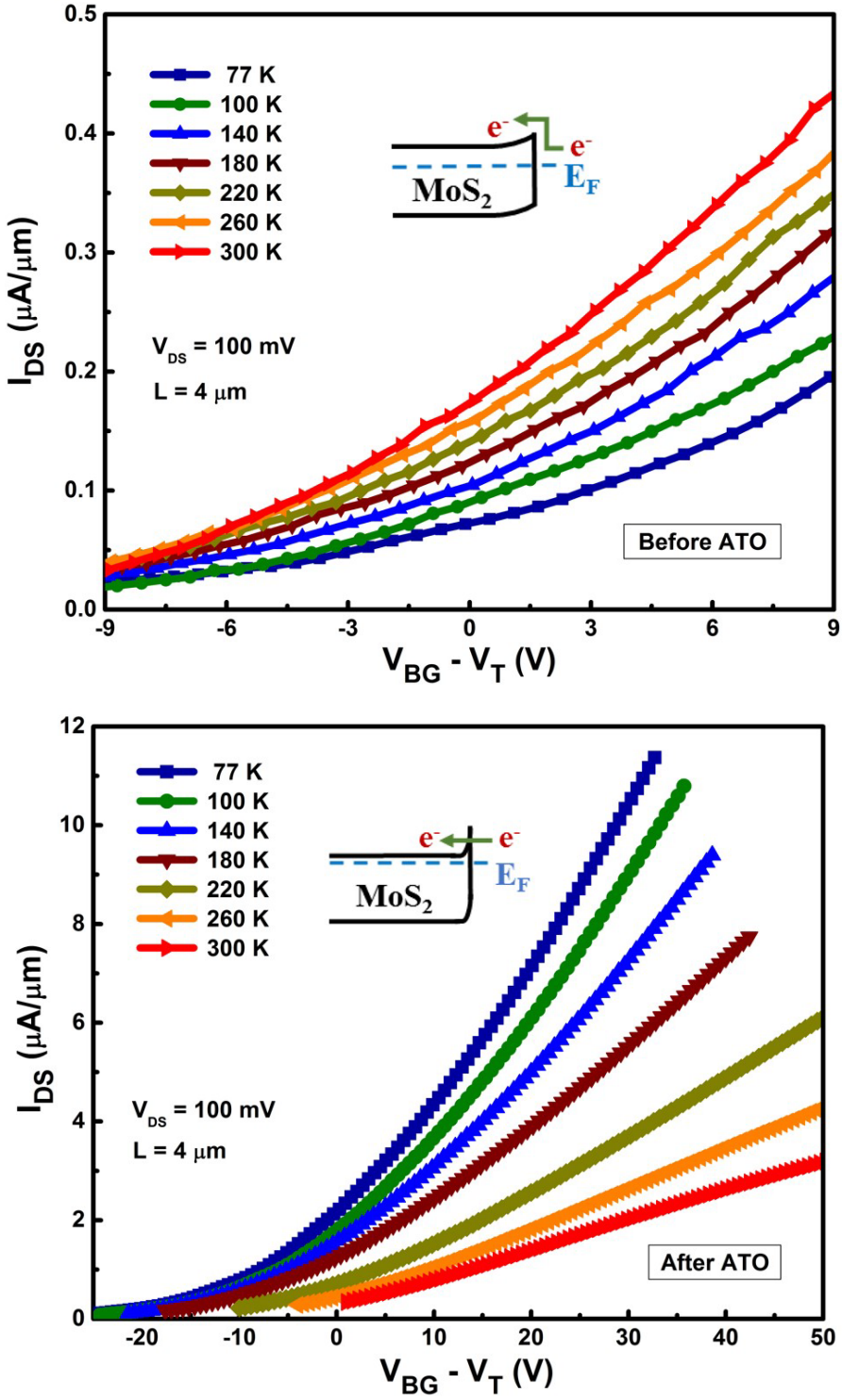

Figure 2.9: Temperature dependent transfer characteristics of a back-gated ML MoS_2 FET before (top plot) and after (bottom plot) ATO encapsulation.

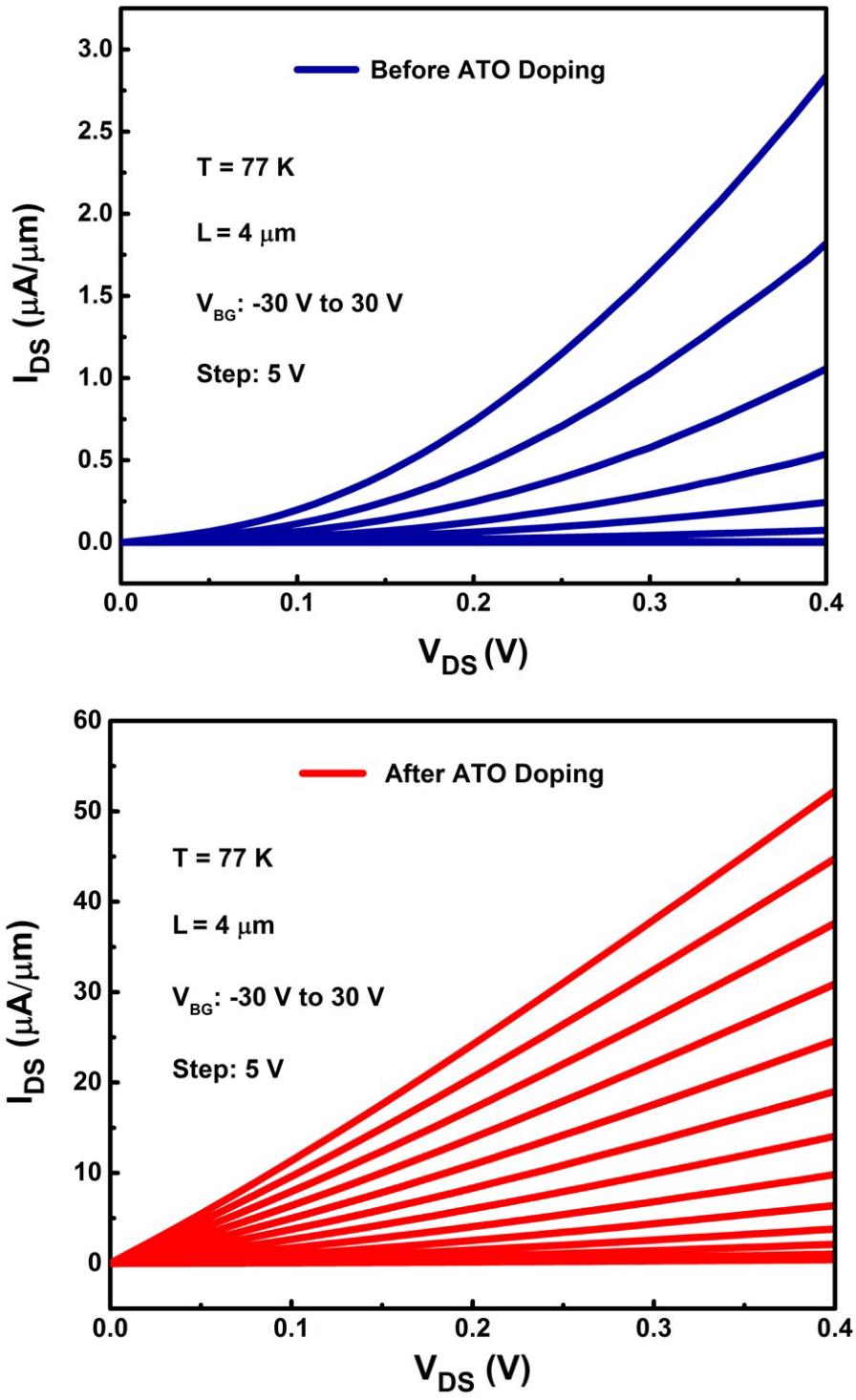

Figure 2.10: Output characteristics of the back-gated ML MoS_2 FET from Figure 2.9 at 77 K before (top plot; blue curves) and after (bottom plot; red curves) ATO encapsulation.

Figure 2.10 above shows the output characteristics of the back-gated ML MoS_2 FET, presented in Figure 2.9, measured at a temperature of 77 K before and after ATO doping. The effect of Schottky barriers on electron transport will be greater at 77 K owing to the reduced thermal energy of the carriers. The plot on the left (blue curves) depicts the bare MoS_2 FET clearly illustrating the exponential $I_{DS} - V_{DS}$ behavior indicative of substantial Schottky barriers between the MoS_2 and the Ag contact. In contrast, after the device is encapsulated in ATO, the output characteristics show a linear transport behavior indicating Ohmic contacts as depicted in the plot on the right (red curves). This linear behavior results due to the doping-induced thinning of the Schottky barrier width, thereby allowing the electrons to easily tunnel through.

2.4.5 Deposition Method of Stoichiometric TiO_2 and its Effect on MoS_2 FET Performance

The method to deposit TiO_2 on MoS_2 was adopted from a recent report of forming TiO_2 dielectrics on graphene as demonstrated by Corbet *et al.*[225] Using an SEC-600 e-beam evaporator from CHA Industries, high purity titanium pellets were evaporated from a titanium carbide crucible at a base pressure of 5×10^{-6} Torr which further reduced to 1×10^{-6} Torr during Ti deposition. Ti films with a thickness of 1 nm were evaporated at a rate of < 0.1 Å/s with the chamber being vented to atmosphere after each 1 nm of deposition in order to oxidize the Ti film to TiO_2. A 5 cycle deposition was performed which resulted in a TiO_2 film about 6 nm thick as has been demonstrated using ellipsometry and TEM analysis[225]. Furthermore, XPS measurements reported on titanium oxide deposited in this manner revealed a pure TiO_2 film[225].

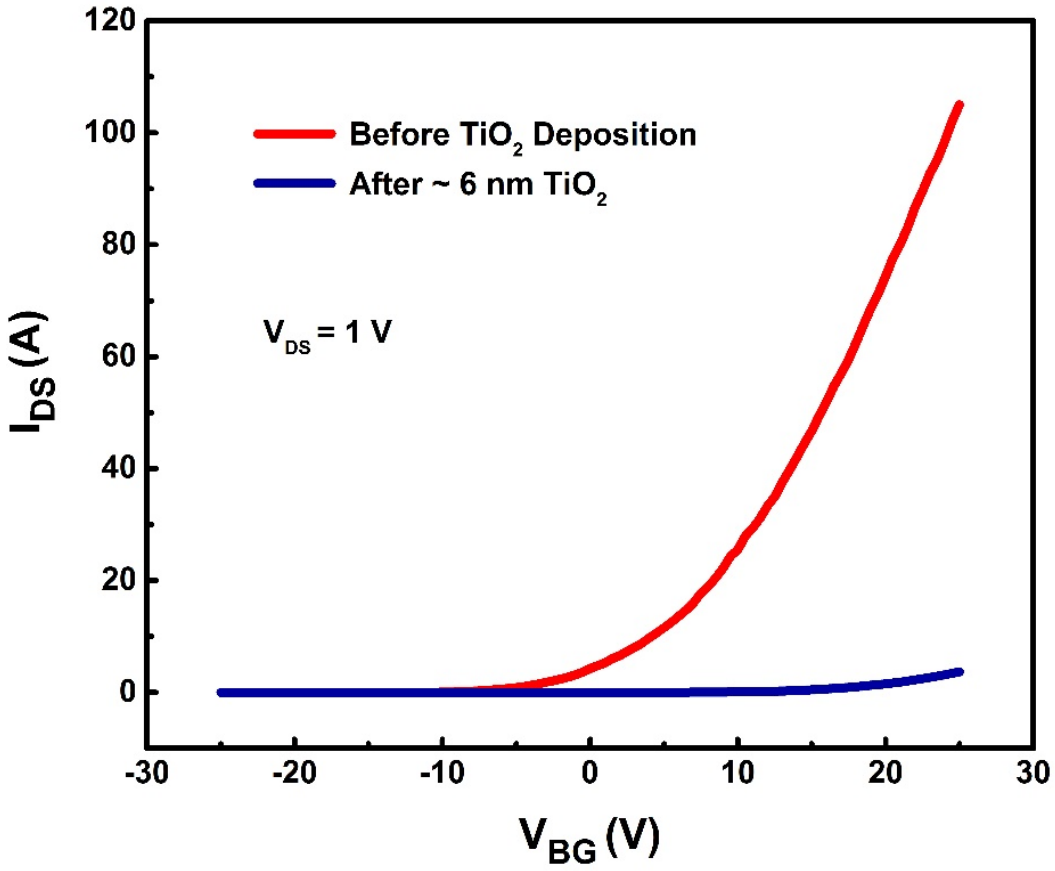

Figure 2.11: Transfer characteristics of a back-gated ML MoS_2 FET before (red) and after (blue) ~ 6 nm TiO_2 deposition at a V_{DS} of 1 V.

Unlike the ATO films, the stoichiometric TiO_2 film did not show any doping effect when deposited on back-gated ML MoS_2 FETs. Instead, as illustrated in Figure 2.11 above, the device showed a performance degradation. This can be explained by the poor interface quality that probably forms between MoS_2 and PVD deposited TiO_2. In fact, mobility degradation was also reported in graphene FETs with TiO_2 gate dielectrics[225]. Furthermore, the degradation could also be due to short range scattering by TiO_2 impurities as has been observed in the case of graphene[224].

2.5 THEORETICAL INVESTIGATION OF THE DOPING MECHANISM OF MoS_2 BY ATO USING DENSITY FUNCTIONAL THEORY

To gain further insight into the doping mechanism of MoS_2 by ATO, an *ab initio* DFT analysis was carried out to study the effects of both a Ti-rich and an O-rich interface of an underlying TiO_2 slab on the electronic structure of ML MoS_2 *via* band structure and atom-projected density-of-states (AP-DOS) calculations. The DFT simulation was performed using the Vienna *ab initio* simulation package (VASP)[226,227] and exact details of the methodology employed here are described elsewhere[228]. Briefly, our simulations were performed by constructing a supercell of ML MoS_2 on an approximately 1 nm thick TiO_2 slab. Atomic relaxation was performed within a rectangular supercell (a = 9.366 Å, b = 5.407 Å) chosen to reduce the lattice mismatch between ML MoS_2 and rutile-TiO_2 as shown in Figure 2.12. The rutile phase was chosen for the simulation because it is the most common natural form of TiO_2[229]. As stated before, we consider two possible terminations for the TiO_2 slab, a Ti-rich TiO_2 slab and an O-rich TiO_2 slab. For the Ti-rich TiO_2 case, the surface O atoms were removed from the supercell corresponding to an O-vacancy density of $7.896 \times 10^{14}/cm^2$ in order to mimic the ATO structure with interfacial O-vacancies. In these 0 K simulations, the highest occupied state corresponds to the 0 eV reference energy.

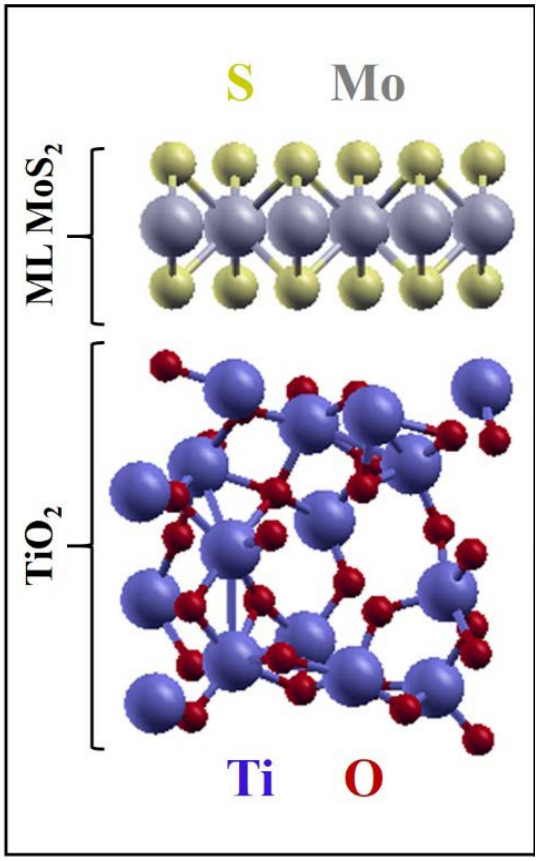

Figure 2.12: Supercell showing the composite crystal structure consisting of ML MoS_2 on an underlying rutile-TiO_2 slab as simulated in VASP. For simulating the O-rich TiO_2 case, the TiO_2 slab was left unaltered. In contrast, for the Ti-rich TiO_2 case, a suitable number of O vacancies were created in TiO_2 at the ML MoS_2–TiO_2 interface so as to mimic the MoS_2–ATO scenario. Note: All DFT simulations presented in Chapters 2 and 3 were performed at The University of Texas at Austin by Amithraj Valsaraj under the supervision of Professor Leonard F. Register.

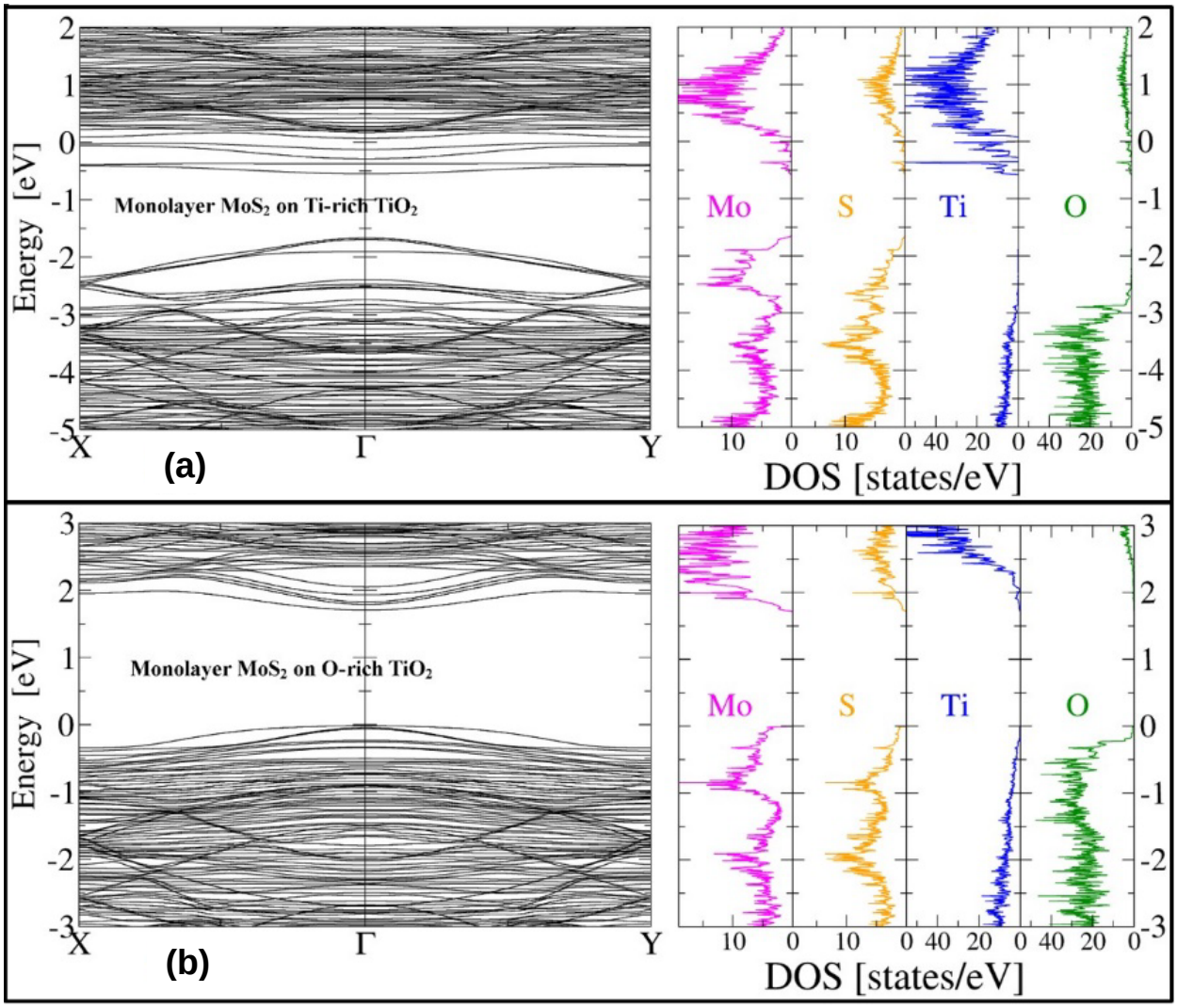

Figure 2.13: (a) Band structure and atom-projected density-of-states (AP-DOS) plots for the ML MoS_2–Ti-rich TiO_2 case. From the plots, it can be deduced that in the presence of O vacancies, electronic states from Ti atoms are introduced near the conduction band edge of ML MoS_2 causing the Fermi level to get pinned above the conduction band indicating strong doping. (b) Band structure and AP-DOS plots for the ML MoS_2–O-rich TiO_2 case. No doping effect is seen in this case and the Fermi level remains pinned at the valence band edge. (Simulations were done assuming 0 K).

Figure 2.13(a) shows the band structure of ML MoS_2 on a Ti-rich TiO_2 slab depicting occupied conduction bands below the Fermi level leading to a system that appears metallic. From the corresponding AP-DOS plot shown at the right, we can observe

that the occupied conduction bands can be attributed to Ti, Mo, and S atom states implying that the additional states introduced by the Ti atoms appear near the conduction band states of ML MoS_2. For the composite MoS_2–TiO_2 system, this phenomenon can be interpreted as a transfer of electrons into the lower conduction-band-edge of the ML MoS_2 layer analogous to modulation doping. In contrast, this phenomenon is absent in the case of ML MoS_2 on the O-rich TiO_2 slab, as depicted in Figure 2.13(b), wherein we have an ideal TiO_2 surface without any O-vacancies in the supercell. Here, the Fermi level is pinned at the valence band edge and the conduction band states remain unoccupied. Hence, our theoretical findings are in excellent agreement with our experimental results. It is to be noted that in the band structures depicted in Figures 2.13(a) and (b), the conduction band minima and the valence band maxima are located at the Γ point as opposed to the K point for ML MoS_2. This is because using a bigger supercell in the DFT simulations results in the corresponding Brillouin zone being smaller and hence the K point folds into the Γ point[228].

2.6 Investigation of Intrinsic Mobility Enhancement in ATO-Encapsulated ML MoS_2 using Four-Point Back-Gated Devices

An added advantage of using high-κ ATO as a self-encapsulating dopant is the intrinsic mobility enhancement of ML MoS_2 as extracted from four-point back-gated devices that exclude contact resistance effects. High-κ dielectric engineering, using ALD deposited hafnia and alumina, has been used widely on MoS_2 and other TMDs[40,66,136,158,211,230]. Although the exact mechanism is still unclear, it is believed that the presence of a high-κ environment enhances the carrier mobility by "screening" the Coulomb interactions with charged impurities, as well as by quenching the homopolar phonon modes of MoS_2[130,196,231]. Although ATO films have been shown to have a κ-value ranging between 70–120[232], the κ-value of our solution-processed ATO films was extracted to be ~ 10 from capacitance–voltage measurements, a value comparable to the κ-values reported for alumina and hafnia[233]. Figure 2.14 shows the measured four-point conductance ($G_{4\text{-pt}}$) as a function of $V_{BG} - V_T$ for a ML MoS_2 device (shown in the inset

with the flake outlined at its edges) before and after ATO encapsulation. The four left-most contacts of the device (a, b, c, and d) were used for the four point measurement that was done at RT. Current was passed between the outer two contacts (a, d) while the inner two contacts (b, c) served as the voltage probes. A marked difference exists between the slopes of the curves from the bare device (blue) and after its encapsulation in ATO (red). Intrinsic mobility (μ_{int}) was calculated using the expression $\mu_{int} = (L/W)\ (1/C_{OX})\ (dG_{4\text{-}pt}/dV_{BG}|_{max})$ where $L = 1.45$ μm and $W = 1.42$ μm are the length and width of the active region bounded by contacts b and c, respectively, C_{OX} is the geometric oxide capacitance, and ($dG_{4\text{-}pt}/dV_{BG}|_{max}$) is the maximum slope of the four point conductance curves as marked by dashed light-green lines in the figure. For the bare ML MoS_2, we extracted a μ_{int} of 48 cm^2/V-s at RT, whereas after encapsulation μ_{int} increased to 102 cm^2/V-s (~ 2× improvement). This value is among the highest intrinsic mobilities reported for ML MoS_2 at RT and comes close to the calculated RT phonon-limited mobility of 130 cm^2/V-s, a more realistic estimation in which the effect of intervalley scattering between the K and Q valleys, separated from each other in energy by just 70 meV, was also considered[131]. Though this was the best RT intrinsic mobility enhancement we observed upon ATO encapsulation (>2× improvement), the effect itself was observed in five other four-point devices. The two-point μ_{FE} measured between contacts "d" and "e" ($L = 0.46$ μm, $W = 1.42$ μm) at a V_{DS} of 100 mV before and after encapsulation was 24 cm^2/V-s and 83 cm^2/V-s, respectively, showing > 3× improvement [the linear transfer curves of this FET is shown in Figure 2.15]. Comparing the two point μ_{FE} of this device with the four-point μ_{int} of the parent MoS_2 flake, we see that the ratio μ_{int}/μ_{FE} decreases from 2.02 before ATO encapsulation to 1.23 after ATO encapsulation implying that the two-point μ_{FE} of this device approaches the four-point μ_{int} of the parent flake due to the doping by ATO.

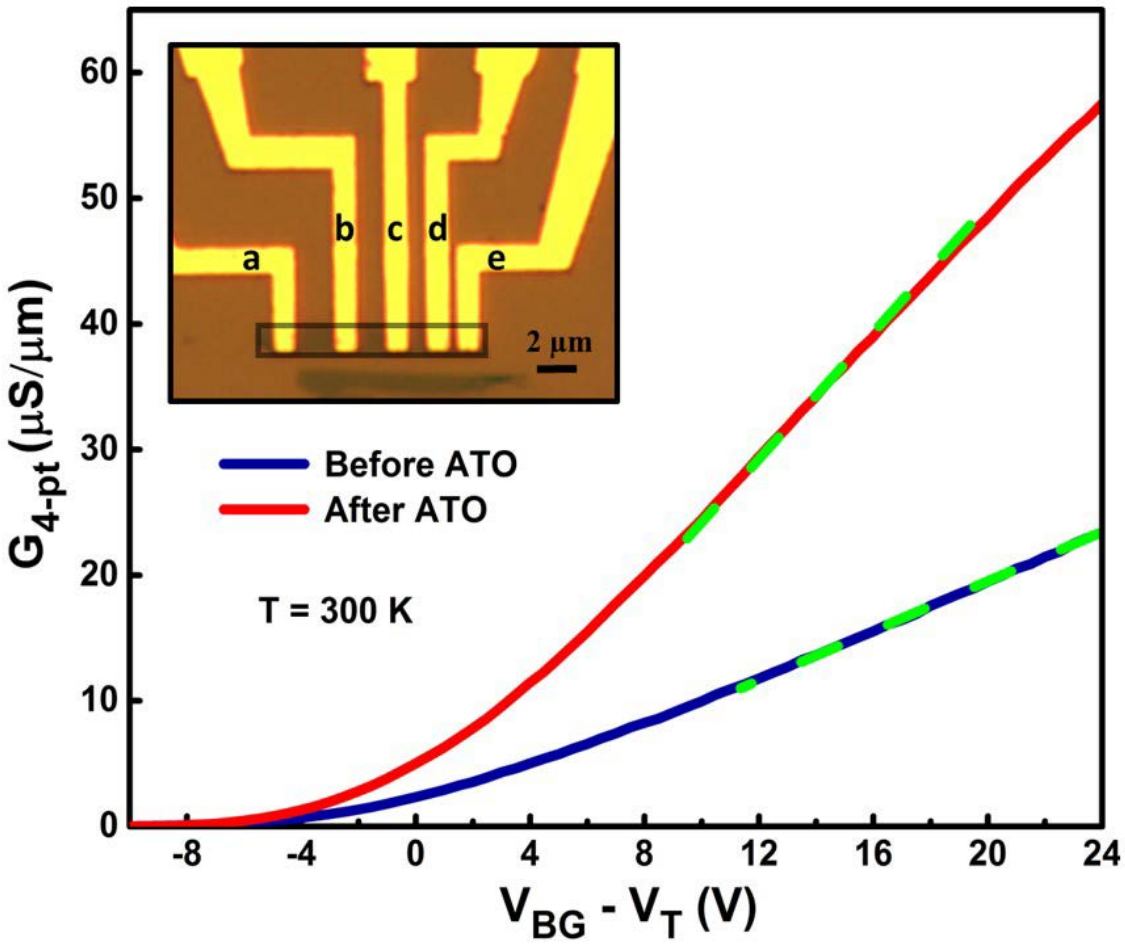

Figure 2.14: Four-point conductance ($G_{4\text{-pt}}$) curves as a function of the gate overdrive ($V_{BG} - V_T$), measured between contacts a, b, c, and d of the device shown in the inset, before (blue) and after (red) ATO encapsulation at RT. Dashed light green lines represent the regions from where the maximum slope was extracted for the calculation of intrinsic mobility of the ML MoS_2 flake before/after ATO encapsulation. The length and width of the active region are 1.45 and 1.42 μm, respectively. Contacts d and e (separated by 460 nm) were used to extract the two-point field effect mobility before/after ATO encapsulation (ML MoS_2 flake is outlined at its edge).

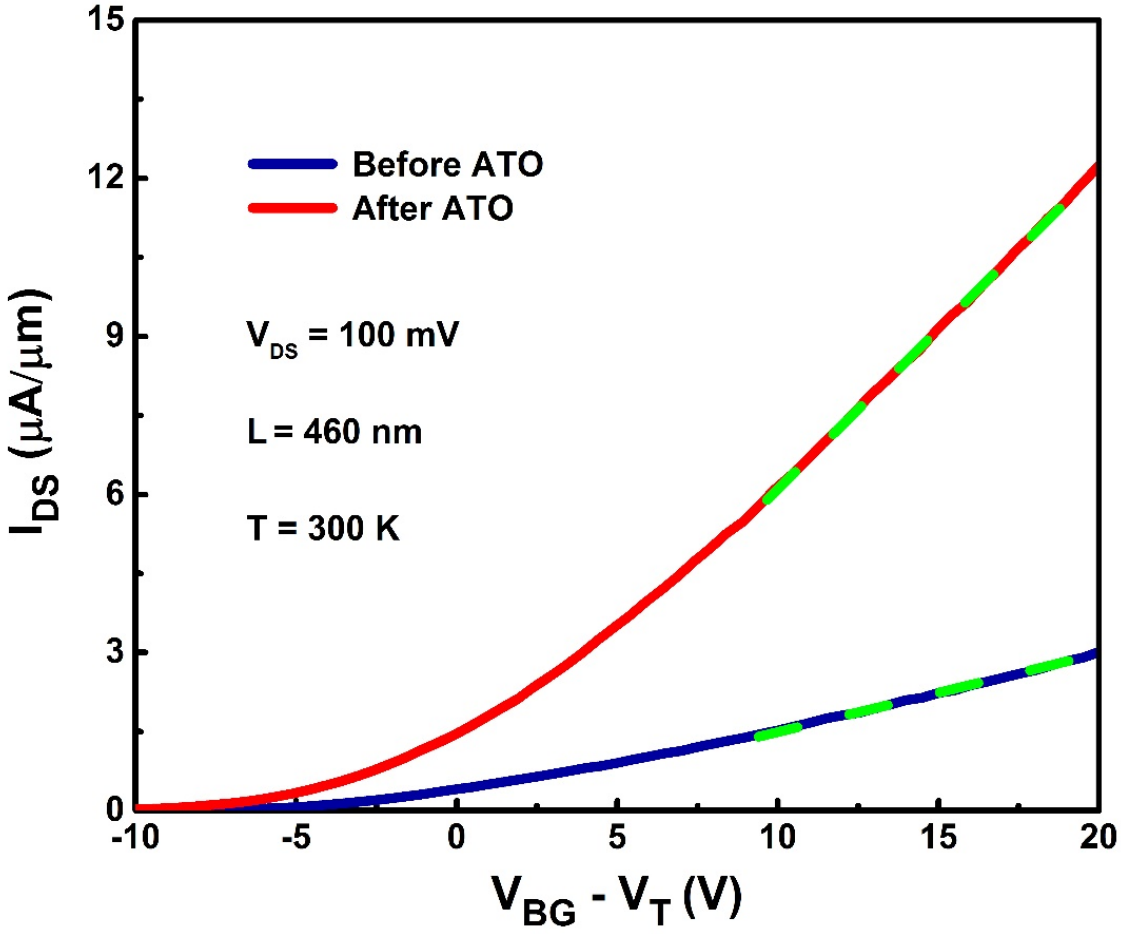

Figure 2.15: Transfer characteristics of the FET between contacts 'd' & 'e' of the multi-contact device shown in Figure 2.14.

Figure 2.15 above shows the transfer curves of the two-point FET between contacts 'd' & 'e' of Figure 2.14 at a V_{DS} of 100 mV measured at RT before (blue) and after (red) ATO encapsulation. From the regions of maximum slope as marked in the figure by dashed light-green lines, the peak g_m was extracted both before and after ATO doping. The μ_{FE} calculated before doping was ~ 24 cm^2/V-s which increased to ~ 83 cm^2/V-s after doping showing a > 3X improvement in the field effect mobility. This two-point device with a channel length of 460 nm showed the best mobility enhancement upon ATO encapsulation among all other two-point devices with a similar channel length.

Figure 2.16 below shows the maximum four-point intrinsic mobility of another ML MoS_2 device (shown in the inset) as a function of temperature. The length and width of the active region are 2.3 and 2.5 μm (flake width), respectively. Before ATO encapsulation (blue), the intrinsic mobility varies from 30 cm^2/V-s at RT to 285 cm^2/V-s at 77 K. After ATO encapsulation (red), the values range from 52 cm^2/V-s at RT to 501 cm^2/V-s at 77 K following a similar trend. This value of 501 cm^2/V-s in ATO-encapsulated MoS_2 is among the highest intrinsic mobilities reported to date on ML MoS_2 at 77 K and compares well with the recent work on ultrahigh mobility MoS_2 that is encapsulated in hexagonal boron nitride and contacted by graphene[234]. Although this mobility enhancement may be attributed to the high-κ nature of the encapsulating ATO, we know that the n_{2D} in the MoS_2 channel is increased as the high-κ ATO film dopes the MoS_2 owing to its interfacial oxygen vacancies. Increased carrier densities in a nondegenerate 2D channel aids in enhancing the carrier mobility by screening the charged impurities, as has been demonstrated both theoretically[231] and experimentally[197] in ML MoS_2. Furthermore, the increased electron concentration also serves to soften the homopolar phonons of MoS_2 as evident from the red shift and broadening of the out-of-plane A_{1g} Raman mode of ML MoS_2 upon ATO encapsulation. Our results, therefore, give important insight into the mechanism of mobility enhancement in MoS_2 devices effected by high-κ dielectrics. In light of our ATO–MoS_2 results, it is plausible that this doping effect can be caused by other high-κ dielectrics, such as ALD-deposited alumina or hafnia, if they have inherent oxygen vacancies at their interfaces with MoS_2. Given the amorphous nature of the ALD grown high-κ dielectrics, it is highly possible that oxygen vacancies exist in their structure. In fact, our recent investigation[228] reveals that interfacial oxygen vacancies in alumina or hafnia lead to the creation of donor states near the conduction band of MoS_2. These donor states originate from the uncompensated aluminum and hafnium atoms at the high-κ–MoS_2 interface, much akin to our case of uncompensated titanium atoms at the ATO–MoS_2 interface, resulting in n-type doping of the ML MoS_2 channel. On the other hand, when the alumina or hafnia is perfectly stoichiometric, no doping effect is observed. Therefore, we propose that this interfacial-oxygen-vacancy-mediated doping effect plays a prominent

role in enhancing both the intrinsic and field-effect mobility in high-κ encapsulated TMD devices. Upon high-κ encapsulation, there would be an increase in the n_{2D} of the TMD channel even before the application of external gate or drain biases, and this increased n_{2D} would screen out the charged impurities, suppress the homopolar phonons, and reduce the effective Schottky barriers at the contacts to a greater extent than in bare devices. Hence, when external biases are applied, the electrons would be injected more easily and will move across the channel with less scattering, resulting in higher transconductance at relatively lower gate/drain biases in high-κ encapsulated TMD FETs.

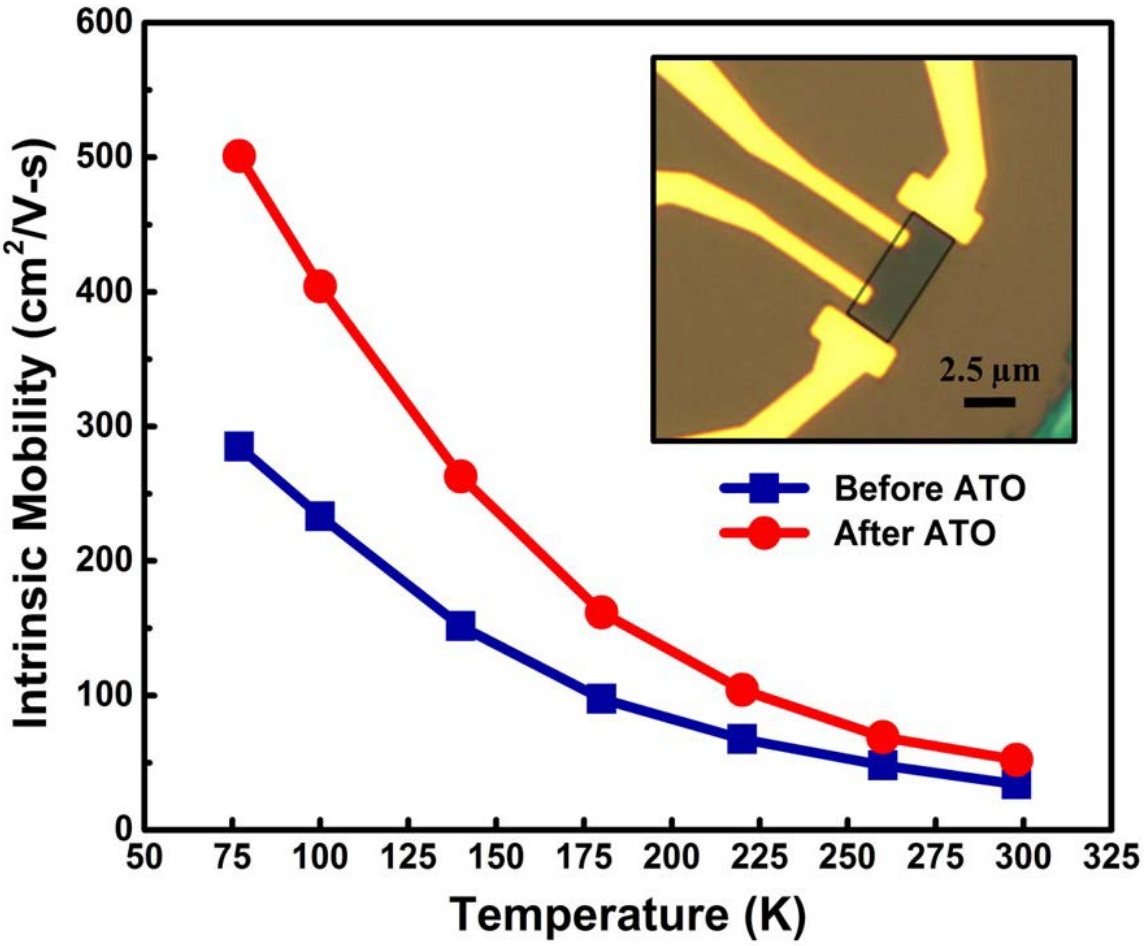

Figure 2.16: Intrinsic mobility of ML MoS_2 as a function of temperature before (blue) and after (red) ATO encapsulation. Optical micrograph of the four-point device is shown in the inset. The length and width of the active region are 2.3 and 2.5 μm, respectively. The

intrinsic mobilities are enhanced after ATO encapsulation reaching up to 501 cm^2/V-s at 77 K (ML MoS_2 flake is outlined at its edge).

2.7 CONCLUSION

To conclude, we have demonstrated that high-κ ATO films can be used as an n-type charge transfer dopant on ML MoS_2. The fact that ATO encapsulated ML MoS_2 devices exhibited comparable or better performance than previous doping and high-κ studies bears testimony to the superior doping and mobility enhancing capabilities of ATO thin films. Moreover, high-κ ATO can be deposited by a simple spin coating process that makes this doping approach attractive when compared to other time-consuming doping techniques. Utilizing this technique on ML MoS_2, we demonstrated two-point field effect mobility as high as 83 cm^2/V-s at RT, four-point intrinsic mobility as high as 102 cm^2/V-s at RT and 501 cm^2/V-s at 77 K. ON-currents as high as 240 μA/μm for a 450 nm channel length device, and a record low R_C of 180 Ω·μm were demonstrated on ML MoS_2 after ATO encapsulation. In addition, we also shed light on the interfacial-oxygen-vacancy mediated doping of MoS_2 by high-κ dielectrics, in general, leading to improved screening of charged impurities, suppression of homopolar phonon scattering, and reduction of the effective Schottky barriers at the contacts. Future work includes studying the stoichiometry and thickness scalability of ATO films and their effect on the performance and air stability of TMD-based devices.

Chapter 3: Interfacial-Oxygen-Vacancy Mediated N-Doping of MoS_2 by Atomic Layer Deposited HfO_x and Al_2O_x

3.1 INTRODUCTION

The atomically thin form of ML TMDs translates to excellent electrostatic gate control even at nanoscale channel length dimensions[30,37,62]. However, the two-dimensional (2D) nature of ML TMDs makes their properties susceptible to the surrounding environment, as evidenced by the mobility enhancement of ML MoS_2 when placed on a high-κ dielectric such as hafnia (HfO_2)[40]. Dielectric engineering using high-κ oxides, such as atomic layer deposited (ALD) Al_2O_x and HfO_x, has been in widespread use to enhance the mobility of molybdenum disulfide (MoS_2)-based field effect transistors (FETs)[196,212]. This mobility improvement in 2D materials was attributed to the damping of Columbic impurity scattering, as well as the quenching of homopolar phonon modes of MoS_2, by high-κ dielectrics[235]. However, the exact mechanism is still unclear. Theoretical calculations of HfO_2 interfaces have indicated that band offsets can be altered chemically by utilizing different interface terminations[236]. The conductive characteristics of MoS_2 deposited on SiO_2 have been shown to be dependent on the interface structure[237]. Controllable n-type doping of graphene transistors with extended air stability have been demonstrated by using self-encapsulated doping layers of titanium sub-oxide (TiO_x) thin films[217]. These results puts into stark focus the need to consider the effect of surrounding materials and the interfaces with them on the characteristics of ML TMDs.

In this Chapter, we focus on the effects of O vacancies (O deficiency) in MoS_2 on HfO_2 and on Al_2O_3. We have used both theoretical DFT and experimental analysis to study the n-doping of MoS_2 mediated by interfacial-oxygen-vacancies at the high-κ-MoS_2

Much of the results, discussions and figures presented in this Chapter have been adapted with permission from the following two references: (1) Rai, A., Valsaraj, A., Movva, H. C. P., Roy, A., Tutuc, E., Register, L. F., & Banerjee, S. K. (2015, June). Interfacial-Oxygen-Vacancy Mediated Doping of MoS_2 by High-κ Dielectrics. In *2015 73rd Annual Device Research Conference (DRC)* (pp. 189-190). IEEE. (2) Valsaraj, A., Chang, J., Rai, A., Register, L. F., & Banerjee, S. K. (2015). Theoretical and Experimental Investigation of Vacancy-Based Doping of Monolayer MoS_2 on Oxide. *2D Materials*, *2*(4), 045009. The dissertator, A. Rai, helped conceive and design the experiments, fabricated the devices with high-κ dielectrics, performed the electrical, Raman and photoluminescence measurements, and contributed to data analysis and writing the manuscripts.

interface and, based on these results, propose a mechanism for the mobility enhancement effect in MoS_2 devices upon high-κ encapsulation. For the O deficient systems, two possible terminations for the HfO_2 (Al_2O_3) slab are considered using DFT: an O-terminated HfO_2 (Al_2O_3) slab with H passivation and an Hf (Al)-terminated HfO_2 (Al_2O_3). The naming of two possible terminations is indicative of the initial structures used as starting point in our atomistic relaxations. The effects of O-vacancies in the first few layers of oxide on the band structure of the MoS_2-oxide system were simulated, with results for vacancies in the topmost/MoS_2-adjacent O layer shown here. Among our findings, O vacancies can lead to modulation-like doping of the MoS_2 from donor states in the oxide depending on the oxide terminations. Moreover, consistent with our theoretical results, electron doping of ML MoS_2 *via* O deficiency in the high-κ oxides was experimentally demonstrated by electrically and spectroscopically characterizing back-gated MoS_2 field-effect transistors (FETs) encapsulated by O deficient versions of either alumina (Al_2O_x) or hafnia (HfO_x).

3.2 Details of Experimental and Theoretical Methods

3.2.1 Experimental Method

Monolayer (ML) or bilayer (BL) MoS_2 was mechanically exfoliated from commercially available bulk MoS_2 crystals (SPI Supplies) onto a degenerately doped n-type Si-(100) substrate, which served as the back-gate, covered by a 90 nm thick thermal oxide. Upon exfoliation, the samples were annealed at 350°C in high vacuum (~ 10^{-6} Torr) for 8 h to minimize tape residues and trapped adsorbates between the MoS_2 and the silicon dioxide substrate. A combination of optical microscopy, atomic force microscopy, Raman and photoluminescence measurements were used to identify atomically flat ML MoS_2 flakes of interest. Source and drain contacts were patterned using electron beam lithography followed by electron beam evaporation and solvent lift-off of an Ag/Au (20/30 nm) stack or just Au (50 nm). Finally, devices were covered by ~ 30 nm of either alumina or hafnia deposited at 200°C using atomic layer deposition (ALD) *via* the reaction of water with standard ALD precursors, namely trimethyl aluminum for alumina and tetrakis (dimethylamido) hafnium for hafnia. Figure 3.1 shows the 3D schematic of the back-gated

MoS_2 FET encapsulated by high-κ oxide. The stoichiometry of the as-deposited ALD high-κ oxides were changed by altering the ratio of their precursor pulse times as well as the precursor pulsing order so as to achieve either an O-rich oxide or an O-deficient oxide. The thickness of the as-deposited ALD oxides were determined using ellipsometry and their dielectric constant values (or 'κ' values) were determined from standard high frequency capacitance-voltage (HFCV) measurements done on MOSCAP structures utilizing the Keysight B1500A Semiconductor Parameter Analyzer. Electrical transport measurements were carried out in the ambient, and in the dark, utilizing either the Keysight B1500A or the Keysight 4156C Semiconductor Parameter Analyzers. All electrical measurements were done on a Cascade Summit 11000 AP probe station. Note that the gate voltage sweep direction was from positive to negative voltages for the FET data presented in this Chapter. The stoichiometry of the as-deposited high-κ oxide was determined using x-ray photoelectron spectroscopy (XPS). An in-depth look at the experimental details and device fabrication procedures can be found in the work by Rai *et al.*[238,239].

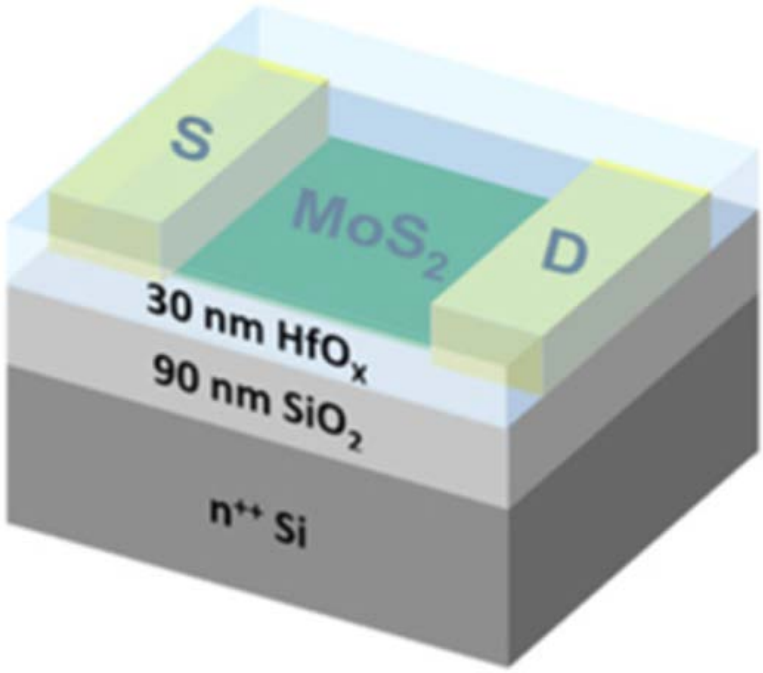

Figure 3.1: 3D schematic of a back-gated ML MoS_2 FET encapsulated by HfO_x.

3.2.2 DFT Computational Details

The theoretical DFT calculations were performed using the projector-augmented wave method with a plane-wave basis set as implemented in the Vienna *ab initio* simulation package[226,227]. We chose a kinetic energy cutoff of 400 eV. The *k*-mesh grid of 7 × 7 × 1 for the sampling of the first Brillouin zone (BZ) of the supercell was selected according to Monkhorst–Pack type meshes with the origin being at the Γ point for all calculations except the band structure calculation. The local density approximation (LDA)[240] was employed primarily for the exchange-correlation potential as LDA has been shown to reproduce the apparent experimental band gap ($E_g = 1.8$ eV)[241] of ML MoS_2 well[171,242]. The calculated lattice constant for the MoS_2 layer after volume relaxation, $a = 3.122$ Å, is also a good match to the experimental value[243]. We have also re-checked some of the DFT results using the generalized gradient approximation (GGA)[244]. We note, however, that both the LDA and the GGA underestimate the band gap of at least the bulk HfO_2 and Al_2O_3, which makes the prediction of band offsets from theoretical calculations unreliable. With approximately 150 atoms per supercell, use of presumably more accurate hybrid functionals or GW methods for atomistic relaxations was not practical. However, we have utilized hybrid functionals, namely HSE06[245], to perform band structure calculations using the relaxed structures from our GGA simulations to further check our key conclusions. However, the primary objective of this theoretical work is to explore possible pathways to insulating and doping MoS_2 MLs qualitatively toward device applications, ultimately for experimental follow-up for promising cases. Similarly, we did not include spin–orbit coupling here, which causes substantial spin splitting in the valence band, for similar reason. However, only conduction band doping is observed in our results, mitigating the impact of this latter approximation. Van der Waal's forces also were simulated due to the absence of covalent bonding between the TMD and the oxides[213]. In our computations, we have adopted the DFT-D2 scheme to model the non-local dispersive forces wherein a semi-empirical correction is added to the conventional Kohn–Sham DFT theory[246].

The two representative dielectrics, HfO_2 and Al_2O_3, were chosen for high-κ value and minimal lattice mismatch, respectively. The MoS_2 ML of principle interest, with its hexagonal lattice, was taken to be unstrained with its above-noted volume-relaxed lattice constant of a = 3.122 Å. For the dielectric oxide, the energetically stable crystalline phases of bulk HfO_2 and Al_2O_3 at ambient conditions, namely, monoclinic HfO_2[247] and hexagonal Al_2O_3[248], respectively, were utilized. Our simulations were performed by constructing a supercell of ML MoS_2 on an approximately 2 nm thick oxide slab. For HfO_2, atomic relaxation was performed within a rectangular supercell (a = 9.366 Å, b = 5.407 Å) chosen to reduce the lattice mismatch between ML MoS_2 and monoclinic HfO_2. However, a roughly 6% strain remains along the in-plane directions in the HfO_2 - see Figure 3.2(a). For Al_2O_3, atomic relaxation was performed in a (rotated) hexagonal supercell (a = 8.260 Å) with a strain of only about 0.2% - see Figure 3.2(b). The systems were relaxed until the Hellmann–Feynman forces on the atoms were less than 0.02 eV $Å^{-1}$. During relaxation, all the MoS_2 ML atoms and the top half of the layers of the dielectric oxide were allowed to move in all three spatial dimensions. Oxygen vacancies were modeled by removing a single O atom from an O-layer of the supercell. Since we have periodic supercells, the O vacancy is repeated in each instance of the supercell. The system is then allowed to relax again with the introduced O-vacancy. All simulations were performed at a temperature of 0 K.

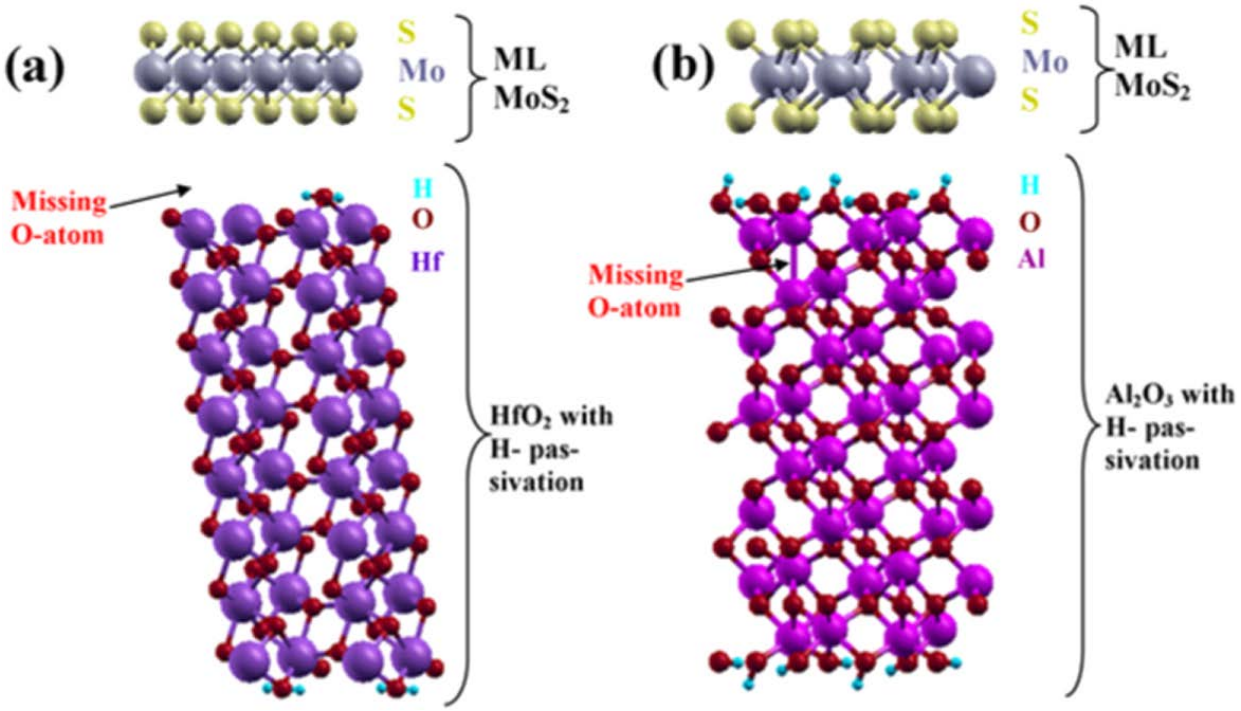

Figure 3.2: (a) Supercell of ML MoS_2 on an H-passivated, O-terminated HfO_2 slab of approximately 2 nm thickness with O-vacancy (side view). (b) Supercell of ML MoS_2 on an H-passivated, O-terminated Al_2O_3 slab of approximately 2 nm thickness with O-vacancy (side view). The monolayer of MoS_2 belongs to the space group P-6m2 (point group D_{3h}).

3.3 THEORETICAL DFT RESULTS

The band structure and atom-projected density-of-states (AP-DOS) have been calculated for the ML MoS_2-oxide system considering different possible terminations of the oxide at the interface in the presence of O vacancies in the oxide or Mo and S vacancies in the MoS_2. We compared (overlaid) the band structures for the MoS_2-oxide systems with vacancies to the ideal MoS_2-oxide results. In all cases, the highest occupied state of the system with vacancies serves as the zero energy reference in these 0 K simulations. However, the reference band structures absent vacancies are shifted up or down to provide a rough fit to the former in terms of band structure and the AP-DOS of the Mo and S atoms. Otherwise, the zero energy reference for the latter would be the valence band edge.

3.3.1 Monolayer MoS_2 on HfO_2 Slab with O Vacancy

When an O vacancy is introduced into the top layer of the O-terminated and H-passivated HfO_2 slab, in these 0 K simulations, an occupied defect state (band) is introduced within the band gap of ML MoS_2 – see Figure 3.3(a), which is associated primarily with Hf atoms in the oxide. Analogous Hf-associated defect states also arise in an isolated O-terminated and H-passivated HfO_2 slab[228]. In this latter case (and for analogous cases below) we simply removed the MoS_2 layer from the combined system, while otherwise holding the crystal structure fixed as a control. However, the close proximity of the occupied defect band to the conduction band (of the reference band structure) suggests that these states might be able to act as donors. As can be seen from the AP-DOS in Figure 3.3(b), the conduction band edge for MoS_2 is pinned at the Fermi level indicating n-type doping. However, the defect band formation due to the limited supercell size and associated very large (1.97×10^{14} cm^{-2}) O-vacancy density in these simulations leaves the binding energy for lower defect densities uncertain. Alternatively, these interface states could function as relatively shallow charge traps, leading to degradation of device performance. Since a rectangular supercell was used in these simulations of MoS_2 on HfO_2, the corresponding BZ is smaller and the *K* point of the primitive unit cell—where the ML MoS_2 band edges are located—folds into the Γ point in the supercell's BZ.

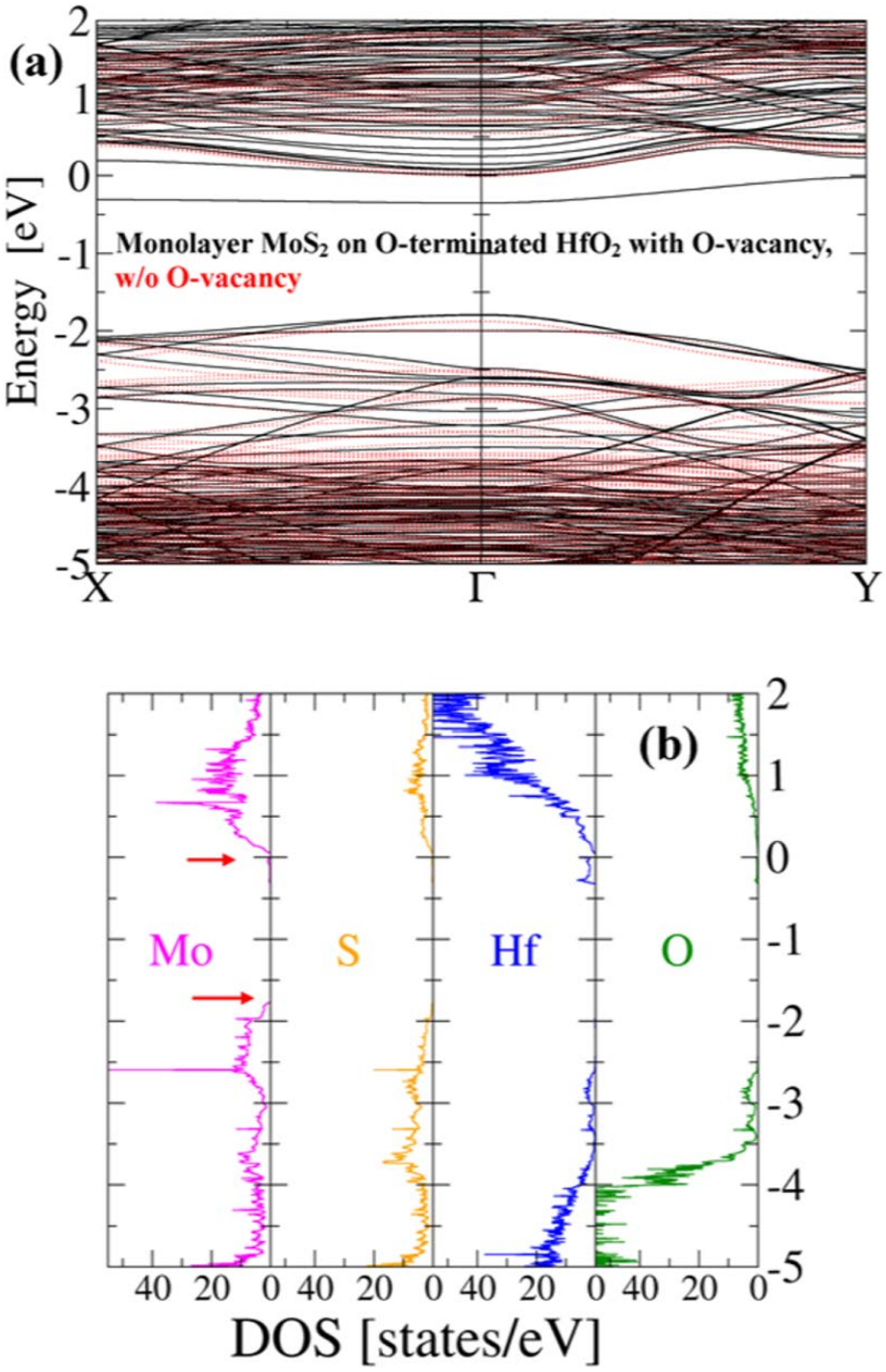

Figure 3.3: (a) Band structure of ML MoS_2 on an H-passivated, O-terminated HfO_2 slab with an O-vacancy in the top layer, plotted along the high symmetry directions of the BZ (black solid lines). The 0 eV reference corresponds to the highest occupied state in these 0

K simulations. The band structure of vacancy-free ML MoS_2–HfO_2 system (O-terminated) is superimposed for comparison (red dashed lines). However, this latter band structure, which otherwise would have its zero reference energy at the upper edge of the valence band, is shifted up or down to provide a reasonable fit to the former. (b) Atom-projected density-of-states for the ML MoS_2 and O-terminated HfO_2 system with an O-vacancy. Red arrows indicate the conduction and valence band edges. An occupied defect state (band) is introduced within the band gap of ML MoS_2.

In the case of Hf-terminated HfO_2–MoS_2 system with an O vacancy in the top layer of oxide, there is a straddling gap alignment (Type 1) as seen in the AP-DOS of Figure 3.4(b) for this large O-vacancy density, much as for O-terminated HfO_2. Moreover, there are now two partially occupied bands at the bottom of the conduction band as can be seen in Figure 3.4(a), both of which are largely localized to the MoS_2 layer, resulting in a system that now appears metallic. Calculation of the band structure for a freestanding Hf-terminated HfO_2 slab with an O vacancy exhibits occupied conduction band states associated with the Hf atoms[228]. In the combined HfO_2–MoS_2 system, these electrons are then transferred into the lower conduction-band-edge MoS_2 layer, in a modulation-doping-like process. In MoS_2, the DOS at the conduction and valence band edges are dominated by d_{xz} and d_{z^2} orbitals from the Mo atoms while in the HfO_2 the band edge states arise mainly from the contribution of Hf—d orbitals and O—p orbitals.

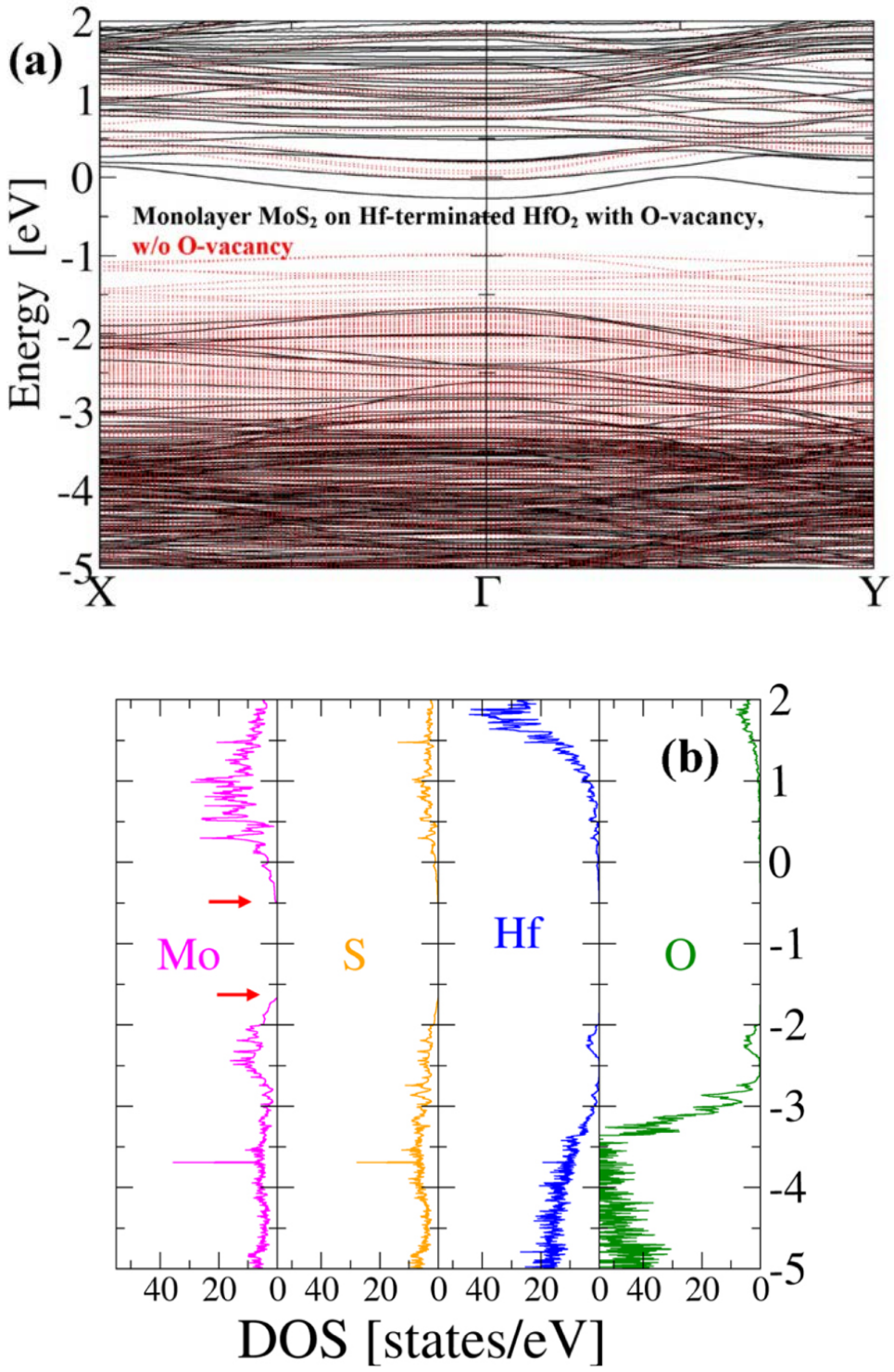

Figure 3.4: (a) Band structure of ML MoS_2 on Hf-terminated HfO_2 slab with an O-vacancy in the top layer, plotted along the high symmetry directions of the BZ (black solid lines).

The energy-shifted band structure of vacancy free ML MoS_2–HfO_2 system with Hf-termination is superimposed for comparison (red dashed lines). (b) Atom-projected density-of-states for the ML MoS_2 and Hf-terminated HfO_2 system with an O-vacancy. A straddling gap band alignment is now observed along with two partially occupied bands at the conduction band edge both of which are largely localized to the MoS_2 layer, resulting in a system that now appears metallic.

For the HfO_2–MoS_2 with O vacancy systems, we also repeated the simulations with the GGA approximation for comparison with the above LDA results. Figure 3.5(a) shows the band structure of ML MoS_2 on Hf-terminated HfO_2 with an O-vacancy, as obtained using both the GGA and the LDA approximations. The same nominal crystal structure was used, but a separate relaxation was performed for the LDA and GGA calculations (the latter, however, starting with the former for computational efficiency). As can be seen, the results match closely, including the degree of degenerate doping. A similar comparison (not shown) was performed for MoS_2 on O-terminated HfO_2, again with good agreement between the results obtained with the GGA and with the LDA including the location of the occupied defect band just below the conduction band. Finally, in Figure 3.5(b), we have used hybrid functionals, specifically HSE06, which provide a more accurate value for the band gap of bulk HfO_2 to simulate the band structure of ML MoS_2 on Hf-terminated HfO_2, to further check key results. The much larger computational demands required for hybrid method combined with the large supercell size constrained us to use a coarse *k*-point grid for evaluation of the band structure and precluded us from running any relaxations of the structure using the hybrid method. Instead, we reused the structure obtained from the GGA relaxations. As shown in Figure 3.5(b), with the hybrid method, the conduction band edge is again pulled below the Fermi level as in our previous GGA and LDA results, indicating the n-type doping of ML MoS_2 modulated by dielectric oxide.

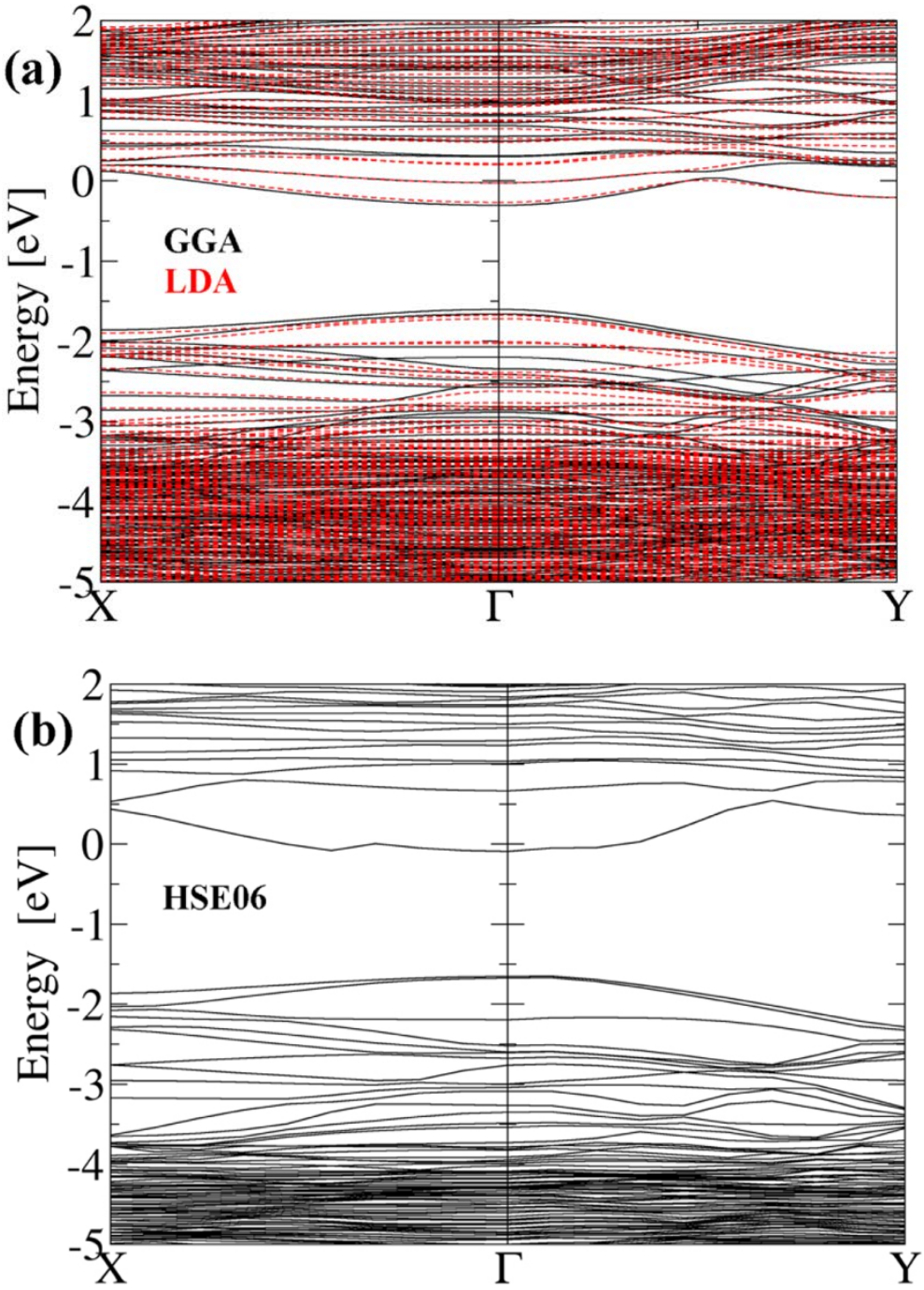

Figure 3.5: (a) Band structure of ML MoS_2 on an Hf-terminated HfO_2 with an O vacancy obtained using the GGA (solid lines, black online). The band structure obtained using the LDA is overlaid on top for comparison (dashed lines, red online). Both results exhibit n-type doping, and essentially the same degree of degeneracy. (The zero energy reference

remains the Fermi level in each case.) (b) Band structure of ML MoS_2 on an Hf-terminated HfO_2 with an O vacancy obtained using the HSE06. The conduction band edge is pulled below the Fermi level indicating n-type doping of MoS_2.

3.3.2 Monolayer MoS_2 on Al_2O_3 Slab with O Vacancy

For the O-terminated and H-passivated Al_2O_3–MoS_2 system, creation of an O vacancy in the top O-layer of Al_2O_3 produces only a modest effect on the conduction band edge states in comparison to the vacancy free reference system. However, the O-vacancy pulls the conduction band edge below the Fermi level, filling the lower MoS_2 conduction band states as shown in Figure 3.6(a), which remain largely localized in space to the MoS_2 layer as shown in the AP-DOS plot in Figure 3.6(b), resulting in a system that now appears metallic, much as for the Hf-terminated HfO_2–MoS_2 system with an O vacancy. Calculation of the band structure for an isolated O-terminated Al_2O_3 slab with an O vacancy exhibits occupied conduction band states associated with the O atoms[228]. In the combined Al_2O_3–MoS_2 system, these electrons again are transferred into the lower conduction-band-edge MoS_2 layer, in a modulation-doping-like process.

For Al-terminated Al_2O_3–MoS_2 system, the system retains a straddling gap alignment after the introduction of an O vacancy in the oxide layer. However, an occupied state (band) deep in the band gap of the MoS_2 is produced as shown in Figure 3.7(a), which is localized to the Al and O atoms in the oxide layer as shown in the AP-DOS plot in Figure 3.7(b). Such defect states could serve as recombination centers or charge traps. In addition, however, a direct band gap is found at these doping concentrations, in contrast to the Al-terminated Al_2O_3–MoS_2 system without an O vacancy.

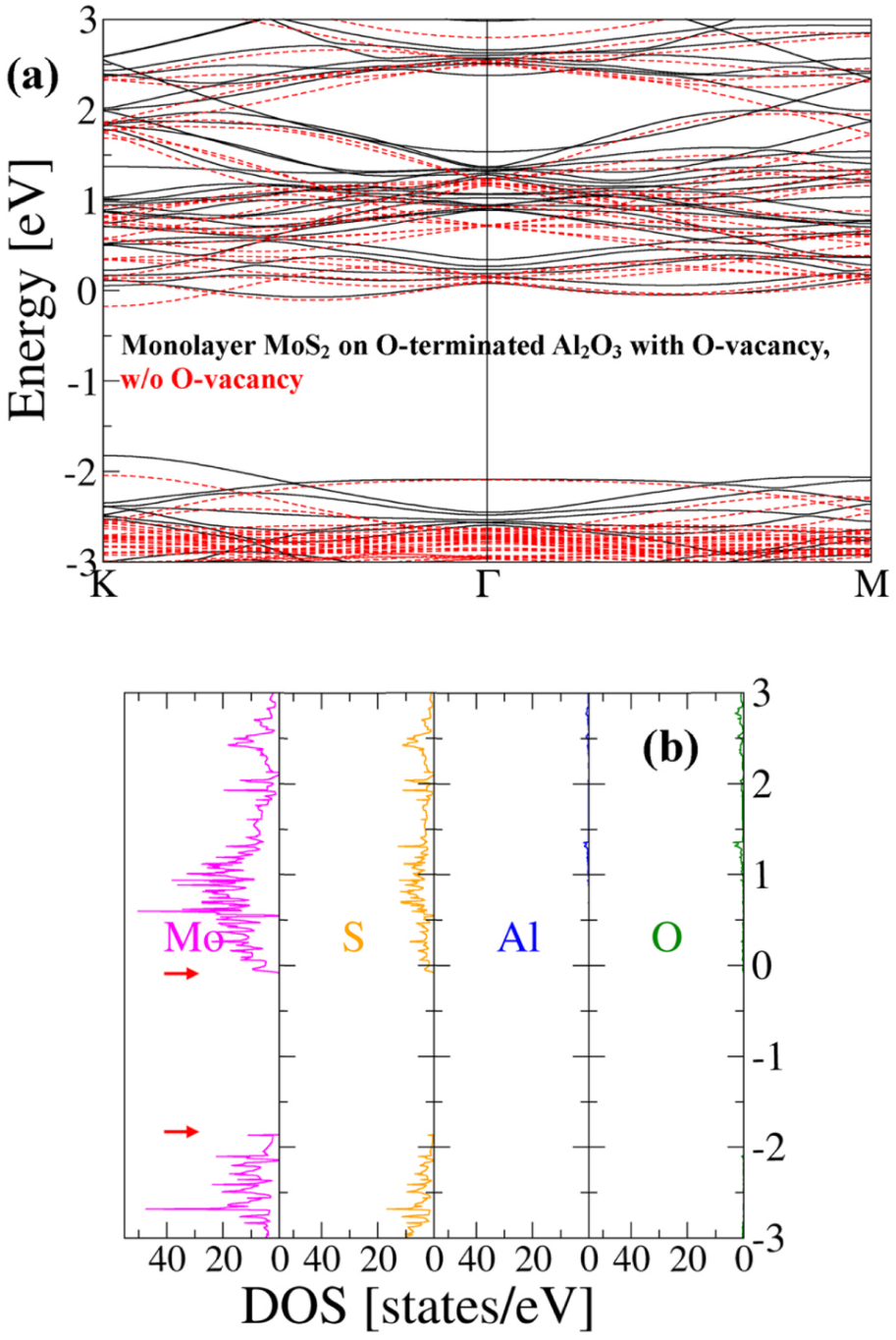

Figure 3.6: (a) Band structure of ML MoS_2 on an H-passivated, O-terminated Al_2O_3 slab with an O-vacancy in the top layer, plotted along the high symmetry directions of the BZ (black solid lines). The energy-shifted band structure of vacancy free ML MoS_2–Al_2O_3 system (O-terminated) is superimposed for comparison (red dashed lines). (b) Atom-projected density-of-states for the ML MoS_2 and O-terminated Al_2O_3 system with an O-

vacancy. A new partially filled band, largely localized to the MoS_2 layer, is introduced at the edge of the MoS_2 conduction band resulting in a system that now appears metallic.

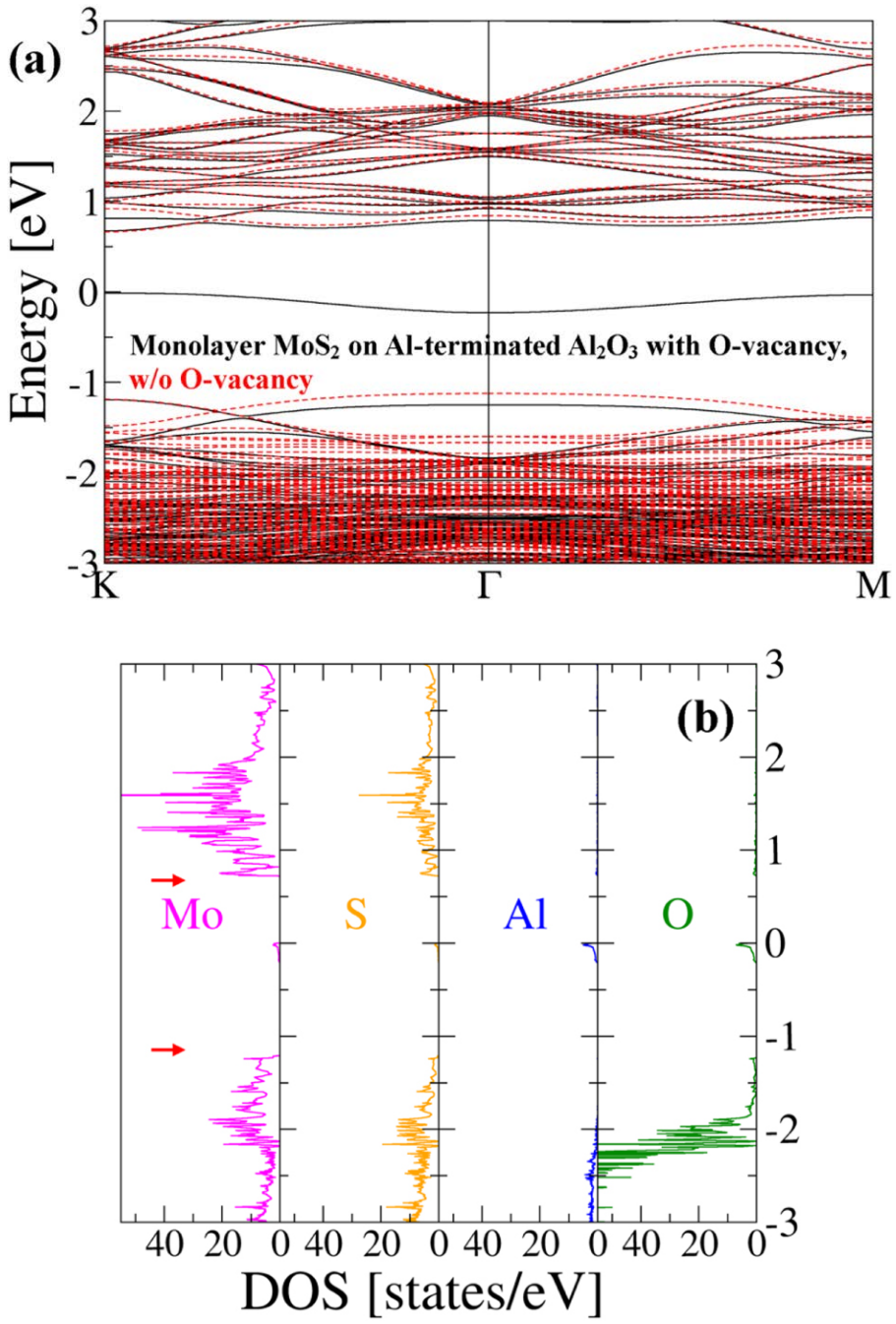

Figure 3.7: (a) Band structure of ML MoS_2 on Al-terminated Al_2O_3 slab with an O-vacancy in the top layer, plotted along the high symmetry directions of the BZ (black solid lines).

The energy-shifted band structure of vacancy free ML MoS_2–Al_2O_3 system (Al-terminated) is superimposed for comparison (red dashed lines). (b) Atom-projected density-of-states for the ML MoS_2 and Al-terminated Al_2O_3 system with an O-vacancy. An occupied state (band) deep in the band gap of the MoS_2 is produced, which is localized to the Al and O atoms in the oxide layer.

3.4 Electrical and Spectroscopic Characterization Results

Electron doping of ML MoS_2 by O deficient high-κ oxides was experimentally demonstrated by electrically and spectroscopically characterizing back-gated ML MoS_2 FETs encapsulated by alumina (Al_2O_x) and hafnia (HfO_x). The DFT calculations would suggest that an O-deficient high-κ oxide encapsulating the MoS_2 ML would produce a combination of n-type modulation doping of the bands and occupied defect states within the gap in bulk materials, the latter contributing perhaps little to the doping but important when trying to pull the Fermi level below them. On exposure to air, the Hf (Al)-terminated HfO_2 (Al_2O_3) is unrealistic while the O-termination provides a more accurate model for surface termination in the oxide. However, in our experimental system as shown in Figure 3.1, the high-κ oxide encloses the MoS_2 ML and MoS_2-oxide interface is not exposed to air allowing us to investigate both O-rich and O-deficient oxide interfaces.

3.4.1 MoS_2 FETs with O-deficient and O-rich HfO_x

Figure 3.8(a) shows the room temperature (RT) transfer characteristics of a back-gated ML MoS_2 FET before (blue) and after (red) encapsulation by ALD HfO_x. The length (L_{CH}) and width (W) of the device are 900 nm and 2 μm, respectively, and the data was collected at a drain-source voltage (V_{DS}) of 50 mV. Before encapsulation, the device exhibits a threshold voltage (V_T) near -15 to -20 V. After encapsulation in ALD HfO_x, there is a large negative shift in V_T consistent with n-type doping, as well as pronounced stretch-out of the transfer characteristic as V_{BG} is made more negative, consistent with near-band-edge defects in the band gap as predicted by the DFT for O-deficient HfO_x. Note that for the FET data presented in Figure 3.8(a), the transfer curve after ALD HfO_x encapsulation was measured about two months after the initial HfO_x encapsulation and still shows

pronounced n-doping effects, thus, reflecting the long-term air stability of this ALD high-κ doping process. The n-type doping was further confirmed by Raman spectroscopy performed on the ML MoS_2 in the channel region of the same FET before (blue) and after (red) HfO_x encapsulation as shown in Figure 3.8(b). Before HfO_x, the peak positions of the out-of-plane A_{1g} and the in-plane E^1_{2g} peaks are at ~ 402 cm^{-1} and ~ 383 cm^{-1}, respectively, which is characteristic of ML MoS_2[221]. After HfO_x encapsulation, the E^1_{2g} peak remains relatively unchanged, while the A_{1g} peak shows a distinct broadening and a red shift in its peak position from ~ 402 cm^{-1} to ~ 399 cm^{-1}. These changes in the A_{1g} Raman peak upon HfO_x encapsulation are indicative of the increased electron concentration in the ML MoS_2 channel, and also have been observed in previous n-type doping studies of MoS_2[207]. The Hf:O atomic ratio in the as-deposited HfO_x was determined to be ~ 1:1.56 from XPS analysis, thereby establishing the correlation between oxygen deficiency and n-type doping of ML MoS_2 caused by HfO_x.

The results for the control sample of O-rich HfO_x on ML MoS_2 are shown in Figure 3.9. The Hf:O ratio for the ALD deposited O-rich HfO_x was determined to be ~ 1:2.1 from XPS measurements in exactly the same manner and using the same number of components that were used in peak fitting of the O-deficient HfO_x. As can be clearly seen, there is negligible change in the Raman spectra of MoS_2 after O-rich HfO_x deposition – see Figure 3.9(b). There is no red shift or peak broadening of the A_{1g} Raman mode implying negligible n-type doping of MoS_2. Moreover, from the transfer curve we can see that the device can be turned off within the same back-gate voltage sweep range after deposition of the O-rich HfO_x – see Figure 3.9(a). These results depict negligible doping of the ML MoS_2 after O-rich HfO_x deposition, which contrast to the strong doping of the MoS_2 when an O-deficient HfO_x was deposited.

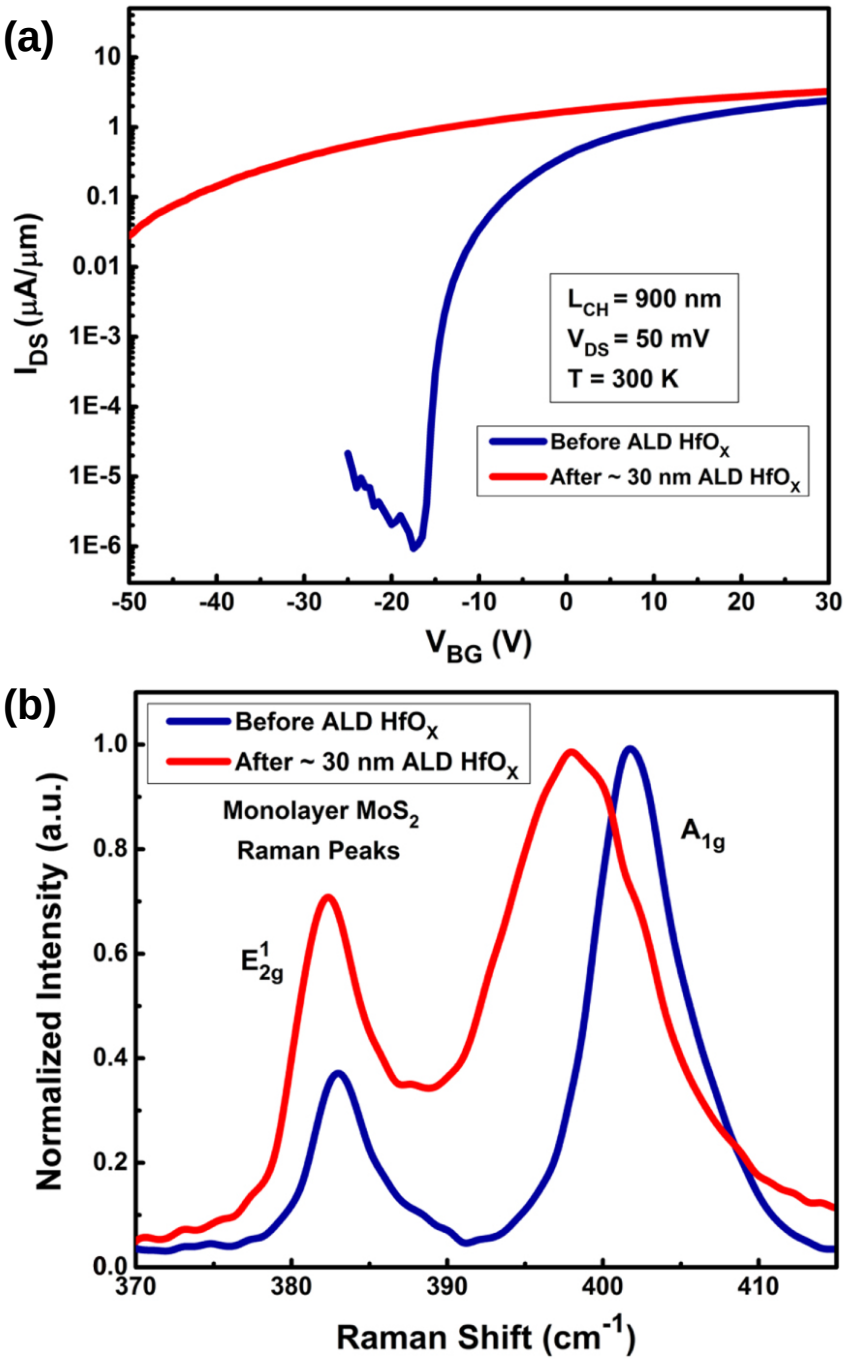

Figure 3.8: (a) Room temperature transfer characteristics of a back-gated ML MoS_2 FET before (blue) and after (red) ~ 30 nm ALD HfO_x ($x \sim 1.56$) encapsulation, and (b) corresponding normalized Raman spectra of the ML MoS_2 FET channel before (blue) and after (red) ALD HfO_x encapsulation. The shifted threshold voltage and A_{1g} peak are consistent with n-type doping after encapsulation.

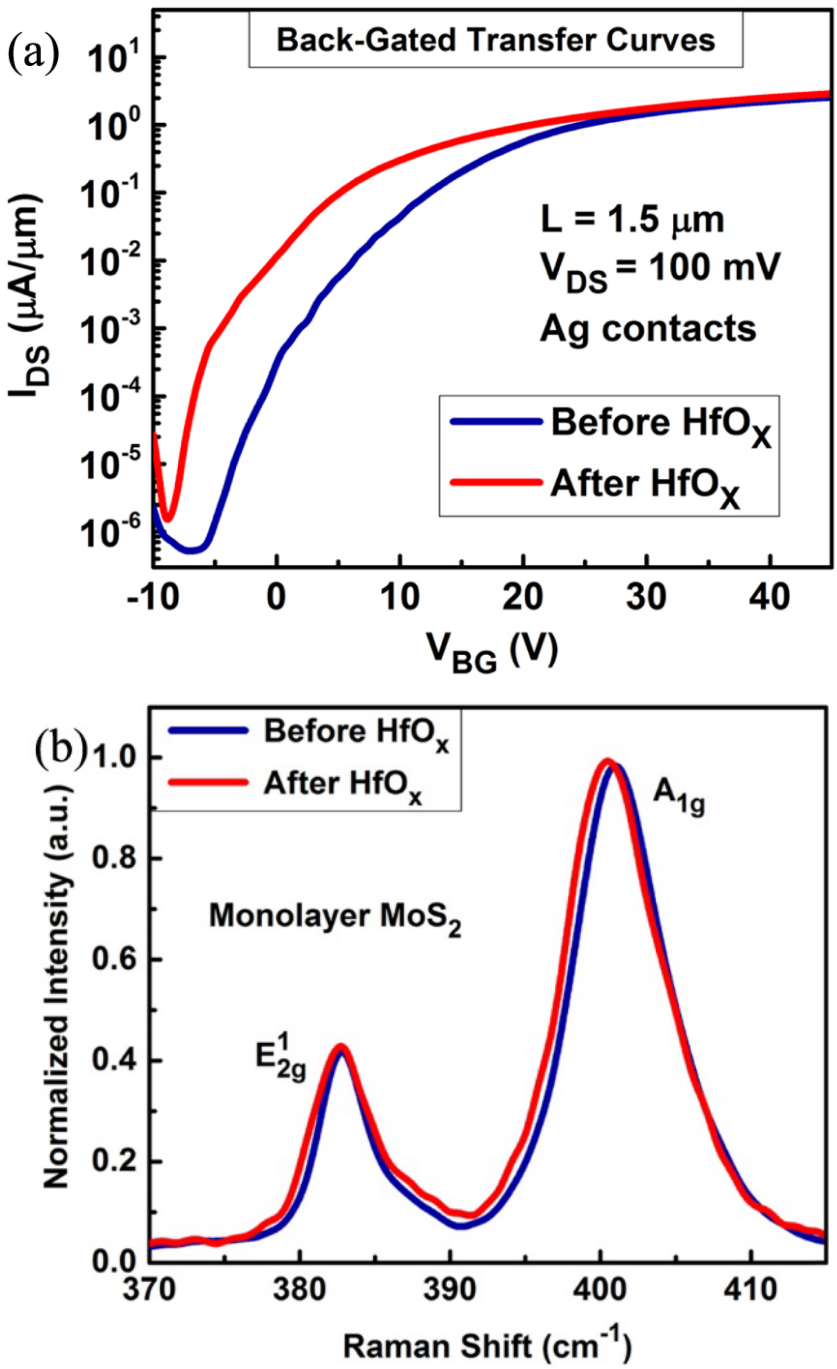

Figure 3.9: (a) Room temperature transfer characteristics of a back-gated ML MoS_2 FET before (blue) and after (red) ~ 30 nm ALD HfO_x ($x \sim 2.1$) encapsulation, and (b) corresponding normalized Raman spectra of the ML MoS_2 FET channel before (blue) and after (red) ALD HfO_x encapsulation. There is no red shift or peak broadening of the A_{1g} Raman mode implying negligible n-type doping of MoS_2.

To further study the effects of O-deficient and O-rich ALD HfO_x films on the field-effect mobility of MoS_2 FETs, top-gated FETs were fabricated on exfoliated BL MoS_2 flakes. The procedure first involved the fabrication of typical back-gated FET structures on a degenerately doped n-type Si-(100) substrate covered by a 90 nm thick thermal oxide. Thereafter, the ALD HfO_x layer was deposited followed by fabrication of the top-gate stack (Cr/Au ~ 10/30 nm) using standard e-beam lithography, metal deposition and solvent lift-off. The top-gate was fabricated in such a way so as to ensure a slight overlap with the underlying source/drain contact electrodes, thereby, allowing complete top-gating of the BL MoS_2 channel regions. During all top-gated measurements, the back-gate was kept grounded. The linear top-gated transfer characteristics of the BL MoS_2 FET (channel length L = 1.5 µm) with the O-rich HfO_x top-gate dielectric (Hf:O ~ 1:2.1), measured at a V_{DS} of 100 mV, is shown below in Figure 3.10(a). The inset of the figure shows the optical image of the top-gated BL MoS_2 FET. The ALD deposition recipe of the O-rich HfO_x was: H_2O pulse time = 0.3 s (pulsed first), Hf precursor pulse time = 0.15 s, deposition temperature = 200°C, number of deposition cycles = 300. The oxide thickness was determined to be ~ 35 nm from ellipsometry and the dielectric constant was extracted to be ~ 21 from MOSCAP HFCV measurements. As can be seen in Figure 3.10(a), the n-branch ON-current achieved in the BL MoS_2 FET with O-rich HfO_x was only ~ 160 nm/µm and the extracted top-gated field-effect mobility (μ_{FE}) for this FET was found to be 2.4 cm^2/V-s.

In contrast, the linear top-gated transfer characteristics of a similar BL MoS_2 FET (L = 1.5 µm) with O-deficient HfO_x top-gate dielectric (Hf:O ~ 1:1.56), measured under the same biasing conditions (V_{DS} = 100 mV; V_{TG} sweep range = -3 to 3 V), shows a significant improvement in the n-branch ON-current (I_{ON} ~ 3 µA/µm) as well as the top-gated field-effect mobility (μ_{FE} ~ 16.1 cm^2/V-s), as shown in Figure 3.10(b), when compared to the BL MoS_2 FET with O-rich HfO_x. The improved n-branch behavior in the O-deficient HfO_x case can be attributed to the n-doping of the BL MoS_2 FET channel region which helps in enhanced screening of the Coulombic charge impurity scattering sources as well as reduction of the contact resistance due to heavy n-doping near the S/D contact regions. The ALD deposition recipe of the O-deficient HfO_x was:

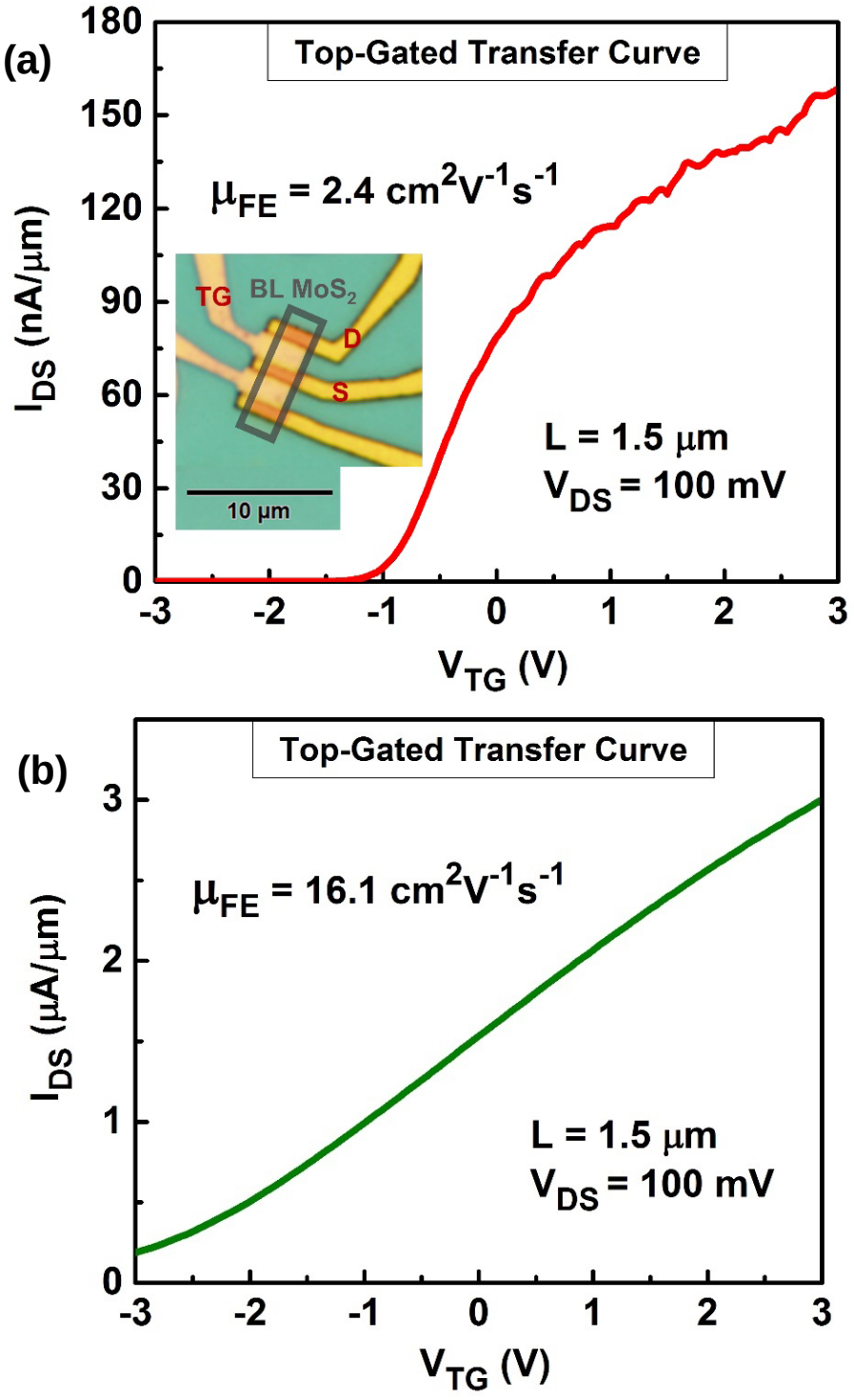

Figure 3.10: Comparison of the top-gated transfer characteristics of BL MoS_2 FETs having ALD-deposited O-rich HfO_x (a) and O-deficient HfO_x (b) as the top-gate dielectric.

Hf precursor pulse time = 0.25 s (pulsed first), H_2O pulse time = 0.06 s, deposition temperature = 200°C, number of deposition cycles = 300. The oxide thickness was determined to be ~ 32 nm from ellipsometry and the dielectric constant was extracted to be ~ 18 from MOSCAP HFCV measurements.

3.4.2 MoS_2 FETs with O-deficient Al_2O_x

Similar n-type doping results were obtained after encapsulating back-gated ML MoS_2 FETs with ALD Al_2O_x. Figures 3.11(a) and (b) show the RT transfer characteristics of a ML MoS_2 FET (L_{CH} = 500 nm, W = 2.3 μm, V_{DS} = 100 mV, Au contacts) and the normalized Raman spectra of the ML MoS_2 channel, respectively, before (blue) and after (red) ALD Al_2O_x deposition. As in the case of HfO_x, the negative V_T shift, as shown in Figure 3.11(a), and the broadening and red shift of the A_{1g} Raman peak, as shown in Figure 3.11(b), of ML MoS_2 after encapsulation in ALD Al_2O_x is indicative of n-type doping, again consistent with the DFT results with oxygen vacancies. The Al:O atomic ratio was determined to be ~ 2:1.55 from XPS analysis[239], thereby, confirming the inherent oxygen deficiency in the as-deposited high-κ oxide.

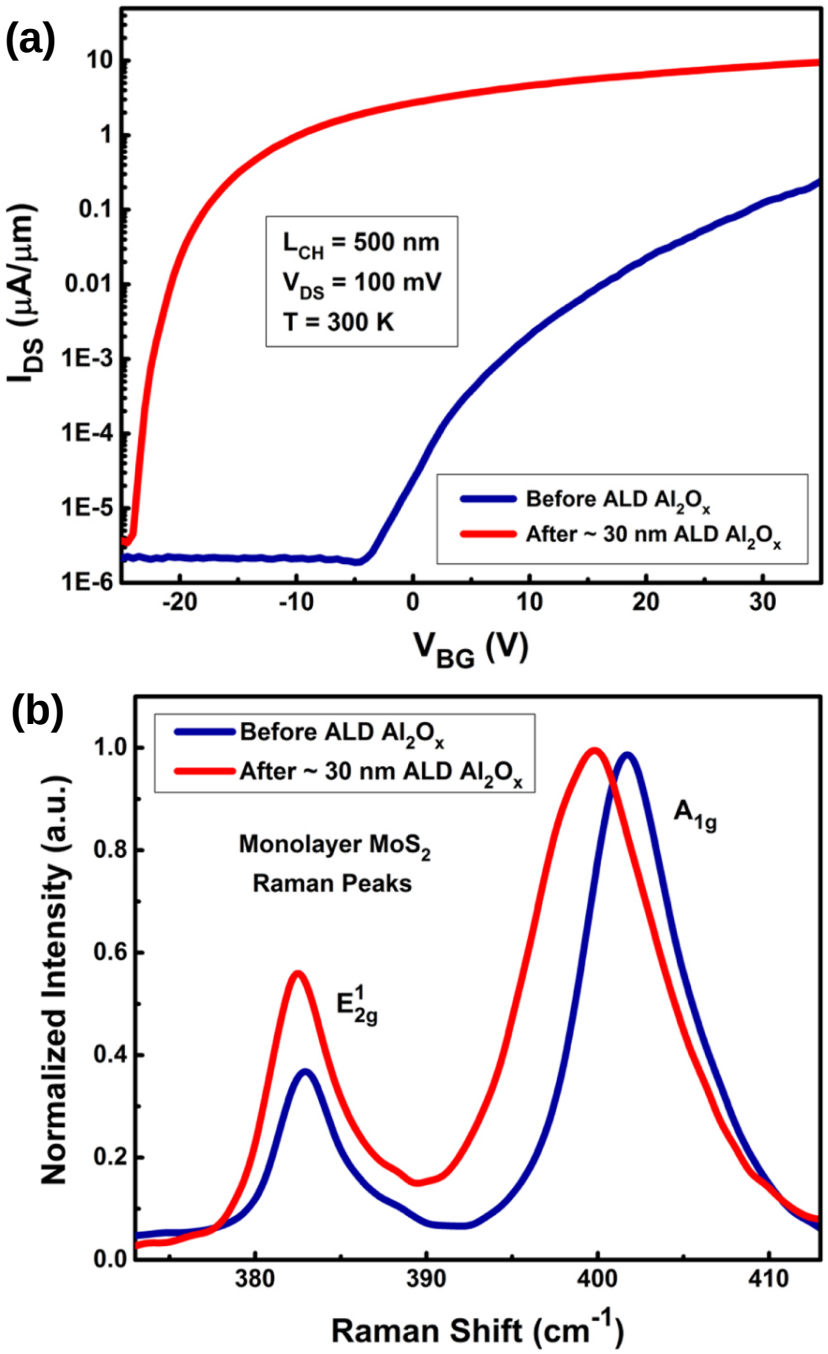

Figure 3.11: (a) Room temperature transfer characteristics of a back-gated ML MoS_2 FET before (blue) and after (red) ~ 30 nm ALD Al_2O_x ($x \sim 1.55$) encapsulation and (b) corresponding normalized Raman spectra of the ML MoS_2 FET channel before (blue) and after (red) ALD Al_2O_x encapsulation. The shifted threshold voltage and A_{1g} peak are consistent with n-type doping after encapsulation.

3.5 CONCLUSION

In summary, we have experimentally and theoretically verified the interfacial-oxygen-vacancy mediated n-doping effect of high-κ dielectrics on MoS_2. DFT simulations suggest that occupied near-conduction-band-edge states that might function either as donors or shallow traps are introduced in the MoS_2-oxide system by O vacancies in the O-terminated and H-passivated HfO_2–MoS_2 system. More promising as a means of doping, with O vacancies, both the Hf-terminated HfO_2–MoS_2 system, and the O-terminated and H-passivated Al_2O_3–MoS_2 system appear metallic due to doping of the oxide slab followed by electron transfer into the MoS_2, in manner analogous to modulation doping. Consistent with these latter theoretical results, n-type doping of ML MoS_2 by high-κ oxides with oxygen vacancies was demonstrated experimentally by electrically and spectroscopically characterizing back-gated ML and BL MoS_2 FETs encapsulated by ALD alumina (Al_2O_x) and hafnia (HfO_x). Our results provide insight on the performance enhancement observed in MoS_2 devices upon encapsulation in a high-κ dielectric environment. The interfacial-oxygen-vacancy mediated n-doping of MoS_2 by high-κ dielectrics could very well be responsible for the mobility enhancement in high-κ-encapsulated MoS_2 FETs due to improved screening of charged impurities, suppression of homopolar phonon scattering and reduction of the Schottky barrier-induced contact resistance by the enhanced sheet electron density in the MoS_2 channel.

Chapter 4: Band Structure Engineering and P-Doping of Layered WSe_2 *via* One-Step Chemical Functionalization

4.1 INTRODUCTION

A monolayer (ML) TMD consists of a mono-atomic layer of transition-metal atoms 'M' (*e.g.*, Mo or W) sandwiched in between two layers of chalcogen atoms 'X' (*e.g.*, S or Se) in the form of an X–M–X (MX_2) triple-atomic layer structure. By combination of different M and X atoms, the band structure of TMDs can be altered to achieve band gaps in the range of ~ 1–2 eV[249,250], resulting in different electrical or optical characteristics in TMD-based devices. Since the electronic structure of TMDs is the most important determinant of the electrical performance as well as the intrinsic limitation of TMD-based field-effect transistors (FETs)[251,252], engineering the band structure of TMDs is critical. The band structure of TMDs originates from the orbital overlap of d orbitals of transition metals and p orbitals of chalcogens in the mirror symmetry crystal structure[253], therefore, the band structure of TMDs can be tuned by perturbing the overlapped orbital configuration of their constituent atoms[208,254-258]. Moreover, if molecular adsorption is intentionally introduced in TMDs (typically *via* surface doping), both the band gap and the carrier concentration can be controlled[259-261]. Typically, high-density molecular adsorption on the channel of TMD FETs can act as scattering or trapping centers for charge carriers[168,262-264]. However, if the molecular dopant adsorption sites are spatially confined to the desired regions in a FET, for example, source/drain (S/D) contact and access regions, they can boost the FET performance by decreasing the resistance at the contact metal/TMD interface resulting in enhancement of I_{ON} and field-effect mobilities due to a more efficient charge carrier injection into the FET channel[204,207,238,259-261,265-271].

The results, discussions and figures presented in this Chapter have been adapted with permission from the following reference: [#]Park, J. H., [#]Rai, A., Hwang, J., Zhang, C., Kwak, I., *et al.* (2019). Band Structure Engineering of Layered WSe_2 *via* One-Step Chemical Functionalization. *ACS Nano 13* (7), 7545-7555. ([#]equal contribution). The dissertator, A. Rai, helped conceive and design the experiment, fabricated the devices, performed the electrical, Raman and photoluminescence measurements, contributed to data analysis and largely wrote the manuscript with contributions from all the authors.

In the present Chapter, band structure engineering is demonstrated to enhance the electrical performance of layered tungsten diselenide (WSe_2) FETs using a one-step dipping process in $(NH_4)_2S$(aq) solution. Although various aqueous chemical treatment methods have been demonstrated to enhance the electronic performance of TMDs, their underlying mechanisms have not been fully understood at the molecular level in previous studies[272-276]. WSe_2 is chosen as the representative TMD in this study since it is simple to achieve both n-type[230] and p-type[277] transport in WSe_2-based devices, thereby, making it attractive for complementary-metal-oxide-semiconductor (CMOS) applications[45,70]. $(NH_4)_2S$(aq) solution, on the other hand, has been widely employed in semiconductor research for the passivation of semiconductor surfaces[278]. Thus, it can be expected that the chemical treatment of WSe_2 with $(NH_4)_2S$(aq) solution can be easily integrated into existing CMOS fabrication processes. Moreover, previous reports have revealed that the $(NH_4)_2S$(aq) chemical treatment of 2D molybdenum disulfide (MoS_2) leads to an enhanced electrical performance, and sulfur and its related compounds have been considered possible candidates for functionalization of 2D materials[279,280].

$(NH_4)_2S$(aq) chemical treatment of WSe_2 is investigated at the molecular level using scanning tunneling microscopy (STM) and spectroscopy (STS) to elucidate the mechanism of the electronic transition in WSe_2. The $(NH_4)_2S$(aq) chemical treatment of ML WSe_2 induces an electronic band gap reduction to almost half of the value of bare ML WSe_2 and increases the density of positive charge carriers or holes. This Fermi level shift toward the WSe_2 valence band edge (VBE) is confirmed by density functional theory (DFT) calculations which reveal that this shift is induced due to the adsorption of molecular "SH" species on the bare WSe_2 surface. As a consequence of this $(NH_4)_2S$(aq) chemical treatment, I_{ON} at the p-branch increases more than an order of magnitude in back-gated few-layer (FL) WSe_2 FETs. This electrical enhancement in WSe_2 FETs can be achieved by a simple and facile one-step dipping method without employing any additional complicated processes or specialized equipment, thereby, enabling easy integration of this $(NH_4)_2S$(aq) chemical treatment technique into the conventional TMD transistor fabrication process.

4.2 DETAILS OF EXPERIMENTAL AND THEORETICAL METHODS

4.2.1 MBE and STM/STS Method

For STM/STS experiments, the WSe_2 layers were grown by molecular beam epitaxy (MBE) in an ultrahigh-vacuum (UHV) system (RIBER, MBE 32) on HOPG substrates. HOPG substrates were first cleaned by multiple exfoliation cycles. Afterward, the cleaned substrates were transferred immediately into the UHV chamber. WSe_2 layers were grown while the HOPG substrates were held at 1073 K for 20 min. Elemental W and Se were simultaneously dosed onto the HOPG surface using an electron beam source and a Knudsen cell, respectively. After the growth of WSe_2 layers on the HOPG substrates, about 20 nm Se capping layers were deposited on the WSe_2/HOPG samples to prevent unintentional oxidation of the samples during transfer to the separate STM/STS UHV chamber (Omicron, base pressure: $<1 \times 10^{-10}$ Torr). After transferring the WSe_2/HOPG samples into the STM chamber, Se capping layers were removed from the WSe_2/HOPG samples by annealing at 750 K for 120 min. STM and STS measurements were performed using electrochemically etched tungsten tips.

It is noted that it is extremely difficult to approach the STM tips to micron-sized exfoliated WSe_2 flakes supported on insulating SiO_2/Si substrates due to its low electrical conductivity. Therefore, STM/STS was performed on MBE-grown WSe_2 (~ 0.75 ML) on conductive HOPG substrates to elucidate the effects of $(NH_4)_2S$(aq) chemical treatments on the electronic properties of WSe_2. Moreover, as shown in previous reports, MBE-grown TMD samples have nearly the same physical properties as mechanically exfoliated samples, including band structure and optical properties[281-283]. Therefore, the experimental STM/STS results derived on MBE-grown WSe_2 can be used to understand the properties of the mechanically exfoliated WSe_2 flakes, and it can be expected that the electronic effects of $(NH_4)_2S$(aq) chemical treatment on MBE-grown WSe_2 will be nearly identical to the effects of the same treatments on mechanically exfoliated WSe_2. However, since MBE-grown WSe_2 samples typically have very small domain sizes (typically 500 – 800 nm), devices fabricated with MBE-grown WSe_2 would have more grain boundaries which

can severely degrade the electrical performance of WSe_2 FETs. Thus, exfoliated WSe_2 flakes were used for studying the electrical current-voltage characteristics.

4.2.2 Device Fabrication Process, Chemical Treatment Method, and Raman Characterization

Back-gated FL WSe_2 FETs were fabricated by first mechanically exfoliating WSe_2 flakes from commercially available bulk crystals (source: HQ Graphene) onto a degenerately doped p-type Si-100 substrate with 90 nm of thermally grown SiO_2. Upon exfoliation, the samples were subjected to a high-vacuum annealing step (340°C for 6 h; base pressure: 10^{-6} mbar) to minimize tape residues as well as trapped adsorbates between the WSe_2 flakes and the underlying SiO_2 substrate. FL WSe_2 flakes (3–4 nm, *i.e.*, 4–5 atomic layers thick) were identified using a combination of optical microscopy and atomic force microscopy (AFM) imaging. Top contact electrodes were patterned using standard electron-beam lithography (EBL) utilizing a poly methyl(methacrylate) (PMMA) resist, following which Ni/Au (20/30 nm) metal electrodes were deposited using electron-beam evaporation and solvent lift-off steps to serve as the source/drain (S/D) electrodes. After device fabrication, the WSe_2 FET samples were dipped in the 20% $(NH_4)_2S$(aq) solution for a specified time period, following which the samples were rinsed in IPA and dried in air. All chemical treatments were performed for 10 min unless otherwise noted. Note that, although acetone is a widely employed solvent to remove hydrocarbon residues, IPA does remove hydrocarbons as well, and, thus, a single step rinsing process with IPA was utilized in the present study. It is noted that the effect of $(NH_4)_2S$(aq) chemical treatment on layered TMDs persists even after washing with acetone and water, as reported in previous publications[272,273]. Raman spectroscopy measurements were taken with a Renishaw inVia micro-Raman system with an excitation wavelength of 532 nm and a grating of 3000 l/mm.

4.2.3 Theoretical DFT Computational Details

To explain the underlying mechanism behind the *p*-type doping and electronic band gap reduction in WSe_2 after $(NH_4)_2S$(aq) chemical treatment, density functional theory (DFT) calculations were performed using the Vienna *ab initio* simulation package

(VASP)[226]. The projector augmented wave pseudopotentials were employed[284] with Perdew–Burke–Ernzerhof (PBE) exchange-correlation functional[285]. A 4 x 4 supercell of monolayer WSe_2 was used to investigate the effect of molecular adsorption on the electronic structure of WSe_2, and a vacuum size of ~ 20 Å was employed to avoid periodic image interactions. With a cutoff energy of 450 eV, the atomic coordinates were relaxed until the residual force on each atom was less than 0.01 eV $Å^{-1}$. The Monkhorst-Pack k-point sampling in the Brillouin zone (BZ) is Γ-centered with 4 × 4 × 1 and 6 × 6 × 1 meshes for the ionic and electronic optimizations, respectively.

Based on the possible dissociation reaction of $(NH_4)_2S$ molecule in H_2O solution, SH, H_2S, and NH_3 molecules as well as elementary S were considered as possible candidates that could introduce *p*-type doping in WSe_2. The binding energy of an adsorbate on the ML WSe_2 surface was calculated using the following formula:

$$E_{form}(\mathrm{q}) = E_{tot}^{adsorption} - E_{tot}^{bare} - \sum N_i \mu_i \qquad (1)$$

where $E_{tot}^{adsorption}$ is the total energy of the ML WSe_2 with the adsorbed species, E_{tot}^{bare} is the total energy of the bare ML WSe_2, N_i is the number of species, and μ_i is the chemical potential of the adsorbate (for example, SH). The calculation of the binding energy for each molecule showed that molecular SH and elementary S can be adsorbed on the WSe_2 surface with binding energies of 0.48 eV and 1.58 eV, respectively, while H_2S and NH_3 molecules showed negligible interaction with WSe_2 (binding energies of ~ 20 meV). Afterwards, the effect of different adsorbates on the electronic band structure of WSe_2 was investigated as shown later in Figure 4.9; the Fermi level of the bare ML WSe_2 is located close to the center of the band gap, which is about 0.78 eV above the valence band edge. Femi level (μ) of the intrinsic semiconductor was calculated from $\mu = \varepsilon_v + \frac{1}{2}E_{gap} + \frac{1}{2}k_B T\, ln\left(\frac{P_v}{N_c}\right)$, where ε_v is the energy of the valence band edge and E_{gap} is the band gap. N_c and P_v are related to the number of carriers present at temperature *T*, *i.e.*, n_c (electron) and p_v (hole), by $n_c(T) = N_c(T)\exp(-(\varepsilon_c - \mu)/k_B T)$ and $p_v(T) = P_v(T)\exp(-(\mu - \varepsilon_v)/k_B T)$, respectively. $n_c(T)$ and $p_v(T)$ were calculated from the following expressions:

$$n_c(T) = \int_{\varepsilon_c}^{\infty} d\varepsilon \, g_c(\varepsilon) \, \frac{1}{\exp(-(\varepsilon - \mu)/k_B T) + 1}$$

$$p_v(T) = \int_{-\infty}^{\varepsilon_v} d\varepsilon \, g_v(\varepsilon) \, \frac{1}{\exp(-(\mu - \varepsilon)/k_B T) + 1}$$

, where $g_c(\varepsilon)$ and $g_v(\varepsilon)$ are the density of states at the conduction and valence band edges, respectively. Fermi level of the WSe_2 with adsorbate was calculated using the same approach. It is noted that the density of states shown later in Section 4.4 were smoothened by the Gaussian smearing method, with the smearing parameter σ of 0.1, for better visualization.

4.3 SURFACE ANALYSIS RESULTS OF BARE AND CHEMICALLY TREATED WSe_2

4.3.1 STM/STS on MBE-Grown Bare ML WSe_2

The bare surface of ML WSe_2 grown *via* molecular beam epitaxy (MBE) was probed using STM and STS. Schematic diagrams in Figure 4.1(a) represent the side and top views of WSe_2. As shown in Figure 4.1(b), a WSe_2 ML (lateral size ~ 100 nm) grown on a highly oriented pyrolytic graphite (HOPG) surface was observed *via* STM, and a triangular island of bilayer (BL) WSe_2 was identified within the scanned area of the STM image along with the ML WSe_2 region. Note that the applied sample bias and the measured tunneling current during STM/STS measurements are denoted by V_S and I_T, respectively, in the figure captions. Atomically resolved STM imaging was performed on the ML WSe_2; as shown in Figure 4.1(c), a honeycomb array of Se atoms in ML WSe_2 was observed through a hexagonal moiré pattern, consistent with the hexagonal pattern observed in the Fourier transform image as shown in the inset[286,287]. It is noted that the periodic brightness pattern observed in the Se atom array is consistent with the presence of different local density of states (LDOS). This variation of LDOS can result from different orbital overlapping with the underlying HOPG, consistent with the moiré pattern. The interatomic spacing in the dotted white triangle drawn in Figure 4.1(c) was determined to be about 0.33 ± 0.01 nm, in good agreement with previously reported results[287,288].

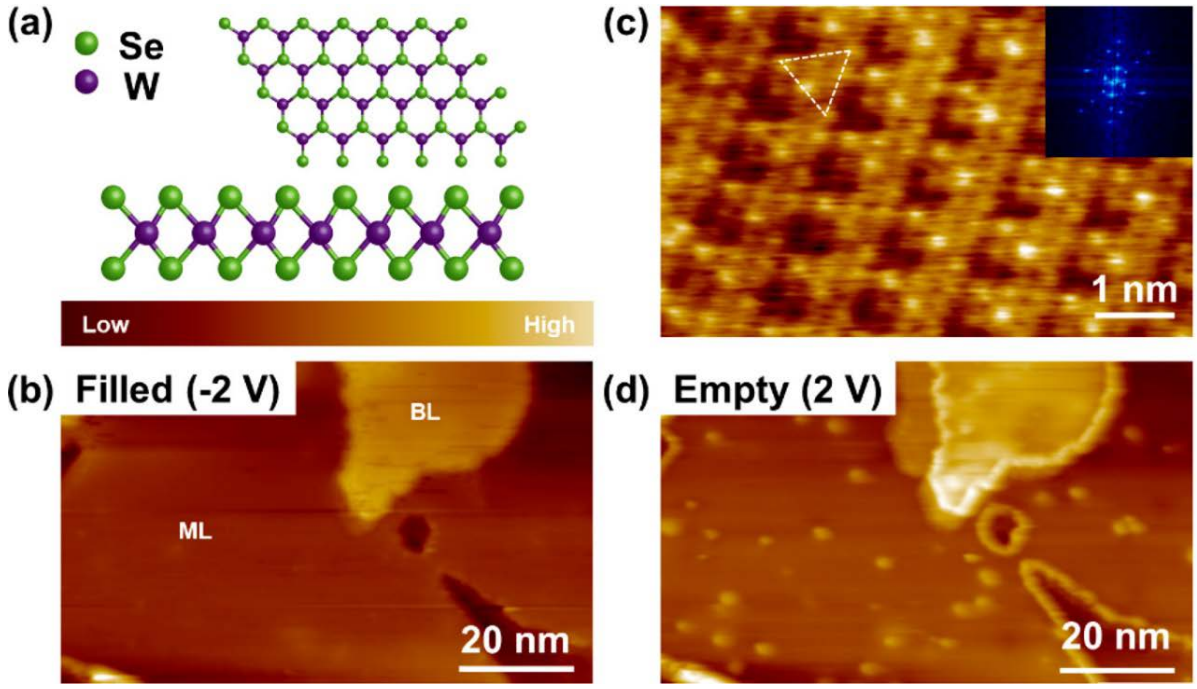

Figure 4.1: (a) Schematic diagrams of the ML WSe_2 atomic structure with top and cross-sectional views. (b) Filled state STM image of bare ML WSe_2 (V_S = − 2 V, I_T = 20 pA). A small triangular BL WSe_2 region is also observed within the scanned image. (c) Atomically resolved STM image of ML WSe_2 (V_S = − 0.8 V, I_T = 320 pA). It is noted that the STM image is slightly distorted due to thermal drifting during STM imaging. Inset shows the Fourier transform of the STM image. (d) Empty state STM image of the bare ML WSe_2 scanned over the same area as in (b) (V_S = 2 V, I_T = 20 pA).

The defects in the basal plane of ML WSe_2 were probed by applying a variable sample bias during STM imaging. It is noted that the density of defects has flake-to-flake variation. As shown in Figure 4.1(b), a flat and smooth terrace was only observed under the "filled state" imaging with a −2 V sample bias. However, when the imaging mode was switched to "empty states" using a +2 V sample bias, bright protrusions were observed on the terrace along with bright brims of step edges as shown in Figure 4.1(d). The asymmetrically enhanced brightness of defects indicates that the defects have a different electronic structure from the defect-free terrace in ML WSe_2. To elucidate the nature of the asymmetric bias dependence of defects, LDOS was probed using STS. As shown in Figure 4.2(a), STS was recorded with the STM tip at the defects (red '×') and far away from the

defects (white '×'). The measured LDOS from STS of defects and defect-free regions are compared as shown in Figure 4.2(b). The black curves, corresponding to the defect-free areas, have an apparent gap centered at the Fermi level (0 V) and states at both conduction band (CB) and valence band (VB) edges. However, as the STM tip was moved to the defect site, the acquired STS curves (shown in red) reveal a larger LDOS at both CB and VB edges than the black curve. Furthermore, the Fermi level is pinned closer to the VBE indicating a large density of positive charge carriers or holes.

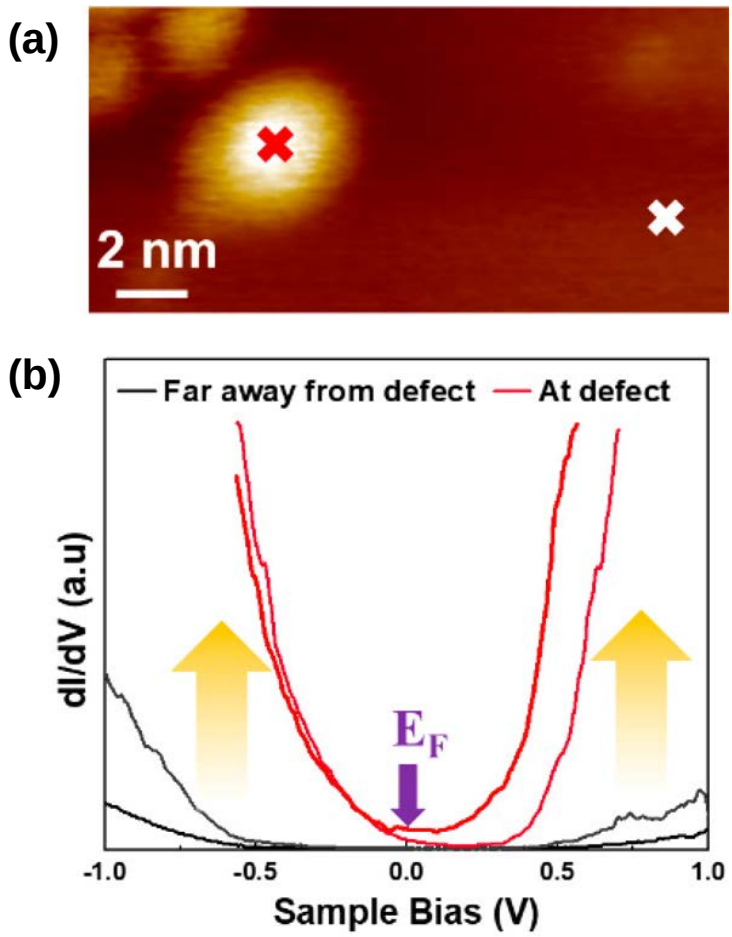

Figure 4.2: (a) Enlarged empty state STM image showing defects (bright protrusion marked by a red cross) and defect-free areas (marked by white cross) ($V_S = -1$ V, $I_T = 50$ pA). (b) LDOS probed using STS at the defect sites (red curves) and defect-free areas (black curves) corresponding to the red and white cross '×' marks, respectively, as shown in (a).

4.3.2 STM/STS on MBE-Grown Chemically Treated ML WSe_2

The effect of chemical treatment on ML WSe_2 was probed after dipping the as-prepared ML WSe_2 sample in a 20% $(NH_4)_2S$(aq) solution (source: Sigma-Aldrich; 98% purity)[272,273]. As shown in Figure 4.3(a) below, the dissociation of $(NH_4)_2S$ in H_2O solution is expected to result in the generation of SH and H_2S species as per the following chemical reactions[289,290]:

$$(NH_4)_2S(aq) \rightarrow 2NH_3(aq) + H^+(aq) + HS^-(aq),$$
$$\leftrightarrow 2NH_3(aq) + H_2S(aq) \qquad (1)$$

As shown in previous reports, the $(NH_4)_2S$ molecules are readily dissociated into molecular species such as NH_3, SH, and H_2S in H_2O solution. Thus, these dissociated molecular species, including NH_3, SH, H_2S, *etc.*, can readily adsorb on the bare WSe_2 surface when the WSe_2 samples are dipped in $(NH_4)_2S$(aq) solution. The $(NH_4)_2S$(aq) chemical treatments were performed at 300 K followed by a gentle spray of isopropyl alcohol (IPA) to remove unintentional contaminants such as hydrocarbons, following which the samples were air-dried.

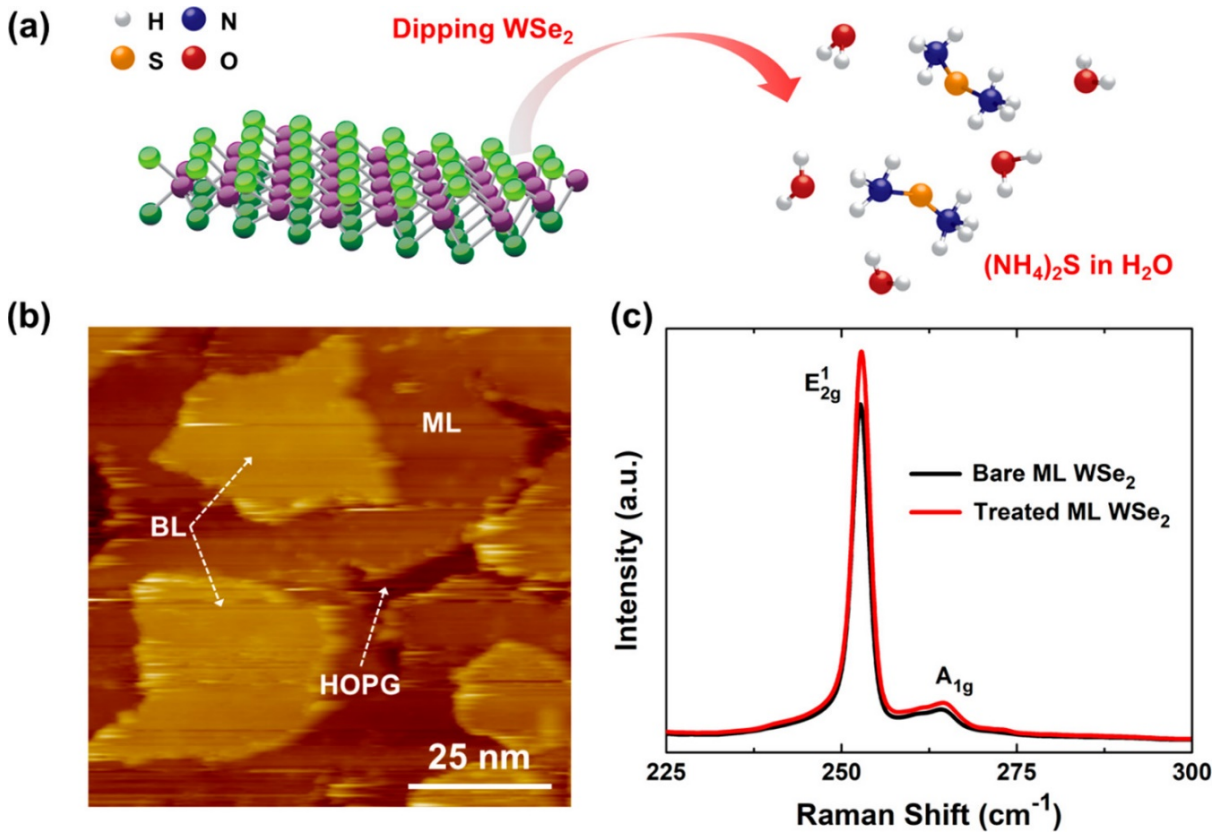

Figure 4.3: (a) Schematic diagram illustrating the one-step chemical treatment process of ML WSe_2 using 20% $(NH_4)_2S$(aq) solution. (b) Large area empty state STM image of chemically treated MBE-grown ML WSe_2 (V_S = 2.5 V, I_T = 10 pA). It is noted that there is an imaging noise induced by weak interactions between the adsorbates and the STM tip. From the line trace, the expected step height of 6–7 Å was determined for the ML WSe_2. (c) Raman spectra of mechanically exfoliated ML WSe_2 before (black curve) and after (red curve) $(NH_4)_2S$(aq) chemical treatment, showing negligible change in its characteristic Raman modes.

The large area empty state STM image shown in Figure 4.3(b) reveals the surface of chemically treated MBE-grown ML WSe_2 with interspersed BL WSe_2 islands; noticeable surface changes were not clearly observed in the large area empty state STM imaging in this case, possibly due to imaging noise induced by weak interactions between the adsorbates and the STM tip. Moreover, as shown in Figure 4.3(c), Raman spectra acquired on a mechanically exfoliated ML WSe_2 surface before (black curve) and after (red curve) $(NH_4)_2S$(aq) chemical treatment shows a negligible change in the characteristic

Raman modes, that is, the A_{1g} and 2LM(M) modes, suggesting no change in the structural integrity of ML WSe_2 post-chemical treatment. It is noted that there is no clear evidence for the intercalation of SH molecules in the van der Waals (vdW) gap between adjacent WSe_2 layers. If a large number of SH molecules were indeed intercalated between adjacent WSe_2 layers, then the top WSe_2 layers should get delaminated. However, the Raman plots shown in Figure 4.3(c), and later in Figure 4.11(b), indicate that there is no noticeable change in the peak positions and peak widths (*i.e.*, FWHM) of the WSe_2 Raman modes after chemical treatment. This implies that the structural integrity of WSe_2 is maintained even after chemical treatment. Therefore, it is hypothesized that SH molecules mostly adsorb on the top surface of WSe_2 rather than intercalating between adjacent WSe_2 layers.

After the chemical treatment of ML WSe_2 using 20% $(NH_4)_2S$(aq) solution, a large density of electronic states was indeed observed by STM on the WSe_2 surface under optimized imaging conditions. As shown in Figure 4.4(a), the chemically treated ML WSe_2 showed filled state STM imaging (−1 V bias) similar to that of a bare ML WSe_2 surface, as shown in Figure 4.1(b), that is, the step edges are electrically enhanced, while defects are not clearly observed on the terraces. However, switching the imaging mode to empty states with a +1 V sample bias in Figure 4.4(b) below, a high density of adsorbate-like features was observed on the terraces as well as step edges which can be denoted as chemical treatment-induced (CTI) defects.

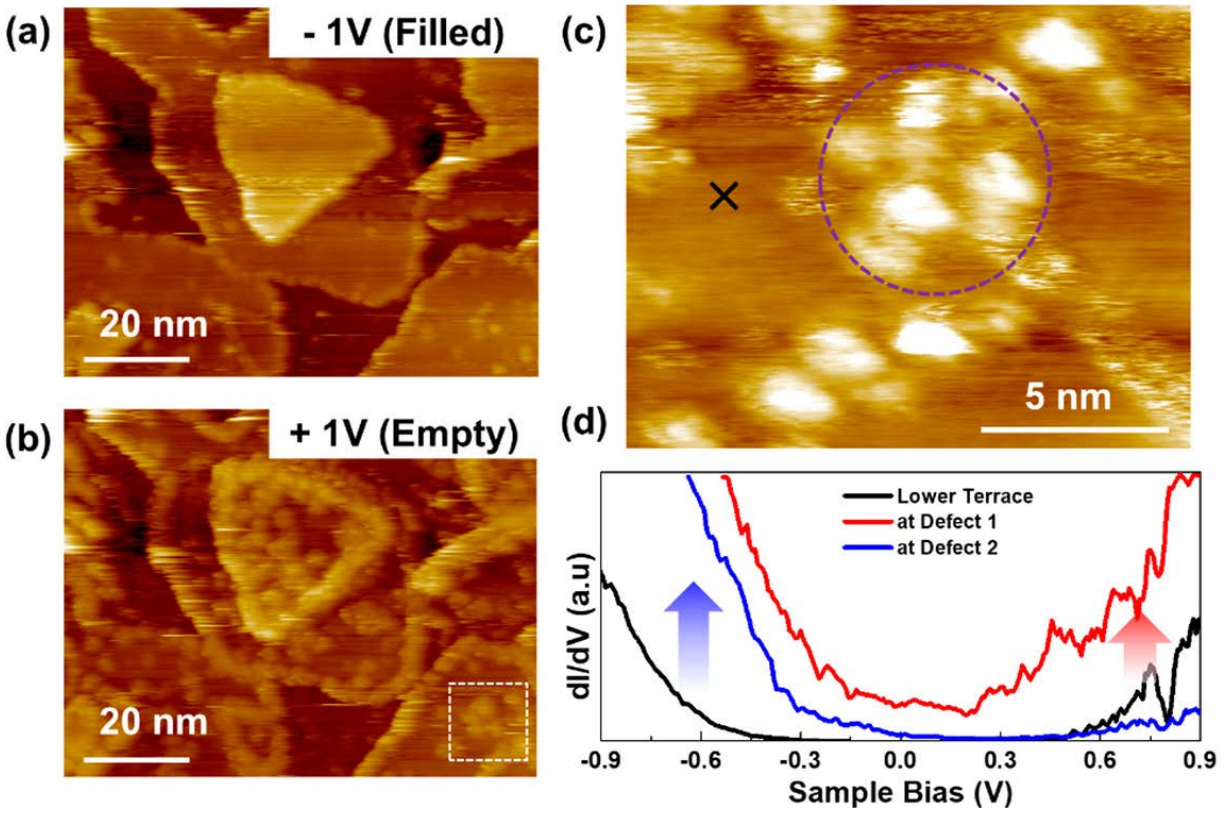

Figure 4.4: (a) A chemically treated WSe_2 surface with filled state STM imaging (V_S = −1 V, I_T = 40 pA). (b) Defects in chemically treated WSe_2 revealed with empty state STM imaging (V_S = 1 V, I_T = 20 pA). Note that (b) is imaged on the same surface area as (a). (c) High-resolution zoomed-in filled state STM image of the chemically treated WSe_2 surface acquired from the dashed square region marked in (b). The dashed purple circle marks the location of the CTI defects, whereas black '×' denotes the defect-free lower terrace (V_S = −0.8 V, I_T = 100 pA). (d) STS plots obtained after $(NH_4)_2S$(aq) chemical treatment from the lower defect-free terrace point X (black curve) and defect points inside the dashed purple circle (red and blue curves) as shown in (c).

To elucidate the nature of these CTI defects, the LDOS on the surface of chemically treated ML WSe_2 was probed using STS. Figure 4.4(c) shows the high-resolution zoomed-in filled state STM image of the CTI defects, acquired from the dashed square region marked in Figure 4.4(b), by precisely positioning the STM tip at their locations. STS curves were measured at the defect-free lower terrace (marked by ×) and at the location of the CTI defects (inside the dashed purple circle). As shown in the STS spectra in Figure 4.4(d),

three different STS curves were observed, as depicted by the red, blue, and black curves, within the voltage range of −1 V to +1 V. In comparison to the black curve acquired at the defect-free lower terrace, both the red and blue STS curves acquired on the adsorbed CTI defects reveal that the band edge states expand across the Fermi level position (0 V) and have larger LDOS near the WSe_2 VBE (*i.e.*, below the Fermi level), thereby, confirming that the Fermi level at the CTI defect sites is positioned closer to the ML WSe_2 VBE after $(NH_4)_2S$(aq) chemical treatment. It is noted that probing the sample surface using STM tips relies on the feedback of tunneling current between metal tips and sample surfaces, while maintaining only a few angstrom (Å) distance. Thus, if mobile molecules or atoms are placed between the metal tip and sample surfaces, the interaction of metal tip with molecules induces STM imaging noise (horizontal lines) as shown in Figure 4.3(b) and Figures 4.4(a)–(c)[291,292].

Based on the observation of STS measurements on adsorbed CTI defects, it can be hypothesized that if the density of CTI defects increases on ML WSe_2, then the overall charge carrier density increases. Moreover, since both the blue and red STS curves corresponding to CTI adsorption sites reveal a larger density of electronic states near the WSe_2 VBE, it can be hypothesized that the population of positive charge carriers (holes) should be larger than the population of negative charge carriers (electrons), resulting in an enhanced p-type behavior. This CTI electronic transition in ML WSe_2 is further confirmed by the large range STS spectra shown in Figure 4.5. It is noted that in Figure 4.5, during STS measurements on the surface of $(NH_4)_2S$(aq)-treated WSe_2, the STM tip mostly approaches the adsorbed molecules on WSe_2 (physical distance <1–3 nm to molecules). Each STS curve was averaged over 5–7 curves with each curve recorded from random positions on multiple ML WSe_2 samples while intentionally avoiding domain boundaries and step edges, but not the defects. Although some of the recorded STS data may have been on defects, the final STS curves should represent a random sampling of terrace sites. As shown in the LDOS of bare ML WSe_2 (black curve), an electronic band gap of ~ 2.1 eV can be observed consistent with previously reported values[293-295]. However, $(NH_4)_2S$(aq) chemical treatment of ML WSe_2 for 15 min at 300 K induces a reduction of

this electronic band gap to ~ 1.1 eV and pins the Fermi level closer to the edge of the valence band, as shown by the red STS curve in Figure 4.5. Therefore, both the density of charge carriers and the electronic band gap of WSe_2 can be tuned by defect engineering utilizing $(NH_4)_2S$(aq) solution. Based on the averaged STS data, a greater enhancement in hole concentration than electron concentration can be predicted over the chemically treated ML WSe_2 surface. It is noted that the detectable limit of tunneling current is about ±1 nA in the *I*–*V* curves during STM/STS probing. Therefore, current levels above ±1 nA cannot be measured, and, instead, they are only shown as a steady current of ±1 nA.

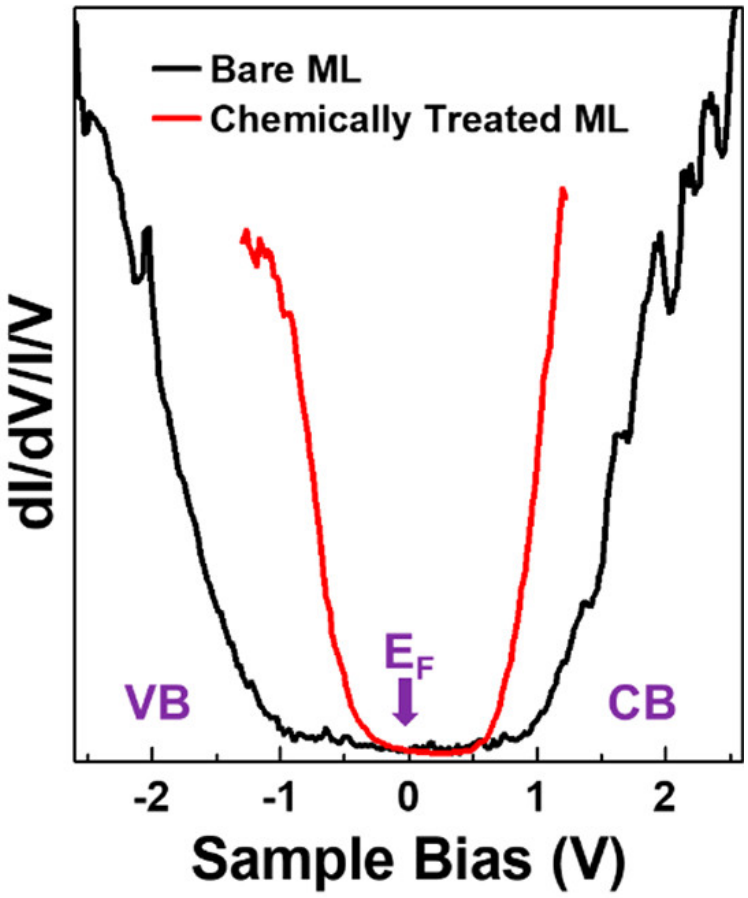

Figure 4.5: Averaged STS curves of ML WSe_2 before (black curve) and after (red curve) $(NH_4)_2S$(aq) chemical treatment. Each STS curve was averaged over 5–7 different STS curves measured on the WSe_2 surface distant from the step edges and domain boundaries.

4.3.3 AFM Study of the Removal of Carbon Composites and Oxides in WSe_2 after $(NH_4)_2S$(aq) Chemical Treatment

To elucidate the effect of $(NH_4)_2S$(aq) chemical treatment on WSe_2, the topography of ML WSe_2 exfoliated mechanically from bulk WSe_2 was probed using atomic force microscopy (AFM). A large area of bare ML WSe_2 is displayed in Figure 4.6(a) with a few pinholes and step edges. Typically, carbonaceous deposits are introduced during the mechanical exfoliation and transfer processes onto SiO_2 substrates using Scotch tape and polydimethylsiloxane (PDMS) stamps in ambient conditions[296,297]. Furthermore, hydrocarbons can be introduced from ambient air, which has been confirmed in a previous report[298]. Therefore, the observed pinholes and the step edges are hypothesized to be filled by carbonaceous deposits. It is known that removal of these carbon contaminants requires annealing in a UHV chamber above 573 K[296]. However, after $(NH_4)_2S$(aq) chemical treatment, the AFM image of Figure 4.6(b) reveals that the carbon contaminants are mostly removed. The data is consistent with the carbon composites being washed out by the reaction with $(NH_4)_2S$(aq) solution.

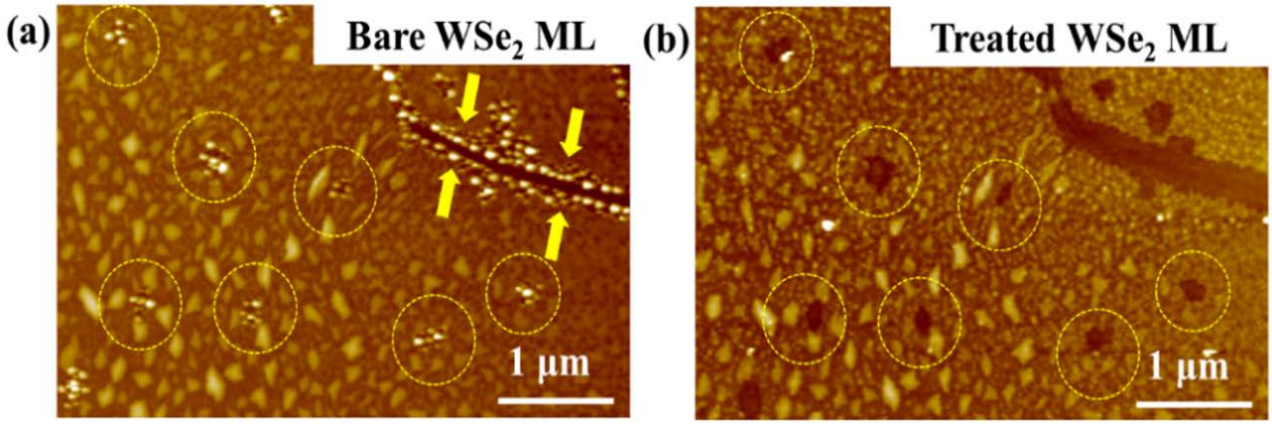

Figure 4.6: Atomic force microscopy (AFM) images of mechanically exfoliated ML WSe_2 (a) before $(NH_4)_2S$(aq) chemical treatment and (b) after $(NH_4)_2S$(aq) chemical treatment showing a cleaner surface topography. Pinholes and step edges are marked with dotted yellow circles and solid yellow arrows, respectively.

During transfer of the WSe_2 sample in ambient conditions or during fabrication processes, the WSe_2 surface is exposed to ambient air resulting in the partial oxidation of

WSe_2. To elucidate the effect of chemical treatments on oxidized WSe_2, the surface of WSe_2 was intentionally oxidized by treating it with ultraviolet-ozone (UV-O_3) which generates WO_x particles on the surface. As shown in Figure 4.7 below, $(NH_4)_2S$(aq) chemical treatment of oxidized WSe_2 induces the removal of UV-O_3-induced WO_x particles at the surface. Oxidized WSe_2 surfaces were probed using AFM, before and after chemical treatments. As shown in Figure 4.7(a), bulk WSe_2 surface was exposed to UV-O_3 for 20 min at 473 K to oxidize the WSe_2; AFM shows particle-like features consistent with WO_x particles of variable sizes. However, after dipping in diluted $(NH_4)_2S$(aq) solution for 1 hr. at 323 K, most of the WO_x particles were removed, and only a few particles remain on the bulk WSe_2 surface as shown in Figure 4.7(b). It is hypothesized that the entire oxidized WSe_2, including both agglomerated and layered WO_x, is removed by the $(NH_4)_2S$(aq) chemical treatment, thereby, exposing a fresh WSe_2 surface as observed in the AFM image. Although complete removal of WO_x requires dipping in the $(NH_4)_2S$(aq) solution for a few hours, it can be estimated that the small coverage of WO_x on just ambient-exposed WSe_2 is removed by a 10 to 15 min $(NH_4)_2S$(aq) chemical treatment, which is the typical time duration of the $(NH_4)_2S$(aq) chemical treatments used in the STM/STS and FET studies in this work.

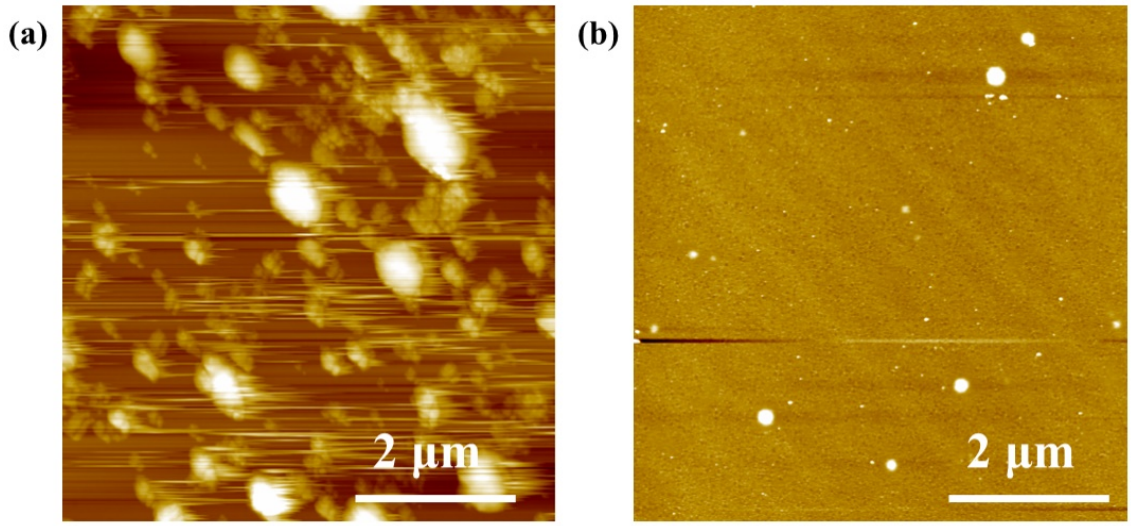

Figure 4.7: Atomic force microscopy (AFM) images of bulk WSe_2 exposed to UV-O_3 (a) after UV-O_3 and before $(NH_4)_2S$(aq) chemical treatment and (b) after $(NH_4)_2S$(aq) chemical

treatment showing a cleaner surface topography. Most of the UV-O_3-generated WO_x particles are removed by the $(NH_4)_2S$(aq) chemical treatment.

4.3.4 Chemical Analysis of Chemically Treated Bulk WSe_2 using XPS

To track the chemical change in bulk WSe_2 after dipping in $(NH_4)_2S$(aq) solution, X-ray photoelectron spectroscopy (XPS) was performed. The spectra of W 4f, Se 3d and O 1s for bare bulk WSe_2 and chemically treated WSe_2 show negligible change in W 4f and Se 3d peaks – see Figures 4.8(a) and (b) below.

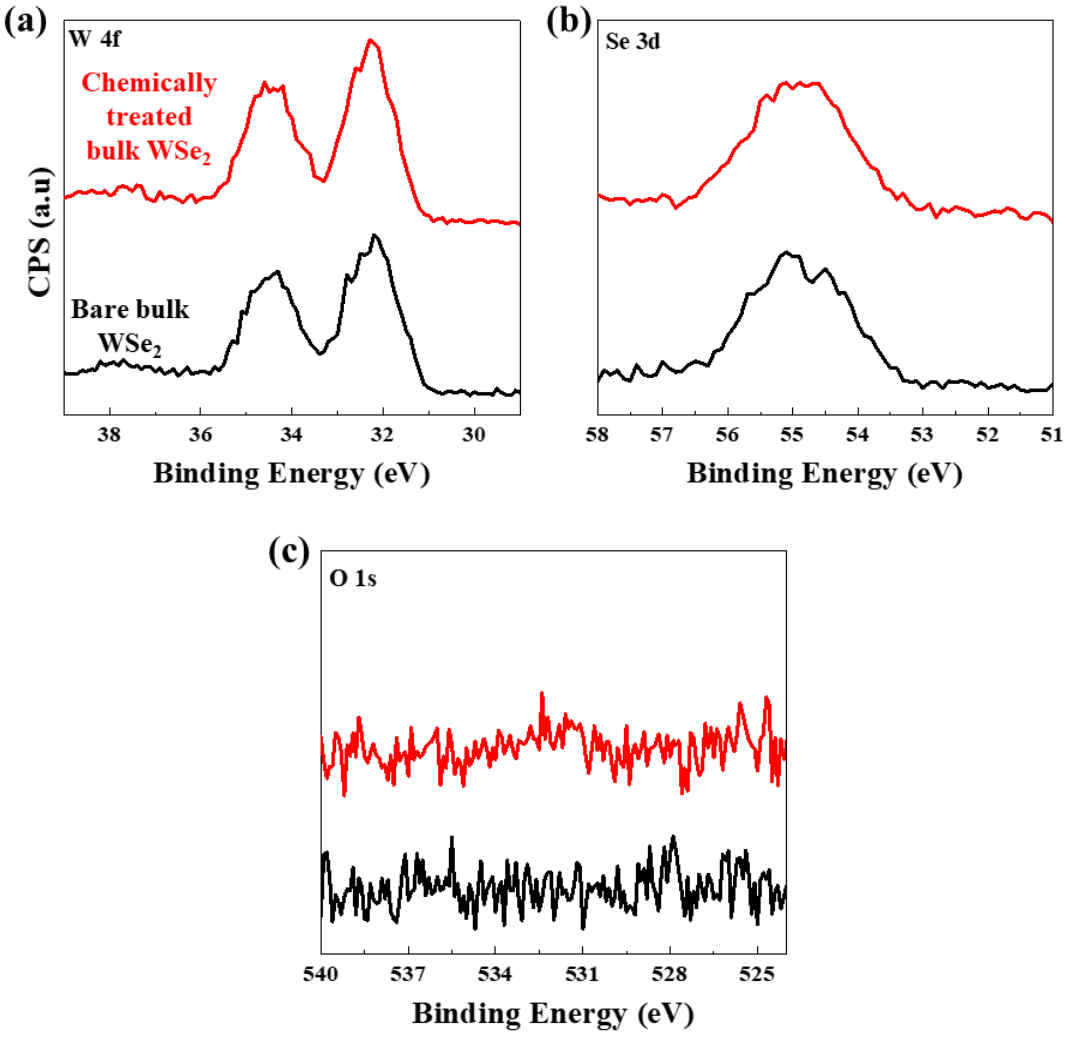

Figure 4.8: XPS spectra of bulk WSe_2 before and after $(NH_4)_2S$(aq) chemical treatment. The black curves correspond to the bare bulk WSe_2, while the red curves correspond to

$(NH_4)_2S$(aq)-treated bulk WSe_2. (a) Spectra of W 4f peaks. (b) Spectra of Se 3d peak. (c) Spectra of O 1s peak.

The peak positions and the peak widths are nearly constant after chemical treatment, consistent with the absence of direct influence of the chemical treatment on the chemical binding configuration of the atoms in WSe_2. The atomic ratio of elementary Se 3d to W 4f in chemically treated bulk WSe_2 (1.92:1) was also found to be nearly identical to Se 3d/W 4f ratio (1.96:1) in untreated bulk WSe_2. This reveals that the $(NH4)_2S$(aq) chemical treatment does not induce any decomposition of WSe_2.

Since the bulk WSe_2 was exposed to ambient air during chemical treatments, O 1s spectra of bulk WSe_2 is probed before and after $(NH_4)_2S$(aq) chemical treatment to quantify the oxidation in ambient air. As shown in Figure 4.8(c), there was no observable O 1s peak in both cases. It is noted that both the bare and chemically treated bulk WSe_2 samples were gently annealed at 573 K for 10 min in the UHV chamber to remove any ambient molecular adsorption from their surface before doing XPS. Therefore, it can be concluded that the $(NH_4)_2S$(aq) chemical treatment does not induce any oxidation of the WSe_2 surface in ambient air.

4.4 THEORETICAL DFT INVESTIGATION OF THE CHEMICAL TREATMENT-INDUCED BAND STRUCTURE TRANSITION AND P-DOPING IN WSE_2

To determine the exact mechanism underlying the aforementioned electronic transition in WSe_2 after $(NH_4)_2S$(aq) chemical treatment, DFT calculations were performed to compare the electronic band structures of ML WSe_2 before and after $(NH_4)_2S$(aq) chemical treatment. The surface interaction between WSe_2 and various chemically generated molecular species in the $(NH_4)_2S$(aq) solution was determined; calculations were performed to model all the possible adsorbates (S, SH, H_2S, NH_3) from the sequence of reactions in (1), but only the "SH" adsorbates produced an electronic surface structure consistent with the experiments. As shown in Figure 4.9(a), the adsorption of SH molecule on the WSe_2 surface exhibits a noticeable change in its electronic band structure; it induces the formation of acceptor-like in-gap states as well as an increase in the density of states

(DOS) right below the WSe_2 VBE and shifts the Fermi level toward the WSe_2 VBE. Conversely, the adsorption of elementary S introduces additional states near both band edges without a Fermi level shift and slightly reduces the electronic band gap from 1.55 to 1.49 eV. When a H_2S or NH_3 adsorbate is applied on WSe_2, the DOS of WSe_2 is nearly consistent with extremely weak interactions.

The effect of SH adsorbates on the WSe_2 band structure was investigated in more detail. The calculated electronic band structure of bare ML WSe_2 is shown in Figure 4.9(b); an electronic band gap of about 1.55 eV is calculated with the Fermi level positioned closed to the middle of the band gap. However, as shown in Figure 4.9(c), the adsorption of SH on WSe_2 induces the electronic band structure modification due to an increase in the DOS right below the WSe_2 VBE and formation of additional acceptor-like states in the band gap, thereby, causing a shift of the Fermi level toward the WSe_2 VBE. It is noted that the calculated binding energy of SH molecules at the Se atom site of WSe_2 is 0.48 eV. Introduction of the second SH molecule onto the surface of WSe_2 induces an additional increase in both the DOS below the WSe_2 VBE and acceptor-like in-gap states, as shown in Figure 4.9(d). Based on the DFT modeling results, it can be hypothesized that the adsorption of “SH” molecules is responsible for the p-type doping and electronic band gap reduction in WSe_2 after $(NH_4)_2S$(aq) chemical treatment.

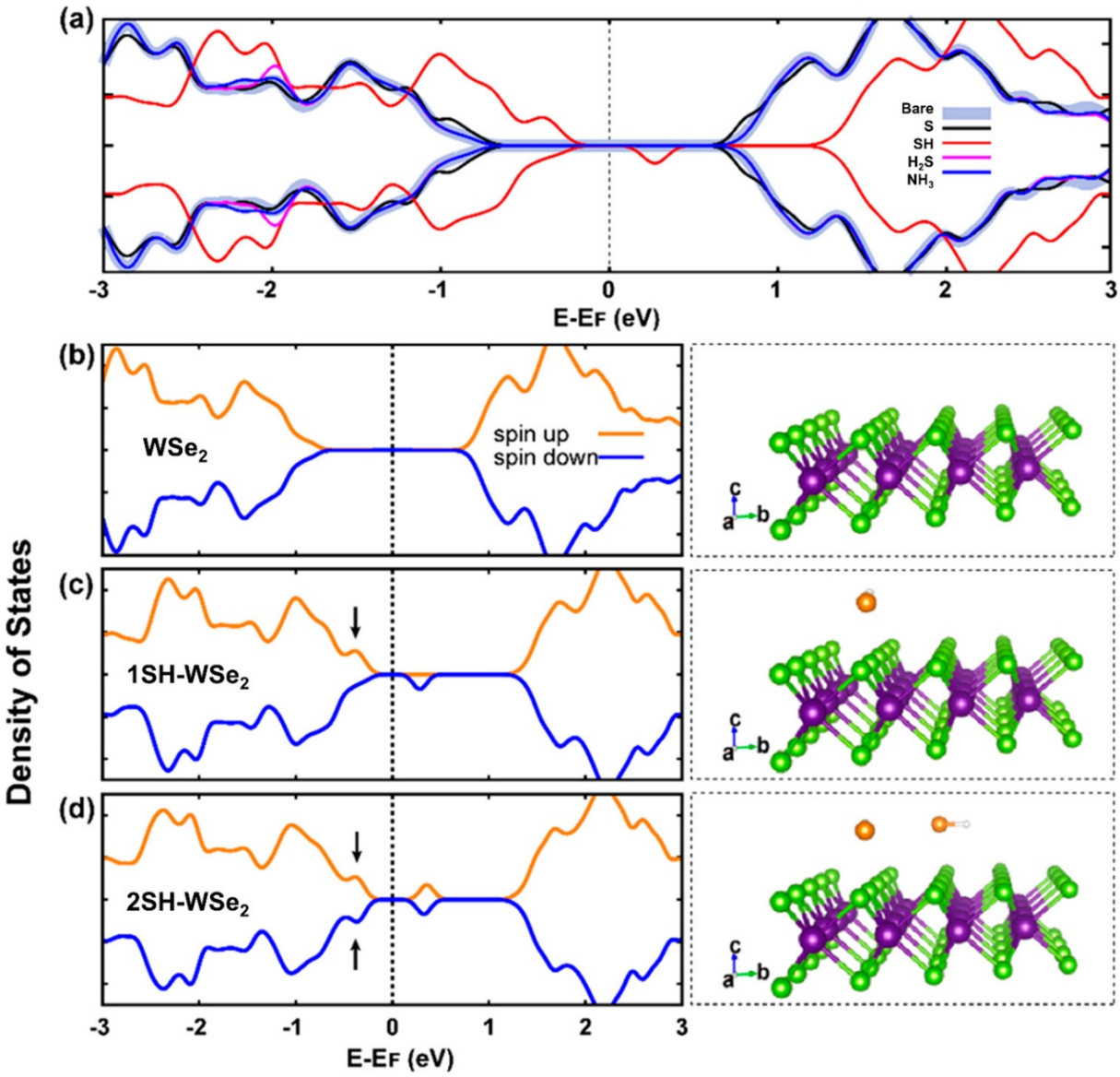

Figure 4.9: (a) Calculated band structure of ML WSe_2, with and without adsorbed species, *versus* energy. Only the adsorption of chemically generated "SH" molecules on the WSe_2 surface introduces in-gap states and shifts the Fermi level toward the WSe_2 valence band edge (red curves). Adsorption of other molecular species (S, H_2S, and NH_3) has a negligible effect on the ML WSe_2 band structure. Total DOS for (b) bare ML WSe_2, (c) ML WSe_2 with a single SH molecule adsorbed, and (d) ML WSe_2 with two SH molecules adsorbed. In the latter two cases, the increase in the DOS right below the VBE is indicated by black arrows. The modeled atomic structure corresponding to each of these cases is shown on the right. A free-standing ML WSe_2 layer is considered in all cases. Note

that for the localized defect-induced states, the partial occupancy of both spin up and spin down states is energetically unfavorable due to the strong repulsive interaction between localized electrons – see Figure 4.10(b) below. Note: The DFT simulations presented in this Chapter were performed at The University of Texas at Dallas by Jeongwoon Hwang and Chenxi Zhang under the supervision of Professor Kyeongjae Cho.

It is noted that in Figures 4.9(b), (c) and (d) above, introducing one SH adsorbate on the bare ML WSe_2 supercell leads to one unoccupied acceptor-like in-gap state as shown in Figure 4.9(c), which originates from the pz orbital of S (with spin down). The occupied pz orbital-dominant state with the opposite spin (orange line for spin up) increases the density of states (DOS) below the valence band edge (VBE) as marked with a black arrow in Figure 4.9(c). As a result, the overall density of states near the WSe_2 VBE increases. When one additional SH adsorbate is introduced (*i.e.*, a total of two adsorbed SH molecules on the WSe_2 surface), two pz orbital-dominant states with opposite spins are occupied leaving two unoccupied acceptor-like in-gap states with opposite spins. As shown in Figure 4.9(d), this additional acceptor-like in-gap state from the second SH molecule corresponds to the increase in the orange line at ~ 0.3 eV, whereas the occupied pz orbital-dominant state with the opposite spin (blue line for spin down) from the second SH molecule further increases the DOS below the VBE as marked with the lower black arrow in Figure 4.9(d).

These acceptor-like in-gap states as well as the additional states near the VBE induced by molecular SH adsorption can effectively reduce the electronic band gap of WSe_2, which is consistent with the experimentally observed electronic band gap reduction. Figure 4.10(a) below compares the projected DOS on SH with the total DOS of the SH-WSe_2 system, whereas Figure 4.10(b) illustrates the iso-surface of the charge density of SH adsorbate-induced states for the spin up and spin down cases as marked by the blue and red arrows, respectively, in Figure 4.10(a). Thus, these DFT calculation results are consistent with the adsorption of SH molecules on the WSe_2 surface being the underlying mechanism for the experimentally observed p-type doping and electronic band gap reduction in WSe_2 after $(NH_4)_2S$(aq) chemical treatment.

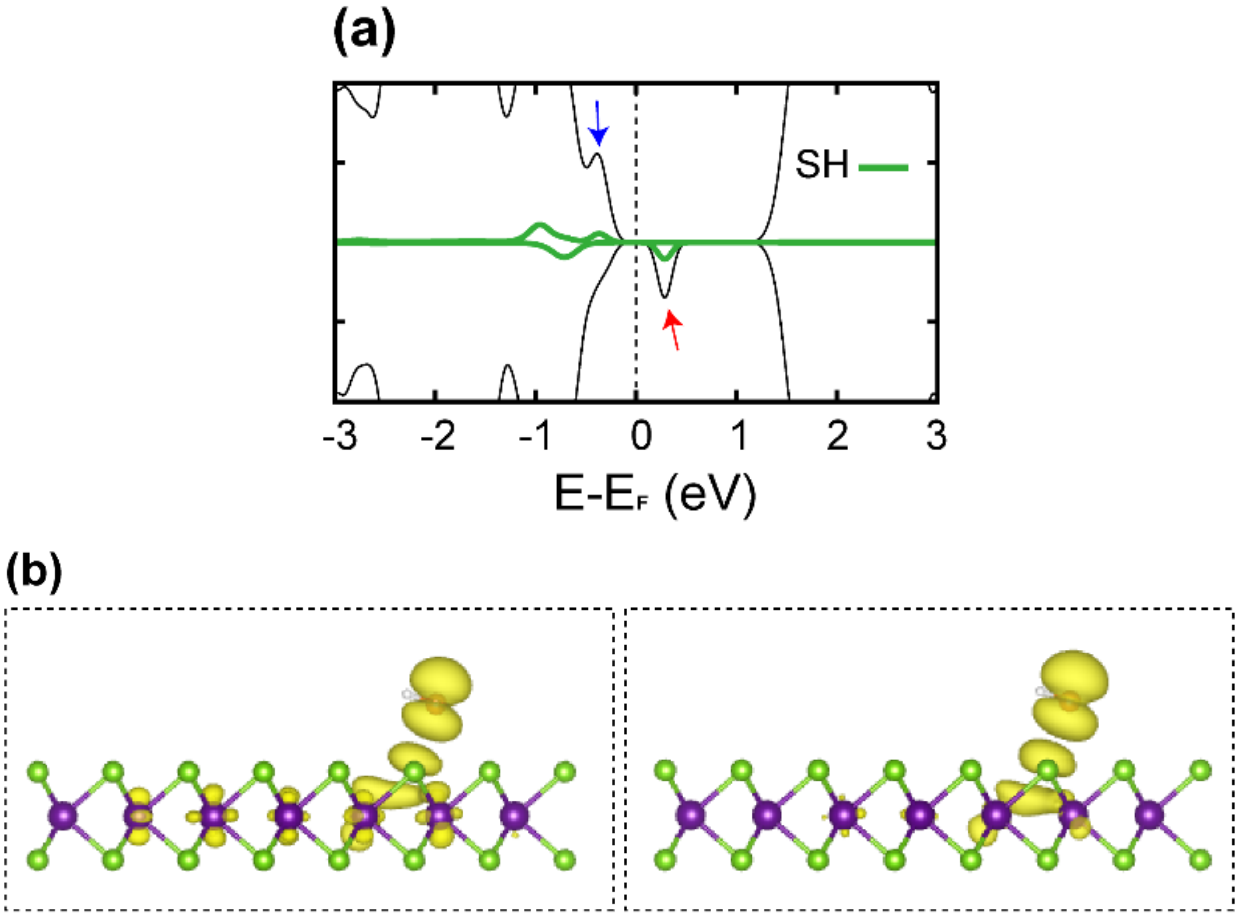

Figure 4.10: (a) Projected density of states on SH (green line) is shown with the total density of states (black line). (b) Illustration of the iso-surface of the charge density of SH adsorbate-induced states for the spin up (left) and spin down (right) cases as marked by the blue and red arrows, respectively, in (a).

It is noted that in the STS curves shown earlier in Figure 4.5, quantification of the exact change of ML WSe_2 electronic band gap with $(NH_4)_2S$(aq) chemical treatment is challenging because of the limited energy resolution and relatively high sample temperature (100 K). In addition, STM lacks chemical selectivity, and, thus, identifying a chemically induced adsorbate using STM is challenging. However, as shown in Figure 4.9, DFT reveals that as SH molecules adsorb on the surface of WSe_2, additional electronic states are introduced in the band gap as well as right below the VBE consistent with p-doping and band gap narrowing. Therefore, it is hypothesized that the p-doping and

electronic band gap reduction in $(NH_4)_2S$(aq)-treated ML WSe_2 results from the introduction of additional energy states in the WSe_2 band structure with the adsorption of a large density of SH molecules[299-301]. It is noted that the present DFT model is simplified with a limited number of SH adsorption sites (only one and two) on the WSe_2 surface, because a DFT calculation with a large density of SH adsorption on WSe_2 would require an enormous processing time and complicated models. Conversely, as shown earlier in the STM images of $(NH_4)_2S$(aq)-treated ML WSe_2, a large coverage of adsorbate-like CTI defects is observed on the WSe_2 surface which includes SH molecular adsorbates among others, and, therefore, it can be inferred that multiple adsorbed SH molecules induce the generation of a large DOS in the WSe_2 band structure consistent with p-type doping and electronic band gap reduction.

4.5 Electrical and Spectroscopic Characterization of the P-Doping in WSe_2 after Chemical Treatment

4.5.1 Transfer Characteristics and Raman Characterization of Back-Gated Few-Layer WSe_2 FETs

To further substantiate the STS and DFT results, the hole doping induced in WSe_2 by the one-step $(NH_4)_2S$(aq) chemical treatment process was also investigated *via* the electrical characterization of FL WSe_2-based FETs. Figure 4.11(a) illustrates the schematic of a back-gated FL WSe_2 FET along with an optical micrograph of a typical FET used in this study. The FL WSe_2 flake is first characterized using Raman spectroscopy. Figure 4.11(b) shows the Raman spectra acquired on the FL WSe_2 device flake before (black curve) and after (red curve) $(NH_4)_2S$(aq) chemical treatment (10 min at 300 K + quick IPA rinse + air-dry), revealing a negligible change in the peak positions or sharpness of the characteristic Raman modes of FL WSe_2, that is, the A_{1g}, 2LA(M), and B_{2g}^1 modes[302], suggesting that the material/structural quality of the FL WSe_2 flake, much like the case of ML WSe_2 as shown in Figure 4.3(c), remains unaffected by the $(NH_4)_2S$(aq) chemical treatment.

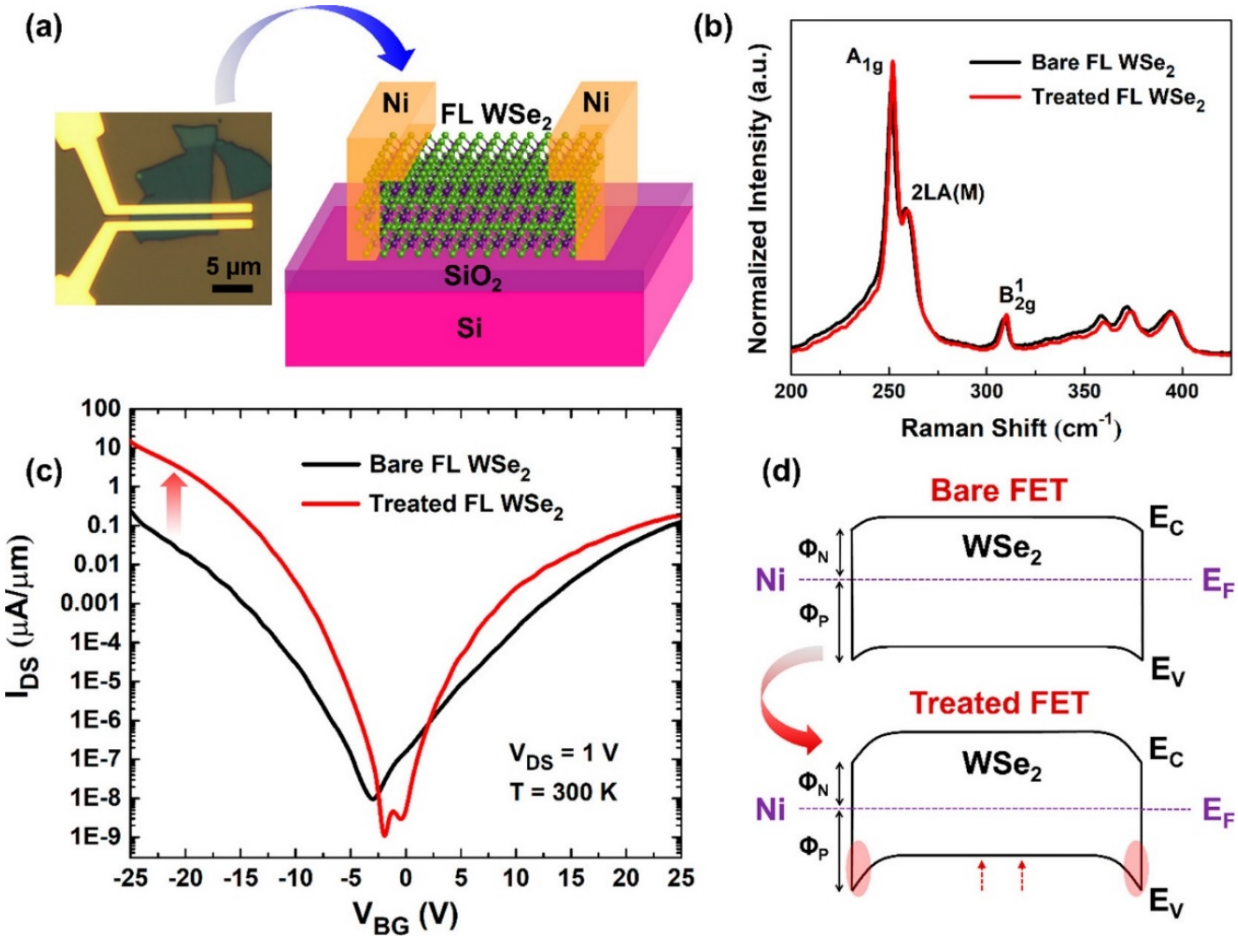

Figure 4.11: (a) Optical image and schematic illustration of the back-gated FL WSe_2 FET with Ni/Au top contact electrodes. (b) Raman spectra taken on a FL WSe_2 device flake (~ 3–4 nm thickness) before (black curve) and after (red curve) $(NH_4)_2S$(aq) chemical treatment. (c) Room temperature back-gated transfer characteristics of the FL WSe_2 FET shown in (a) before (black curve) and after (red curve) $(NH_4)_2S$(aq) chemical treatment. A clear enhancement of I_{ON} in the p-branch is observed after $(NH_4)_2S$(aq) chemical treatment. (d) Qualitative equilibrium band diagrams along the FL WSe_2 FET channel before (top; bare FET) and after $(NH_4)_2S$(aq) chemical treatment (bottom; treated FET) explaining the enhanced p-type behavior and hole field-effect mobilities observed in chemically treated back-gated FL WSe_2 FETs.

The back-gated FL WSe_2 FETs were electrically characterized at room temperature (300 K) under vacuum (base pressure: 6×10^{-6} mbar) in the dark, utilizing a Lakeshore probe station and a Keysight B1500A semiconductor parameter analyzer. The back-gate

voltage V_{BG} was swept from negative to positive for all the current–voltage transfer characteristic measurements presented, unless otherwise noted. The source and drain electrodes were kept constant for all measurements taken on any given FET. The flake thickness used in our FL WSe_2 FETs was in the range of 3–4 nm, corresponding to 4–5 atomic layers. Figure 4.11(c) shows the semilog transfer characteristics (*i.e.*, log I_{DS} *vs* V_{BG}) of the back-gated FL WSe_2 FET shown in Figure 4.11(a), measured at V_{DS} = 1 V. The channel length (L) and width (W) of this device are 0.75 and 10 μm, respectively. Before the $(NH_4)_2S$(aq) chemical treatment, the as-fabricated FET displays an ambipolar behavior, typical of FL WSe_2 FETs with Nickel (Ni) contacts[161], as shown by the black curve. The I_{ON} in the p-branch and the n-branch are comparable, consistent with the contact metal Fermi level being pinned close to the midgap of FL WSe_2. After the $(NH_4)_2S$(aq) chemical treatment, the measured transfer characteristic shows a pronounced difference as evidenced by the red curve in Figure 4.11(c). The back-gate voltage at which the p-branch current starts to emerge is slightly shifted toward more positive V_{BG} values after $(NH_4)_2S$(aq) chemical treatment, suggesting a positive threshold voltage shift indicative of p-type channel doping. There is a large increase (~ 70×) in the p-branch I_{ON} (from ~ 200 nA/μm to ~ 14 μA/μm), whereas the n-branch I_{ON} remains largely unchanged (~ 100–150 nA/μm).

4.5.1.1 Reasons for Ambipolarity in FL WSe_2 FETs Post Chemical Treatment

Note that the present WSe_2 FETs display ambipolar behavior even after chemical treatment with fairly significant n-branch ON-currents. This is expected because the Fermi level of Ni typically pins slightly above the midgap in WSe_2 at the Ni/WSe_2 contact interface[161], and the present chemical treatment is done after complete FET fabrication (*i.e.*, after the fabrication of Ni/Au top source/drain (S/D) electrodes), implying that the p-doping is effective only on the exposed WSe_2 channel regions and not the channel extensions underneath the Ni/Au top contacts. Moreover, as elucidated *via* the STS and DFT results discussed before, the $(NH_4)_2S$(aq) chemical treatment also induces a reduction in the overall electronic band gap of WSe_2, and it is likely that this electronic band gap reduction in the chemically treated WSe_2 channel regions contributes to such sustained n-

branch currents in the present FETs. Therefore, owing to these reasons, ambipolarity is expected in our FL WSe_2 FETs even after chemical treatment.

4.5.1.2 Detailed Investigation of the P-Branch of the FL WSe_2 FET

Since only the p-branch of the FL WSe_2 FET shows significant relative changes after $(NH_4)_2S$(aq) chemical treatment, it is analyzed in more detail. As can be seen in Figure 4.11(c), due to the increase in the p-branch I_{ON} after $(NH_4)_2S$(aq) chemical treatment, the p-branch I_{ON}/I_{OFF} ratio increases by 2 orders of magnitude (from ~ 10^7 to ~ 10^9). The extrinsic or two-point (2-pt) field-effect hole mobility ($\mu_{FE\text{-}h}$) is calculated from the linear transfer curves of the FET data shown in Figure 4.11(c), using the expression:

$$\mu_{FE} = (\delta I_{DS}/\delta V_{BG}|_{max})(L/W)(1/C_{OX})(1/V_{DS})$$

where $\delta I_{DS}/\delta V_{BG}|_{max}$ is the maximum back-gated transconductance, L and W are the length and width of the channel, respectively, C_{OX} represents the geometric back-gate capacitance, and V_{DS} is the drain/source voltage. The present chemical treatment induces p-doping consistent with molecular SH adsorption on the WSe_2 FET channel. Since doping the channel near the contact regions reduces the contact resistance and increases the field-effect mobility of charge carriers in TMD-based FETs, the 'extrinsic' or '2-pt' mobility equation (which includes the voltage drop across the series resistance of the contacts) was employed to estimate the relationship between the p-doping and changes in the hole field-effect mobility ($\mu_{FE\text{-}h}$) in the back-gated WSe_2 FETs. The $\mu_{FE\text{-}h}$ of the bare FL WSe_2 FET was extracted to be ~ 3.5 cm^2/V-s (*i.e.*, before $(NH_4)_2S$(aq) chemical treatment), while the $\mu_{FE\text{-}h}$ after $(NH_4)_2S$(aq) chemical treatment was ~ 22.7 cm^2/V-s, showing about a 6× enhancement in the hole field-effect mobility. Similar device results, that is, enhancement of the p-branch I_{ON} and improvement in $\mu_{FE\text{-}h}$, were obtained on four different back-gated FL WSe_2 FETs after $(NH_4)_2S$(aq) chemical treatment. The ambient stability of this $(NH_4)_2S$(aq) chemical treatment process was studied by remeasuring the FET transfer characteristics after a period of 10 days following the initial measurement post-chemical treatment. The FETs displayed good ambient stability as they retained a majority of the chemical treatment-induced enhanced p-type behavior. Moreover, the $(NH_4)_2S$(aq)

chemical treatment process shows reversibility as the WSe_2 FET transfer characteristic almost returns to its initial state after subjecting the samples to a high-vacuum annealing step at 340°C. The repeatability, stability, and reversibility of the $(NH_4)_2S$(aq) chemical treatment process can be seen in the transfer characteristics of another similar back-gated FL WSe_2 FET as discussed later in Section 4.5.3.

4.5.1.3 Mechanism of WSe_2 FET Operation Before and After Chemical Treatment

To understand the mechanism of WSe_2 FET operation before and after $(NH_4)_2S$(aq) chemical treatment, simple qualitative equilibrium band diagrams along the FL WSe_2 FET channel are illustrated in Figure 4.11(d). Before $(NH_4)_2S$(aq) chemical treatment, the FL WSe_2 FET shows typical ambipolar behavior as the Ni Fermi level pins slightly above the midgap in WSe_2 at the Ni/WSe_2 contact interface, resulting in large Schottky barrier heights for both electron and hole injections as represented by Φ_N and Φ_P, respectively, in Figure 4.11(d). After $(NH_4)_2S$(aq) chemical treatment in the exposed channel region, the band profile along the channel changes due to the enhanced p-doping induced by the adsorbed SH species on the WSe_2 surface. This chemical p-doping results in an enhanced "upward" band bending in the entire WSe_2 channel region, resulting in a narrowing of the p-type Schottky barrier width as illustrated by the shaded light red oval regions in the bottom band diagram of Figure 4.11(d). Note that the WSe_2 channel extensions directly underneath the Ni contacts are not affected by the $(NH_4)_2S$(aq) chemical treatment, and, thus, the chemical p-doping is confined only to the exposed WSe_2 channel/access regions in this study.

The overall effect of this $(NH_4)_2S$(aq) chemical treatment-induced p-doping in the WSe_2 channel and access regions is that when similar negative back-gate voltages are applied (which causes an upward band bending in the WSe_2 layer due to electrostatic p-doping), it makes it relatively easier for the holes to get injected into the valence band of WSe_2 *via* tunneling through the p-type Schottky barrier width present at the Ni/WSe_2 contact interface. In other words, after $(NH_4)_2S$(aq) chemical treatment on our WSe_2 FETs, the combined effect of the chemical p-doping and electrostatic p-doping by

the negative back-gate voltage results in an enhanced upward band bending in the WSe_2 channel leading to enhanced narrowing of the p-type Schottky barrier width, as opposed to the case before chemical treatment where the band bending is effected only by the negative back-gate voltage. Thus, enhanced p-branch ON-currents and hole field-effect mobilities were obtained in our FL WSe_2 FETs after chemical treatment. Since Schottky barriers result in large contact resistances, it can be said that the $(NH_4)_2S$(aq) chemical p-doping helps alleviate the p-type Schottky barrier-induced contact resistance in our FL WSe_2 FETs. This is consistent with other reports on TMD-based FETs where chemical doping in the channel/access regions has been shown to improve the FET performance by alleviating the Schottky barrier-induced contact resistance[303].

4.5.2 Detailed Analysis of the FL WSe_2 FET Current-Voltage Characteristics After Chemical Treatment

In this Section, detailed current-voltage characterization of another representative back-gated few-layer (FL) WSe_2 FET before/after $(NH_4)_2S$(aq) chemical treatment is shown. Optical images of the FET before/after chemical treatment elucidate the effects of the $(NH_4)_2S$(aq) chemical treatment on the Ni/Au contact electrodes. The transfer characteristics at two different drain voltages show the reproducibility of our chemical treatment-induced p-doping. The p-branch output characteristics demonstrate the relative improvement in the linearity of the p-branch drain currents indicative of a reduced Schottky contact behavior. The data also show the hysteresis in the transfer characteristics as well as an evolution of the p-doping with increasing chemical treatment time (5, 10 and 15 min).

4.5.2.1 Optical Images of the FL WSe_2 FET

As shown in Figure 4.12 below, the back-gated FL WSe_2 FET was imaged both before chemical treatment and after 15 min chemical treatment followed by an IPA rinse + air dry. Although there was some discoloration of the WSe_2 flake near its bulk bottom left region, the majority of the FL device flake and the Ni/Au top contact electrodes were not significantly affected by a 15 min chemical treatment in $(NH_4)_2S$(aq) solution. All electrical data shown in Section 4.5.2 was collected from this FET.

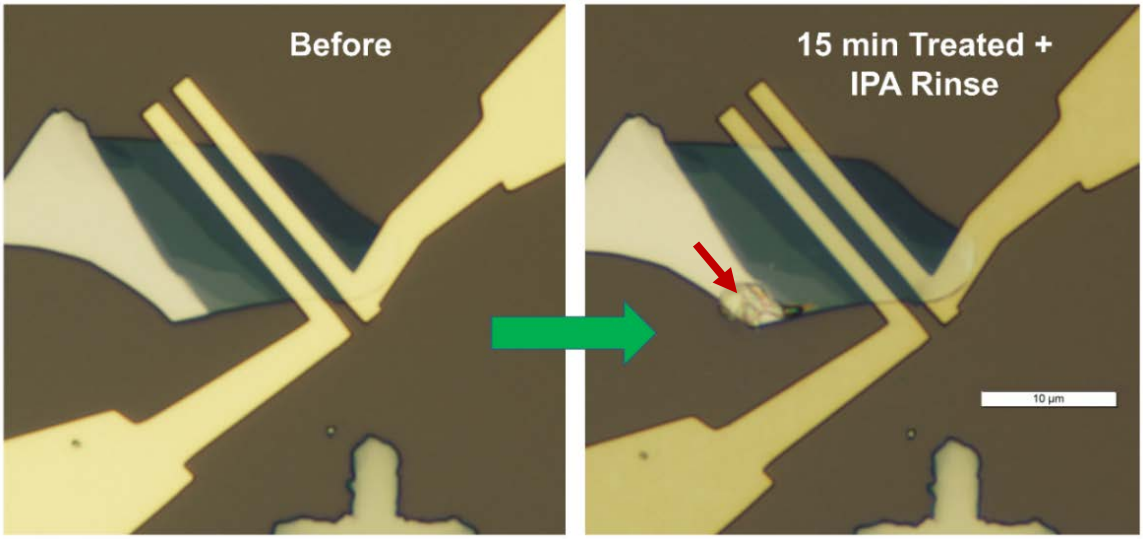

Figure 4.12: Optical images of a representative back-gated FL WSe_2 FET with Ni/Au top contact electrodes before and after 15 min chemical treatment showing no significant change in the Ni/Au contact electrodes as well as majority of the WSe_2 flake regions. The channel length L of the FET is about 1.5 µm. Scale bar is 10 µm. Red arrow points to the small bulk region of the WSe_2 affected by the chemical treatment.

4.5.2.2 Transfer Characteristics of the FL WSe_2 FET at Different Drain Biases

Figure 4.13 below shows the semi-log transfer characteristics of the back-gated FL WSe_2 FET (shown in Figure 4.12) before and after 10 min chemical treatment at two different drain voltages (V_{DS} = 1 V and 200 mV). The V_{BG} sweep direction was from negative to positive. Before chemical treatment (black curves), the FET displayed ambipolar behavior as expected with Ni contact electrodes, the Fermi level of which pins near the WSe_2 midgap at the Ni/WSe_2 interface. However, the n-branch currents were greater than the p-branch currents before chemical treatment, consistent with the contact Fermi level pinning being in the upper half of the WSe_2 band gap. The chemical treatment resulted in enhanced p-branch ON-currents (about a 100x increase) and a positive shift in the p-branch threshold voltage as shown by the red curves in Figure 4.13. The n-branch ON-currents remained similar or were slightly lower after chemical treatment. These results are similar to the FET results presented in Figure 4.11(c) above and Figure 4.17 below.

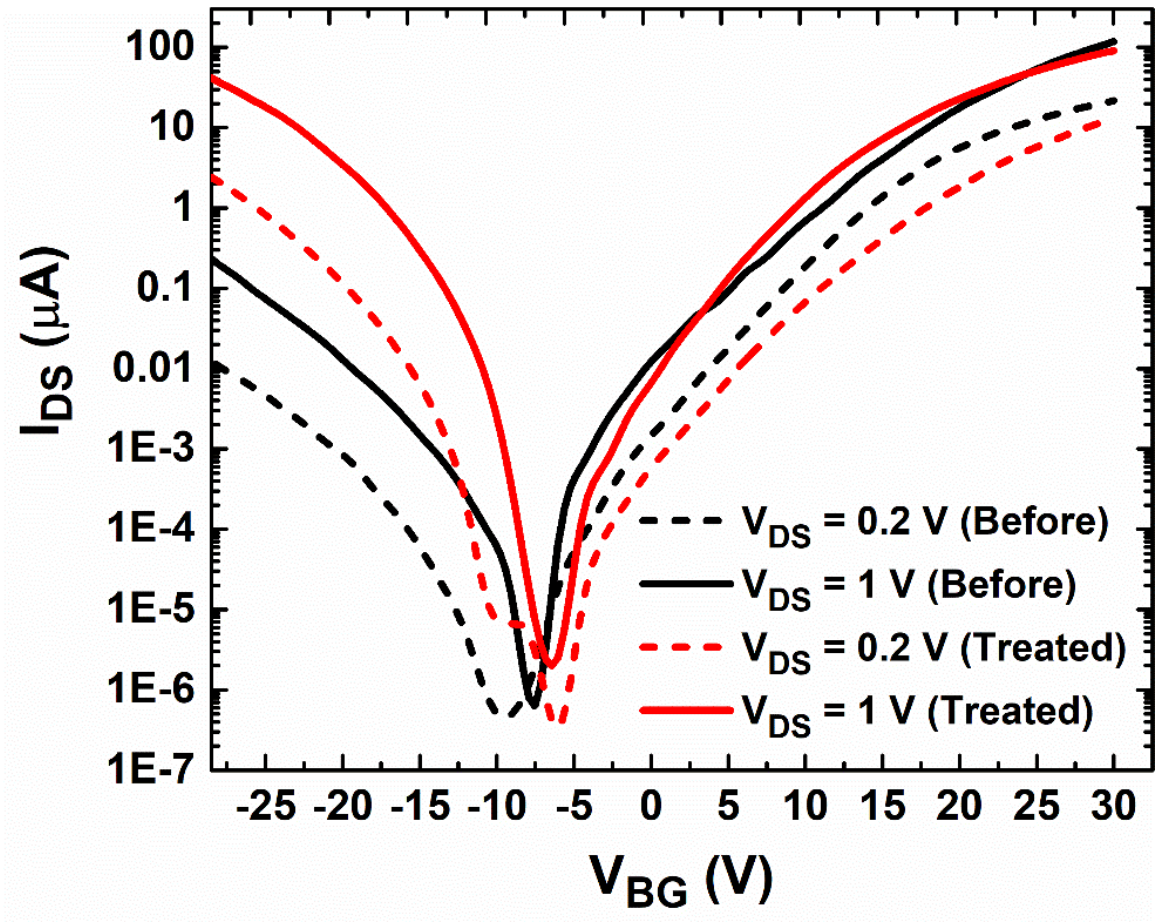

Figure 4.13: Transfer characteristics of the back-gated FL WSe_2 FET before and after 10 min chemical treatment at two different drain voltages (V_{DS} = 1 V and 200 mV) showing a clear enhancement in the p-branch ON-currents (up to 100x) accompanied with a positive threshold voltage shift. The n-branch ON-currents remain similar after chemical treatment.

4.5.2.3 P-Branch Output Characteristics of the FL WSe_2 FET

Figure 4.14 below compares the p-branch output characteristics of the FL WSe_2 FET before (left plot) and after (right plot) chemical treatment. The V_{BG} is decremented in -5 V steps from -15 V to -30 V to probe the p-branch of the WSe_2 FET. Before chemical treatment (top plot), the output current levels are fairly low (I_{ON} ~ 0.3 μA for V_{BG} = -30 V and V_{DS} = -1.5 V), and the current vs. voltage displays large non-linearity, especially at low V_{DS} values between -0.5 V and 0 V, consistent with the presence of a significant p-branch Schottky barrier height. However, after chemical treatment for 5, 10 and 15 mins (bottom

plot), there is a significant increase in the p-branch currents with increasing chemical treatment time (I_{ON} ~ 63 μA for V_{BG} = -30 V and V_{DS} = -1.5 V after 15 min treatment) as well as a relative improvement in the linearity of the I_{DS}-V_{DS} current-voltage curves at low V_{DS} values. This indicates that the chemical treatment-induced p-doping of the FL WSe_2 channel near the contact regions, coupled with the electrostatic p-doping induced by the negative V_{BG}, causes an enhanced 'upward' band bending at the WSe_2/Ni contact interface leading to narrowing of the p-type Schottky barrier width – see Figure 4.11(d) in Section 4.5.1 – which, in turn, facilitates enhanced hole injection from the Ni contacts into the WSe_2 valence band *via* tunneling through the Schottky barrier.

Although the chemical treatment leads to an improvement in the ON-currents and linearity of the p-branch I_{DS}–V_{DS} curves at low V_{DS} values, some nonlinearity is still present in the p-branch output characteristics of the FL WSe_2 FET consistent with non-ohmic or Schottky-type contacts even after chemical treatment. This signifies that the chemical p-doping technique used in this study only converts the p-type contacts from being "more" Schottky-type before chemical treatment (*i.e.*, more nonlinearity in the output curves) to relatively "less" Schottky-type after chemical treatment. It is noted that Ni S/D contact electrodes were used in this study which typically pins slightly above midgap in WSe_2, resulting in ambipolar FET behavior and large Schottky barrier heights for hole injection[161]. Consequently, Ni contacts are not optimized for efficient hole injection in WSe_2 and are partly responsible for the Schottky-type behavior observed in the p-branch of the FL WSe_2 FETs even after chemical treatment.

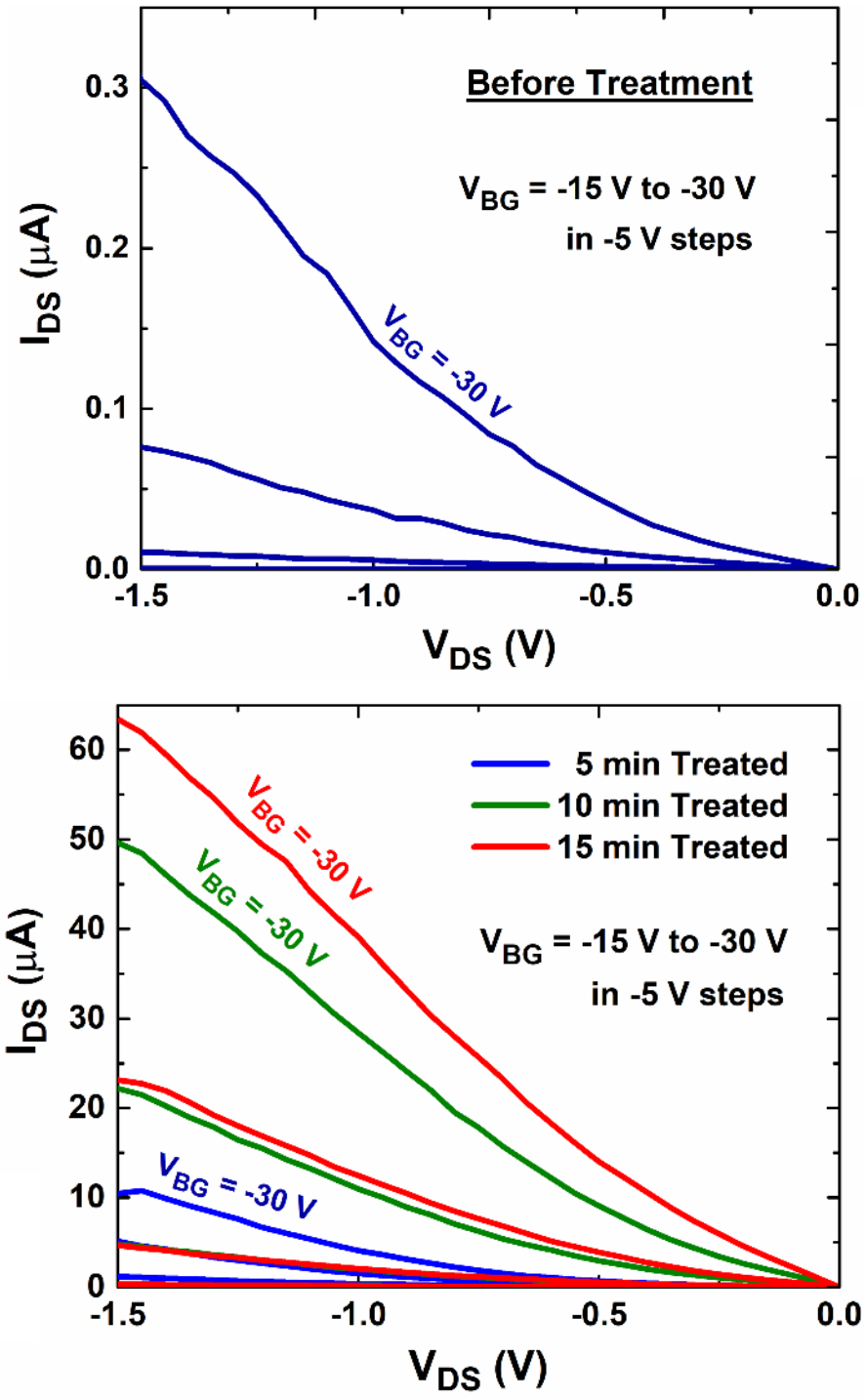

Figure 4.14: P-branch output characteristics of the back-gated FL WSe_2 FET before (top plot) and after (bottom plot) $(NH_4)_2S$(aq) chemical treatment showing a significant enhancement in the p-branch output currents after chemical treatment. For V_{BG} = -30 V and

V_{DS} = -1.5 V, the p-branch ON current increases from 0.3 µA to 10 µA, 50 µA and 63 µA after 5, 10, and 15 min of chemical treatment, respectively. With increasing chemical treatment time, there is also a relative improvement in the linearity of the I_{DS}-V_{DS} current-voltage curves at low V_{DS} values.

Moreover, a $(NH_4)_2S$(aq) solution with a fixed starting concentration (20% in H_2O) was utilized for the chemical p-doping. In principle, the starting concentration as well as the treatment time of the $(NH_4)_2S$(aq) solution can be varied to achieve different concentrations of adsorbed SH species on the WSe_2 surface, thereby, resulting in different p-doping levels ranging from nondegenerate doping in the channel region to degenerate doping in the S/D contact and access regions (as proof of concept, the p-doping evolution with increasing chemical treatment time using the 20% $(NH_4)_2S$(aq) solution is demonstrated in the next Section, along with an estimation of the 2D hole doping concentration after chemical treatment). Therefore, with further optimization of this chemical p-doping process (changing the $(NH_4)_2S$(aq) starting concentration, chemical treatment time *etc.*) and proper choice of the S/D contact electrode (*e.g.*, high work function Pd or Pt), p-type ohmic contacts and high-performance WSe_2 PFETs might be fabricated with the simple one-step $(NH_4)_2S$(aq) chemical functionalization technique.

4.5.2.4 Evolution of P-Doping in FL WSe_2 FETs with Chemical Treatment Time

This one-step chemical treatment technique can induce variable p-doping concentrations in WSe_2. It is hypothesized that changing the starting concentration of the $(NH_4)_2S$(aq) solution and/or changing the chemical treatment time should result in variable SH molecular adsorption on the WSe_2 surface resulting in variable p-doping. Since the starting concentration of the $(NH_4)_2S$(aq) solution used in this study was fixed at 20%, the current-voltage characteristics of the FL WSe_2 FET were probed as a function of varying chemical treatment times. As already shown in the output characteristics of Figure 4.14 above, increasing the chemical treatment time leads to a gradual increase in the p-branch currents. Figure 4.15 below shows the transfer characteristics of the FL WSe_2 FET with changing treatment times (5 min and 10 min) which is consistent with variable p-doping.

Increasing the chemical treatment time increases the p-branch ON-currents by ~ 100x. The 2D hole doping concentration (p_{2D}) after chemical treatment can be estimated as $p_{2D} = (C_{OX}|\Delta V_T|)/q$, where q is the electron charge, $C_{OX} = 3.84 \times 10^{-8}$ F/cm^2 is the geometric back-gate oxide capacitance, and $|\Delta V_T|$ is the magnitude of the p-branch threshold voltage shift after chemical treatment (note that in the present case, V_T was estimated using the constant current method wherein the V_{BG} value corresponding to I_{DS} = 10 nA was taken as the V_T). The extracted value of p_{2D} for each 5 min chemical treatment time is ~ 1.5×10^{12} cm^{-2}. As highlighted in the main manuscript, together with strategic choice of the contact metal, this one-step chemical treatment process can be optimized further to achieve both degenerate and non-degenerate p-doping levels in the contact and channel regions, respectively, to achieve high-performance WSe_2 PFETs.

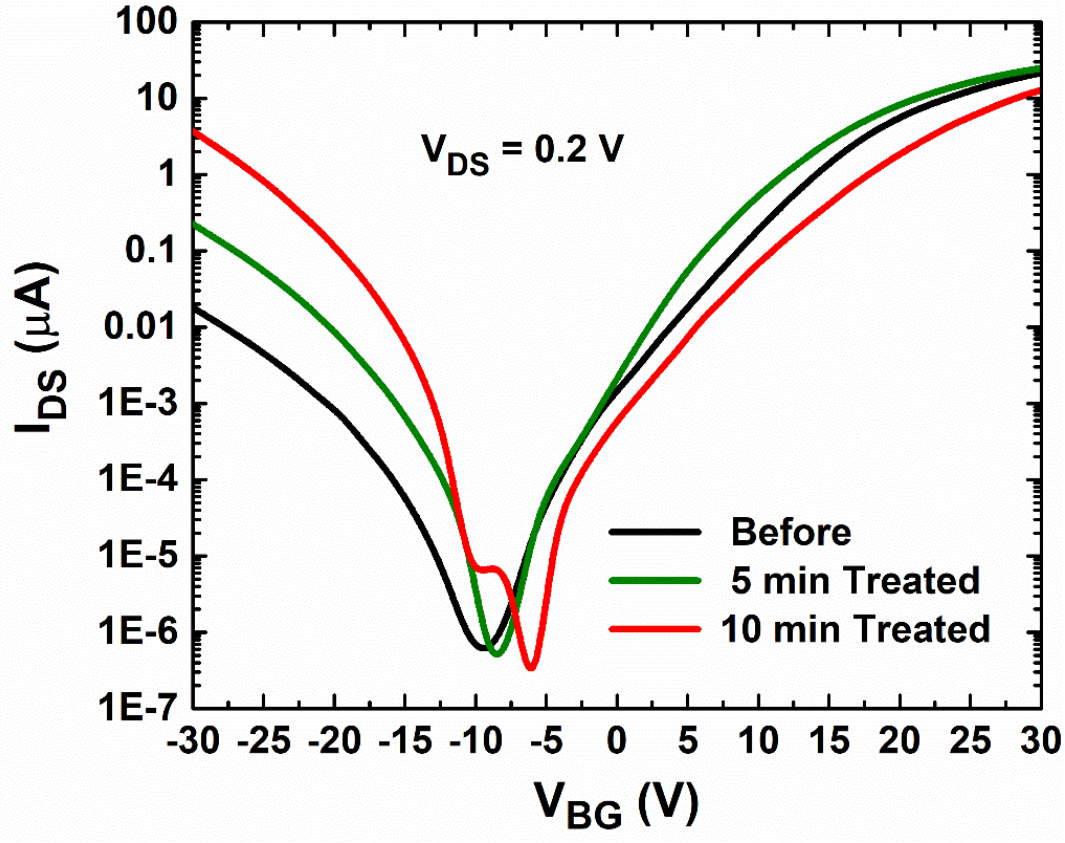

Figure 4.15: Semi-log transfer characteristics of the FL WSe_2 FET showing increasing p-doping levels with increasing chemical treatment time. A consistent increase is observed

in the p-branch ON-current levels of the FL WSe_2 FET after 5 min and 10 min chemical treatment using the 20% $(NH_4)_2S$(aq) solution.

4.5.2.5 Hysteresis in the FL WSe_2 FET After Chemical Treatment

Hysteresis was also observed in the back-gated FL WSe_2 FETs both before and after chemical treatment. Figure 4.16 below compares the semi-log transfer characteristics of the back-gated FL WSe_2 FET, shown earlier in Figure 4.12, before (black curves) and after 15 min chemical treatment (red curves) with the back-gate swept in both directions (the sweep direction is indicated by the corresponding dashed arrows in the figure). Although all the current-voltage measurements were carried out in vacuum (base pressure: 6×10^{-6} mbar) to minimize the hysteretic effects of atmospheric adsorbates, the FETs used in this study were back-gated and un-passivated. The hysteresis shown in the as-fabricated FETs is consistent with defects in the SiO_2 back-gate dielectric. After chemical treatment, there was only a small increase in the hysteresis. Note that there was no deliberate attempt to either minimize the water content from the chemically treated WSe_2 sample surface after dipping in 20% $(NH_4)_2S$(aq) solution or to minimize the impurity content of the $(NH_4)_2S$(aq) solution which had a purity rating of 98%. Both water and other impurities are major sources of hysteresis in 2D TMD-based FETs and could be responsible for the observed increase in the hysteresis in the transfer curves of the FL WSe_2 FET after chemical treatment[304].

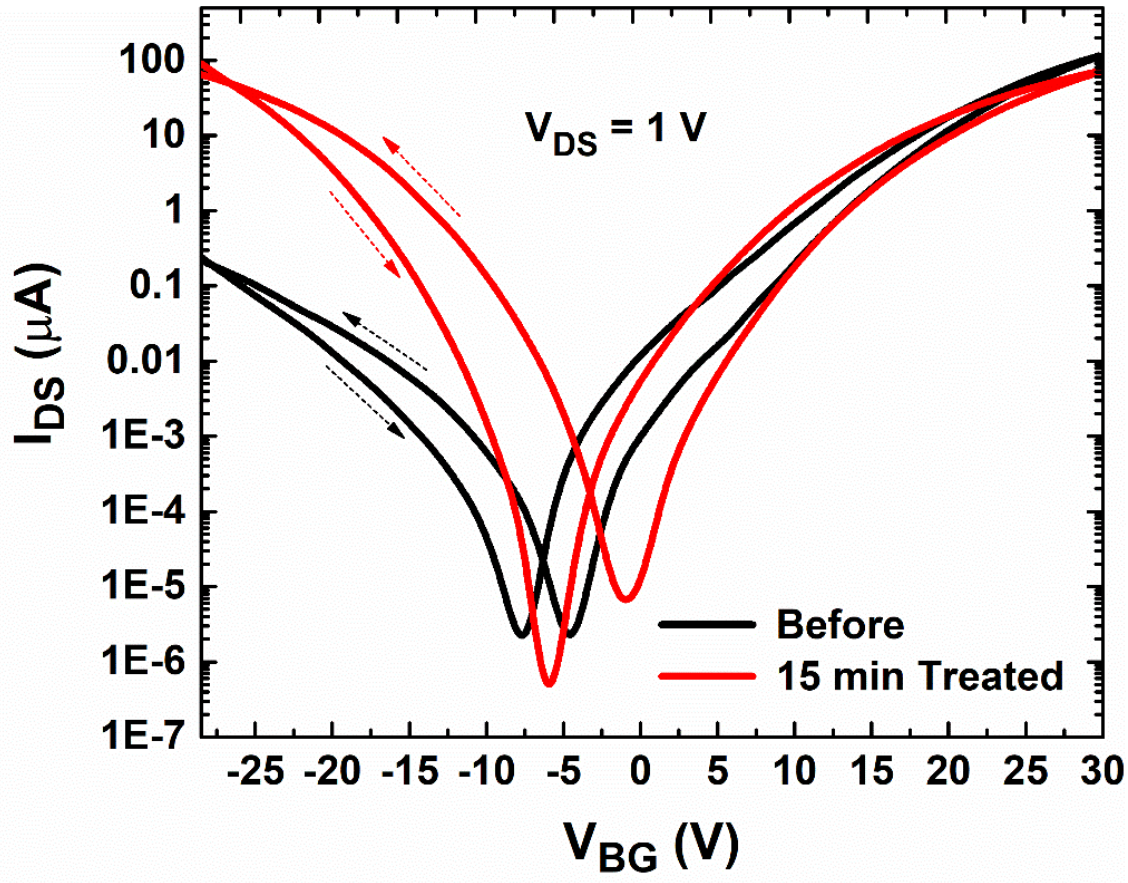

Figure 4.16: Semi-log transfer characteristics of the back-gated FL WSe_2 FET before and after chemical treatment showing both sweeping directions. Hysteresis is observed in the FET before chemical treatment which increases slightly after a 15 min chemical treatment in $(NH_4)_2S$(aq) solution.

4.5.3 Stability and Reversibility of the Chemical Treatment Process

As mentioned earlier, a total of five different back-gated FL WSe_2 FETs displayed similar device characteristics after chemical treatment. The semi-log transfer characteristics of another representative FL WSe_2 FET is shown in Figure 4.17. The V_{BG} sweep direction was from positive to negative in this case. Again, there was significant enhancement in its p-branch I_{ON} of more than two orders of magnitude [~ 300x increase; I_{ON} increases from about 0.01 μA/μm before chemical treatment (black curve) to about 3 μA/μm after chemical treatment (red curve)], consistent with the enhanced p-type behavior

observed in the transfer curve of the back-gated FL WSe_2 FET after chemical treatment as shown in Figure 4.11(c). Moreover, after chemical treatment, the p-branch threshold voltage showed a more prominent shift towards positive back-gate voltages as evidenced by the location of the current minima in the red curve as compared to the black curve. It is known that chemically doping a TMD channel with electrons or holes will shift the threshold voltage towards more negative or more positive voltages, respectively[303]. This is consistent with the present threshold voltage shift towards more positive back-gate voltages for the p-branch of the WSe_2 FETs after chemical treatment because we are doping the WSe_2 channel with holes. Additionally, the blue curve in Figure 4.17 reveals that the effect of the chemical treatment is well retained even after leaving the FL WSe_2 FET sample in a desiccator under low vacuum conditions (~ 745 mbar) for 10 days (the p-branch I_{ON} at V_{BG} = -20 V decreases by only about ~ 2 μA/μm upon remeasuring the FET in vacuum after 10 days, and the p-branch threshold voltage remains similar). It is noted that the ambient stability of this p-doping in WSe_2 due to the adsorbed SH molecules can potentially be further improved when combined with other surface passivation techniques.

Finally, it was observed that a high vacuum annealing step (340°C for 6 h; base pressure: 10^{-6} mbar) after the chemical treatment reversed the p-doping effect and largely restored the transfer curve of the FL WSe_2 FET to its initial state, *i.e.*, similar p-branch ON-current and threshold voltage as before chemical treatment, as shown by the green curve in Figure 4.17. This is consistent with the fact that the high vacuum annealing step can desorb the adsorbed SH species (DFT-calculated binding energy of SH on WSe_2 = 0.48 eV) from the surface of the WSe_2 channel, thus, restoring the original band structure profile along the channel.

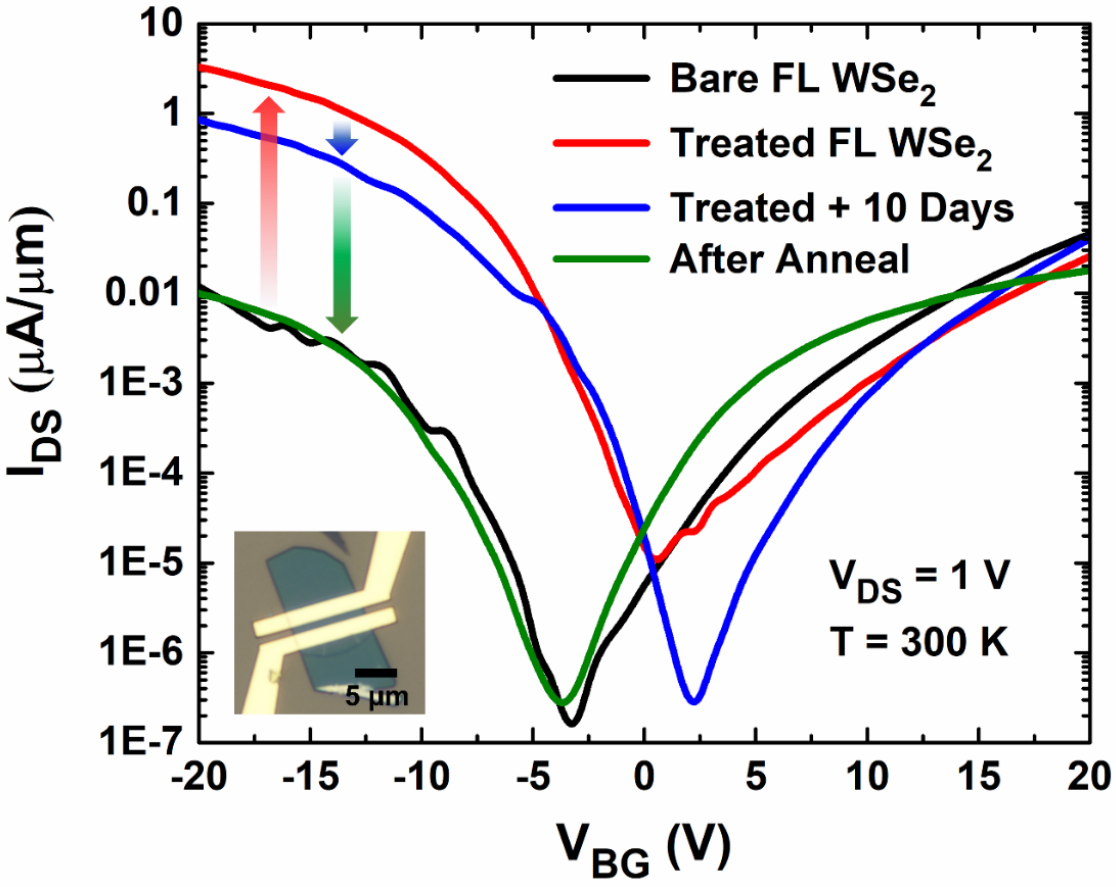

Figure 4.17: Room temperature back-gated transfer characteristics of a FL WSe_2 FET before $(NH_4)_2S$(aq) chemical treatment (black curve), after $(NH_4)_2S$(aq) chemical treatment (red curve), after 10 days of ambient exposure (blue curve), and after a final high vacuum annealing step (green curve). Inset shows the optical image of the measured back-gated FL WSe_2 FET with Ni/Au top contacts. Scale bar is 5 µm.

It is also noted that the pre-treatment of conventional bulk semiconductor surfaces (Ge, SiGe and III-V) using $(NH_4)_2S$(aq) solution has been demonstrated to suppress the interface trap sites or unsaturated chemical bonds at the semiconductor/dielectric interface after deposition of dielectrics *via* atomic layer deposition (ALD)[305-307]. Although SH molecules do not directly bond to WSe_2, it is hypothesized that the adsorption of SH molecules on the surface of WSe_2 provides a van der Waals (vdW) gap which can effectively suppress any damage of the WSe_2 surface during the subsequent deposition of a top dielectric as well as atomic intermixing between the dielectric and WSe_2.

4.5.4 Photoluminescence Study of ML WSe_2 Before/After Chemical Treatment

To elucidate the effect of $(NH_4)_2S$(aq) chemical treatment on the optical transition in ML WSe_2, room temperature photoluminescence (PL) was performed at 300 K using a Renishaw inVia micro-Raman system configured for PL with specialized optics at an excitation wavelength of 532 nm and a grating of 1200 lines/mm to obtain high energy peaks. PL measurements were recorded before and after $(NH_4)_2S$(aq) chemical treatment keeping all measurement parameters identical. As seen in Figure 4.18 below, after $(NH_4)_2S$(aq) chemical treatment, the ML WSe_2 PL intensity significantly decreases. This possibly results from the acceptor-like in-gap states introduced in WSe_2 by the molecular SH adsorption which act as trap sites for the excited excitons, thereby, lowering the efficiency of radiative recombination. It is noted that PL probes the optical band gap of ML WSe_2, whereas the STS measurements and DFT calculations reveal its electronic band gap. Thus, the electronic effects of the chemical treatment on ML WSe_2 are not observed in PL.

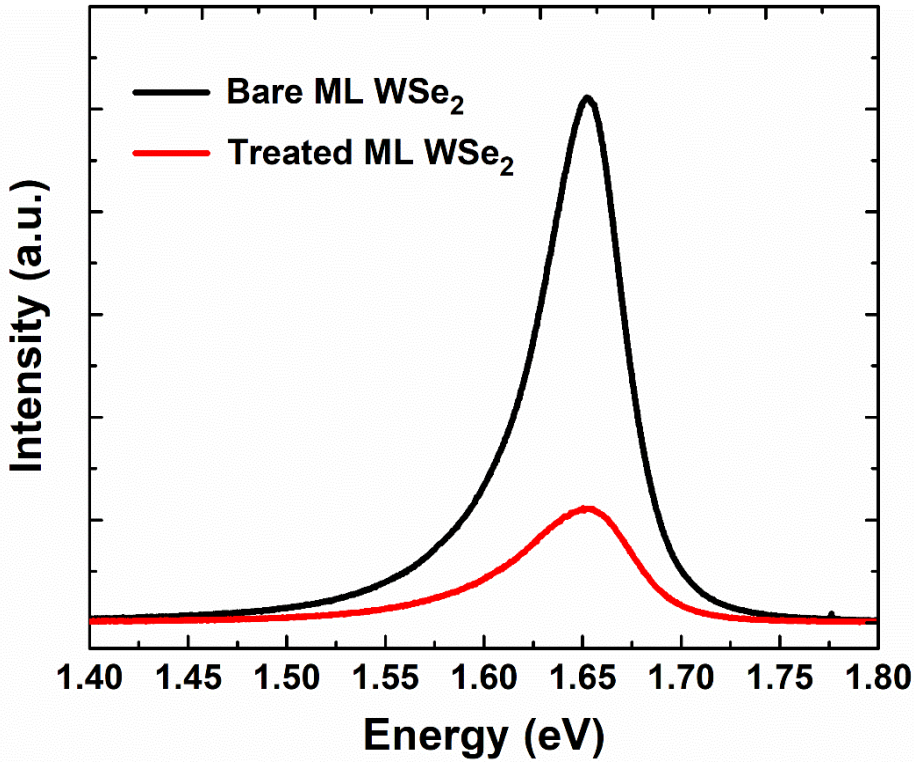

Figure 4.18: Room temperature photoluminescence spectra of ML WSe_2 before and after $(NH_4)_2S$(aq) chemical treatment. The ML PL intensity decreases after chemical treatment.

4.6 CONCLUSION

The band structure engineering of 2D layered WSe_2 *via* the one-step $(NH_4)_2S$(aq) chemical treatment method is demonstrated to enhance its p-type electrical performance. Molecularly resolved STM and STS reveal that chemical treatment-induced defect adsorption on the WSe_2 surface induces this band structure transition; the electronic band gap of ML WSe_2 decreases from 2.1 to 1.1 eV, and the position of the Fermi level is shifted toward the WSe_2 VBE. The underlying mechanism responsible for this WSe_2 band structure modification is elucidated *via* DFT calculations which reveal that the adsorption of chemically generated "SH" molecules on the bare WSe_2 surface is consistent with the formation of additional acceptor-like states in the WSe_2 band gap as well as states right below the WSe_2 VBE, resulting in the overall electronic band gap reduction and shifting of the Fermi level toward the WSe_2 VBE. As a result of this electronic band structure transition in chemically treated WSe_2, an enhancement of the p-branch I_{ON} (up to 2 orders of magnitude) as well as the hole field-effect mobilities (up to 6×) is observed in back-gated ambipolar FL WSe_2 FETs. The facile nature of this one-step $(NH_4)_2S$(aq) chemical functionalization process to tune the band structure of layered WSe_2 at room temperature, without requiring additional vacuum or other complicated processes, can provide a potential pathway to easily integrate the band structure engineering of TMDs into the conventional TMD transistor fabrication process.

Chapter 5: Conclusions and Future Work

5.1 DISSERTATION SUMMARY

Atomically thin semiconducting TMDs, such as MoS_2 and WSe_2, indeed hold great promise for use as a transistor channel material and can be advantageous for a wide variety of electronic and optoelectronic device applications. The material and device performance projections for these 2D TMDs certainly seem to give them an edge over conventional bulk semiconductors in ultra-scaled future technology nodes. Moreover, as ultra-thin, flexible and transparent material, MoS_2 and WSe_2 can change the status quo in flexible nanoelectronics and thin-film transistor technologies. However, the promising advantages of these 2D TMD materials can only be utilized to the fullest once several key performance bottlenecks are mitigated. As discussed in Chapter 1 of this dissertation, the challenges associated with contact resistance, doping and mobility engineering are of paramount importance and these parameters must be carefully engineered to extract the maximum efficiency from MoS_2- and WSe_2-based devices and to make any TMD-based technology commercially viable. This dissertation presents a thorough and in-depth analyses of two very novel engineering solutions to help mitigate the challenges associated with doping, contact resistance and mobility engineering in 2D MoS_2 and WSe_2 devices. Moving forward, the doping techniques discussed here must be further optimized to ensure their robustness for use on both rigid and flexible platforms, as well as to improve their doping selectivity and controllability in order to enable TMD devices with tailored electrical properties. The brief chapter-wise summaries are given below.

Chapter 1 gives an overview of 2D materials in the context of graphene and semiconducting TMDs and discusses the advantages of semiconducting TMDs over graphene, as well as of 2D TMDs over conventional bulk 3D semiconductors. The unique properties that set these 2D semiconducting TMDs apart have been described. Thereafter, a discussion of the projected performance of 2D MoS_2 and WSe_2 has been provided which is followed by a thorough discussion of the major engineering challenges that confront these 2D semiconducting TMDs before they can be successfully implemented in ultra-

scaled, low-power and high-performance transistor technologies for commercial applications. One of the key goals of Chapter 1 is to give the reader a good sense of expectation *versus* current reality when it comes to these 2D semiconducting materials, as well as of the existing non-idealities that can have a detrimental effect on the key performance metrics of devices based on 2D TMDs.

Chapter 2 describes a novel doping technique wherein a solution-processed sub-stoichiometric high-κ dielectric, namely, amorphous titanium suboxide (TiO_x or ATO), has been demonstrated to serve as an effective n-type charge transfer dopant on monolayer (ML) MoS_2. Detailed experimental and theoretical investigations reveal that ATO could be utilized to reduce the Schottky-barrier-induced contact and access resistance, and the impact of charged impurity scattering on mobility in devices based on 2D MoS_2. Utilizing ATO as the "high-κ dopant", low contact resistances, enhanced ON currents, as well as enhanced field-effect and intrinsic electron mobilities were achieved in ATO-encapsulated ML MoS_2 devices. It was revealed that the doping effect of ATO films on ML MoS_2, a phenomenon that is absent when stoichiometric TiO_2 is used, is due to the interfacial-oxygen-vacancies that exist in the high-κ ATO film at the MoS_2-dielectric interface.

In Chapter 3, the study of the interfacial-oxygen-vacancy mediated n-doping of MoS_2 by high-κ dielectrics has been extended to atomic layer deposited hafnium oxide (HfO_x) and aluminum oxide (Al_2O_x). HfO_x and Al_2O_x are widely used in conventional Silicon CMOS technology and, thus, offer an easy pathway for integration with 2D MoS_2 using commercially available tools. Once again, detailed theoretical and experimental investigations reveal that the n-doping of MoS_2 is only effected when oxygen vacancies are present in the high-κ oxide at the MoS_2-dielectric interface. Band structures and atom-projected density-of-states for each MoS_2-dielectric system and with differing oxide terminations were calculated, as well as those for the defect-free MoS_2-dielectric system. It is revealed that electrons are transferred from the high-κ oxide into the MoS_2 layer in a manner analogous to modulation doping. Electrical and spectroscopic characterization of MoS_2 FETs encapsulated by oxygen deficient hafnium and aluminum oxides confirm the n-doping effect.

Chapter 4 describes a novel chemical functionalization technique to enhance the p-type electrical performance of 2D layered WSe_2 FETs using a one-step dipping process in an aqueous solution of ammonium sulfide [$(NH_4)_2S$(aq)]. Molecularly resolved scanning tunneling microscopy and spectroscopy reveal that molecular adsorption on a monolayer WSe_2 surface induces a reduction of the electronic band gap from 2.1 to 1.1 eV and a Fermi level shift toward the WSe_2 valence band edge, consistent with an increase in the density of positive charge carriers. The mechanism of electronic transformation of WSe_2 by $(NH_4)_2S$(aq) chemical treatment is elucidated using density functional theory calculations which reveal that molecular "SH" adsorption on the WSe_2 surface introduces additional in-gap states near the VBE, thereby, inducing a Fermi level shift toward the VBE along with a reduction in the electronic band gap. As a result of this chemical treatment, the p-branch ON-currents of few-layer ambipolar WSe_2 FETs are enhanced by about 2 orders of magnitude, and an increase in the hole field-effect mobility is observed. Detailed electrical characterizations of chemically treated WSe_2 FETs shed further light on the feasibility of this one-step chemical functionalization approach.

5.2 DIRECTIONS FOR FUTURE WORK

Although the research studies presented in this dissertation provide an in-depth analysis and understanding of some novel approaches to engineer the mobility, contact resistance and doping concentrations in devices based on semiconducting TMDs such as MoS_2 and WSe_2, they also open up several avenues for further investigations and optimizations of these novel doping techniques for their successful integration with 2D semiconducting TMDs in order to realize more energy efficient (*i.e.*, low-power) and high-performance transistors. Some promising future research directions are outlined below.

5.2.1 Extending the High-κ Dielectric Doping Technique to Other Semiconducting TMDs

While we have demonstrated the interfacial-oxygen-vacancy mediated n-doping of MoS_2 by high-κ dielectrics leading to an improvement in the MoS_2 device performance, we do not yet know whether the same doping mechanism is applicable to other members

of the semiconducting 2D TMD family. Therefore, a natural extension of our work would be to explore, both experimentally and theoretically, the high-κ dielectric doping of other TMDs such as tungsten disulfide (WS_2) and molybdenum diselenide ($MoSe_2$). Just like MoS_2, other semiconducting TMDs also suffer from the problem of Schottky barrier-induced high n-type contact resistances which degrade their device performance[303]. Moreover, this problem is exacerbated in large band gap TMDs such as WS_2[214]. Therefore, it'll be of great value if we can demonstrate that the deleterious contact resistance issue in other TMDs can also be alleviated using CMOS-compatible high-κ dielectrics deposited using industry-standard techniques like ALD.

5.2.2 Top-Gated Enhancement-Mode MoS_2 Devices using Spatially-Confined and Stoichiometry-Controlled High-κ Dielectrics

While we have demonstrated promising operation, contact resistance reduction and field-effect mobility enhancement in back-gated exfoliated n-type MoS_2 transistors utilizing the sub-stoichiometric high-κ dielectric doping technique, it is to be noted that the high-κ dielectric doping effect was realized all across the MoS_2 device including the channel as well as the source/drain access regions. Consequently, due to the strong high-κ n-doping, this led to depletion-mode MoS_2 transistors (*i.e.*, normally-on transistors) with negative operating gate voltages[238]. However, to realize MoS_2 transistors geared towards ultra-low-power and high-performance operation, it is extremely important to realize top-gated enhancement-mode MoS_2 transistors (*i.e.*, normally-off transistors having positive threshold voltages). This can be achieved by spatially confining the sub-stoichiometric high-κ n-doping effect only in the source/drain contact and access regions of the device to help mitigate the Schottky barrier-induced contact resistance, whereas using a 'stoichiometric' high-κ dielectric in the channel regions under the top-gate to prevent any intentional n-doping and associated negative threshold voltage shifts in the MoS_2 channel. This would enable the realization of MoS_2 transistors with both high current ON/OFF ratios, low contact resistances and high ON-currents. Moreover, optimizing the process flow to attain strict control over the stoichiometry of the as-deposited high-κ dielectrics

(either *via* ALD or spin coating) on MoS_2 would enable on-demand fabrication of MoS_2 transistors having fixed electron doping densities and threshold voltages with reproducible results. In addition to improving the DC performance, this scheme would naturally enable energy-efficient top-gated MoS_2 RF transistors. Figure 5.1 below depicts the cross-section schematic of a top-gated MoS_2 RF device structure (having two MoS_2 FETs in parallel) wherein the sub-stoichiometric high-κ HfO_x layer (*i.e.*, the layer responsible for n-doping) is confined only to the source/drain access regions of the device (as represented by the red shaded regions), whereas the HfO_x directly underneath the top-gate is fully stoichiometric (*i.e.*, x = 2).

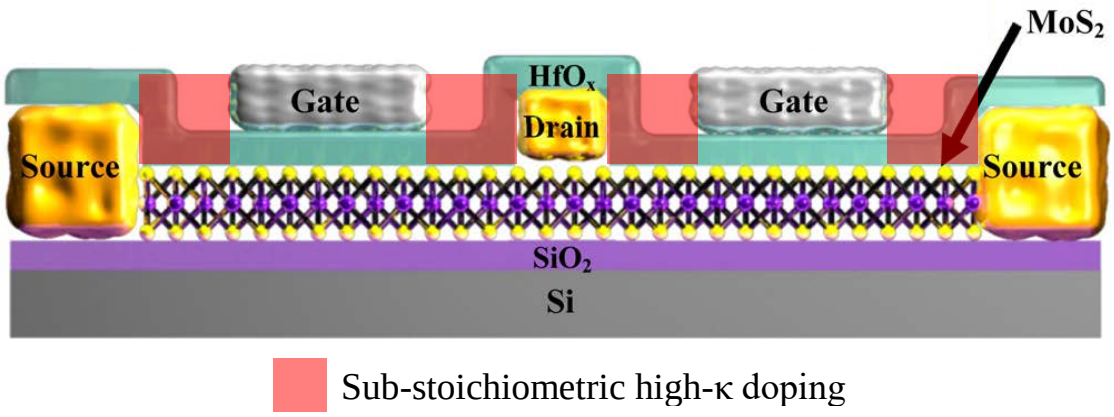

Figure 5.1: Schematic illustration of the top-gated ML MoS_2 RF device structure with the sub-stoichiometric high-κ HfO_x n-doping effect spatially-confined only to the source/drain contact and access regions of the device as represented by the shaded red boxes. Adapted with permission from [79]. Copyright 2015 American Chemical Society.

5.2.3 Further Optimizations of the One-Step $(NH_4)_2S$(aq) Chemical Functionalization Technique for High-Performance WSe_2 Transistors

While we thoroughly analyzed the novel one-step $(NH_4)_2S$(aq) chemical functionalization of WSe_2 and uncovered the underlying mechanism responsible for the enhanced p-type behavior in WSe_2 devices *via* detailed experimental and theoretical studies, this one-step chemical functionalization technique could be further optimized and integrated with other processes to yield WSe_2 transistors having enhanced DC and RF performance. The starting concentration of the commercially purchased $(NH_4)_2S$(aq) solution used in our work was fixed at 20% and it had a purity rating of only 98%. However,

using a $(NH_4)_2S$(aq) solution with enhanced purity and variable starting concentrations could lead to better performing WSe_2 devices and would allow the fabrication of WSe_2 devices with variable p-doping densities in the channel and contact/access regions. Thus, one could potentially achieve extremely low p-type contact resistances in WSe_2 devices by degenerately doping only its contact/access regions using a more concentrated $(NH_4)_2S$(aq) solution, while maintaining non-degenerate and fixed p-doping levels in the WSe_2 channel regions to allow efficient gating and threshold voltage control. Moreover, this one-step chemical functionalization technique could be easily integrated with the bottom-contacted device architecture for WSe_2 using high work-function platinum contacts, an architecture that was recently developed by our group, to yield high room temperature hole mobilities and enhanced p-type charge transport in WSe_2 FETs[277].

Appendix: List of Publications

JOURNAL PUBLICATIONS

1. Zhou, Yongjian, Nikhilesh Maity, **Amritesh Rai**, Rinkle Juneja, Xianghai Meng, Anupam Roy, Jung-Fu Lin, Sanjay K. Banerjee, Abhishek Singh, and Yaguo Wang. "Band Structure Changing and Dielectric Screening Effect from Different Stacking Orders to the Rydberg Excitonic State in Few-Layers and Bulk ReS_2." (**manuscript under review**)
2. [*]Park, Jun Hong, [*]**Amritesh Rai**, Jeongwoon Hwang, Chenxi Zhang, Iljo Kwak, Steven F. Wolf, Suresh Vishwanath *et al.* "Band Structure Engineering of Layered WSe_2 *via* One-Step Chemical Functionalization." *ACS Nano* 13, no. 7 (2019): 7545-7555 ([*]**Equal Contribution**)
3. Tran, Kha, Galan Moody, Fengcheng Wu, Xiaobo Lu, Junho Choi, Kyounghwan Kim, **Amritesh Rai** *et al.* "Evidence for Moiré Excitons in van der Waals Heterostructures." *Nature* 567, no. 7746 (2019): 71.
4. Wu, Di, Wei Li, **Amritesh Rai**, Xiaoyu Wu, Hema C. P. Movva, Maruthi N. Yogeesh, Zhaodong Chu, Sanjay K. Banerjee, Deji Akinwande, and Keji Lai. "Visualization of Local Conductance in MoS_2/WSe_2 Heterostructure Transistors." *Nano Letters* 19, no. 3 (2019): 1976-1981.
5. **Rai, Amritesh**, Hema C. P. Movva, Anupam Roy, Deepyanti Taneja, Sayema Chowdhury, and Sanjay K. Banerjee. "Progress in Contact, Doping and Mobility Engineering of MoS_2: An Atomically Thin 2D Semiconductor." *Crystals* 8, no. 8 (2018): 316. (**Invited Feature Review Article**)
6. Chen, Ke, Anupam Roy, **Amritesh Rai**, Hema C. P. Movva, Xianghai Meng, Feng He, Sanjay K. Banerjee, and Yaguo Wang. "Accelerated Carrier Recombination by Grain Boundary/Edge Defects in MBE Grown Transition Metal Dichalcogenides." *APL Materials* 6, no. 5 (2018): 056103.
7. Chen, Ke, Anupam Roy, **Amritesh Rai**, Amithraj Valsaraj, Xianghai Meng, Feng He, Xiaochuan Xu, Leonard F. Register, Sanjay K. Banerjee, and Yaguo Wang. "Carrier Trapping by Oxygen Impurities in Molybdenum Diselenide." *ACS Applied Materials & Interfaces* 10, no. 1 (2017): 1125-1131.
8. Kim, Joon-Seok, Rafia Ahmad, Tribhuwan Pandey, **Amritesh Rai**, Simin Feng, Jing Yang, Zhong Lin *et al.* "Towards Band Structure and Band Offset Engineering of Monolayer $Mo_{(1-x)}W_{(x)}S_2$ *via* Strain." *2D Materials* 5, no. 1 (2017): 015008.
9. Pramanik, Tanmoy, Anupam Roy, Rik Dey, **Amritesh Rai**, Samaresh Guchhait, Hema C. P. Movva, Cheng-Chih Hsieh, and Sanjay K. Banerjee. "Angular Dependence of Magnetization Reversal in Epitaxial Chromium Telluride Thin

Films with Perpendicular Magnetic Anisotropy." *Journal of Magnetism and Magnetic Materials* 437 (2017): 72-77.

10. Hsu, William, **Amritesh Rai**, Xiaoru Wang, Yun Wang, Taegon Kim, and Sanjay K. Banerjee. "Impact of Junction Depth and Abruptness on the Activation and the Leakage Current in Germanium n^+/p Junctions." *arXiv preprint arXiv:1705.06733* (2017).

11. Roy, Anupam, Rudresh Ghosh, **Amritesh Rai**, Atresh Sanne, Kyounghwan Kim, Hema C. P. Movva, Rik Dey *et al.* "Intra-Domain Periodic Defects in Monolayer MoS_2." *Applied Physics Letters* 110, no. 20 (2017): 201905.

12. Larentis, Stefano, Babak Fallahazad, Hema C. P. Movva, Kyounghwan Kim, **Amritesh Rai**, Takashi Taniguchi, Kenji Watanabe, Sanjay K. Banerjee, and Emanuel Tutuc. "Reconfigurable Complementary Monolayer $MoTe_2$ Field-Effect Transistors for Integrated Circuits." *ACS Nano* 11, no. 5 (2017): 4832-4839.

13. Dey, Rik, Anupam Roy, Tanmoy Pramanik, **Amritesh Rai**, Seung Heon Shin, Sarmita Majumder, Leonard F. Register, and Sanjay K. Banerjee. "Detection of Current Induced Spin Polarization in Epitaxial Bi_2Te_3 Thin Film." *Applied Physics Letters* 110, no. 12 (2017): 122403.

14. Lim, Hyungseob, Jae Young Kim, Edward J. Evans, **Amritesh Rai**, Jun-Hyuk Kim, Bryan R. Wygant, and C. Buddie Mullins. "Activation of a Nickel-Based Oxygen Evolution Reaction Catalyst on a Hematite Photoanode *via* Incorporation of Cerium for Photoelectrochemical Water Oxidation." *ACS Applied Materials & Interfaces* 9, no. 36 (2017): 30654-30661.

15. Dey, Rik, Anupam Roy, Tanmoy Pramanik, Samaresh Guchhait, Sushant Sonde, **Amritesh Rai**, Leonard F. Register, and Sanjay K. Banerjee. "Localization and Interaction Effects of Epitaxial Bi_2Se_3 Bulk States in Two-Dimensional Limit." *Journal of Applied Physics* 120, no. 16 (2016): 164301.

16. Hsu, William, Taegon Kim, Harry Chou, **Amritesh Rai**, and Sanjay K. Banerjee. "Novel BF+ Implantation for High Performance Ge pMOSFETs." *IEEE Electron Device Letters*37, no. 8 (2016): 954-957.

17. Kang, Sangwoo, Nitin Prasad, Hema C. P. Movva, **Amritesh Rai**, Kyounghwan Kim, Xuehao Mou, Takashi Taniguchi *et al.* "Effects of Electrode Layer Band Structure on the Performance of Multilayer Graphene–hBN–Graphene Interlayer Tunnel Field Effect Transistors." *Nano Letters* 16, no. 8 (2016): 4975-4981.

18. Hsu, William, Taegon Kim, Alfredo Benítez-Lara, Harry Chou, Andrei Dolocan, **Amritesh Rai**, M. Josefina Arellano-Jiménez, Marylene Palard, Miguel José-Yacamán, and Sanjay K. Banerjee. "Diffusion and Recrystallization of B Implanted in Crystalline and Pre-Amorphized Ge in the Presence of F." *Journal of Applied Physics* 120, no. 1 (2016): 015701.

19. Kang, Sangwoo, Hema C. P. Movva, Atresh Sanne, **Amritesh Rai**, and Sanjay K. Banerjee. "Influence of Electron-Beam Lithography Exposure Current Level on the Transport Characteristics of Graphene Field Effect Transistors." *Journal of Applied Physics* 119, no. 12 (2016): 124502.

20. Roy, Anupam, Hema C. P. Movva, Biswarup Satpati, Kyounghwan Kim, Rik Dey, **Amritesh Rai**, Tanmoy Pramanik, Samaresh Guchhait, Emanuel Tutuc, and Sanjay K. Banerjee. "Structural and Electrical Properties of $MoTe_2$ and $MoSe_2$ Grown by Molecular Beam Epitaxy." *ACS Applied Materials & Interfaces* 8, no. 11 (2016): 7396-7402.

21. Chang, Hsiao-Yu, Maruthi N. Yogeesh, Rudresh Ghosh, **Amritesh Rai**, Atresh Sanne, Shixuan Yang, Nanshu Lu, Sanjay K. Banerjee, and Deji Akinwande. "Large-Area Monolayer MoS_2 for Flexible Low-Power RF Nanoelectronics in the GHz Regime." *Advanced Materials* 28, no. 9 (2016): 1818-1823.

22. Valsaraj, Amithraj, Jiwon Chang, **Amritesh Rai**, Leonard F. Register, and Sanjay K. Banerjee. "Theoretical and Experimental Investigation of Vacancy-Based Doping of Monolayer MoS_2 on Oxide." *2D Materials* 2, no. 4 (2015): 045009.

23. Movva, Hema C. P., **Amritesh Rai**, Sangwoo Kang, Kyounghwan Kim, Babak Fallahazad, Takashi Taniguchi, Kenji Watanabe, Emanuel Tutuc, and Sanjay K. Banerjee. "High-Mobility Holes in Dual-Gated WSe_2 Field-Effect Transistors." *ACS Nano* 9, no. 10 (2015): 10402-10410.

24. Sanne, Atresh, Rudresh Ghosh, **Amritesh Rai**, Maruthi N. Yogeesh, Seung Heon Shin, Ankit Sharma, Karalee Jarvis *et al.* "Radio Frequency Transistors and Circuits Based on CVD MoS_2." *Nano Letters* 15, no. 8 (2015): 5039-5045.

25. **Rai, Amritesh**, Amithraj Valsaraj, Hema C. P. Movva, Anupam Roy, Rudresh Ghosh, Sushant Sonde, Sangwoo Kang *et al.* "Air Stable Doping and Intrinsic Mobility Enhancement in Monolayer Molybdenum Disulfide by Amorphous Titanium Suboxide Encapsulation." *Nano Letters* 15, no. 7 (2015): 4329-4336.

26. Hsieh, Cheng-Chih, Anupam Roy, **Amritesh Rai**, Yao-Feng Chang, and Sanjay K. Banerjee. "Characteristics and Mechanism Study of Cerium Oxide Based Random Access Memories." *Applied Physics Letters* 106, no. 17 (2015): 173108.

27. Roy, Anupam, Samaresh Guchhait, Rik Dey, Tanmoy Pramanik, Cheng-Chih Hsieh, **Amritesh Rai**, and Sanjay K. Banerjee. "Perpendicular Magnetic Anisotropy and Spin Glass-Like Behavior in Molecular Beam Epitaxy Grown Chromium Telluride Thin Films." *ACS Nano* 9, no. 4 (2015): 3772-3779.

28. Sanne, Atresh, Rudresh Ghosh, **Amritesh Rai**, Hema C. P. Movva, Ankit Sharma, Rajesh Rao, Leo Mathew, and Sanjay K. Banerjee. "Top-Gated Chemical Vapor Deposited MoS_2 Field-Effect Transistors on Si_3N_4 Substrates." *Applied Physics Letters* 106, no. 6 (2015): 062101.

29. Corbet, Chris M., Connor McClellan, **Amritesh Rai**, Sushant S. Sonde, Emanuel Tutuc, and Sanjay K. Banerjee. "Field Effect Transistors with Current Saturation and Voltage Gain in Ultrathin ReS_2." *ACS Nano* 9, no. 1 (2014): 363-370.

30. Dey, Rik, Tanmoy Pramanik, Anupam Roy, **Amritesh Rai**, Samaresh Guchhait, Sushant Sonde, Hema C. P. Movva, Luigi Colombo, Leonard F. Register, and Sanjay K. Banerjee. "Strong Spin-Orbit Coupling and Zeeman Spin Splitting in Angle Dependent Magnetoresistance of Bi_2Te_3." *Applied Physics Letters* 104, no. 22 (2014): 223111.

31. Ramón, Michael E., Hema C. P. Movva, Sk. Fahad Chowdhury, Kristen N. Parrish, **Amritesh Rai**, Carl W. Magnuson, Rodney S. Ruoff, Deji Akinwande, and Sanjay K. Banerjee. "Impact of Contact and Access Resistances in Graphene Field-Effect Transistors on Quartz Substrates for Radio Frequency Applications." *Applied Physics Letters* 104, no. 7 (2014): 073115.

32. Roy, Anupam, Samaresh Guchhait, Sushant Sonde, Rik Dey, Tanmoy Pramanik, **Amritesh Rai**, Hema C. P. Movva, Luigi Colombo, and Sanjay K. Banerjee. "Two-Dimensional Weak Anti-Localization in Bi_2Te_3 Thin Film Grown on Si (111)-(7× 7) Surface by Molecular Beam Epitaxy." *Applied Physics Letters*102, no. 16 (2013): 163118.

CONFERENCE PROCEEDINGS

1. Guo, Wei, Agham Posadas, Alexander Demkov, Anupam Roy, **Amritesh Rai**, Omar Mohammed, Sanjay K. Banerjee, Kevin Olsson, and Xiaoqin Elaine Li. "Two Dimensional $SrTiO_3$ Membranes." In *APS Meeting Abstracts*. 2019.

2. Tran, Kha, Galan Moody, Fengcheng Wu, Xiaobo Lu, Junho Choi, Jiamin Quan, Akshay Singh, Jacob Embley, Andre Zepeda, Marshall Campbell, Kyounghwan Kim, **Amritesh Rai** *et al.* "Evidence of Moiré Excitons in van der Waals (vdW) Heterostructure." In *APS Meeting Abstracts*. 2019.

3. **Rai, Amritesh**, Jun Hong Park, Chenxi Zhang, Iljo Kwak, Steven Wolf, Suresh Vishwanath, Xinyu Lin *et al.* "Enhanced P-Type Behavior in 2D WSe_2 *via* Chemical Defect Engineering." In *2018 76th Device Research Conference (DRC)*, pp. 1-2. IEEE, 2018.

4. Wu, Di, Wei Li, Maruthi Yogeesh, **Amritesh Rai**, Sanjay K. Banerjee, Deji Akinwande, and Keji Lai. "Nano-Imaging of Electrical Properties of $MoSe_2$/WSe_2 Vertical Heterostructures." In *APS Meeting Abstracts*. 2017.

5. **Rai, Amritesh**, Hema C. P. Movva, Sangwoo Kang, Stefano Larentis, Anupam Roy, Emanuel Tutuc, and Sanjay K. Banerjee. "Dual-Gated $MoTe_2$/MoS_2 van der Waals Heterojunction P–N Diode." In *APS Meeting Abstracts*. 2017.

6. Movva, Hema C. P., Sangwoo Kang, **Amritesh Rai**, Kyounghwan Kim, Babak Fallahazad, Takashi Taniguchi, Kenji Watanabe, Emanuel Tutuc, and Sanjay K.

Banerjee. "Room Temperature Gate-Tunable Negative Differential Resistance in MoS_2/hBN/WSe_2 Heterostructures." In *2016 74th Annual Device Research Conference (DRC)*, pp. 1-2. IEEE, 2016.

7. Yogeesh, Maruthi, Hsiao-Yu Chang, Wei Li, Somayyeh Rahimi, **Amritesh Rai**, Atresh Sanne, Rudresh Ghosh, Sanjay K. Banerjee, and Deji Akinwande. "Towards Wafer Scale Monolayer MoS_2 Based Flexible Low-Power RF Electronics for IoT Systems." In *2016 74th Annual Device Research Conference (DRC)*, pp. 1-2. IEEE, 2016.
8. Hsu, William, Taegon Kim, Harry Chou, **Amritesh Rai**, M. J. Arellano-Jiménez, M. José-Yacamán, Marylene Palard, and Sanjay K. Banerjee. "Enhancing the Performance of Ge pFETs using Novel BF+ Implantation." In *2016 74th Annual Device Research Conference (DRC)*, pp. 1-2. IEEE, 2016.
9. Kang, Sangwoo, Nitin Prasad, Hema C. P. Movva, **Amritesh Rai**, Kyounghwan Kim, Takashi Taniguchi, Kenji Watanabe, Leonard F. Register, Emanuel Tutuc, and Sanjay K. Banerjee. "Insights into Interlayer Tunnel FET Performance Improvement: Lessons Learned from Graphene Hexagonal Boron Nitride Heterostructures." In *2016 74th Annual Device Research Conference (DRC)*, pp. 1-2. IEEE, 2016.
10. **Rai, Amritesh**, Laxman Thoutam, Wei Zhang, Kiran Kovi, Sanjay K. Banerjee, and Saptarshi Das. "Effects of High-Energy X-Ray Radiation on MoS_2 FETs." In *APS Meeting Abstracts*. 2016.
11. **Rai, Amritesh**, Amithraj Valsaraj, Hema C. P. Movva, Anupam Roy, Emanuel Tutuc, Leonard F. Register, and Sanjay K. Banerjee. "Interfacial-Oxygen-Vacancy Mediated Doping of MoS_2 by High-κ Dielectrics." In *2015 73rd Annual Device Research Conference (DRC)*, pp. 189-190. IEEE, 2015.
12. Movva, Hema C. P., **Amritesh Rai**, Sangwoo Kang, Kyounghwan Kim, Samaresh Guchhait, Takashi Taniguchi, Kenji Watanabe, Emanuel Tutuc, and Sanjay K. Banerjee. "Top-Gated WSe_2 Field-Effect Transistors with Pt Contacts." In *2015 73rd Annual Device Research Conference (DRC)*, pp. 131-132. IEEE, 2015.
13. Sanne, Atresh, Maruthi Yogeesh, Rudresh Ghosh, **Amritesh Rai**, Seung H. Shin, Ankit Sharma, Leo Mathew, Rajesh Rao, Deji Akinwande, and Sanjay K. Banerjee. "Radio Frequency Transistors and Circuit Applications Based on CVD MoS_2." In *2015 73rd Annual Device Research Conference (DRC)*, pp. 215-216. IEEE, 2015.
14. Hsieh, Cheng-Chih, Anupam Roy, Yao-Feng Chang, **Amritesh Rai**, and Sanjay K. Banerjee. "Cerium Oxide Based Bipolar Resistive Switching Memory with Low Operation Voltage and High Resistance Ratio." In *2015 73rd Annual Device Research Conference (DRC)*, pp. 101-102. IEEE, 2015.

15. **Rai, Amritesh**, Rudresh Ghosh, Anupam Roy, Amithraj Valsaraj, Hema C. P. Movva, Sangwoo Kang, Emanuel Tutuc, Leonard F. Register, and Sanjay K. Banerjee. "Air Stable Doping of MoS_2 FETs Using TiO_x Sol-Gel." *Bulletin of the American Physical Society* 60 (2015).

16. McClellan, Connor, Chris Corbet, **Amritesh Rai**, Hema C. P. Movva, Emanuel Tutuc, and Sanjay K. Banerjee. "Rhenium Disulfide Depletion-Load Inverter." In *APS March Meeting Abstracts*. 2015.

17. Corbet, Chris, Connor McClellan, **Amritesh Rai**, Sushant Sonde, Emanuel Tutuc, and Sanjay K. Banerjee. "Semiconducting Behavior, Schottky Barriers and Field Effect Transistors in Ultrathin Rhenium Disulfide." In *APS March Meeting Abstracts*. 2015.

18. Dey, Rik, Anupam Roy, Tanmoy Pramanik, Samaresh Guchhait, Sushant Sonde, **Amritesh Rai**, Sarmita Majumder, Bahniman Ghosh, Leonard F. Register, and Sanjay K. Banerjee. "Low Temperature Magnetoresistance Studies in MBE Grown Topological Insulator Thin Films." In *APS March Meeting Abstracts*. 2015.

19. Movva, Hema C. P., Sangwoo Kang, **Amritesh Rai**, and Sanjay K. Banerjee. "Ambipolar Conduction in MoS_2/WSe_2 Hetero-Bilayers." In *APS March Meeting Abstracts*. 2015.

20. Roy, Anupam, Samaresh Guchhait, Rik Dey, Tanmoy Pramanik, Cheng-Chih Hsieh, **Amritesh Rai**, and Sanjay K. Banerjee. "Magnetic and Magneto-Transport Studies of MBE Grown Cr_2Te_3 Thin Films with Perpendicular Magnetic Anisotropy." In *APS March Meeting Abstracts*. 2015.

References

(1) Novoselov, K. S.; Geim, A. K.; Morozov, S. V.; Jiang, D.; Zhang, Y.; Dubonos, S. V.; Grigorieva, I. V.; Firsov, A. A. Electric Field Effect in Atomically Thin Carbon Films. *Science* **2004**, *306* (5696), 666–669. https://doi.org/10.1126/science.1102896.

(2) Moore, G. E. No Exponential Is Forever: But "Forever" Can Be Delayed! [Semiconductor Industry]. In *2003 IEEE International Solid-State Circuits Conference, 2003. Digest of Technical Papers. ISSCC.*; 2003; pp 20–23 vol.1. https://doi.org/10.1109/ISSCC.2003.1234194.

(3) Schaller, R. R. Moore's Law: Past, Present and Future. *IEEE Spectr.* **1997**, *34* (6), 52–59. https://doi.org/10.1109/6.591665.

(4) Moore, G. E. Cramming More Components onto Integrated Circuits, Reprinted from Electronics, Volume 38, Number 8, April 19, 1965, Pp.114 Ff. *IEEE Solid-State Circuits Soc. Newsl.* **2006**, *11* (3), 33–35. https://doi.org/10.1109/N-SSC.2006.4785860.

(5) MISTRY, K. A 45 nm Logic Technology with High-κ/Metal Gate Transistors, Strained Silicon, 9 Cu Interconnect Layers. 193 nm Dry Patterning, and 100% Pb-Free Packaging. *IEDM Tech. Dig. 2007* **2007**, 247–250.

(6) Davari, B.; Dennard, R. H.; Shahidi, G. G. CMOS Scaling for High Performance and Low Power - The Next Ten Years. *Proc. IEEE* **1995**, *83* (4), 595–606. https://doi.org/10.1109/5.371968.

(7) Cartwright, J. Intel Enters the Third Dimension. *Nat. News* **2011**. https://doi.org/10.1038/news.2011.274.

(8) Auth, C.; Allen, C.; Blattner, A.; Bergstrom, D.; Brazier, M.; Bost, M.; Buehler, M.; Chikarmane, V.; Ghani, T.; Glassman, T.; *et al.* A 22 nm High Performance and Low-Power CMOS Technology Featuring Fully-Depleted Tri-Gate Transistors, Self-Aligned Contacts and High Density MIM Capacitors. In *2012 Symposium on VLSI Technology (VLSIT)*; 2012; pp 131–132. https://doi.org/10.1109/VLSIT.2012.6242496.

(9) Thompson, S. E.; Parthasarathy, S. Moore's Law: The Future of Si Microelectronics. *Mater. Today* **2006**, *9* (6), 20–25. https://doi.org/10.1016/S1369-7021(06)71539-5.

(10) Alamo, J. A. del. Nanometre-Scale Electronics with III–V Compound Semiconductors. *Nature* **2011**, *479* (7373), 317. https://doi.org/10.1038/nature10677.

(11) Waldrop, M. M. The Chips Are Down for Moore's Law. *Nat. News* **2016**, *530* (7589), 144. https://doi.org/10.1038/530144a.

(12) Thompson, S. MOS Scaling: Transistor Challenges for the 21st Century. *Intel Technol. J.* **1998**.

(13) Haron, N. Z.; Hamdioui, S. Why Is CMOS Scaling Coming to an END? In *2008 3rd International Design and Test Workshop*; 2008; pp 98–103. https://doi.org/10.1109/IDT.2008.4802475.

(14) Frank, D. J. Power-Constrained CMOS Scaling Limits. *IBM J. Res. Dev.* **2002**, *46* (2.3), 235–244. https://doi.org/10.1147/rd.462.0235.

(15) Kim, Y.-B. Challenges for Nanoscale MOSFETs and Emerging Nanoelectronics. *Trans. Electr. Electron. Mater.* **2010**, *11* (3), 93–105. https://doi.org/10.4313/TEEM.2010.11.3.093.

(16) Horowitz, M.; Alon, E.; Patil, D.; Naffziger, S.; Kumar, R.; Bernstein, K. Scaling, Power, and the Future of CMOS. In *IEEE International Electron Devices Meeting, 2005. IEDM Technical Digest.*; 2005; pp 7 pp. – 15. https://doi.org/10.1109/IEDM.2005.1609253.

(17) Kuhn, K. J. Considerations for Ultimate CMOS Scaling. *IEEE Trans. Electron Devices* **2012**, *59* (7), 1813–1828. https://doi.org/10.1109/TED.2012.2193129.

(18) Skotnicki, T.; Hutchby, J. A.; King, T.-J.; Wong, H. S. P.; Boeuf, F. The End of CMOS Scaling: Toward the Introduction of New Materials and Structural Changes to Improve MOSFET Performance. *IEEE Circuits Devices Mag.* **2005**, *21* (1), 16–26. https://doi.org/10.1109/MCD.2005.1388765.

(19) Cavin, R. K.; Lugli, P.; Zhirnov, V. V. Science and Engineering Beyond Moore's Law. *Proc. IEEE* **2012**, *100* (Special Centennial Issue), 1720–1749. https://doi.org/10.1109/JPROC.2012.2190155.

(20) Kuhn, K. J.; Avci, U.; Cappellani, A.; Giles, M. D.; Haverty, M.; Kim, S.; Kotlyar, R.; Manipatruni, S.; Nikonov, D.; Pawashe, C.; *et al.* The Ultimate CMOS Device and Beyond. In *2012 International Electron Devices Meeting*; 2012; pp 8.1.1-8.1.4. https://doi.org/10.1109/IEDM.2012.6479001.

(21) Geim, A. K. Graphene: Status and Prospects. *Science* **2009**, *324* (5934), 1530–1534. https://doi.org/10.1126/science.1158877.

(22) Zhu, Y.; Murali, S.; Cai, W.; Li, X.; Suk, J. W.; Potts, J. R.; Ruoff, R. S. Graphene and Graphene Oxide: Synthesis, Properties, and Applications. *Adv. Mater.* **2010**, *22* (35), 3906–3924. https://doi.org/10.1002/adma.201001068.

(23) Novoselov, K. S.; Fal′ko, V. I.; Colombo, L.; Gellert, P. R.; Schwab, M. G.; Kim, K. A Roadmap for Graphene. *Nature* **2012**, *490* (7419), 192. https://doi.org/10.1038/nature11458.

(24) Schwierz, F. Graphene Transistors. *Nat. Nanotechnol.* **2010**, *5* (7), 487. https://doi.org/10.1038/nnano.2010.89.

(25) Schwierz, F. Graphene Transistors: Status, Prospects, and Problems. *Proc. IEEE* **2013**, *101* (7), 1567–1584. https://doi.org/10.1109/JPROC.2013.2257633.

(26) Mas-Ballesté, R.; Gómez-Navarro, C.; Gómez-Herrero, J.; Zamora, F. 2D Materials: To Graphene and Beyond. *Nanoscale* **2011**, *3* (1), 20–30. https://doi.org/10.1039/C0NR00323A.

(27) Xu, M.; Liang, T.; Shi, M.; Chen, H. Graphene-Like Two-Dimensional Materials. *Chem. Rev.* **2013**, *113* (5), 3766–3798. https://doi.org/10.1021/cr300263a.

(28) Gibney, E. The Super Materials That Could Trump Graphene. *Nat. News* **2015**, *522* (7556), 274. https://doi.org/10.1038/522274a.

(29) Chhowalla, M.; Shin, H. S.; Eda, G.; Li, L.-J.; Loh, K. P.; Zhang, H. The Chemistry of Two-Dimensional Layered Transition Metal Dichalcogenide Nanosheets. *Nat. Chem.* **2013**, *5* (4), 263. https://doi.org/10.1038/nchem.1589.

(30) Wang, Q. H.; Kalantar-Zadeh, K.; Kis, A.; Coleman, J. N.; Strano, M. S. Electronics and Optoelectronics of Two-Dimensional Transition Metal Dichalcogenides. *Nat. Nanotechnol.* **2012**, *7* (11), 699–712. https://doi.org/10.1038/nnano.2012.193.

(31) Das, S.; Robinson, J. A.; Dubey, M.; Terrones, H.; Terrones, M. Beyond Graphene: Progress in Novel Two-Dimensional Materials and van der Waals Solids. *Annu. Rev. Mater. Res.* **2015**, *45* (1), null. https://doi.org/10.1146/annurev-matsci-070214-021034.

(32) Gong, C.; Zhang, H.; Wang, W.; Colombo, L.; Wallace, R. M.; Cho, K. Band Alignment of Two-Dimensional Transition Metal Dichalcogenides: Application in Tunnel Field Effect Transistors. *Appl. Phys. Lett.* **2013**, *103* (5), 053513. https://doi.org/10.1063/1.4817409.

(33) McDonnell, S. J.; Wallace, R. M. Atomically-Thin Layered Films for Device Applications Based upon 2D TMDC Materials. *Thin Solid Films* **2016**, *616*, 482–501. https://doi.org/10.1016/j.tsf.2016.08.068.

(34) Kang, J.; Cao, W.; Xie, X.; Sarkar, D.; Liu, W.; Banerjee, K. Graphene and Beyond-Graphene 2D Crystals for Next-Generation Green Electronics; International Society for Optics and Photonics, 2014; Vol. 9083, p 908305. https://doi.org/10.1117/12.2051198.

(35) Chhowalla, M.; Jena, D.; Zhang, H. Two-Dimensional Semiconductors for Transistors. *Nat. Rev. Mater.* **2016**, *1* (11), 16052. https://doi.org/10.1038/natrevmats.2016.52.

(36) Fiori, G.; Bonaccorso, F.; Iannaccone, G.; Palacios, T.; Neumaier, D.; Seabaugh, A.; Banerjee, S. K.; Colombo, L. Electronics Based on Two-Dimensional Materials. *Nat. Nanotechnol.* **2014**, *9* (10), 768–779. https://doi.org/10.1038/nnano.2014.207.

(37) Jariwala, D.; Sangwan, V. K.; Lauhon, L. J.; Marks, T. J.; Hersam, M. C. Emerging Device Applications for Semiconducting Two-Dimensional Transition Metal Dichalcogenides. *ACS Nano* **2014**, *8* (2), 1102–1120. https://doi.org/10.1021/nn500064s.

(38) Bhimanapati, G. R.; Lin, Z.; Meunier, V.; Jung, Y.; Cha, J.; Das, S.; Xiao, D.; Son, Y.; Strano, M. S.; Cooper, V. R.; *et al.* Recent Advances in Two-Dimensional Materials beyond Graphene. *ACS Nano* **2015**, *9* (12), 11509–11539. https://doi.org/10.1021/acsnano.5b05556.

(39) Schwierz, F.; Pezoldt, J.; Granzner, R. Two-Dimensional Materials and Their Prospects in Transistor Electronics. *Nanoscale* **2015**, *7* (18), 8261–8283. https://doi.org/10.1039/C5NR01052G.

(40) Radisavljevic, B.; Radenovic, A.; Brivio, J.; Giacometti, V.; Kis, A. Single-Layer MoS_2 Transistors. *Nat. Nanotechnol.* **2011**, *6* (3), 147–150. https://doi.org/10.1038/nnano.2010.279.

(41) Splendiani, A.; Sun, L.; Zhang, Y.; Li, T.; Kim, J.; Chim, C.-Y.; Galli, G.; Wang, F. Emerging Photoluminescence in Monolayer MoS_2. *Nano Lett.* **2010**, *10* (4), 1271–1275. https://doi.org/10.1021/nl903868w.

(42) Ellis, J. K.; Lucero, M. J.; Scuseria, G. E. The Indirect to Direct Band Gap Transition in Multilayered MoS_2 as Predicted by Screened Hybrid Density Functional Theory. *Appl. Phys. Lett.* **2011**, *99* (26), 261908. https://doi.org/10.1063/1.3672219.

(43) Cheiwchanchamnangij, T.; Lambrecht, W. R. L. Quasiparticle Band Structure Calculation of Monolayer, Bilayer, and Bulk MoS_2. *Phys. Rev. B* **2012**, *85* (20), 205302. https://doi.org/10.1103/PhysRevB.85.205302.

(44) Kuc, A.; Zibouche, N.; Heine, T. Influence of Quantum Confinement on the Electronic Structure of the Transition Metal Sulfide TS_2. *Phys. Rev. B* **2011**, *83* (24), 245213. https://doi.org/10.1103/PhysRevB.83.245213.

(45) Yu, L.; Zubair, A.; Santos, E. J. G.; Zhang, X.; Lin, Y.; Zhang, Y.; Palacios, T. High-Performance WSe_2 Complementary Metal Oxide Semiconductor Technology and Integrated Circuits. *Nano Lett.* **2015**, *15* (8), 4928–4934. https://doi.org/10.1021/acs.nanolett.5b00668.

(46) Zhao, W.; Ghorannevis, Z.; Chu, L.; Toh, M.; Kloc, C.; Tan, P.-H.; Eda, G. Evolution of Electronic Structure in Atomically Thin Sheets of WS_2 and WSe_2. *ACS Nano* **2013**, *7* (1), 791–797. https://doi.org/10.1021/nn305275h.

(47) Schwierz, F. Nanoelectronics: Flat Transistors Get off the Ground. *Nat. Nanotechnol.* **2011**, *6* (3), 135. https://doi.org/10.1038/nnano.2011.26.

(48) Lembke, D.; Bertolazzi, S.; Kis, A. Single-Layer MoS_2 Electronics. *Acc. Chem. Res.* **2015**, *48* (1), 100–110. https://doi.org/10.1021/ar500274q.

(49) Ganatra, R.; Zhang, Q. Few-Layer MoS_2: A Promising Layered Semiconductor. *ACS Nano* **2014**, *8* (5), 4074–4099. https://doi.org/10.1021/nn405938z.

(50) Venkata Subbaiah, Y. P.; Saji, K. J.; Tiwari, A. Atomically Thin MoS_2: A Versatile Nongraphene 2D Material. *Adv. Funct. Mater.* **2016**, *26* (13), 2046–2069. https://doi.org/10.1002/adfm.201504202.

(51) Wang, F.; Wang, Z.; Jiang, C.; Yin, L.; Cheng, R.; Zhan, X.; Xu, K.; Wang, F.; Zhang, Y.; He, J. Progress on Electronic and Optoelectronic Devices of 2D Layered Semiconducting Materials. *Small* **2017**, *13* (35), p.1604298. https://doi.org/10.1002/smll.201604298.

(52) Tan, C.; Cao, X.; Wu, X.-J.; He, Q.; Yang, J.; Zhang, X.; Chen, J.; Zhao, W.; Han, S.; Nam, G.-H.; *et al.* Recent Advances in Ultrathin Two-Dimensional Nanomaterials. *Chem. Rev.* **2017**, *117* (9), 6225–6331. https://doi.org/10.1021/acs.chemrev.6b00558.

(53) Cao, W.; Kang, J.; Liu, W.; Khatami, Y.; Sarkar, D.; Banerjee, K. 2D Electronics: Graphene and Beyond. In *2013 Proceedings of the European Solid-State Device Research Conference (ESSDERC)*; 2013; pp 37–44. https://doi.org/10.1109/ESSDERC.2013.6818814.

(54) Liu, Y.; Weiss, N. O.; Duan, X.; Cheng, H.-C.; Huang, Y.; Duan, X. Van der Waals Heterostructures and Devices. *Nat. Rev. Mater.* **2016**, *1* (9), 16042. https://doi.org/10.1038/natrevmats.2016.42.

(55) Novoselov, K. S.; Neto, A. H. C. Two-Dimensional Crystals-Based Heterostructures: Materials with Tailored Properties. *Phys. Scr.* **2012**, *2012* (T146), 014006. https://doi.org/10.1088/0031-8949/2012/T146/014006.

(56) Geim, A. K.; Grigorieva, I. V. Van der Waals Heterostructures. *Nature* **2013**, *499* (7459), 419. https://doi.org/10.1038/nature12385.

(57) Lotsch, B. V. Vertical 2D Heterostructures. *Annu. Rev. Mater. Res.* **2015**, *45* (1), 85–109. https://doi.org/10.1146/annurev-matsci-070214-020934.

(58) Zhang, W.; Wang, Q.; Chen, Y.; Wang, Z.; Wee, A. T. S. Van der Waals Stacked 2D Layered Materials for Optoelectronics. *2D Mater.* **2016**, *3* (2), 022001. https://doi.org/10.1088/2053-1583/3/2/022001.

(59) Novoselov, K. S.; Mishchenko, A.; Carvalho, A.; Neto, A. H. C. 2D Materials and van der Waals Heterostructures. *Science* **2016**, *353* (6298), aac9439. https://doi.org/10.1126/science.aac9439.

(60) Hamann, D. M.; Hadland, E. C.; Johnson, D. C. Heterostructures Containing Dichalcogenides-New Materials with Predictable Nanoarchitectures and Novel Emergent Properties. *Semicond. Sci. Technol.* **2017**, *32* (9), 093004. https://doi.org/10.1088/1361-6641/aa7785.

(61) Jariwala, D.; Marks, T. J.; Hersam, M. C. Mixed-Dimensional van der Waals Heterostructures. *Nat. Mater.* **2017**, *16* (2), 170. https://doi.org/10.1038/nmat4703.

(62) Liu, H.; Neal, A. T.; Ye, P. D. Channel Length Scaling of MoS_2 MOSFETs. *ACS Nano* **2012**, *6* (10), 8563–8569. https://doi.org/10.1021/nn303513c.

(63) Liu, Y.; Guo, J.; Wu, Y.; Zhu, E.; Weiss, N. O.; He, Q.; Wu, H.; Cheng, H.-C.; Xu, Y.; Shakir, I.; *et al.* Pushing the Performance Limit of Sub-100 nm Molybdenum Disulfide Transistors. *Nano Lett.* **2016**, *16* (10), 6337–6342. https://doi.org/10.1021/acs.nanolett.6b02713.

(64) Nourbakhsh, A.; Zubair, A.; Sajjad, R. N.; Tavakkoli K. G., A.; Chen, W.; Fang, S.; Ling, X.; Kong, J.; Dresselhaus, M. S.; Kaxiras, E.; *et al.* MoS_2 Field-Effect Transistor with Sub-10 nm Channel Length. *Nano Lett.* **2016**, *16* (12), 7798–7806. https://doi.org/10.1021/acs.nanolett.6b03999.

(65) Desai, S. B.; Madhvapathy, S. R.; Sachid, A. B.; Llinas, J. P.; Wang, Q.; Ahn, G. H.; Pitner, G.; Kim, M. J.; Bokor, J.; Hu, C.; *et al.* MoS_2 Transistors with 1-Nanometer Gate Lengths. *Science* **2016**, *354* (6308), 99–102. https://doi.org/10.1126/science.aah4698.

(66) Radisavljevic, B.; Whitwick, M. B.; Kis, A. Integrated Circuits and Logic Operations Based on Single-Layer MoS_2. *ACS Nano* **2011**, *5* (12), 9934–9938. https://doi.org/10.1021/nn203715c.

(67) Wang, H.; Yu, L.; Lee, Y.-H.; Shi, Y.; Hsu, A.; Chin, M. L.; Li, L.-J.; Dubey, M.; Kong, J.; Palacios, T. Integrated Circuits Based on Bilayer MoS_2 Transistors. *Nano Lett.* **2012**, *12* (9), 4674–4680. https://doi.org/10.1021/nl302015v.

(68) Sachid, A. B.; Tosun, M.; Desai, S. B.; Hsu, C.-Y.; Lien, D.-H.; Madhvapathy, S. R.; Chen, Y.-Z.; Hettick, M.; Kang, J. S.; Zeng, Y.; *et al.* Monolithic 3D CMOS Using Layered Semiconductors. *Adv. Mater.* **2016**, *28* (13), 2547–2554. https://doi.org/10.1002/adma.201505113.

(69) Das, S.; Dubey, M.; Roelofs, A. High Gain, Low Noise, Fully Complementary Logic Inverter Based on Bi-Layer WSe_2 Field Effect Transistors. *Appl. Phys. Lett.* **2014**, *105* (8), 083511. https://doi.org/10.1063/1.4894426.

(70) Tosun, M.; Chuang, S.; Fang, H.; Sachid, A. B.; Hettick, M.; Lin, Y.; Zeng, Y.; Javey, A. High-Gain Inverters Based on WSe_2 Complementary Field-Effect Transistors. *ACS Nano* **2014**, *8* (5), 4948–4953. https://doi.org/10.1021/nn5009929.

(71) Shokouh, S. H. H.; Pezeshki, A.; Raza, S. R. A.; Lee, H. S.; Min, S.-W.; Jeon, P. J.; Shin, J. M.; Im, S. High-Gain Subnanowatt Power Consumption Hybrid Complementary Logic Inverter with WSe_2 Nanosheet and ZnO Nanowire Transistors on Glass. *Adv. Mater.* **2015**, *27* (1), 150–156. https://doi.org/10.1002/adma.201403992.

(72) Bertolazzi, S.; Krasnozhon, D.; Kis, A. Nonvolatile Memory Cells Based on MoS_2/Graphene Heterostructures. *ACS Nano* **2013**, *7* (4), 3246–3252. https://doi.org/10.1021/nn3059136.

(73) Kshirsagar, C. U.; Xu, W.; Su, Y.; Robbins, M. C.; Kim, C. H.; Koester, S. J. Dynamic Memory Cells Using MoS_2 Field-Effect Transistors Demonstrating Femtoampere Leakage Currents. *ACS Nano* **2016**, *10* (9), 8457–8464. https://doi.org/10.1021/acsnano.6b03440.

(74) Zhang, E.; Wang, W.; Zhang, C.; Jin, Y.; Zhu, G.; Sun, Q.; Zhang, D. W.; Zhou, P.; Xiu, F. Tunable Charge-Trap Memory Based on Few-Layer MoS_2. *ACS Nano* **2015**, *9* (1), 612–619. https://doi.org/10.1021/nn5059419.

(75) Chen, M.; Wang, Y.; Shepherd, N.; Huard, C.; Zhou, J.; Guo, L. J.; Lu, W.; Liang, X. Abnormal Multiple Charge Memory States in Exfoliated Few-Layer WSe_2 Transistors. *ACS Nano* **2017**, *11* (1), 1091–1102. https://doi.org/10.1021/acsnano.6b08156.

(76) Hou, X.; Zhang, H.; Liu, C.; Ding, S.; Bao, W.; Zhang, D. W.; Zhou, P. Charge-Trap Memory Based on Hybrid 0D Quantum Dot–2D WSe_2 Structure. *Small* **2018**, *14* (20), 1800319. https://doi.org/10.1002/smll.201800319.

(77) Liu, C.; Yan, X.; Wang, J.; Ding, S.; Zhou, P.; Zhang, D. W. Eliminating Overerase Behavior by Designing Energy Band in High-Speed Charge-Trap Memory Based on WSe_2. *Small* **2017**, *13* (17), 1604128. https://doi.org/10.1002/smll.201604128.

(78) Radisavljevic, B.; Whitwick, M. B.; Kis, A. Small-Signal Amplifier Based on Single-Layer MoS_2. *Appl. Phys. Lett.* **2012**, *101* (4), 043103. https://doi.org/10.1063/1.4738986.

(79) Sanne, A.; Ghosh, R.; Rai, A.; Yogeesh, M. N.; Shin, S. H.; Sharma, A.; Jarvis, K.; Mathew, L.; Rao, R.; Akinwande, D.; *et al.* Radio Frequency Transistors and Circuits Based on CVD MoS_2. *Nano Lett.* **2015**, *15* (8), 5039–5045. https://doi.org/10.1021/acs.nanolett.5b01080.

(80) Chang, H.-Y.; Yogeesh, M. N.; Ghosh, R.; Rai, A.; Sanne, A.; Yang, S.; Lu, N.; Banerjee, S. K.; Akinwande, D. Large-Area Monolayer MoS_2 for Flexible Low-Power RF Nanoelectronics in the GHz Regime. *Adv. Mater.* **2016**, *28* (9), 1818–1823. https://doi.org/10.1002/adma.201504309.

(81) Sanne, A.; Park, S.; Ghosh, R.; Yogeesh, M. N.; Liu, C.; Mathew, L.; Rao, R.; Akinwande, D.; Banerjee, S. K. Embedded Gate CVD MoS_2 Microwave FETs. *Npj 2D Mater. Appl.* **2017**, *1* (1), 26. https://doi.org/10.1038/s41699-017-0029-z.

(82) Choi, M. S.; Qu, D.; Lee, D.; Liu, X.; Watanabe, K.; Taniguchi, T.; Yoo, W. J. Lateral MoS_2 P–N Junction Formed by Chemical Doping for Use in High-Performance Optoelectronics. *ACS Nano* **2014**, *8* (9), 9332–9340. https://doi.org/10.1021/nn503284n.

(83) Deng, Y.; Luo, Z.; Conrad, N. J.; Liu, H.; Gong, Y.; Najmaei, S.; Ajayan, P. M.; Lou, J.; Xu, X.; Ye, P. D. Black Phosphorus–Monolayer MoS_2 van der Waals Heterojunction P–N Diode. *ACS Nano* **2014**, *8* (8), 8292–8299. https://doi.org/10.1021/nn5027388.

(84) Ii, E. W. L.; Lee, C. H.; Paul, P. K.; Ma, L.; McCulloch, W. D.; Krishnamoorthy, S.; Wu, Y.; Arehart, A. R.; Rajan, S. Layer-Transferred MoS_2/GaN PN Diodes. *Appl. Phys. Lett.* **2015**, *107* (10), 103505. https://doi.org/10.1063/1.4930234.

(85) Chuang, S.; Kapadia, R.; Fang, H.; Chia Chang, T.; Yen, W.-C.; Chueh, Y.-L.; Javey, A. Near-Ideal Electrical Properties of InAs/WSe_2 van der Waals Heterojunction Diodes. *Appl. Phys. Lett.* **2013**, *102* (24), 242101. https://doi.org/10.1063/1.4809815.

(86) Chen, J.-W.; Lo, S.-T.; Ho, S.-C.; Wong, S.-S.; Vu, T.-H.-Y.; Zhang, X.-Q.; Liu, Y.-D.; Chiou, Y.-Y.; Chen, Y.-X.; Yang, J.-C.; *et al.* A Gate-Free Monolayer WSe_2 PN Diode. *Nat. Commun.* **2018**, *9* (1), 3143. https://doi.org/10.1038/s41467-018-05326-x.

(87) Lopez-Sanchez, O.; Lembke, D.; Kayci, M.; Radenovic, A.; Kis, A. Ultrasensitive Photodetectors Based on Monolayer MoS_2. *Nat. Nanotechnol.* **2013**, *8* (7), 497–501. https://doi.org/10.1038/nnano.2013.100.

(88) Kufer, D.; Konstantatos, G. Highly Sensitive, Encapsulated MoS_2 Photodetector with Gate Controllable Gain and Speed. *Nano Lett.* **2015**, *15* (11), 7307–7313. https://doi.org/10.1021/acs.nanolett.5b02559.

(89) Zheng, Z.; Zhang, T.; Yao, J.; Zhang, Y.; Xu, J.; Yang, G. Flexible, Transparent and Ultra-Broadband Photodetector Based on Large-Area WSe_2 film for Wearable Devices. *Nanotechnology* **2016**, *27* (22), 225501. https://doi.org/10.1088/0957-4484/27/22/225501.

(90) Nguyen, D. A.; Oh, H. M.; Duong, N. T.; Bang, S.; Yoon, S. J.; Jeong, M. S. Highly Enhanced Photoresponsivity of a Monolayer WSe_2 Photodetector with Nitrogen-Doped Graphene Quantum Dots. *ACS Appl. Mater. Interfaces* **2018**, *10* (12), 10322–10329. https://doi.org/10.1021/acsami.7b18419.

(91) Sundaram, R. S.; Engel, M.; Lombardo, A.; Krupke, R.; Ferrari, A. C.; Avouris, Ph.; Steiner, M. Electroluminescence in Single Layer MoS_2. *Nano Lett.* **2013**, *13* (4), 1416–1421. https://doi.org/10.1021/nl400516a.

(92) Lopez-Sanchez, O.; Alarcon Llado, E.; Koman, V.; Fontcuberta i Morral, A.; Radenovic, A.; Kis, A. Light Generation and Harvesting in a van der Waals Heterostructure. *ACS Nano* **2014**, *8* (3), 3042–3048. https://doi.org/10.1021/nn500480u.

(93) Cheng, R.; Li, D.; Zhou, H.; Wang, C.; Yin, A.; Jiang, S.; Liu, Y.; Chen, Y.; Huang, Y.; Duan, X. Electroluminescence and Photocurrent Generation from

Atomically Sharp WSe_2/MoS_2 Heterojunction P–N Diodes. *Nano Lett.* **2014**, *14* (10), 5590–5597. https://doi.org/10.1021/nl502075n.

(94) Ross, J. S.; Klement, P.; Jones, A. M.; Ghimire, N. J.; Yan, J.; Mandrus, D. G.; Taniguchi, T.; Watanabe, K.; Kitamura, K.; Yao, W.; *et al.* Electrically Tunable Excitonic Light-Emitting Diodes Based on Monolayer WSe_2 P–N Junctions. *Nat. Nanotechnol.* **2014**, *9* (4), 268–272. https://doi.org/10.1038/nnano.2014.26.

(95) Baugher, B. W. H.; Churchill, H. O. H.; Yang, Y.; Jarillo-Herrero, P. Optoelectronic Devices Based on Electrically Tunable P–N Diodes in a Monolayer Dichalcogenide. *Nat. Nanotechnol.* **2014**, *9* (4), 262–267. https://doi.org/10.1038/nnano.2014.25.

(96) Salehzadeh, O.; Djavid, M.; Tran, N. H.; Shih, I.; Mi, Z. Optically Pumped Two-Dimensional MoS_2 Lasers Operating at Room-Temperature. *Nano Lett.* **2015**, *15* (8), 5302–5306. https://doi.org/10.1021/acs.nanolett.5b01665.

(97) Woodward, R. I.; Howe, R. C. T.; Hu, G.; Torrisi, F.; Zhang, M.; Hasan, T.; Kelleher, E. J. R. Few-Layer MoS_2 Saturable Absorbers for Short-Pulse Laser Technology: Current Status and Future Perspectives [Invited]. *Photonics Res.* **2015**, *3* (2), A30–A42. https://doi.org/10.1364/PRJ.3.000A30.

(98) Liu, W.; Liu, M.; Yin, J.; Chen, H.; Lu, W.; Fang, S.; Teng, H.; Lei, M.; Yan, P.; Wei, Z. Tungsten Diselenide for All-Fiber Lasers with the Chemical Vapor Deposition Method. *Nanoscale* **2018**, *10* (17), 7971–7977. https://doi.org/10.1039/C8NR00471D.

(99) Liu, W.; Liu, M.; OuYang, Y.; Hou, H.; Ma, G.; Lei, M.; Wei, Z. Tungsten Diselenide for Mode-Locked Erbium-Doped Fiber Lasers with Short Pulse Duration. *Nanotechnology* **2018**, *29* (17), 174002. https://doi.org/10.1088/1361-6528/aaae40.

(100) Fontana, M.; Deppe, T.; Boyd, A. K.; Rinzan, M.; Liu, A. Y.; Paranjape, M.; Barbara, P. Electron-Hole Transport and Photovoltaic Effect in Gated MoS_2 Schottky Junctions. *Sci. Rep.* **2013**, *3*. https://doi.org/10.1038/srep01634.

(101) Tsai, M.-L.; Su, S.-H.; Chang, J.-K.; Tsai, D.-S.; Chen, C.-H.; Wu, C.-I.; Li, L.-J.; Chen, L.-J.; He, J.-H. Monolayer MoS_2 Heterojunction Solar Cells. *ACS Nano* **2014**, *8* (8), 8317–8322. https://doi.org/10.1021/nn502776h.

(102) Rehman, A. ur; Khan, M. F.; Shehzad, M. A.; Hussain, S.; Bhopal, M. F.; Lee, S. H.; Eom, J.; Seo, Y.; Jung, J.; Lee, S. H. N-MoS_2/p-Si Solar Cells with Al_2O_3 Passivation for Enhanced Photogeneration. *ACS Appl. Mater. Interfaces* **2016**, *8* (43), 29383–29390. https://doi.org/10.1021/acsami.6b07064.

(103) Pospischil, A.; Furchi, M. M.; Mueller, T. Solar-Energy Conversion and Light Emission in an Atomic Monolayer P–N Diode. *Nat. Nanotechnol.* **2014**, *9* (4), 257–261. https://doi.org/10.1038/nnano.2014.14.

(104) Perkins, F. K.; Friedman, A. L.; Cobas, E.; Campbell, P. M.; Jernigan, G. G.; Jonker, B. T. Chemical Vapor Sensing with Monolayer MoS_2. *Nano Lett.* **2013**, *13* (2), 668–673. https://doi.org/10.1021/nl3043079.

(105) Cho, B.; Hahm, M. G.; Choi, M.; Yoon, J.; Kim, A. R.; Lee, Y.-J.; Park, S.-G.; Kwon, J.-D.; Kim, C. S.; Song, M.; *et al.* Charge-Transfer-Based Gas Sensing Using Atomic-Layer MoS_2. *Sci. Rep.* **2015**, *5*, 8052. https://doi.org/10.1038/srep08052.

(106) Park, M.; Park, Y. J.; Chen, X.; Park, Y.-K.; Kim, M.-S.; Ahn, J.-H. MoS_2-Based Tactile Sensor for Electronic Skin Applications. *Adv. Mater.* **2016**, *28* (13), 2556–2562. https://doi.org/10.1002/adma.201505124.

(107) Nam, H.; Oh, B.-R.; Chen, M.; Wi, S.; Li, D.; Kurabayashi, K.; Liang, X. Fabrication and Comparison of MoS_2 and WSe_2 Field-Effect Transistor Biosensors. *J. Vac. Sci. Technol. B* **2015**, *33* (6), 06FG01. https://doi.org/10.1116/1.4930040.

(108) Hosseini, M.; Elahi, M.; Pourfath, M.; Esseni, D. Very Large Strain Gauges Based on Single Layer $MoSe_2$ and WSe_2 for Sensing Applications. *Appl. Phys. Lett.* **2015**, *107* (25), 253503. https://doi.org/10.1063/1.4937438.

(109) Roy, T.; Tosun, M.; Cao, X.; Fang, H.; Lien, D.-H.; Zhao, P.; Chen, Y.-Z.; Chueh, Y.-L.; Guo, J.; Javey, A. Dual-Gated MoS_2/WSe_2 van der Waals Tunnel Diodes and Transistors. *ACS Nano* **2015**, *9* (2), 2071–2079. https://doi.org/10.1021/nn507278b.

(110) Krishnamoorthy, S.; Lee, E. W.; Lee, C. H.; Zhang, Y.; McCulloch, W. D.; Johnson, J. M.; Hwang, J.; Wu, Y.; Rajan, S. High Current Density 2D/3D MoS_2/GaN Esaki Tunnel Diodes. *Appl. Phys. Lett.* **2016**, *109* (18), 183505. https://doi.org/10.1063/1.4966283.

(111) Movva, H. C. P.; Kang, S.; Rai, A.; Kim, K.; Fallahazad, B.; Taniguchi, T.; Watanabe, K.; Tutuc, E.; Banerjee, S. K. Room Temperature Gate-Tunable Negative Differential Resistance in MoS_2/hBN/WSe_2 Heterostructures. In *2016 74th Device Research Conference (DRC)*; IEEE, 2016; pp 1–2. https://doi.org/10.1109/DRC.2016.7548486.

(112) Balaji, Y.; Smets, Q.; Rosa, C. J. L. de la; Lu, A. K. A.; Chiappe, D.; Agarwal, T.; Lin, D.; Huyghebaert, C.; Radu, I.; Mocuta, D.; *et al.* Tunneling Transistors Based on $MoS_2/MoTe_2$ van der Waals Heterostructures. In *2017 47th European Solid-State Device Research Conference (ESSDERC)*; 2017; pp 106–109. https://doi.org/10.1109/ESSDERC.2017.8066603.

(113) Nourbakhsh, A.; Zubair, A.; Dresselhaus, M. S.; Palacios, T. Transport Properties of a MoS_2/WSe_2 Heterojunction Transistor and Its Potential for Application. *Nano Lett.* **2016**, *16* (2), 1359–1366. https://doi.org/10.1021/acs.nanolett.5b04791.

(114) Roy, T.; Tosun, M.; Hettick, M.; Ahn, G. H.; Hu, C.; Javey, A. 2D-2D Tunneling Field-Effect Transistors Using $WSe_2/SnSe_2$ Heterostructures. *Appl. Phys. Lett.* **2016**, *108* (8), 083111. https://doi.org/10.1063/1.4942647.

(115) Zhu, H.; Wang, Y.; Xiao, J.; Liu, M.; Xiong, S.; Wong, Z. J.; Ye, Z.; Ye, Y.; Yin, X.; Zhang, X. Observation of Piezoelectricity in Free-Standing Monolayer MoS_2. *Nat. Nanotechnol.* **2015**, *10* (2), 151. https://doi.org/10.1038/nnano.2014.309.

(116) Wu, W.; Wang, L.; Li, Y.; Zhang, F.; Lin, L.; Niu, S.; Chenet, D.; Zhang, X.; Hao, Y.; Heinz, T. F.; *et al.* Piezoelectricity of Single-Atomic-Layer MoS_2 for Energy Conversion and Piezotronics. *Nature* **2014**, *514* (7523), 470. https://doi.org/10.1038/nature13792.

(117) Lee, J.-H.; Park, J. Y.; Cho, E. B.; Kim, T. Y.; Han, S. A.; Kim, T.-H.; Liu, Y.; Kim, S. K.; Roh, C. J.; Yoon, H.-J.; *et al.* Reliable Piezoelectricity in Bilayer WSe_2 for Piezoelectric Nanogenerators. *Adv. Mater.* **2017**, *29* (29), 1606667. https://doi.org/10.1002/adma.201606667.

(118) Lin, P.; Zhu, L.; Li, D.; Xu, L.; Pan, C.; Wang, Z. Piezo-Phototronic Effect for Enhanced Flexible MoS_2/WSe_2 van der Waals Photodiodes. *Adv. Funct. Mater.* **2018**, *28* (35), 1802849. https://doi.org/10.1002/adfm.201802849.

(119) Liu, H. F.; Wong, S. L.; Chi, D. Z. CVD Growth of MoS_2-Based Two-Dimensional Materials. *Chem. Vap. Depos.* **2015**, *21* (10-11–12), 241–259. https://doi.org/10.1002/cvde.201500060.

(120) Walsh, L. A.; Hinkle, C. L. Van der Waals Epitaxy: 2D Materials and Topological Insulators. *Appl. Mater. Today* **2017**, *9*, 504–515. https://doi.org/10.1016/j.apmt.2017.09.010.

(121) Wong, S. L.; Liu, H.; Chi, D. Recent Progress in Chemical Vapor Deposition Growth of Two-Dimensional Transition Metal Dichalcogenides. *Prog. Cryst. Growth Charact. Mater.* **2016**, *62* (3), 9–28. https://doi.org/10.1016/j.pcrysgrow.2016.06.002.

(122) Manzeli, S.; Ovchinnikov, D.; Pasquier, D.; Yazyev, O. V.; Kis, A. 2D Transition Metal Dichalcogenides. *Nat. Rev. Mater.* **2017**, *2* (8), natrevmats201733. https://doi.org/10.1038/natrevmats.2017.33.

(123) Eichfeld, S. M.; Hossain, L.; Lin, Y.-C.; Piasecki, A. F.; Kupp, B.; Birdwell, A. G.; Burke, R. A.; Lu, N.; Peng, X.; Li, J.; *et al.* Highly Scalable, Atomically Thin WSe_2 Grown *via* Metal–Organic Chemical Vapor Deposition. *ACS Nano* **2015**, *9* (2), 2080–2087. https://doi.org/10.1021/nn5073286.

(124) Zhang, X.; Choudhury, T. H.; Chubarov, M.; Xiang, Y.; Jariwala, B.; Zhang, F.; Alem, N.; Wang, G.-C.; Robinson, J. A.; Redwing, J. M. Diffusion-Controlled Epitaxy of Large Area Coalesced WSe_2 Monolayers on Sapphire. *Nano Lett.* **2018**, *18* (2), 1049–1056. https://doi.org/10.1021/acs.nanolett.7b04521.

(125) Landauer, R. Spatial Variation of Currents and Fields Due to Localized Scatterers in Metallic Conduction. *IBM J. Res. Dev.* **1957**, *1* (3), 223–231. https://doi.org/10.1147/rd.13.0223.

(126) Sharvin, Yu. V. A Possible Method for Studying Fermi Surfaces. *Sov. J. Exp. Theor. Phys.* **1965**, *21*, 655.

(127) Allain, A.; Kang, J.; Banerjee, K.; Kis, A. Electrical Contacts to Two-Dimensional Semiconductors. *Nat. Mater.* **2015**, *14* (12), 1195–1205. https://doi.org/10.1038/nmat4452.

(128) Jena, D.; Banerjee, K.; Xing, G. H. 2D Crystal Semiconductors: Intimate Contacts. *Nat. Mater.* **2014**, *13* (12), 1076. https://doi.org/10.1038/nmat4121.

(129) ITRS 2.0 Home Page http://www.itrs2.net/ (accessed June 18, 2019).

(130) Kaasbjerg, K.; Thygesen, K. S.; Jacobsen, K. W. Phonon-Limited Mobility in N-Type Single-Layer MoS_2 from First Principles. *Phys. Rev. B* **2012**, *85* (11), 115317. https://doi.org/10.1103/PhysRevB.85.115317.

(131) Li, X.; Mullen, J. T.; Jin, Z.; Borysenko, K. M.; Buongiorno Nardelli, M.; Kim, K. W. Intrinsic Electrical Transport Properties of Monolayer Silicene and MoS_2 from First Principles. *Phys. Rev. B* **2013**, *87* (11), 115418. https://doi.org/10.1103/PhysRevB.87.115418.

(132) Jin, Z.; Li, X.; Mullen, J. T.; Kim, K. W. Intrinsic Transport Properties of Electrons and Holes in Monolayer Transition-Metal Dichalcogenides. *Phys. Rev. B* **2014**, *90* (4), 045422. https://doi.org/10.1103/PhysRevB.90.045422.

(133) Gunst, T.; Markussen, T.; Stokbro, K.; Brandbyge, M. First-Principles Method for Electron-Phonon Coupling and Electron Mobility: Applications to Two-Dimensional Materials. *Phys. Rev. B* **2016**, *93* (3), 035414. https://doi.org/10.1103/PhysRevB.93.035414.

(134) Cai, Y.; Zhang, G.; Zhang, Y.-W. Polarity-Reversed Robust Carrier Mobility in Monolayer MoS_2 Nanoribbons. *J. Am. Chem. Soc.* **2014**, *136* (17), 6269–6275. https://doi.org/10.1021/ja4109787.

(135) Akinwande, D.; Petrone, N.; Hone, J. Two-Dimensional Flexible Nanoelectronics. *Nat. Commun.* **2014**, *5*, 5678. https://doi.org/10.1038/ncomms6678.

(136) Chang, H.-Y.; Yang, S.; Lee, J.; Tao, L.; Hwang, W.-S.; Jena, D.; Lu, N.; Akinwande, D. High-Performance, Highly Bendable MoS_2 Transistors with High-κ Dielectrics for Flexible Low-Power Systems. *ACS Nano* **2013**, *7* (6), 5446–5452. https://doi.org/10.1021/nn401429w.

(137) Pu, J.; Yomogida, Y.; Liu, K.-K.; Li, L.-J.; Iwasa, Y.; Takenobu, T. Highly Flexible MoS_2 Thin-Film Transistors with Ion Gel Dielectrics. *Nano Lett.* **2012**, *12* (8), 4013–4017. https://doi.org/10.1021/nl301335q.

(138) Schwierz, F. (Invited) Performance of Graphene and Beyond Graphene 2D Semiconductor Devices. *ECS Trans.* **2015**, *69* (10), 231–240. https://doi.org/10.1149/06910.0231ecst.

(139) Yoon, Y.; Ganapathi, K.; Salahuddin, S. How Good Can Monolayer MoS_2 Transistors Be? *Nano Lett.* **2011**, *11* (9), 3768–3773. https://doi.org/10.1021/nl2018178.

(140) Liu, L.; Lu, Y.; Guo, J. On Monolayer Field-Effect Transistors at the Scaling Limit. *IEEE Trans. Electron Devices* **2013**, *60* (12), 4133–4139. https://doi.org/10.1109/TED.2013.2284591.

(141) Liu, W.; Cao, W.; Kang, J.; Banerjee, K. (Invited) High-Performance Field-Effect-Transistors on Monolayer-WSe_2. *ECS Trans.* **2013**, *58* (7), 281–285. https://doi.org/10.1149/05807.0281ecst.

(142) Granzner, R.; Geng, Z.; Kinberger, W.; Schwierz, F. MOSFET Scaling: Impact of Two-Dimensional Channel Materials. In *2016 13th IEEE International Conference on Solid-State and Integrated Circuit Technology (ICSICT)*; 2016; pp 466–469. https://doi.org/10.1109/ICSICT.2016.7998953.

(143) Uchida, K.; Watanabe, H.; Kinoshita, A.; Koga, J.; Numata, T.; Takagi, S. Experimental Study on Carrier Transport Mechanism in Ultrathin-Body SOI N and P-MOSFETs with SOI Thickness Less than 5 nm. In *Digest. International Electron Devices Meeting,*; 2002; pp 47–50. https://doi.org/10.1109/IEDM.2002.1175776.

(144) Jena, D. Tunneling Transistors Based on Graphene and 2-D Crystals. *Proc. IEEE* **2013**, *101* (7), 1585–1602. https://doi.org/10.1109/JPROC.2013.2253435.

(145) Lee, J.; Chang, H. Y.; Ha, T. J.; Li, H.; Ruoff, R. S.; Dodabalapur, A.; Akinwande, D. High-Performance Flexible Nanoelectronics: 2D Atomic Channel Materials for Low-Power Digital and High-Frequency Analog Devices. In *2013 IEEE International Electron Devices Meeting*; 2013; pp 19.2.1-19.2.4. https://doi.org/10.1109/IEDM.2013.6724658.

(146) Park, S.; Zhu, W.; Chang, H. Y.; Yogeesh, M. N.; Ghosh, R.; Banerjee, S. K.; Akinwande, D. High-Frequency Prospects of 2D Nanomaterials for Flexible Nanoelectronics from Baseband to Sub-THz Devices. In *2015 IEEE International Electron Devices Meeting (IEDM)*; 2015; pp 32.1.1-32.1.4. https://doi.org/10.1109/IEDM.2015.7409812.

(147) Zhu, W.; Park, S.; Yogeesh, M. N.; Akinwande, D. Advancements in 2D Flexible Nanoelectronics: From Material Perspectives to RF Applications. *Flex. Print. Electron.* **2017**, *2* (4), 043001. https://doi.org/10.1088/2058-8585/aa84a4.

(148) Yu, Z.; Ong, Z.-Y.; Li, S.; Xu, J.-B.; Zhang, G.; Zhang, Y.-W.; Shi, Y.; Wang, X. Analyzing the Carrier Mobility in Transition-Metal Dichalcogenide MoS_2 Field-

Effect Transistors. *Adv. Funct. Mater.* **2017**, *27* (19), p.1604093. https://doi.org/10.1002/adfm.201604093.

(149) Smithe, K. K. H.; English, C. D.; Suryavanshi, S. V.; Pop, E. Intrinsic Electrical Transport and Performance Projections of Synthetic Monolayer MoS_2 Devices. *2D Mater.* **2017**, *4* (1), 011009. https://doi.org/10.1088/2053-1583/4/1/011009.

(150) Cao, W.; Kang, J.; Sarkar, D.; Liu, W.; Banerjee, K. Performance Evaluation and Design Considerations of 2D Semiconductor Based FETs for Sub-10 nm VLSI. In *2014 IEEE International Electron Devices Meeting*; 2014; pp 30.5.1-30.5.4. https://doi.org/10.1109/IEDM.2014.7047143.

(151) Cao, W.; Kang, J.; Sarkar, D.; Liu, W.; Banerjee, K. 2D Semiconductor FETs – Projections and Design for Sub-10 nm VLSI. *IEEE Trans. Electron Devices* **2015**, *62* (11), 3459–3469. https://doi.org/10.1109/TED.2015.2443039.

(152) Singh, S.; Thakar, K.; Kaushik, N.; Muralidharan, B.; Lodha, S. Performance Projections for Two-Dimensional Materials in Radio-Frequency Applications. *Phys. Rev. Appl.* **2018**, *10* (1), 014022. https://doi.org/10.1103/PhysRevApplied.10.014022.

(153) Peng, B.; Zheng, W.; Qin, J.; Zhang, W. Two-Dimensional MX_2 Semiconductors for Sub-5 nm Junctionless Field Effect Transistors. *Materials* **2018**, *11* (3), 430. https://doi.org/10.3390/ma11030430.

(154) Thiele, S.; Kinberger, W.; Granzner, R.; Fiori, G.; Schwierz, F. The Prospects of Transition Metal Dichalcogenides for Ultimately Scaled CMOS. *Solid-State Electron.* **2018**, *143*, 2–9. https://doi.org/10.1016/j.sse.2017.11.004.

(155) Xu, Y.; Cheng, C.; Du, S.; Yang, J.; Yu, B.; Luo, J.; Yin, W.; Li, E.; Dong, S.; Ye, P.; *et al.* Contacts between Two- and Three-Dimensional Materials: Ohmic, Schottky, and P–N Heterojunctions. *ACS Nano* **2016**, *10* (5), 4895–4919. https://doi.org/10.1021/acsnano.6b01842.

(156) Giannazzo, F.; Fisichella, G.; Piazza, A.; Di Franco, S.; Greco, G.; Agnello, S.; Roccaforte, F. Impact of Contact Resistance on the Electrical Properties of MoS_2 Transistors at Practical Operating Temperatures. *Beilstein J. Nanotechnol.* **2017**, *8*, 254–263. https://doi.org/10.3762/bjnano.8.28.

(157) Liu, W.; Sarkar, D.; Kang, J.; Cao, W.; Banerjee, K. Impact of Contact on the Operation and Performance of Back-Gated Monolayer MoS_2 Field-Effect-Transistors. *ACS Nano* **2015**, *9* (8), 7904–7912. https://doi.org/10.1021/nn506512j.

(158) Das, S.; Chen, H.-Y.; Penumatcha, A. V.; Appenzeller, J. High Performance Multilayer MoS_2 Transistors with Scandium Contacts. *Nano Lett.* **2012**, *13* (1), 100–105. https://doi.org/10.1021/nl303583v.

(159) Kaushik, N.; Nipane, A.; Basheer, F.; Dubey, S.; Grover, S.; Deshmukh, M. M.; Lodha, S. Schottky Barrier Heights for Au and Pd Contacts to MoS_2. *Appl. Phys. Lett.* **2014**, *105* (11), 113505. https://doi.org/10.1063/1.4895767.

(160) Dong, H.; Gong, C.; Addou, R.; McDonnell, S.; Azcatl, A.; Qin, X.; Wang, W.; Wang, W.; Hinkle, C. L.; Wallace, R. M. Schottky Barrier Height of Pd/MoS_2 Contact by Large Area Photoemission Spectroscopy. *ACS Appl. Mater. Interfaces* **2017**. https://doi.org/10.1021/acsami.7b10974.

(161) Das, S.; Appenzeller, J. WSe_2 Field Effect Transistors with Enhanced Ambipolar Characteristics. *Appl. Phys. Lett.* **2013**, *103* (10), 103501. https://doi.org/10.1063/1.4820408.

(162) Smyth, C. M.; Walsh, L. A.; Bolshakov, P.; Catalano, M.; Addou, R.; Wang, L.; Kim, J.; Kim, M. J.; Young, C. D.; Hinkle, C. L.; *et al.* Engineering the Palladium–WSe_2 Interface Chemistry for Field Effect Transistors with High-Performance Hole Contacts. *ACS Appl. Nano Mater.* **2019**, *2* (1), 75–88. https://doi.org/10.1021/acsanm.8b01708.

(163) Liu, Y.; Stradins, P.; Wei, S.-H. Van der Waals Metal-Semiconductor Junction: Weak Fermi Level Pinning Enables Effective Tuning of Schottky Barrier. *Sci. Adv.* **2016**, *2* (4), e1600069. https://doi.org/10.1126/sciadv.1600069.

(164) McDonnell, S.; Addou, R.; Buie, C.; Wallace, R. M.; Hinkle, C. L. Defect-Dominated Doping and Contact Resistance in MoS_2. *ACS Nano* **2014**, *8* (3), 2880–2888. https://doi.org/10.1021/nn500044q.

(165) Addou, R.; Colombo, L.; Wallace, R. M. Surface Defects on Natural MoS_2. *ACS Appl. Mater. Interfaces* **2015**, *7* (22), 11921–11929. https://doi.org/10.1021/acsami.5b01778.

(166) Addou, R.; McDonnell, S.; Barrera, D.; Guo, Z.; Azcatl, A.; Wang, J.; Zhu, H.; Hinkle, C. L.; Quevedo-Lopez, M.; Alshareef, H. N.; *et al.* Impurities and Electronic Property Variations of Natural MoS_2 Crystal Surfaces. *ACS Nano* **2015**, *9* (9), 9124–9133. https://doi.org/10.1021/acsnano.5b03309.

(167) Bampoulis, P.; van Bremen, R.; Yao, Q.; Poelsema, B.; Zandvliet, H. J. W.; Sotthewes, K. Defect Dominated Charge Transport and Fermi Level Pinning in MoS_2/Metal Contacts. *ACS Appl. Mater. Interfaces* **2017**, *9* (22), 19278–19286. https://doi.org/10.1021/acsami.7b02739.

(168) KC, S.; Longo, R. C.; Addou, R.; Wallace, R. M.; Cho, K. Impact of Intrinsic Atomic Defects on the Electronic Structure of MoS_2 Monolayers. *Nanotechnology* **2014**, *25* (37), 375703. https://doi.org/10.1088/0957-4484/25/37/375703.

(169) Han, Y.; Wu, Z.; Xu, S.; Chen, X.; Wang, L.; Wang, Y.; Xiong, W.; Han, T.; Ye, W.; Lin, J.; *et al.* Probing Defect-Induced Midgap States in MoS_2 Through Graphene–MoS_2 Heterostructures. *Adv. Mater. Interfaces* **2015**, *2* (8), p.1500064. https://doi.org/10.1002/admi.201500064.

(170) Lu, C.-P.; Li, G.; Mao, J.; Wang, L.-M.; Andrei, E. Y. Bandgap, Mid-Gap States, and Gating Effects in MoS_2. *Nano Lett.* **2014**, *14* (8), 4628–4633. https://doi.org/10.1021/nl501659n.

(171) Kang, J.; Liu, W.; Sarkar, D.; Jena, D.; Banerjee, K. Computational Study of Metal Contacts to Monolayer Transition-Metal Dichalcogenide Semiconductors. *Phys. Rev. X* **2014**, *4* (3), 031005. https://doi.org/10.1103/PhysRevX.4.031005.

(172) Gong, C.; Colombo, L.; Wallace, R. M.; Cho, K. The Unusual Mechanism of Partial Fermi Level Pinning at Metal–MoS_2 Interfaces. *Nano Lett.* **2014**, *14* (4), 1714–1720. https://doi.org/10.1021/nl403465v.

(173) Farmanbar, M.; Brocks, G. First-Principles Study of van der Waals Interactions and Lattice Mismatch at MoS_2/metal Interfaces. *Phys. Rev. B* **2016**, *93* (8), 085304. https://doi.org/10.1103/PhysRevB.93.085304.

(174) Guo, Y.; Liu, D.; Robertson, J. 3D Behavior of Schottky Barriers of 2D Transition-Metal Dichalcogenides. *ACS Appl. Mater. Interfaces* **2015**, *7* (46), 25709–25715. https://doi.org/10.1021/acsami.5b06897.

(175) Monch, W. On the Physics of Metal-Semiconductor Interfaces. *Rep. Prog. Phys.* **1990**, *53* (3), 221. https://doi.org/10.1088/0034-4885/53/3/001.

(176) Louie, S. G.; Chelikowsky, J. R.; Cohen, M. L. Ionicity and the Theory of Schottky Barriers. *Phys. Rev. B* **1977**, *15* (4), 2154–2162. https://doi.org/10.1103/PhysRevB.15.2154.

(177) Tersoff, J. Schottky Barrier Heights and the Continuum of Gap States. *Phys. Rev. Lett.* **1984**, *52* (6), 465–468. https://doi.org/10.1103/PhysRevLett.52.465.

(178) Kim, C.; Moon, I.; Lee, D.; Choi, M. S.; Ahmed, F.; Nam, S.; Cho, Y.; Shin, H.-J.; Park, S.; Yoo, W. J. Fermi Level Pinning at Electrical Metal Contacts of Monolayer Molybdenum Dichalcogenides. *ACS Nano* **2017**, *11* (2), 1588–1596. https://doi.org/10.1021/acsnano.6b07159.

(179) Kaushik, N.; Grover, S.; Deshmukh, M. M.; Lodha, S. Metal Contacts to MoS_2. In *2D Inorganic Materials beyond Graphene*; WORLD SCIENTIFIC (EUROPE), 2016; pp 317–347. https://doi.org/10.1142/9781786342706_0008.

(180) Wang, Z.; Li, Q.; Chen, Y.; Cui, B.; Li, Y.; Besenbacher, F.; Dong, M. The Ambipolar Transport Behavior of WSe_2 Transistors and Its Analogue Circuits. *NPG Asia Mater.* **2018**, *10* (8), 703. https://doi.org/10.1038/s41427-018-0062-1.

(181) Resta, G. V.; Sutar, S.; Balaji, Y.; Lin, D.; Raghavan, P.; Radu, I.; Catthoor, F.; Thean, A.; Gaillardon, P.-E.; de Micheli, G. Polarity Control in WSe_2 Double-Gate Transistors. *Sci. Rep.* **2016**, *6*, 29448. https://doi.org/10.1038/srep29448.

(182) Liu, H.; Si, M.; Deng, Y.; Neal, A. T.; Du, Y.; Najmaei, S.; Ajayan, P. M.; Lou, J.; Ye, P. D. Switching Mechanism in Single-Layer Molybdenum Disulfide

Transistors: An Insight into Current Flow Across Schottky Barriers. *ACS Nano* **2014**, *8* (1), 1031–1038. https://doi.org/10.1021/nn405916t.

(183) Sze, S. M.; Ng, K. K. *Physics of Semiconductor Devices*; John Wiley & Sons, 2006.

(184) Ahmed, F.; Sup Choi, M.; Liu, X.; Jong Yoo, W. Carrier Transport at the Metal–MoS_2 Interface. *Nanoscale* **2015**, *7* (20), 9222–9228. https://doi.org/10.1039/C5NR01044F.

(185) Li, S.-L.; Tsukagoshi, K.; Orgiu, E.; Samorì, P. Charge Transport and Mobility Engineering in Two-Dimensional Transition Metal Chalcogenide Semiconductors. *Chem. Soc. Rev.* **2016**, *45* (1), 118–151. https://doi.org/10.1039/C5CS00517E.

(186) Kang, J.; Sarkar, D.; Liu, W.; Jena, D.; Banerjee, K. A Computational Study of Metal-Contacts to Beyond-Graphene 2D Semiconductor Materials. In *2012 International Electron Devices Meeting*; 2012; pp 17.4.1-17.4.4. https://doi.org/10.1109/IEDM.2012.6479060.

(187) Deng, J.; Kim, K.; Chuang, C. T.; Wong, H. S. P. The Impact of Device Footprint Scaling on High-Performance CMOS Logic Technology. *IEEE Trans. Electron Devices* **2007**, *54* (5), 1148–1155. https://doi.org/10.1109/TED.2007.894596.

(188) Wei, L.; Deng, J.; Chang, L. W.; Kim, K.; Chuang, C. T.; Wong, H. S. P. Selective Device Structure Scaling and Parasitics Engineering: A Way to Extend the Technology Roadmap. *IEEE Trans. Electron Devices* **2009**, *56* (2), 312–320. https://doi.org/10.1109/TED.2008.2010573.

(189) English, C. D.; Shine, G.; Dorgan, V. E.; Saraswat, K. C.; Pop, E. Improved Contacts to MoS_2 Transistors by Ultra-High Vacuum Metal Deposition. *Nano Lett.* **2016**, *16* (6), 3824–3830. https://doi.org/10.1021/acs.nanolett.6b01309.

(190) Taur, Y.; Ning, T. H. *Fundamentals of Modern VLSI Devices*; Cambridge University Press, 2013.

(191) Yuan, H.; Cheng, G.; Yu, S.; Walker, A. R. H.; Richter, C. A.; Pan, M.; Li, Q. Field Effects of Current Crowding in Metal-MoS_2 Contacts. *Appl. Phys. Lett.* **2016**, *108* (10), 103505. https://doi.org/10.1063/1.4942409.

(192) Guo, Y.; Han, Y.; Li, J.; Xiang, A.; Wei, X.; Gao, S.; Chen, Q. Study on the Resistance Distribution at the Contact between Molybdenum Disulfide and Metals. *ACS Nano* **2014**, *8* (8), 7771–7779. https://doi.org/10.1021/nn503152r.

(193) Berger, H. H. Models for Contacts to Planar Devices. *Solid-State Electron.* **1972**, *15* (2), 145–158. https://doi.org/10.1016/0038-1101(72)90048-2.

(194) Zhao, Y.; Xu, K.; Pan, F.; Zhou, C.; Zhou, F.; Chai, Y. Doping, Contact and Interface Engineering of Two-Dimensional Layered Transition Metal Dichalcogenides Transistors. *Adv. Funct. Mater.* **2016**, p.1603484. https://doi.org/10.1002/adfm.201603484.

(195) Porte, L.; de Villeneuve, C. H.; Phaner, M. Scanning Tunneling Microscopy Observation of Local Damages Induced on Graphite Surface by Ion Implantation. *J. Vac. Sci. Technol. B Microelectron. Nanometer Struct. Process. Meas. Phenom.* **1991**, *9* (2), 1064–1067. https://doi.org/10.1116/1.585261.

(196) Radisavljevic, B.; Kis, A. Mobility Engineering and a Metal–Insulator Transition in Monolayer MoS_2. *Nat. Mater.* **2013**, *12* (9), 815–820. https://doi.org/10.1038/nmat3687.

(197) Baugher, B. W. H.; Churchill, H. O. H.; Yang, Y.; Jarillo-Herrero, P. Intrinsic Electronic Transport Properties of High-Quality Monolayer and Bilayer MoS_2. *Nano Lett.* **2013**, *13* (9), 4212–4216. https://doi.org/10.1021/nl401916s.

(198) Jena, D.; Li, M.; Ma, N.; Hwang, W. S.; Esseni, D.; Seabaugh, A.; Xing, H. G. Electron Transport in 2D Crystal Semiconductors and Their Device Applications. In *2014 Silicon Nanoelectronics Workshop (SNW)*; 2014; pp 1–2. https://doi.org/10.1109/SNW.2014.7348543.

(199) He, G.; Ghosh, K.; Singisetti, U.; Ramamoorthy, H.; Somphonsane, R.; Bohra, G.; Matsunaga, M.; Higuchi, A.; Aoki, N.; Najmaei, S.; *et al.* Conduction Mechanisms in CVD-Grown Monolayer MoS_2 Transistors: From Variable-Range Hopping to Velocity Saturation. *Nano Lett.* **2015**, *15* (8), 5052–5058. https://doi.org/10.1021/acs.nanolett.5b01159.

(200) Khair, K.; Ahmed, S. Dissipative Transport in Monolayer MoS_2: Role of Remote Coulomb Scattering. In *2015 International Workshop on Computational Electronics (IWCE)*; 2015; pp 1–2. https://doi.org/10.1109/IWCE.2015.7301937.

(201) Mori, T.; Ninomiya, N.; Kubo, T.; Uchida, N.; Watanabe, E.; Tsuya, D.; Moriyama, S.; Tanaka, M.; Ando, A. Characterization of Effective Mobility and Its Degradation Mechanism in MoS_2 MOSFETs. *IEEE Trans. Nanotechnol.* **2016**, *15* (4), 651–656. https://doi.org/10.1109/TNANO.2016.2570280.

(202) Ahmed, S.; Yi, J. Two-Dimensional Transition Metal Dichalcogenides and Their Charge Carrier Mobilities in Field-Effect Transistors. *Nano-Micro Lett.* **2017**, *9* (4), 50. https://doi.org/10.1007/s40820-017-0152-6.

(203) Mirabelli, G.; Gity, F.; Monaghan, S.; Hurley, P. K.; Duffy, R. Impact of Impurities, Interface Traps and Contacts on MoS_2 MOSFETs: Modelling and Experiments. In *2017 47th European Solid-State Device Research Conference (ESSDERC)*; 2017; pp 288–291. https://doi.org/10.1109/ESSDERC.2017.8066648.

(204) Fang, H.; Tosun, M.; Seol, G.; Chang, T. C.; Takei, K.; Guo, J.; Javey, A. Degenerate N-Doping of Few-Layer Transition Metal Dichalcogenides by Potassium. *Nano Lett.* **2013**, *13* (5), 1991–1995. https://doi.org/10.1021/nl400044m.

(205) Du, Y.; Liu, H.; Neal, A. T.; Si, M.; Ye, P. D. Molecular Doping of Multilayer Field-Effect Transistors: Reduction in Sheet and Contact Resistances. *IEEE*

Electron Device Lett. **2013**, *34* (10), 1328–1330. https://doi.org/10.1109/LED.2013.2277311.

(206) Du, Y.; Yang, L.; Zhang, J.; Liu, H.; Majumdar, K.; Kirsch, P. D.; Ye, P. D. Field-Effect Transistors With Graphene/Metal Heterocontacts. *IEEE Electron Device Lett.* **2014**, *35* (5), 599–601. https://doi.org/10.1109/LED.2014.2313340.

(207) Kiriya, D.; Tosun, M.; Zhao, P.; Kang, J. S.; Javey, A. Air-Stable Surface Charge Transfer Doping of MoS_2 by Benzyl Viologen. *J. Am. Chem. Soc.* **2014**, *136* (22), 7853–7856. https://doi.org/10.1021/ja5033327.

(208) Kappera, R.; Voiry, D.; Yalcin, S. E.; Branch, B.; Gupta, G.; Mohite, A. D.; Chhowalla, M. Phase-Engineered Low-Resistance Contacts for Ultrathin MoS_2 Transistors. *Nat. Mater.* **2014**, *13* (12), 1128–1134. https://doi.org/10.1038/nmat4080.

(209) Yang, L.; Majumdar, K.; Liu, H.; Du, Y.; Wu, H.; Hatzistergos, M.; Hung, P. Y.; Tieckelmann, R.; Tsai, W.; Hobbs, C.; *et al.* Chloride Molecular Doping Technique on 2D Materials: WS_2 and MoS_2. *Nano Lett.* **2014**, *14* (11), 6275–6280. https://doi.org/10.1021/nl502603d.

(210) Yang, L.; Majumdar, K.; Du, Y.; Liu, H.; Wu, H.; Hatzistergos, M.; Hung, P. Y.; Tieckelmann, R.; Tsai, W.; Hobbs, C.; *et al.* High-Performance MoS_2 Field-Effect Transistors Enabled by Chloride Doping: Record Low Contact Resistance (0.5 kΩ·μm) and Record High Drain Current (460 μA/μm). In *2014 Symposium on VLSI Technology (VLSI-Technology): Digest of Technical Papers*; 2014; pp 1–2. https://doi.org/10.1109/VLSIT.2014.6894432.

(211) Liu, H.; Ye, P. D. MoS_2 Dual-Gate MOSFET With Atomic-Layer-Deposited Al_2O_3 as Top-Gate Dielectric. *IEEE Electron Device Lett.* **2012**, *33* (4), 546–548. https://doi.org/10.1109/LED.2012.2184520.

(212) Kim, S.; Konar, A.; Hwang, W.-S.; Lee, J. H.; Lee, J.; Yang, J.; Jung, C.; Kim, H.; Yoo, J.-B.; Choi, J.-Y.; *et al.* High-Mobility and Low-Power Thin-Film Transistors Based on Multilayer MoS_2 Crystals. *Nat. Commun.* **2012**, *3*, 1011. https://doi.org/10.1038/ncomms2018.

(213) McDonnell, S.; Brennan, B.; Azcatl, A.; Lu, N.; Dong, H.; Buie, C.; Kim, J.; Hinkle, C. L.; Kim, M. J.; Wallace, R. M. HfO_2 on MoS_2 by Atomic Layer Deposition: Adsorption Mechanisms and Thickness Scalability. *ACS Nano* **2013**, *7* (11), 10354–10361. https://doi.org/10.1021/nn404775u.

(214) Yang, L.; Majumdar, K.; Liu, H.; Du, Y.; Wu, H.; Hatzistergos, M.; Hung, P. Y.; Tieckelmann, R.; Tsai, W.; Hobbs, C.; *et al.* Chloride Molecular Doping Technique on 2D Materials: WS_2 and MoS_2. *Nano Lett.* **2014**, *14* (11), 6275–6280. https://doi.org/10.1021/nl502603d.

(215) Yuan, H.; Cheng, G.; You, L.; Li, H.; Zhu, H.; Li, W.; Kopanski, J. J.; Obeng, Y. S.; Hight Walker, A. R.; Gundlach, D. J.; *et al.* Influence of Metal–MoS_2 Interface

on MoS_2 Transistor Performance: Comparison of Ag and Ti Contacts. *ACS Appl. Mater. Interfaces* **2015**, *7* (2), 1180–1187. https://doi.org/10.1021/am506921y.

(216) Kim, J. Y.; Kim, S. H.; Lee, H.-H.; Lee, K.; Ma, W.; Gong, X.; Heeger, A. J. New Architecture for High-Efficiency Polymer Photovoltaic Cells Using Solution-Based Titanium Oxide as an Optical Spacer. *Adv. Mater.* **2006**, *18* (5), 572–576. https://doi.org/10.1002/adma.200501825.

(217) Ho, P.-H.; Yeh, Y.-C.; Wang, D.-Y.; Li, S.-S.; Chen, H.-A.; Chung, Y.-H.; Lin, C.-C.; Wang, W.-H.; Chen, C.-W. Self-Encapsulated Doping of N-Type Graphene Transistors with Extended Air Stability. *ACS Nano* **2012**, *6* (7), 6215–6221. https://doi.org/10.1021/nn301639j.

(218) Zhong, N.; Cao, J. J.; Shima, H.; Akinaga, H. Effect of Annealing Temperature on TiO_2-Based Thin-Film-Transistor Performance. *IEEE Electron Device Lett.* **2012**, *33* (7), 1009–1011. https://doi.org/10.1109/LED.2012.2193658.

(219) Shih, W. S.; Young, S. J.; Ji, L. W.; Water, W.; Shiu, H. W. TiO_2-Based Thin Film Transistors with Amorphous and Anatase Channel Layer. *J. Electrochem. Soc.* **2011**, *158* (6), H609–H611. https://doi.org/10.1149/1.3561271.

(220) Wobkenberg, P. H.; Ishwara, T.; Nelson, J.; Bradley, D. D. C.; Haque, S. A.; Anthopoulos, T. D. TiO_2 Thin-Film Transistors Fabricated by Spray Pyrolysis. *Appl. Phys. Lett.* **2010**, *96* (8), 082116-082116–3. https://doi.org/10.1063/1.3330944.

(221) Li, H.; Zhang, Q.; Yap, C. C. R.; Tay, B. K.; Edwin, T. H. T.; Olivier, A.; Baillargeat, D. From Bulk to Monolayer MoS_2: Evolution of Raman Scattering. *Adv. Funct. Mater.* **2012**, *22* (7), 1385–1390. https://doi.org/10.1002/adfm.201102111.

(222) Mak, K. F.; He, K.; Lee, C.; Lee, G. H.; Hone, J.; Heinz, T. F.; Shan, J. Tightly Bound Trions in Monolayer MoS_2. *Nat. Mater.* **2013**, *12* (3), 207–211. https://doi.org/10.1038/nmat3505.

(223) Mouri, S.; Miyauchi, Y.; Matsuda, K. Tunable Photoluminescence of Monolayer MoS_2 *via* Chemical Doping. *Nano Lett.* **2013**, *13* (12), 5944–5948. https://doi.org/10.1021/nl403036h.

(224) McCreary, K. M.; Pi, K.; Kawakami, R. K. Metallic and Insulating Adsorbates on Graphene. *Appl. Phys. Lett.* **2011**, *98* (19), 192101-192101–192103. https://doi.org/10.1063/1.3588035.

(225) Corbet, C. M.; McClellan, C.; Kim, K.; Sonde, S.; Tutuc, E.; Banerjee, S. K. Oxidized Titanium as a Gate Dielectric for Graphene Field Effect Transistors and Its Tunneling Mechanisms. *ACS Nano* **2014**, *8* (10), 10480–10485. https://doi.org/10.1021/nn5038509.

(226) Kresse, G.; Furthmüller, J. Efficiency of Ab-Initio Total Energy Calculations for Metals and Semiconductors Using a Plane-Wave Basis Set. *Comput. Mater. Sci.* **1996**, *6* (1), 15–50. https://doi.org/10.1016/0927-0256(96)00008-0.

(227) Kresse, G.; Furthmüller, J. Efficient Iterative Schemes for *ab initio* Total-Energy Calculations Using a Plane-Wave Basis Set. *Phys. Rev. B* **1996**, *54* (16), 11169–11186. https://doi.org/10.1103/PhysRevB.54.11169.

(228) Valsaraj, A.; Chang, J.; Rai, A.; Register, L. F.; Banerjee, S. K. Theoretical and Experimental Investigation of Vacancy-Based Doping of Monolayer MoS_2 on Oxide. *2D Mater.* **2015**, *2* (4), 045009. https://doi.org/10.1088/2053-1583/2/4/045009.

(229) Muscat, J.; Swamy, V.; Harrison, N. M. First-Principles Calculations of the Phase Stability of TiO_2. *Phys. Rev. B* **2002**, *65* (22), 224112. https://doi.org/10.1103/PhysRevB.65.224112.

(230) Liu, W.; Kang, J.; Sarkar, D.; Khatami, Y.; Jena, D.; Banerjee, K. Role of Metal Contacts in Designing High-Performance Monolayer N-Type WSe_2 Field Effect Transistors. *Nano Lett.* **2013**, *13* (5), 1983–1990. https://doi.org/10.1021/nl304777e.

(231) Ong, Z.-Y.; Fischetti, M. V. Mobility Enhancement and Temperature Dependence in Top-Gated Single-Layer MoS_2. *Phys. Rev. B* **2013**, *88* (16), 165316. https://doi.org/10.1103/PhysRevB.88.165316.

(232) Dover, R. B. van. Amorphous Lanthanide-Doped TiO_x Dielectric Films. *Appl. Phys. Lett.* **1999**, *74* (20), 3041–3043. https://doi.org/10.1063/1.124058.

(233) Robertson, J. High Dielectric Constant Oxides. *Eur. Phys. J. - Appl. Phys.* **2004**, *28* (03), 265–291. https://doi.org/10.1051/epjap:2004206.

(234) Cui, X.; Lee, G.-H.; Kim, Y. D.; Arefe, G.; Huang, P. Y.; Lee, C.-H.; Chenet, D. A.; Zhang, X.; Wang, L.; Ye, F.; *et al.* Multi-Terminal Transport Measurements of MoS_2 Using a van der Waals Heterostructure Device Platform. *Nat. Nanotechnol.* **2015**, *10* (6), 534–540. https://doi.org/10.1038/nnano.2015.70.

(235) Jena, D.; Konar, A. Enhancement of Carrier Mobility in Semiconductor Nanostructures by Dielectric Engineering. *Phys. Rev. Lett.* **2007**, *98* (13), 136805. https://doi.org/10.1103/PhysRevLett.98.136805.

(236) Peacock, P. W.; Xiong, K.; Tse, K.; Robertson, J. Bonding and Interface States of Si:HfO_2 and Si:ZrO_2 Interfaces. *Phys. Rev. B* **2006**, *73* (7), 075328. https://doi.org/10.1103/PhysRevB.73.075328.

(237) Dolui, K.; Rungger, I.; Sanvito, S. Origin of the N-Type and P-Type Conductivity of MoS_2 Monolayers on a SiO_2 Substrate. *Phys. Rev. B* **2013**, *87* (16), 165402. https://doi.org/10.1103/PhysRevB.87.165402.

(238) Rai, A.; Valsaraj, A.; Movva, H. C. P.; Roy, A.; Ghosh, R.; Sonde, S.; Kang, S.; Chang, J.; Trivedi, T.; Dey, R.; *et al.* Air Stable Doping and Intrinsic Mobility Enhancement in Monolayer Molybdenum Disulfide by Amorphous Titanium Suboxide Encapsulation. *Nano Lett.* **2015**, *15* (7), 4329–4336. https://doi.org/10.1021/acs.nanolett.5b00314.

(239) Rai, A.; Valsaraj, A.; Movva, H. C. P.; Roy, A.; Tutuc, E.; Register, L. F.; Banerjee, S. K. Interfacial-Oxygen-Vacancy Mediated Doping of MoS_2 by High-κ Dielectrics. In *2015 73rd Annual Device Research Conference (DRC)*; 2015; pp 189–190. https://doi.org/10.1109/DRC.2015.7175626.

(240) Perdew, J. P.; Wang, Y. Accurate and Simple Analytic Representation of the Electron-Gas Correlation Energy. *Phys. Rev. B* **1992**, *45* (23), 13244–13249. https://doi.org/10.1103/PhysRevB.45.13244.

(241) Mak, K. F.; Lee, C.; Hone, J.; Shan, J.; Heinz, T. F. Atomically Thin MoS_2: A New Direct-Gap Semiconductor. *Phys. Rev. Lett.* **2010**, *105* (13), 136805. https://doi.org/10.1103/PhysRevLett.105.136805.

(242) Chang, J.; Register, L. F.; Banerjee, S. K. Ballistic Performance Comparison of Monolayer Transition Metal Dichalcogenide MX_2 (M = Mo, W; X = S, Se, Te) Metal-Oxide-Semiconductor Field Effect Transistors. *J. Appl. Phys.* **2014**, *115* (8), 084506. https://doi.org/10.1063/1.4866872.

(243) Böker, Th.; Severin, R.; Müller, A.; Janowitz, C.; Manzke, R.; Voß, D.; Krüger, P.; Mazur, A.; Pollmann, J. Band Structure of MoS_2, $MoSe_2$, and α-$MoTe_2$: Angle-Resolved Photoelectron Spectroscopy and *ab initio* Calculations. *Phys. Rev. B* **2001**, *64* (23), 235305. https://doi.org/10.1103/PhysRevB.64.235305.

(244) Perdew, J. P.; Burke, K.; Ernzerhof, M. Generalized Gradient Approximation Made Simple. *Phys. Rev. Lett.* **1996**, *77* (18), 3865–3868. https://doi.org/10.1103/PhysRevLett.77.3865.

(245) Krukau, A. V.; Vydrov, O. A.; Izmaylov, A. F.; Scuseria, G. E. Influence of the Exchange Screening Parameter on the Performance of Screened Hybrid Functionals. *J. Chem. Phys.* **2006**, *125* (22), 224106. https://doi.org/10.1063/1.2404663.

(246) Grimme, S.; Antony, J.; Ehrlich, S.; Krieg, H. A Consistent and Accurate *ab initio* Parametrization of Density Functional Dispersion Correction (DFT-D) for the 94 Elements H-Pu. *J. Chem. Phys.* **2010**, *132* (15), 154104. https://doi.org/10.1063/1.3382344.

(247) Kang, J.; Lee, E.-C.; Chang, K. J. First-Principles Study of the Structural Phase Transformation of Hafnia under Pressure. *Phys. Rev. B* **2003**, *68* (5), 054106. https://doi.org/10.1103/PhysRevB.68.054106.

(248) Mo, S.-D.; Ching, W. Y. Electronic and Optical Properties of θ – Al_2O_3 and Comparison to α – Al_2O_3. *Phys. Rev. B* **1998**, *57* (24), 15219–15228. https://doi.org/10.1103/PhysRevB.57.15219.

(249) Zhang, Y.; Chang, T.-R.; Zhou, B.; Cui, Y.-T.; Yan, H.; Liu, Z.; Schmitt, F.; Lee, J.; Moore, R.; Chen, Y.; *et al.* Direct Observation of the Transition from Indirect to Direct Bandgap in Atomically Thin Epitaxial $MoSe_2$. *Nat. Nanotechnol.* **2014**, *9* (2), 111–115. https://doi.org/10.1038/nnano.2013.277.

(250) Yeh, P.-C.; Jin, W.; Zaki, N.; Zhang, D.; Liou, J. T.; Sadowski, J. T.; Al-Mahboob, A.; Dadap, J. I.; Herman, I. P.; Sutter, P.; *et al.* Layer-Dependent Electronic Structure of an Atomically Heavy Two-Dimensional Dichalcogenide. *Phys. Rev. B* **2015**, *91* (4), 041407. https://doi.org/10.1103/PhysRevB.91.041407.

(251) Capasso, F. Band-Gap Engineering: From Physics and Materials to New Semiconductor Devices. *Science* **1987**, *235* (4785), 172–176. https://doi.org/10.1126/science.235.4785.172.

(252) Peplow, M. Graphene: The Quest for Supercarbon. *Nat. News* **2013**, *503* (7476), 327. https://doi.org/10.1038/503327a.

(253) Zhu, H. L.; Zhou, C. J.; Huang, X. J.; Wang, X. L.; Xu, H. Z.; Lin, Y.; Yang, W. H.; Wu, Y. P.; Lin, W.; Guo, F. Evolution of Band Structures in MoS_2-Based Homo- and Heterobilayers. *J. Phys. Appl. Phys.* **2016**, *49* (6), 065304. https://doi.org/10.1088/0022-3727/49/6/065304.

(254) Komsa, H.-P.; Krasheninnikov, A. V. Two-Dimensional Transition Metal Dichalcogenide Alloys: Stability and Electronic Properties. *J. Phys. Chem. Lett.* **2012**, *3* (23), 3652–3656. https://doi.org/10.1021/jz301673x.

(255) Kang, J.; Tongay, S.; Li, J.; Wu, J. Monolayer Semiconducting Transition Metal Dichalcogenide Alloys: Stability and Band Bowing. *J. Appl. Phys.* **2013**, *113* (14), 143703. https://doi.org/10.1063/1.4799126.

(256) Kutana, A.; S. Penev, E.; I. Yakobson, B. Engineering Electronic Properties of Layered Transition-Metal Dichalcogenide Compounds through Alloying. *Nanoscale* **2014**, *6* (11), 5820–5825. https://doi.org/10.1039/C4NR00177J.

(257) Kim, J.-S.; Ahmad, R.; Pandey, T.; Rai, A.; Feng, S.; Yang, J.; Lin, Z.; Mauricio Terrones; Banerjee, S. K.; Singh, A. K.; *et al.* Towards Band Structure and Band Offset Engineering of Monolayer $Mo_{(1-x)}W_{(x)}S_2$ *via* Strain. *2D Mater.* **2018**, *5* (1), 015008. https://doi.org/10.1088/2053-1583/aa8e71.

(258) Lu, A.-Y.; Zhu, H.; Xiao, J.; Chuu, C.-P.; Han, Y.; Chiu, M.-H.; Cheng, C.-C.; Yang, C.-W.; Wei, K.-H.; Yang, Y.; *et al.* Janus Monolayers of Transition Metal Dichalcogenides. *Nat. Nanotechnol.* **2017**, *12* (8), 744–749. https://doi.org/10.1038/nnano.2017.100.

(259) Lin, Z.; Carvalho, B. R.; Kahn, E.; Lv, R.; Rao, R.; Terrones, H.; Pimenta, M. A.; Terrones, M. Defect Engineering of Two-Dimensional Transition Metal Dichalcogenides. *2D Mater.* **2016**, *3* (2), 022002. https://doi.org/10.1088/2053-1583/3/2/022002.

(260) Azcatl, A.; Qin, X.; Prakash, A.; Zhang, C.; Cheng, L.; Wang, Q.; Lu, N.; Kim, M. J.; Kim, J.; Cho, K.; *et al.* Covalent Nitrogen Doping and Compressive Strain in MoS_2 by Remote N_2 Plasma Exposure. *Nano Lett.* **2016**, *16* (9), 5437–5443. https://doi.org/10.1021/acs.nanolett.6b01853.

(261) Zhao, P.; Kiriya, D.; Azcatl, A.; Zhang, C.; Tosun, M.; Liu, Y.-S.; Hettick, M.; Kang, J. S.; McDonnell, S.; KC, S.; *et al.* Air Stable P-Doping of WSe_2 by Covalent Functionalization. *ACS Nano* **2014**, *8* (10), 10808–10814. https://doi.org/10.1021/nn5047844.

(262) Wu, Z.; Luo, Z.; Shen, Y.; Zhao, W.; Wang, W.; Nan, H.; Guo, X.; Sun, L.; Wang, X.; You, Y.; *et al.* Defects as a Factor Limiting Carrier Mobility in WSe_2: A Spectroscopic Investigation. *Nano Res.* **2016**, *9* (12), 3622–3631. https://doi.org/10.1007/s12274-016-1232-5.

(263) Yu, Z.; Pan, Y.; Shen, Y.; Wang, Z.; Ong, Z.-Y.; Xu, T.; Xin, R.; Pan, L.; Wang, B.; Sun, L.; *et al.* Towards Intrinsic Charge Transport in Monolayer Molybdenum Disulfide by Defect and Interface Engineering. *Nat. Commun.* **2014**, *5*, 5290. https://doi.org/10.1038/ncomms6290.

(264) Liu, D.; Guo, Y.; Fang, L.; Robertson, J. Sulfur Vacancies in Monolayer MoS_2 and Its Electrical Contacts. *Appl. Phys. Lett.* **2013**, *103* (18), 183113. https://doi.org/10.1063/1.4824893.

(265) Derycke, V.; Martel, R.; Appenzeller, J.; Avouris, Ph. Controlling Doping and Carrier Injection in Carbon Nanotube Transistors. *Appl. Phys. Lett.* **2002**, *80* (15), 2773–2775. https://doi.org/10.1063/1.1467702.

(266) Jafri, S. H. M.; Carva, K.; Widenkvist, E.; Blom, T.; Sanyal, B.; Fransson, J.; Eriksson, O.; Jansson, U.; Grennberg, H.; Karis, O.; *et al.* Conductivity Engineering of Graphene by Defect Formation. *J. Phys. Appl. Phys.* **2010**, *43* (4), 045404. https://doi.org/10.1088/0022-3727/43/4/045404.

(267) Komsa, H.-P.; Kotakoski, J.; Kurasch, S.; Lehtinen, O.; Kaiser, U.; Krasheninnikov, A. V. Two-Dimensional Transition Metal Dichalcogenides under Electron Irradiation: Defect Production and Doping. *Phys. Rev. Lett.* **2012**, *109* (3), 035503. https://doi.org/10.1103/PhysRevLett.109.035503.

(268) Suh, J.; Park, T.-E.; Lin, D.-Y.; Fu, D.; Park, J.; Jung, H. J.; Chen, Y.; Ko, C.; Jang, C.; Sun, Y.; *et al.* Doping against the Native Propensity of MoS_2: Degenerate Hole Doping by Cation Substitution. *Nano Lett.* **2014**, *14* (12), 6976–6982. https://doi.org/10.1021/nl503251h.

(269) Chuang, H.-J.; Chamlagain, B.; Koehler, M.; Perera, M. M.; Yan, J.; Mandrus, D.; Tománek, D.; Zhou, Z. Low-Resistance 2D/2D Ohmic Contacts: A Universal Approach to High-Performance WSe_2, MoS_2, and $MoSe_2$ Transistors. *Nano Lett.* **2016**, *16* (3), 1896–1902. https://doi.org/10.1021/acs.nanolett.5b05066.

(270) Tosun, M.; Chan, L.; Amani, M.; Roy, T.; Ahn, G. H.; Taheri, P.; Carraro, C.; Ager, J. W.; Maboudian, R.; Javey, A. Air-Stable N-Doping of WSe_2 by Anion Vacancy Formation with Mild Plasma Treatment. *ACS Nano* **2016**, *10* (7), 6853–6860. https://doi.org/10.1021/acsnano.6b02521.

(271) Yamamoto, M.; Nakaharai, S.; Ueno, K.; Tsukagoshi, K. Self-Limiting Oxides on WSe_2 as Controlled Surface Acceptors and Low-Resistance Hole Contacts. *Nano Lett.* **2016**, *16* (4), 2720–2727. https://doi.org/10.1021/acs.nanolett.6b00390.

(272) Bhattacharjee, S.; Ganapathi, K. L.; Chandrasekar, H.; Paul, T.; Mohan, S.; Ghosh, A.; Raghavan, S.; Bhat, N. Nitride Dielectric Environments to Suppress Surface Optical Phonon Dominated Scattering in High-Performance Multilayer MoS_2 FETs. *Adv. Electron. Mater.* **2017**, *3* (1), p.1600358. https://doi.org/10.1002/aelm.201600358.

(273) Bhattacharjee, S.; Ganapathi, K. L.; Nath, D. N.; Bhat, N. Surface State Engineering of Metal/MoS_2 Contacts Using Sulfur Treatment for Reduced Contact Resistance and Variability. *IEEE Trans. Electron Devices* **2016**, *63* (6), 2556–2562. https://doi.org/10.1109/TED.2016.2554149.

(274) Cho, K.; Min, M.; Kim, T.-Y.; Jeong, H.; Pak, J.; Kim, J.-K.; Jang, J.; Yun, S. J.; Lee, Y. H.; Hong, W.-K.; *et al.* Electrical and Optical Characterization of MoS_2 with Sulfur Vacancy Passivation by Treatment with Alkanethiol Molecules. *ACS Nano* **2015**, *9* (8), 8044–8053. https://doi.org/10.1021/acsnano.5b04400.

(275) Han, H.-V.; Lu, A.-Y.; Lu, L.-S.; Huang, J.-K.; Li, H.; Hsu, C.-L.; Lin, Y.-C.; Chiu, M.-H.; Suenaga, K.; Chu, C.-W.; *et al.* Photoluminescence Enhancement and Structure Repairing of Monolayer $MoSe_2$ by Hydrohalic Acid Treatment. *ACS Nano* **2016**, *10* (1), 1454–1461. https://doi.org/10.1021/acsnano.5b06960.

(276) Amani, M.; Lien, D.-H.; Kiriya, D.; Xiao, J.; Azcatl, A.; Noh, J.; Madhvapathy, S. R.; Addou, R.; Kc, S.; Dubey, M.; *et al.* Near-Unity Photoluminescence Quantum Yield in MoS_2. *Science* **2015**, *350* (6264), 1065–1068. https://doi.org/10.1126/science.aad2114.

(277) Movva, H. C. P.; Rai, A.; Kang, S.; Kim, K.; Fallahazad, B.; Taniguchi, T.; Watanabe, K.; Tutuc, E.; Banerjee, S. K. High-Mobility Holes in Dual-Gated WSe_2 Field-Effect Transistors. *ACS Nano* **2015**, *9* (10), 10402–10410. https://doi.org/10.1021/acsnano.5b04611.

(278) Gu, J. J.; Neal, A. T.; Ye, P. D. Effects of (NH4)2S Passivation on the off-State Performance of 3-Dimensional InGaAs Metal-Oxide-Semiconductor Field-Effect

Transistors. *Appl. Phys. Lett.* **2011**, *99* (15), 152113. https://doi.org/10.1063/1.3651754.

(279) Yang, Z.; Yao, Z.; Li, G.; Fang, G.; Nie, H.; Liu, Z.; Zhou, X.; Chen, X.; Huang, S. Sulfur-Doped Graphene as an Efficient Metal-Free Cathode Catalyst for Oxygen Reduction. *ACS Nano* **2012**, *6* (1), 205–211. https://doi.org/10.1021/nn203393d.

(280) Lv, W.; Yang, B.; Wang, B.; Wan, W.; Ge, Y.; Yang, R.; Hao, C.; Xiang, J.; Zhang, B.; Zeng, Z.; *et al.* Sulfur-Doped Black Phosphorus Field-Effect Transistors with Enhanced Stability. *ACS Appl. Mater. Interfaces* **2018**, *10* (11), 9663–9668. https://doi.org/10.1021/acsami.7b19169.

(281) Park, J. H.; Fathipour, S.; Kwak, I.; Sardashti, K.; Ahles, C. F.; Wolf, S. F.; Edmonds, M.; Vishwanath, S.; Xing, H. G.; Fullerton-Shirey, S. K.; *et al.* Atomic Layer Deposition of Al_2O_3 on WSe_2 Functionalized by Titanyl Phthalocyanine. *ACS Nano* **2016**, *10* (7), 6888–6896. https://doi.org/10.1021/acsnano.6b02648.

(282) Nakano, M.; Wang, Y.; Kashiwabara, Y.; Matsuoka, H.; Iwasa, Y. Layer-by-Layer Epitaxial Growth of Scalable WSe_2 on Sapphire by Molecular Beam Epitaxy. *Nano Lett.* **2017**, *17* (9), 5595–5599. https://doi.org/10.1021/acs.nanolett.7b02420.

(283) Khosravi, A.; Addou, R.; Smyth, C. M.; Yue, R.; Cormier, C. R.; Kim, J.; Hinkle, C. L.; Wallace, R. M. Covalent Nitrogen Doping in Molecular Beam Epitaxy-Grown and Bulk WSe_2. *APL Mater.* **2018**, *6* (2), 026603. https://doi.org/10.1063/1.5002132.

(284) Blöchl, P. E. Projector Augmented-Wave Method. *Phys. Rev. B* **1994**, *50* (24), 17953–17979. https://doi.org/10.1103/PhysRevB.50.17953.

(285) Ceperley, D. M.; Alder, B. J. Ground State of the Electron Gas by a Stochastic Method. *Phys. Rev. Lett.* **1980**, *45* (7), 566–569. https://doi.org/10.1103/PhysRevLett.45.566.

(286) Xue, J.; Sanchez-Yamagishi, J.; Bulmash, D.; Jacquod, P.; Deshpande, A.; Watanabe, K.; Taniguchi, T.; Jarillo-Herrero, P.; LeRoy, B. J. Scanning Tunnelling Microscopy and Spectroscopy of Ultra-Flat Graphene on Hexagonal Boron Nitride. *Nat. Mater.* **2011**, *10* (4), 282–285. https://doi.org/10.1038/nmat2968.

(287) Park, J. H.; Vishwanath, S.; Liu, X.; Zhou, H.; Eichfeld, S. M.; Fullerton-Shirey, S. K.; Robinson, J. A.; Feenstra, R. M.; Furdyna, J.; Jena, D.; *et al.* Scanning Tunneling Microscopy and Spectroscopy of Air Exposure Effects on Molecular Beam Epitaxy Grown WSe_2 Monolayers and Bilayers. *ACS Nano* **2016**, *10* (4), 4258–4267. https://doi.org/10.1021/acsnano.5b07698.

(288) Brixner, L. H. Preparation and Properties of the Single Crystalline AB_2-Type Selenides and Tellurides of Niobium, Tantalum, Molybdenum and Tungsten. *J. Inorg. Nucl. Chem.* **1962**, *24* (3), 257–263. https://doi.org/10.1016/0022-1902(62)80178-X.

(289) Senkevich, J. J.; Yang, G.-R.; Lu, T.-M. Aqueous Ammonium Sulfide to Modify the Surface of Low κ Dielectric Thin Films. *Colloids Surf. Physicochem. Eng. Asp.* **2003**, *214* (1), 119–126. https://doi.org/10.1016/S0927-7757(02)00363-1.

(290) Heslop, S. L.; Peckler, L.; Muscat, A. J. Reaction of Aqueous Ammonium Sulfide on SiGe 25%. *J. Vac. Sci. Technol. A* **2017**, *35* (3), 03E110. https://doi.org/10.1116/1.4982223.

(291) Sumetskii, M.; Kornyshev, A. A. Noise in STM Due to Atoms Moving in the Tunneling Space. *Phys. Rev. B* **1993**, *48* (23), 17493–17506. https://doi.org/10.1103/PhysRevB.48.17493.

(292) Han, P.; Mantooth, B. A.; Sykes, E. C. H.; Donhauser, Z. J.; Weiss, P. S. Benzene on Au{111} at 4 K: Monolayer Growth and Tip-Induced Molecular Cascades. *J. Am. Chem. Soc.* **2004**, *126* (34), 10787–10793. https://doi.org/10.1021/ja049113z.

(293) Chiu, M.-H.; Zhang, C.; Shiu, H.-W.; Chuu, C.-P.; Chen, C.-H.; Chang, C.-Y. S.; Chen, C.-H.; Chou, M.-Y.; Shih, C.-K.; Li, L.-J. Determination of Band Alignment in the Single-Layer MoS_2/WSe_2 Heterojunction. *Nat. Commun.* **2015**, *6*, 7666. https://doi.org/10.1038/ncomms8666.

(294) Liu, H. J.; Jiao, L.; Xie, L.; Yang, F.; Chen, J. L.; Ho, W. K.; Gao, C. L.; Jia, J. F.; Cui, X. D.; Xie, M. H. Molecular-Beam Epitaxy of Monolayer and Bilayer WSe_2: A Scanning Tunneling Microscopy/Spectroscopy Study and Deduction of Exciton Binding Energy. *2D Mater.* **2015**, *2* (3), 034004. https://doi.org/10.1088/2053-1583/2/3/034004.

(295) Zhang, C.; Chen, Y.; Johnson, A.; Li, M.-Y.; Li, L.-J.; Mende, P. C.; Feenstra, R. M.; Shih, C.-K. Probing Critical Point Energies of Transition Metal Dichalcogenides: Surprising Indirect Gap of Single Layer WSe_2. *Nano Lett.* **2015**, *15* (10), 6494–6500. https://doi.org/10.1021/acs.nanolett.5b01968.

(296) Fallahazad, B.; Lee, K.; Kang, S.; Xue, J.; Larentis, S.; Corbet, C.; Kim, K.; Movva, H. C. P.; Taniguchi, T.; Watanabe, K.; *et al.* Gate-Tunable Resonant Tunneling in Double Bilayer Graphene Heterostructures. *Nano Lett.* **2015**, *15* (1), 428–433. https://doi.org/10.1021/nl503756y.

(297) Dahiya, R.; Gottardi, G.; Laidani, N. PDMS Residues-Free Micro/Macrostructures on Flexible Substrates. *Microelectron. Eng.* **2015**, *136*, 57–62. https://doi.org/10.1016/j.mee.2015.04.037.

(298) Park, J. H.; Vishwanath, S.; Wolf, S.; Zhang, K.; Kwak, I.; Edmonds, M.; Breeden, M.; Liu, X.; Dobrowolska, M.; Furdyna, J.; *et al.* Selective Chemical Response of Transition Metal Dichalcogenides and Metal Dichalcogenides in Ambient Conditions. *ACS Appl. Mater. Interfaces* **2017**, *9* (34), 29255–29264. https://doi.org/10.1021/acsami.7b08244.

(299) Pan, X.; Cai, Q.; Chen, W.; Zhuang, G.; Li, X.; Wang, J. A DFT Study of Gas Molecules Adsorption on the Anatase (001) Nanotube Arrays. *Comput. Mater. Sci.* **2013**, *67*, 174–181. https://doi.org/10.1016/j.commatsci.2012.09.006.

(300) Zhang, S.; Wang, C.-G.; Li, M.-Y.; Huang, D.; Li, L.-J.; Ji, W.; Wu, S. Defect Structure of Localized Excitons in a WSe_2 Monolayer. *Phys. Rev. Lett.* **2017**, *119* (4), 046101. https://doi.org/10.1103/PhysRevLett.119.046101.

(301) Villanueva-Cab, J.; Olalde-Velasco, P.; Romero-Contreras, A.; Zhuo, Z.; Pan, F.; Rodil, S. E.; Yang, W.; Pal, U. Photocharging and Band Gap Narrowing Effects on the Performance of Plasmonic Photoelectrodes in Dye-Sensitized Solar Cells. *ACS Appl. Mater. Interfaces* **2018**, *10* (37), 31374–31383. https://doi.org/10.1021/acsami.8b10063.

(302) Zhao, W.; Ghorannevis, Z.; Kumar Amara, K.; Ren Pang, J.; Toh, M.; Zhang, X.; Kloc, C.; Heng Tan, P.; Eda, G. Lattice Dynamics in Mono- and Few-Layer Sheets of WS_2 and WSe_2. *Nanoscale* **2013**, *5* (20), 9677–9683. https://doi.org/10.1039/C3NR03052K.

(303) Rai, A.; Movva, H.; Roy, A.; Taneja, D.; Chowdhury, S.; Banerjee, S.; Rai, A.; Movva, H. C. P.; Roy, A.; Taneja, D.; *et al.* Progress in Contact, Doping and Mobility Engineering of MoS_2: An Atomically Thin 2D Semiconductor. *Crystals* **2018**, *8* (8), 316. https://doi.org/10.3390/cryst8080316.

(304) Late, D. J.; Liu, B.; Matte, H. S. S. R.; Dravid, V. P.; Rao, C. N. R. Hysteresis in Single-Layer MoS_2 Field Effect Transistors. *ACS Nano* **2012**, *6* (6), 5635–5641. https://doi.org/10.1021/nn301572c.

(305) Frank, M. M.; Koester, S. J.; Copel, M.; Ott, J. A.; Paruchuri, V. K.; Shang, H.; Loesing, R. Hafnium Oxide Gate Dielectrics on Sulfur-Passivated Germanium. *Appl. Phys. Lett.* **2006**, *89* (11), 112905. https://doi.org/10.1063/1.2338751.

(306) Yokoyama, M.; Yasuda, T.; Takagi, H.; Miyata, N.; Urabe, Y.; Ishii, H.; Yamada, H.; Fukuhara, N.; Hata, M.; Sugiyama, M.; *et al.* III-V-Semiconductor-on-Insulator N-Channel Metal-Insulator-Semiconductor Field-Effect Transistors with Buried Al_2O_3 Layers and Sulfur Passivation: Reduction in Carrier Scattering at the Bottom Interface. *Appl. Phys. Lett.* **2010**, *96* (14), 142106. https://doi.org/10.1063/1.3374447.

(307) Sardashti, K.; Hu, K.-T.; Tang, K.; Park, S.; Kim, H.; Madisetti, S.; McIntyre, P.; Oktyabrsky, S.; Siddiqui, S.; Sahu, B.; *et al.* Sulfur Passivation for the Formation of Si-Terminated Al_2O_3/SiGe(001) Interfaces. *Appl. Surf. Sci.* **2016**, *366*, 455–463. https://doi.org/10.1016/j.apsusc.2016.01.123.

Vita

Amritesh Rai completed his schooling from The Doon School, Dehradun, India, in 2007 (top 5% of class), received his B.S. (*summa cum laude*) in Electrical and Computer Engineering (ECE) from The Ohio State University (OSU) in 2012, M.S. in ECE from The University of Texas at Austin (UT) in 2016, and Ph.D. in ECE from UT in 2019. He worked as a Graduate Research Assistant at UT's Microelectronics Research Center and was advised by Professor Sanjay K. Banerjee. His specialization track was 'Solid-State Electronics' and his research focused on studying the electronic transport properties as well as the digital/RF device applications of novel atomically thin two-dimensional (2D) semiconducting materials belonging to the family of transition metal dichalcogenides, such as molybdenum disulfide and tungsten diselenide.

Amritesh serves as a reviewer for several high impact factor peer-reviewed scientific journals including ACS Nano, ACS Applied Materials & Interfaces, ACS Applied Nano Materials, 2D Materials, IEEE Transactions on Electron Devices, IEEE Electron Device Letters, Applied Physics Letters, Nanoscale, Nanomaterials, Materials, and Electronics. He has authored and co-authored more than 50 journal publications and conference proceedings, and has an h-index of 15, i10-index of 19, and more than 950 citations, till date, as per Google Scholar. He has also given several guest lectures in the graduate-level course 'Carbon and 2D Devices' taught at UT by Professor Deji Akinwande. During graduate school, Amritesh also worked as a 'Graduate Research Intern' at Argonne National Laboratory's Center for Nanoscale Materials in Lemont, IL, as well as a 'Technology Development Intern' at the U.S. memory chip maker Micron Technology, Inc. in Boise, ID. He will be joining Micron Technology, Inc. as a full-time NAND Process Integration Engineer in Boise.

Amritesh has received several accolades and recognitions for his excellent academic and research performance. While at OSU, he received the 'Academic Excellence Award' from the IEEE Columbus Section, the 'Undergraduate Enrichment Award' from the Honor Society of Phi Kappa Phi, and was inducted into IEEE-Eta Kappa Nu (IEEE-HKN) – the honor society of IEEE. At UT, he was selected by the UT ECE Department as its top-

ranked nominee for the 2016 IBM Ph.D. Fellowship, and by Qualcomm as one of the U.S. Finalists for its highly competitive Qualcomm Innovation Fellowship in 2017. He has received the 'Professional Development Award' twice as well as the 'Academic Enrichment Award' from the UT Graduate School.

Besides research and academia, Amritesh has served in various mentorship, outreach and leadership roles. He has mentored several undergraduates, high school students and teachers as part of various STEM outreach and mentorship programs at UT, and is a two-time recipient of the 'Best Mentor Award' administered by UT's NSF NASCENT Engineering Research Center. He also served as President of the Student Leadership Council of the NASCENT ERC. He is the Founder and Past Chair of the first-ever IEEE Graduate Student Chapter, a chapter of IEEE TEMS affiliated to the IEEE Central Texas Section, in the whole of IEEE Region 5. Amritesh currently serves as the Young Professionals Chair of IEEE Region 5 and is also the Vice Chair of the 2020 IEEE Rising Stars Conference. He was recently recognized by the IEEE YP group and was featured in a Volunteer Spotlight Article published on the IEEE YP IMPACT Blog. For his outstanding leadership and volunteering efforts, Amritesh received the 2018 IEEE Region 5 Outstanding Individual Achievement Award. He is a member of IEEE, IEEE TEMS and IEEE EDS.

Email: amritesh557@gmail.com

This dissertation was typed by Amritesh Rai.